MULTISCALE THERMAL MANAGEMENT FOR ENERGY SAVING, COMFORT WEARING AND FIRE SAFETY APPLICATIONS

HU XIN

PhD

The Hong Kong Polytechnic University

2025

The Hong Kong Polytechnic University

School of Fashion and Textiles

Multiscale Thermal Management for Energy Saving, Comfort Wearing and Fire Safety Applications

HU Xin

A thesis submitted in partial fulfillment of the requirements for the degree of Doctor of Philosophy

August 2024

CERTIFICATE OF ORIGINALITY

I hereby declare that this thesis is my own work and that, to the best of my knowledge and belief, it reproduces no material previously published or written, nor material that has been accepted for the award of any other degree or diploma, except where due acknowledgement has been made in the text.

_____(Signed)

____HU Xin__(Name of student)

Abstract

Buildings are major contributors to global energy use, especially in densely populated urban areas with extreme climates. Therefore, innovative strategies targeting energy savings and sustainability are needed to address these global crises. The thesis explores the thermal management concept across multiple scales, from large buildings to individual and finally the combustion process, providing possible solution for energy savings, comfort wearing and fire safety.

The thesis begins with exploring concept of radiative cooling on transparent wood substrates for novel building thermal management. Using a purely solution-based sonochemical synthesis method that requires no temperature or vacuum control, a ZnO-coated transparent wood (CTW) composite was fabricated. This composite exhibit high emissivity (~0.91) across infrared wavelengths, making it a strong candidate for radiative cooling applications. The CTW also maintained reasonable luminous transmittance (~66.04% at a film thickness of ~360 nm), ensuring both visual comfort and illumination. The CTW window demonstrated reduced cooling energy consumption of 229 MJ·m-2 and 95 MJ·m-2 annually compared to normal and Low-E glass in Hong Kong, positioning it as a potential replacement for existing glazing materials.

Given that radiative cooling is undesirable during colder periods, this thesis further explores the benefits of self-adaptive radiative cooling regulation concept in building thermal management. The emissivity-modulated transparent wood (EMTW) was fabricated by constructing a Fabry-Perot structure consisting of an AgNWs bottom layer, a PMMA spacer, and a W-VO_2 top on TW. The EMTW exhibits an emissivity contrast of 0.44, showing significant energy-saving potential across different climate zones. In addition, positive emissivity contrast was also achieved on three other industrially relevant substrates (e.g., PET, cement, and glass), demonstrating the broad applicability and significance of this approach for promoting radiative cooling regulation in the built environment.

Then, the thesis shifts focus to personal thermal management, exploring radiative cooling regulation on textiles. As a proof-of-concept, a prototype of self-adaptive

radiative cooling fabric (SARCF) was developed, featuring high solar reflectance and variable infrared emissivity. The SARCF was created by depositing W-VO_2(M) nanoparticles on low-emissivity fabrics, followed by stitching with nanoporous polyethylene (NanoPE). This fabric exhibits significant solar reflectance (85.19%) and a promising emissivity contrast (34.82%) for radiative cooling regulation, driven by the temperature-induced phase transition of VO_2(M). Below the phase transition temperature (Tc) of VO_2(M), SARCF suppresses radiative cooling and reflects body heat with low emissivity (39.38%). Above Tc, the fabric's emissivity increases (74.20%), enhancing radiative cooling. This shift is beneficial for effective personal thermal management across various environments. Indoor and outdoor tests revealed that SARCF outperforms low-emissivity fabrics and white cotton, providing better warming (3°C higher than low-emissivity fabrics) and cooling (4.67°C).

Finally, this thesis further extends the thermal management concept downward to the combustion process, aiming to explore the heat control process in combustion. 9,10-Dihydro-10-(2,3-dicarboxypropyl)-9-oxa-10-phosphaphenanthrene 10-oxide (DOPO-ITA) was successfully prepared from 9,10-Dihydro-9-oxa-10-phosphaphenanthrene 10-oxide (DOPO) and itaconic acid (ITA). Then DOPO-ITA was chemically integrated into epoxy chains within a lignin-modified wood framework, the resulting flame retardant transparent wood (FRTW) demonstrated excellent fire safety, with a limiting oxygen index (LOI) of 31.7% and a UL-94 V0 rating. It also enhanced mechanical properties, reaching 94.98 MPa, while maintaining high visual transparency (up to 84.7% at 550 nm). Cone calorimetry revealed that FRTW20 significantly reduced peak heat release rate (HRR), total heat release (THR), and total smoke production (TSP) compared to standard transparent wood. This innovation addresses the critical issue of fire safety in transparent wood, making it a viable glazing material for modern, energy-efficient buildings.

In summary, this thesis presents thermal management at various scales, leveraging radiative cooling coating, radiative cooling regulation coating and flame-retardant curing agent to enhance energy efficiency of building, wearing comfort and fire safety of TW, respectively. The research addresses the fire safety of transparent wood, proposes dynamic radiative cooling regulation for transparent wood in various climates, and extends emissivity regulation concepts to fabrics. The demonstrated approach for

emissivity regulation holds significant potential for widespread adoption across other established materials.

Keywords: Building Thermal Management, Personal Thermal Management, Transparent Wood, Fabrics, Radiative Cooling, Emissivity Modulation, Solar Modulation, Flame Retardant, Vanadium Dioxide, Phase Transition, Fabry Perot.

Publications during Ph.D. study

Journal papers as the first author:

Hu X, Cai W, Zhang Y, et al. Facile and widely applicable route to self-adaptive emissivity modulation: energy-saving demonstration with transparent wood[J]. Nano Letters, 2024, 24(2): 657-666.

Hu X, Yu R, Wang F, et al. Fabrication, functionalities and applications of transparent wood: a review[J]. Advanced Functional Materials, 2023, 33(37): 2303278.

Hu X, Zhang Y, Zhang J, et al. Sonochemically-coated transparent wood with ZnO: Passive radiative cooling materials for energy saving applications[J]. Renewable Energy, 2022, 193: 398-406.

Hu X, Zhang Y, Cai W, et al. Transparent wood with heat shielding and high fire safety properties for energy saving applications[J]. Renewable Energy, 2023, 219: 119426.

Hu X, Zhang Y, Cai W, et al. Colorful and Temperature-Adaptive Radiative Coolers for All-Season Thermal Management Applications[J]. Renewable Energy, 2025: 122447.

Hu X, Noor N, Fei B, et al. Self-Adaptive Radiative Cooling Regulation on Fabrics. To be submitted.

Hu X, Noor N, Fei B, et al. Flame-Retardant Transparent Wood with Enhanced Mechanical Performance via Bio-Based Co-Curing Agent. To be submitted.

Journal papers as the associate author:

Liu C, Hu X, Zhou X, et al. Guanidine-containing double-network silks with enhanced tensile and antibacterial property[J]. International Journal of Biological Macromolecules, 2023, 244: 125470.

Wang Q, Xu B, Tan D, et al. Nature-inspired scalable high-performance triboelectric nanogenerators for energy harvesting and sensing[J]. Nano Energy, 2024, 121: 109217.

Liu I C Y, Hu X, Fei B, et al. Fluorine-free nanoparticle coatings on cotton fabric: comparing the UV-protective and hydrophobic capabilities of silica vs. silica-ZnO nanostructures[J]. RSC advances, 2024, 14(7): 4301-4314.

Ming Y, Liu C, Hu X, et al. Sustainable engineering of wool keratin towards cobalt atoms fixation for enhanced electrocatalytic water splitting[J]. Materials Today Sustainability, 2024, 25: 100635.

Cai W, Xing W, Cui T, et al. Biomimetic and environmentally friendly self-assembly behavior of melamine onto the surface of black phosphorus nanosheets: Constructing advanced P/N-containing nano flame retardants[J]. Composites Part A: Applied Science and Manufacturing, 2024, 178: 108006.

Cai W, Li Z, Xie H, et al. Thermally managed and fireproof composite aerogels for safer and year-round energy saving[J]. Chemical Engineering Journal, 2024, 483: 149006.

Ma X, Fu Y, Yang N, et al. Fluorescence-enhanced light-blue bilayer radiative cooling coatings[J]. Journal of Materials Chemistry A, 2024.

Ma W Y, Choi K L, Younas M W, et al. Exploring the Variation of Sonication Amplitude and Time Parameters on the Ultrasonic Disperse Dyeing of Polyacrylonitrile Fibers[J]. Fibers and Polymers, 2023, 24(3): 1093-1106.

Noor N, Mutalik S, Younas M W, et al. Sonochemical coating of textiles with zinc oxide: robust, silver-seeded growth on cotton for effective UV shielding[J]. ACS Applied

Engineering Materials, 2023, 1(12): 3254-3267.

Acknowledgements

As I near the completion of my PhD thesis, I would like to take a moment to express my deepest gratitude to everyone who has supported and guided me throughout this academic journey.

First and foremost, I extend my heartfelt thanks to my supervisor, Professor Bin Fei. Your wisdom, patience, and unwavering encouragement have been instrumental in my growth as a researcher. Your guidance, from selecting research directions to designing experiments and writing this thesis, has been invaluable.

I also wish to express my sincere appreciation to my former supervisor, Dr. Nuruzzaman Noor. Your early mentorship laid the foundation for my research, and your support during the initial stages of my PhD journey was crucial to my development as a scholar.

I am grateful to my fellow lab members and colleagues, including Ada, Judy, Yang Ming, Rujun Yu, Wei Cai, and others, whose camaraderie and collaborative spirit have made this journey more enjoyable and intellectually stimulating. Thank you for the fruitful discussions, shared experiences, and mutual support.

To my badminton friends at Hong Kong Polytechnic University—Yingbo Zhang, Qian Wang, Zixuan Kang, Junxian Huang, Wei Wu, and others—thank you for the laughter and camaraderie we shared on and off the court. Your companionship has enriched my PhD journey, adding a balance of fun and excitement to the academic rigor.

I am deeply grateful to my girlfriend, Qiao Yang, for her love, understanding, and unwavering support throughout this journey. Your encouragement during the challenging times and your belief in me have been a constant source of strength. Thank you for being by my side and sharing this journey with me.

A special thanks to my parents for their endless love, encouragement, and understanding. Your belief in me has been a constant source of motivation. Without your support, this achievement would not have been possible.

Finally, I would like to acknowledge the financial support from the Hong Kong Environment and Conservation Fund (Grant code: ECF 107/2020, P0034081) and PolyU (1-BBCB), which made this research possible.

Thank you all for being a part of this journey.

August 2024, in Hong Kong

HU Xin

Table of Contents

List of Figures

Chapter 1

Chapter 2

Chapter 5

Chapter 6

List of Tables

Abbreviations

IPCC	Intergovernmental Panel on Climate Change
HVAC	Heating, Ventilation, and Air Conditioning
TW	transparent wood
RC	Radiative cooling
PTM	Personal Thermal Management
DNA	Deoxyribonucleic acid
DOPO	9,10-dihydro-9-oxa-10-phosphaphenanthrene 10-oxide
ITA	Itaconic acid
DOPO-ITA	9,10-Dihydro-10-(2,3-dicarboxypropyl)-9-oxa-10-phosphaphenanthrene 10-oxide
PI	Polyimide
NW	Natural wood
LMW	Lignin modified wood
DW	Delignified wood
FRTW	Flame-retardant transparent wood
PMMA	Polymethyl methacrylate
EP	Epoxy resin
SiNP	Silica nanoparticle
FRs	Flame retardants
NaOH	Sodium hydroxide
DTPA	Diethylenetriaminepentaacetic acid
DI	Deionized water
FTIR	Fourier-transform infrared spectroscopy
XPS	X-ray photoelectron spectroscopy
FREP	Flame retardant epoxy resin
XRD	X-ray diffraction
LOI	Limited oxygen index
HRR	Heat release rate
THR	Total heat release
TSP	Total smoke production
SPR	Smoke production rate

ATO	Antimony-doped tin oxide
ZnO	Zinc dioxide
CTW	Coated transparent wood
AgNWs	Silver nanowires
Low-e	Low-emissivity
MIR	Mid infrared
VO_2	Vanadium Dioxide
W-VO_2	Tungsten doped vanadium dioxide
EMTW	Emissivity-modulated transparent wood
PET	Polyethylene glycol terephthalate
PVP	Polyvinylpyrrolidone
$Na_2WO_4 \cdot 2H_2O$	Sodium tungstate dihydrate
$MgSO_4$	Magnesium sulfate
PDMS	Polydimethylsiloxane
IR	Infrared
ITVOF	IR-transparent, yet visibly opaque fabric
SARCF	Self-adaptive radiative cooling regulation fabric
NanoPE	Nanoporous polyethylene
ERL	Emissivity regulation layer
VO_2(M)	Monoclinic phase of vanadium dioxide
VO_2(R)	Rutile phase of vanadium dioxide
MIT	Metal to insulator transition

Chapter 1 Introduction

1.1 Research Background

As global population and living standards rise, the energy demand in buildings continues to grow. In 2019, buildings accounted for 35% of the world's total energy consumption, with residential buildings comprising over 60% of that total. According to the U.S. Energy Information Administration, this demand is expected to increase by 28% by 2040 (Figure 1. 1)

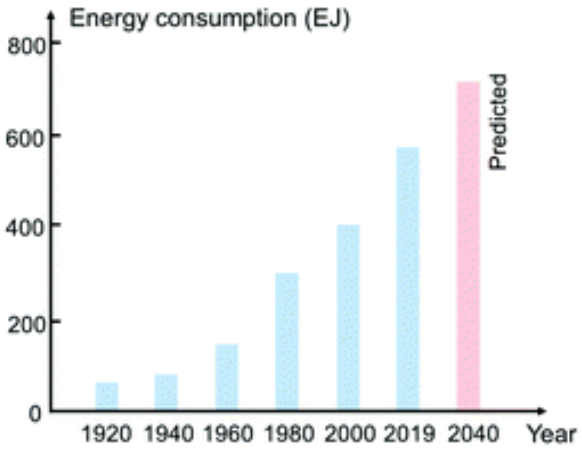

Figure 1. 1 Global energy consumption from 1920 to 2019, with a forecast to 2040(C) [1].

In extremely high-density urban areas like Hong Kong, electricity consumption can account for up to 90% of the total demand, while carbon emissions can contribute to more than 60% of the overall output. As high as 30% of the electricity was consumed by air conditioning system (Figure. 1. 2), highlighting a significant challenge posed by Hong Kong's subtropical climate. Therefore, there is an urgent need for high-efficiency, low-energy thermal management technologies to improve the energy-efficiency of traditional building temperature regulation systems.

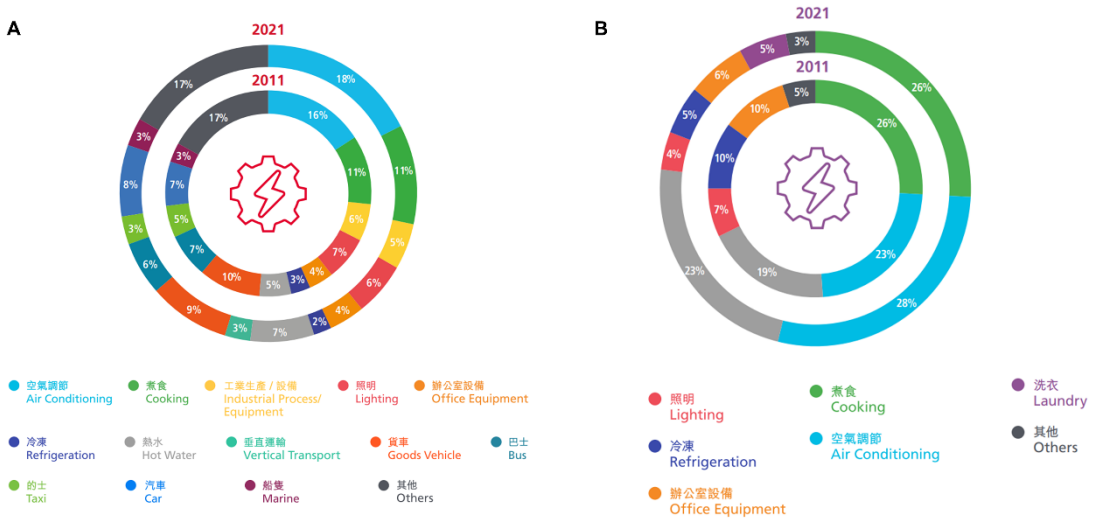

Figure. 1. 2 (A) Total energy consumption by end-use in Hong Kong. (B) Electricity consumption by end-use in Hong Kong

In response to the UN's initiative for green and low-carbon strategies, and to address the excessive energy consumption of Heating, Ventilation, and Air Conditioning (HVAC) systems, the adoption of thermal management techniques for buildings and individuals is gaining traction. Various approaches have been developed for building thermal management, with one of the most effective being the adoption of novel building materials. Traditional windows, with its thermal conductivity of approximately 1 $W \cdot m^{-1} \cdot K^{-1}$, is the most energy-inefficient part of the building envelope[2]. As a result, enhancing the thermal insulation of windows or creating alternative transparent materials that offer both superior thermal insulating and optical properties has become an urgent priority. Among the various novel window materials, transparent wood (TW) has garnered significant attention due to its unique performance. It is considered one of the most promising substitutes for traditional window materials because of its excellent visual transmission, mechanical strength, and thermal performance, showing great potential for energy-efficient building applications[3-8]. Transparent wood has demonstrated superior transparency and thermal insulating performance (thermal conductivity of approximately 0.2 $W \cdot m^{-1} \cdot K^{-1}$), ensuring comfortable visibility while minimizing heat loss through windows.

The final aim of building thermal management is to provide residents with thermal comfort, as extreme temperatures adversely affecting labor productivity and ultimately

social development of mankind[9]. To meet the narrow normal temperature range (36-38°C) required by the human physiological metabolism system[10], HVAC systems consume massive amounts of energy to maintain a narrow normal temperature setpoint rang, typically 18-22°C in winter and 22-26°C in summer. However, individual preferences for thermal comfort vary based on age, gender, and physiology, making it challenging to satisfy all occupants. Under such context, personal Thermal Management (PTM) technologies involving systems or devices that provide a satisfactory local thermal environment by regulating heat and mass transfer around the human body emerged. Personal thermal management (PTM) technology offers a promising solution by creating localized thermal environments around individuals instead of adjusting the temperature of the entire building. By employing PTM, the temperature setpoints for building HVAC systems can be widened, leading to significant energy savings. Early studies indicate that expanding the cooling and heating setpoints by just 1-2°C can reduce energy consumption by more than 15%[11, 12].

1.2 Research challenges

Despite various advancements in novel thermal management materials based on transparent wood and fabrics, holding great promise for significant economic and environmental benefits. However, the development of these technologies faces several challenges.

1. The pure ZnO coating on material usually involves high temperature and vacuum fabrication process. Constructing a pure ZnO coting on transparent wood at mild conditions need to be proposed.

2. While transparent wood with radiative cooling offers considerable energy savings, its continuous cooling power may increase the heating load in cold hours. Therefore, the dynamic manipulation of radiative cooling on TW become a challenge.

3. The continuous cooling provided by radiative cooling textile is not favorable in cold hours. However, the self-adaptively radiative cooling for textile is not unexplored yet.

4. Although the fire safety of transparent wood has been explored, improving the flame retardancy of transparent wood without sacrificing mechanical and optical properties remain challenging.

1.3 Research Objectives

This research project aims to provide effective building thermal management, and personal management solutions based the exploration of radiative cooling and radiative cooling regulation concept on transparent wood and textile, ultimately, lowering the energy consumption used for space cooling and heating. The primary objectives of this thesis are outlined as follows:

(1) Fabricate and optimize functional coatings on transparent wood via sonochemical deposition to improve its radiative cooling potential.

(2) Achieve radiative cooling regulation on transparent wood and evaluate its energy-saving potential across different climates.

(3) Create fabrics with dynamic radiative cooling and assess their impact on personal thermal comfort in various environments.

(4) Enhance the fire safety of transparent wood without compromising its transparency, insulation, or mechanical strength.

1.4 Research significance

This research is significant for its potential to tackle key challenges in building thermal management and personal thermal comfort, thereby contributing to global initiatives in energy conservation and climate change mitigation. In addition, this thesis firstly proposes to extend the thermal management concept downward to the combustion process. The innovative approaches explored in this thesis are poised to offer significant advancements in both material science and energy efficiency, with far-reaching implications for sustainable development.

The development of ZnO-coated transparent wood represents another significant advancement in building thermal management. By applying a zinc oxide (ZnO) film to transparent wood through sonochemical deposition, this research introduces a material with high emissivity and significant radiative cooling potential. The ZnO-coated transparent wood demonstrates a reduction in cooling energy consumption, offering a sustainable alternative to conventional glazing materials.

The development of tungsten-doped vanadium dioxide (W-VO_2) coatings on transparent wood for radiative cooling regulation represents a significant technological advancement. By evaluating the impact of synthesis and coating parameters, this research seeks to optimize the emissivity regulation capacity of these coatings, offering considerable energy saving in various climatic conditions. A positive emissivity contrast was similarly achieved on other industrially relevant substrates using this method, demonstrating the significant potential of this approach for advancing and widely adopting radiative cooling regulation in the built environment. The energy-saving potential of emissivity-regulated materials could play a vital role in reducing the carbon footprint of buildings worldwide.

The creation of textiles with tunable emissivity properties, designed to provide personalized thermal comfort, addresses the limitations of conventional HVAC systems. By allowing wider temperature setpoints for building climate control, this research promises substantial energy savings. As a proof of concept, fabrics with self-adaptive radiative cooling (SARCF) via W-VO_2 were first proposed and fabricated. The integration of W-VO_2-based Fabry-Perot resonators on low-emissivity fabrics and nanoporous polyethylene (NanoPE) enables significant solar reflection and substantial emissivity contrast. This allows SARCF to provide better thermal comfort in both cold and warm periods through radiative heating and cooling. This advancement in wearable applications not only enhances individual comfort but also contributes to broader energy efficiency goals.

By synthesizing DOPO-ITA and integrating it into the epoxy crosslinking network of transparent wood, this research aims to enhance fire safety without compromising key properties such as visual transparency, thermal insulation, and mechanical strength. This advancement is essential for the practical adoption of transparent wood in real-

world applications, potentially revolutionizing the building materials industry with a sustainable and safe alternative to traditional glazing materials.

In summary, this research project offers transformative solutions for building and personal thermal management, with the potential to significantly reduce energy consumption for space cooling and heating. By addressing the fire safety of transparent wood, this thesis eliminates the safety concerns over wide practical adoption of transparent wood. By exploring radiative cooling and radiative cooling regulation concept on transparent wood and textile, this work supports global sustainability initiatives and aligns with the UN Sustainable Development Goals, paving the way for a more energy-efficient and environmentally conscious future.

1.5 Organization of the thesis

The research begins applying radiative cooling and radiative cooling regulation concepts to transparent wood, aiming to leverage its properties for effective thermal management. Subsequently, the thesis shifts focus to personal thermal management by developing textiles with dynamic emissivity. Finally, this thesis explored the thermal management concept in the burning process of TW, enhancing its fire safety while maintaining the optical clarity, and mechanical properties. The topic of each chapter is summarized as follows:

Chapter 1 summarizes the research background, research challenges, research objectives, research significance and the framework of the total thesis.

Chapter 2 will give a comprehensive literature review on the topic that this thesis involved, including transparent wood, radiative cooling for building and personal thermal management, radiative cooling regulation on the building and personal thermal management. Finally, research gaps will be identified at the end of this chapter. The discussion about transparent wood in this chapter has led to a journal publication entitled “Fabrication, functionalities and applications of transparent wood: a review” (Advanced Functional Materials, 2023, 33(37): 2303278).

Chapter 3 lists all the methodologies involved in this thesis.

Chapter 4 explores the construction of a ZnO coating on TW via sonochemical deposition. The chapter details the silver seeding process that facilitates the growth of the ZnO layer through sonochemistry. The impact of the ZnO layer on transparency and infrared emissivity was examined, and the energy-saving potential was demonstrated through simulations. This chapter has resulted in a journal publication entitled "Sonochemically-Coated Transparent Wood with ZnO: Passive Radiative Cooling Materials for Energy-Saving Applications" (Renewable Energy, 2022, 193: 398-406).

Chapter 5 investigates the concept of radiative cooling regulation in TW, focusing on its energy-saving potential for building thermal management. Tungsten-doped vanadium dioxide (W-VO_2) was synthesized through a one-pot hydrothermal process, and its phase transition behaviors were thoroughly characterized. A typical Fabry-Perot resonator, consisting of silver nanowires (AgNWs), polymethylmethacrylate, and W-VO2, was constructed on TW. This structure was also applied to other surfaces using a similar process, demonstrating the wide applicability of the approach, despite the limited emissivity contrast. The coating imparts TW with temperature-dependent infrared emissivity, achieving radiative cooling regulation. The substantial energy-saving potential of integrating TW with radiative cooling regulation into building thermal management envelopes was confirmed through simulations in various climate zones. This chapter has been published in a journal entitled "Facile and Widely Applicable Route to Self-Adaptive Emissivity Modulation: Energy-Saving Demonstration with Transparent Wood" (Nano Letters, 2024, 24(2): 657-666).

Chapter 6 pioneers the concept of self-adaptive radiative cooling regulation for personal thermal management. A functional coating, consisting of polydimethylsiloxane and W-VO_2, was applied to low-emissivity fabrics. NanoPE was then stitched onto the coated fabrics to provide significant solar reflection while allowing infrared radiation to pass through. The optical properties of the resulting self-adaptive radiative cooling fabrics (SARCF) were thoroughly characterized, and the impact of SARCF on personal thermal comfort was assessed through field tests.

Chapter 7 focuses on expanding the adoption of transparent wood (TW) for building thermal management by enhancing its fire safety. A phosphorus-containing co-curing agent (DOPO-ITA) was synthesized from the Michael addition reaction of bio-derived

itaconic acid (ITA) with 9,10-dihydro-9-oxa-10-phosphaphenanthrene 10-oxide (DOPO). DOPO-ITA was then used as a co-curing agent for the fabrication of flame-retardant TW. The visual transparency, fire and mechanical performance of the resulting material were thoroughly studied.

Chapter 8 summarizes the main findings and contributions of the thesis. It also outlines potential avenues for future research and offers recommendations for further studies in the field.

Chapter 2 Literature review

2.1 Thermal management

2.1.1 Building thermal management

Building thermal management is a comprehensive approach to controlling the temperature and heat flow within a building, aiming to achieve both energy efficiency and thermal comfort[13]. The building's energy balance is determined by the thermal contributions of various components and heat transfer pathways, with energy efficiency heavily influenced by innovative material design. The heat loss mainly come from walls (30%), roof (22%), windows (18%), ventilation (12%), floor (11%), and door (7%), as show in Figure 2. 1. Modern temperature regulation in buildings primarily relies on ventilation systems, alongside thermal insulation and storage materials. Therefore, the concept of building thermal management mainly involves three aspects based on the heat transfer mechanism, including conduction, convection and radiation.

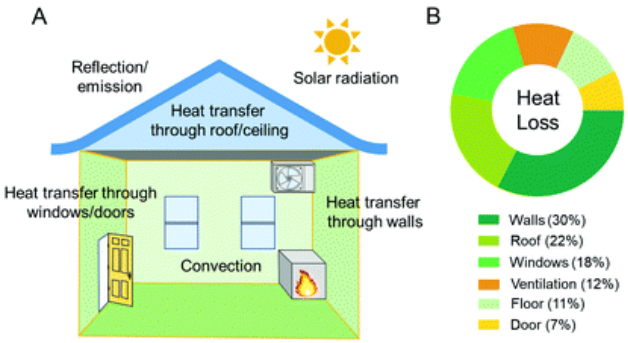

Figure 2. 1 Illustration of energy balance in a representative building envelope (A). Heat dissipation routes and their contribution percentages in a building envelope(B)[1].

Building thermal management via heat conduction focuses on controlling the flow of heat through solid materials in a building. Conduction is the process by which heat energy is transmitted through a material from a region of higher temperature to a region of lower temperature, driven by the temperature gradient. In the context of a building, this typically occurs through walls, roofs, floors, windows, and doors. Materials with high thermal conductivity (like metals) transfer heat more efficiently, which can lead to higher heat loss or gain in buildings. Conversely, materials with low thermal conductivity (like insulation materials) resist heat flow, making them effective at

reducing heat transfer. Therefore, thermal conductivity of the adopted building envelopes is crucial to the energy efficiency of building. Materials with high thermal conductivity allow heat to pass through easily. In cold climates, this can lead to significant heat loss, requiring more energy for heating. In hot climates, it can lead to heat gain, increasing the need for air conditioning. In contrast, materials with low thermal conductivity resist the flow of heat, reducing heat loss in winter and heat gain in summer. This decreases the demand for heating and cooling, resulting in lower energy consumption. Therefore, various innovative insulating materials were proposed to enhance the building energy efficiency, including modifications on many commonly used building blocks and other novel thermal insulators (e.g., aerogel)[14, 15].

The role of convection in building energy efficiency is crucial because it directly affects the temperature distribution and air flow inside the building, thus affecting the energy consumption of heating, cooling and ventilation systems. Heat convection is the process by which heat is transferred through the movement of fluids, such as air or water. In buildings, convection typically occurs through the natural movement of air or through mechanical systems like fans or HVAC systems. The innovation on this topic mainly focuses smart airflow control[16], heat recovery technology[17], natural ventilation integrated with building design[18], etc.

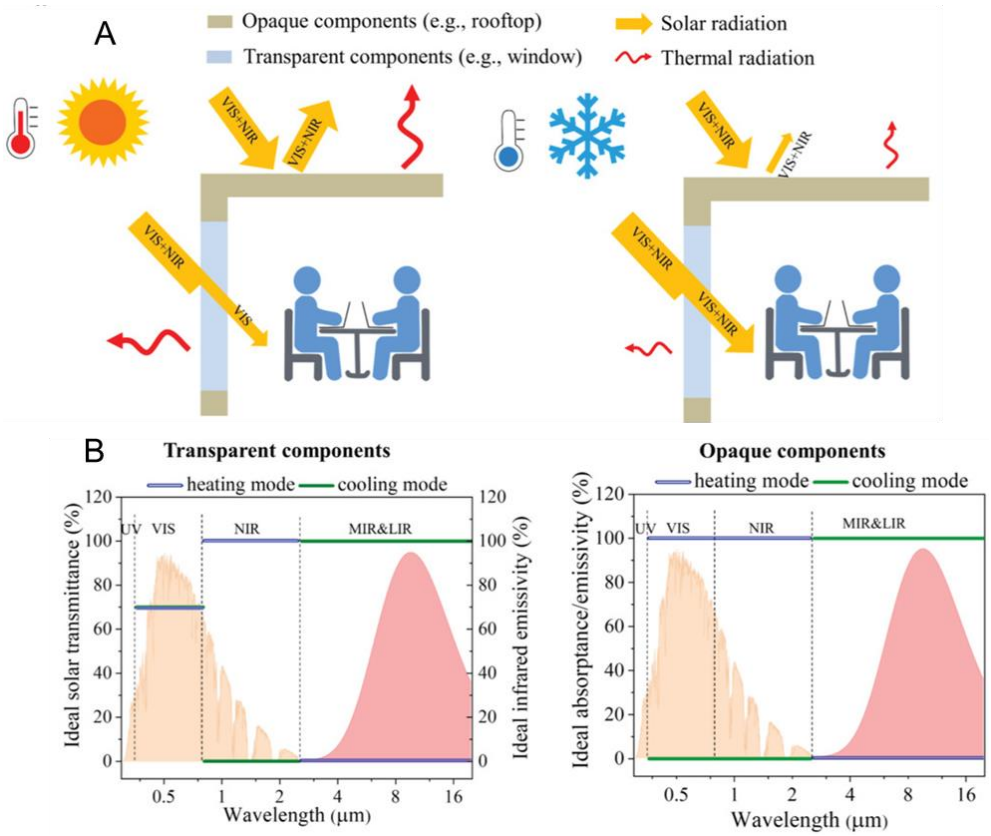

Figure 2. 2 (A)The ideal working principle of solar and infrared radiation in buildings. (B)The ideal optical properties of transparent and opaque building envelopes[19].

Radiation plays a vital role in building thermal balance. Radiation, as a way of heat transfer, propagates through electromagnetic waves in a vacuum or air without relying on a medium, and directly affects the heat gain and heat loss of a building. In recent years, manipulation on thermal radiation, including solar radiation and infrared radiation, drew much attention from both academic and industrial fields due to its huge building energy-saving potentials[20-22]. Solar radiation is the primary source of heat gain in buildings, especially during the daytime. Sunlight entering through windows, walls, and roofs increases indoor temperatures, thus raising cooling loads. At night, building surfaces radiate heat to the cooler sky, leading to heat loss. This radiative cooling can cause indoor temperatures to drop, increasing the heating demand, particularly in cold climates. As shown in Figure 2. 2, transparent building blocks, like windows, must maintain high transparency to visible light (0.38–0.76 μm) in both hot and cold conditions to ensure adequate natural lighting. For opaque components such as walls, it should reflect both visible and NIR light in summer to reduce heat absorption, but in winter, they should have lower reflectance to retain warmth. Additionally, as both

transparent and opaque elements emit thermal radiation to the outdoors, all the building envelopes should minimize infrared thermal emissivity in winter to prevent heat loss, while maximizing it in summer to enhance radiative cooling.

2.1.2 Personal thermal management

Personal thermal management (PTM) refers to strategies and technologies designed to regulate an individual's thermal comfort by managing the temperature of their immediate environment or clothing, rather than relying solely on large-scale climate control systems like HVAC (Heating, Ventilation, and Air Conditioning). PTM aims to improve thermal comfort while reducing energy consumption by targeting the thermal environment around the person, rather than the entire space.

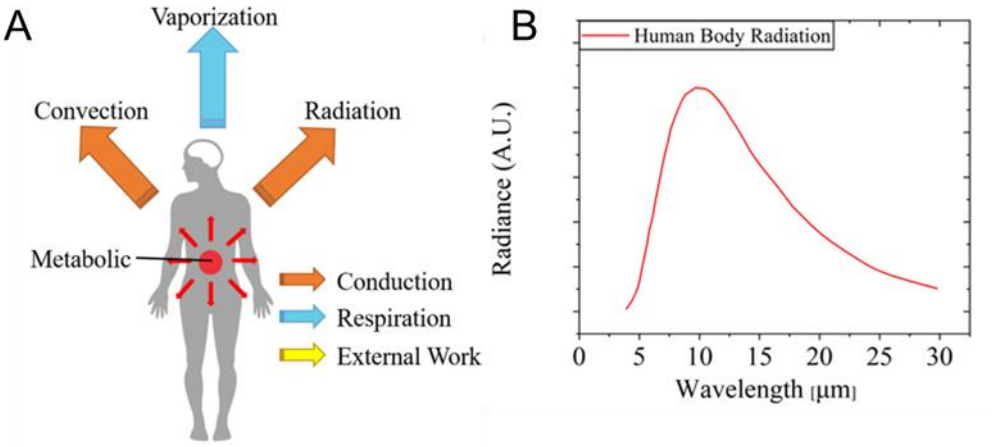

Figure 2. 3 (A)Heat transfer mechanisms of a human body, (B) Human body radiation[9].

Before discussing various advancements for PTM, we should understand the thermal balance of human body. The heat transfer mode between human body environment was presented in Figure 2. 3A, and illustrated as follow in a simple manner[23]:

$$P_{total} = P_{sun} + P_{gen} - P_{rad} - P_{evap} - P_{conv} - P_{cond}$$

Where P_{sun} is heat rate absorbed from the solar irradiance, P_{gen} is human body metabolic heat rate, P_{rad}, P_{evap}, P_{conv} and P_{cond} are net heat loss rates via evaporation, radiation, convection, and conduction, respectively. Please note that heat loss from convective or evaporative respirations are not included here.

The power intensity of the metabolic heat rate (P_{gen}) varies from the physical activities,

ranging from 50-150 $W \cdot m^{-2}$. The power density of solar radiation can be up to 1000 $W \cdot m^{-2}$, distributed within 200-2500 nm. And more than 60% total solar irradiance can be absorbed by human body[24]. For the case of indoor environment, P_{sun} can be gone. The thermal balance is dominated by radiation transfer, making the adjustment of radiative heat transfer highly effective for personal thermal management (PTM). As illustrated in Figure 2. 3B, the blackbody radiation curve at human body temperature indicates that the human body primarily emits thermal energy within the wavelength range of 7–14 μm, with a peak around 9.5 μm. Therefore, the infrared property of clothing is crucial to the thermal comfort of human body, especially in indoor environments.

Bases on the heat dispassion process involved in the thermal balance of human body, PTM technologies aim to provide better thermal comfort via controlling one or more of these processes. Controlling the heat conduction is one of the most direct ways to control localized body temperature. For example, clothing made from materials like wool, down, or synthetic fibers is designed to minimize heat loss from the body by providing an insulating layer. These materials trap air, which has low thermal conductivity, thereby reducing the rate of heat conduction away from the body. In addition, active wearable devices are PTM devices incorporated with garment with external energy input, for example, liquid cooling garment (LCG)[25] and wearable thermoelectric devices[26]. To avoid human body suffering from extremely hot environment, such as mines, foundries, military vehicles, and some outdoor activities in hot summer, a cooling system which could cool human body fast is needed. The cooling media in the garment can be air, liquid, and others such as phase-change materials. Liquid-based cooling system has higher heat transfer coefficient than air-based, and more flexible than solid-based. PTM based on heat convection has also been intensively explored. The most typical one is the ventilated clothing, which adjusts convective and evaporative heat transfer process to achieve thermal comfort. One of the most common methods for ventilated clothing is the employment of wearable fans.

Compared to the conventional and often bulky strategies, advanced strategies for PTM are booming within the recent decade. These progresses have been primarily focused on two fronts. First, passive schemes that aim to deal with radiation and conduction

heat transfer from human body have been studied quite extensively and shown great promise[27]. Radiation has been often overlooked in traditional PTM, but it is an important factor of heat dissipation for human body, especially for indoor environment, As illustrated in Figure 2. 3B, the blackbody radiation curve at human body temperature indicates that the human body primarily emits thermal energy within the wavelength range of 7–14 μm, with a peak around 9.5 μm. Therefore, the infrared property of clothing is crucial to the thermal comfort of human body, especially in indoor environments. The radiation manipulation in PTM mainly focus on two wavelength ranges: solar (200-2500 nm) and MID infrared (2.5-15 μm). Based on the different optical properties in solar and infrared range, textiles can be used for cooling and heating purposes[28]. For cooling purpose, Mid-IR-transparent textile allows human body radiation to be dissipated as much as possible (Figure 2. 4A). The next best solution for cooling is the Mid-IR emissive textiles (Figure 2. 4B), which can greatly emit human body radiation. These two types of textiles only work in indoor environments, where solar radiation can be ignored. For outdoor environments, solar irradiance imposes huge impact on the thermal balance of human body. Therefore, Mid-IR emissive textiles need high solar reflectance and high Mid-IR emittance to achieve cooling effect (Figure 2. 4C). Finally, the low-emissivity textile can reflect the human body radiation, keeping the body warm(Figure 2. 4D).

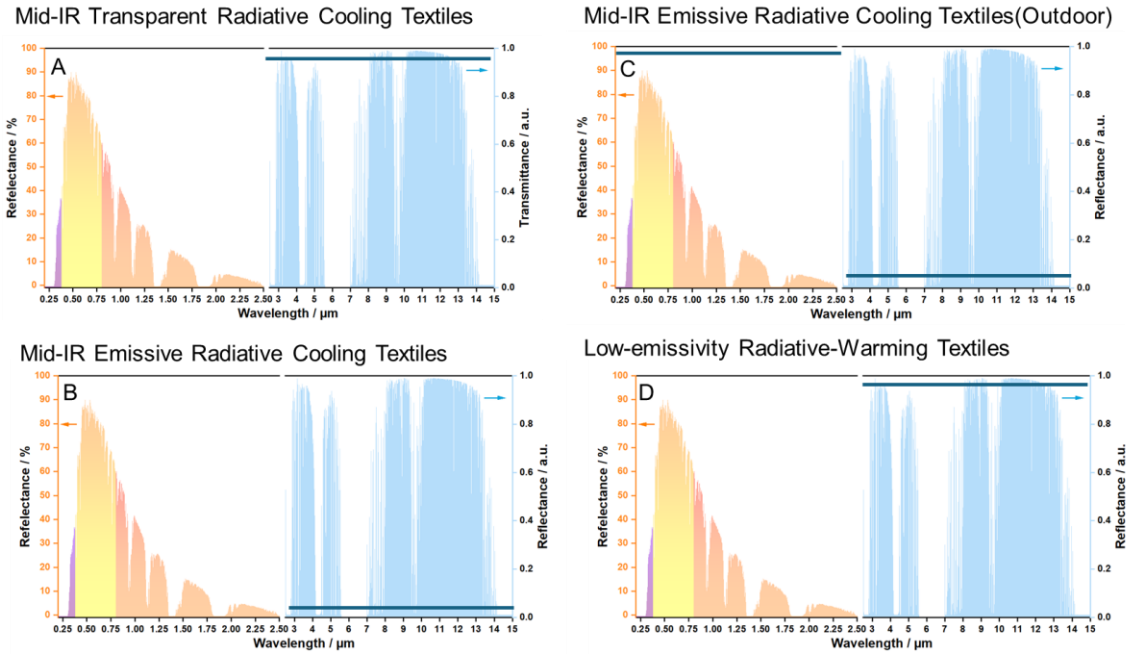

Figure 2. 4 The optical properties of four types of radiative cooling/warming textile.

2.1.3 Thermal management for fire safety purposes

Fire has played a crucial role in the advancement of human civilization, yet it continues to pose significant threats, causing extensive damage to life and property each year. Given the severity of these fire disasters, industries have implemented stringent flame-retardant standards for materials used across various applications. Polymer based materials (including transparent wood), which are fundamental to civilian, industrial, and medical sectors, are particularly vulnerable to fire due to their organic chemical structures[29]. The combustion process of polymer-based materials is resented in Figure 2. 5[30]. When exposed to heat, these materials undergo thermal decomposition, a process where chemical bonds are broken down, leading to the release of flammable gaseous vapors. In the presence of heat and oxygen, these vapors ignite and burn, generating significant amounts of heat. This heat, in turn, feeds back into the polymer, causing further decomposition and the continued release of combustible gases, thereby sustaining the fire. To combat this, numerous flame-retardant techniques have been developed based on these mechanisms, yielding effective results in enhancing the fire resistance of polymeric materials.

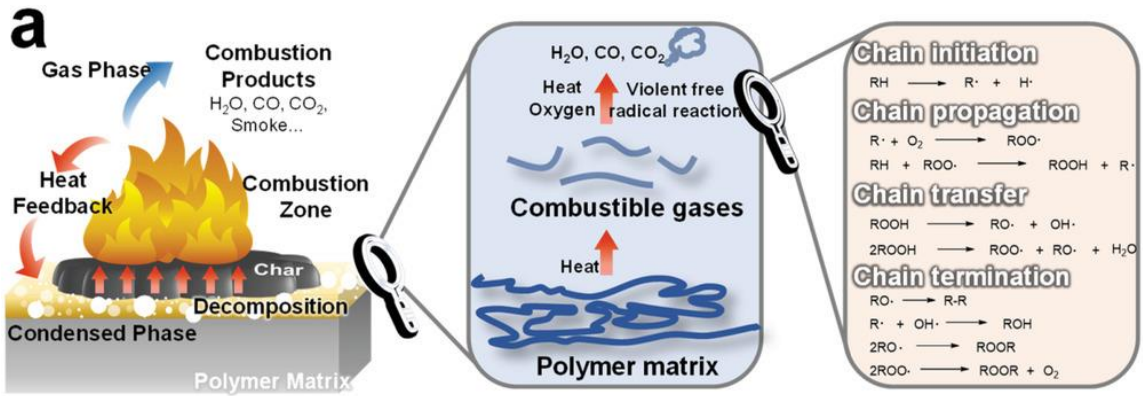

Figure 2. 5 Burning process of polymeric materials[30].

Actually, the process to improve the fire safety of TW can also be considered as a thermal management approach that control or manipulate the heat transfer during the combustion. Therefore, the thermal management concept can be downward to a smaller scale, for instance, manipulation of the heat generated during the combustion. The most direct way to control the heat release during the combustion is to add flame retardants, both inorganic and organic. All types of flame retardants affect the heat transfer process in one or more of the following three ways(Figure 2. 6)[31]: 1) Gas phase flame

retardants, reducing the heat released in the gas phase from combustion by scavenging reactive free radicals.2) Endothermic flame retardants, releasing non-flammable gases (H_2O, CO_2), diluting the fuel, cooling the polymer through endothermic decomposition. 3) Char-forming flame retardants, preventing fuel release through binding up fuel as non-hydrolysable carbon (char) and providing thermal insulation for underlying polymer through the formation of char protection layers.

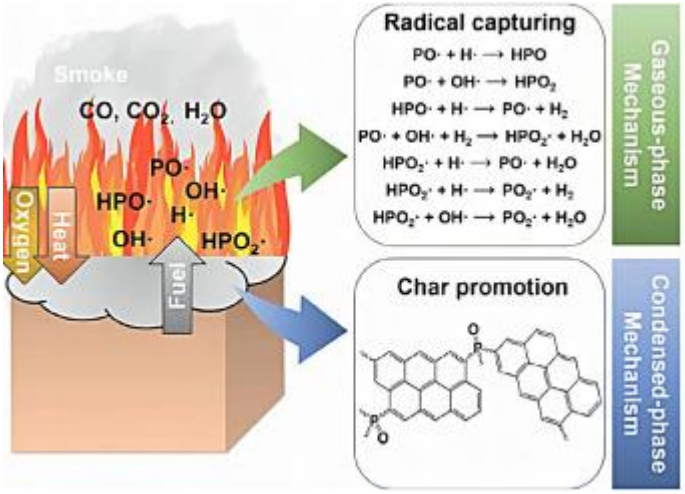

Figure 2. 6 Schematic of three ways that flame retardant affect the heat/mass transfer process of combustion.

2.2 Fundamental physics for radiation manipulation

Radiation manipulation is crucial to both building and personal thermal management. To fully understand function of radiation manipulation for novel thermal management system , the fundamental physics of blackbody radiation and radiative heat transfer will be illustrated in the following section. The main content and figures mentioned in this section were summarized from textbooks exploring thermal radiation and radiative heat transfer[32-41].

Heat conduction and convection require a medium, such as the interaction of electrons and phonons within materials or the movement of gases and liquids. Therefore, thermal radiation does not need any medium to transfer heat. To quantify the energy radiated by a blackbody surface at a given temperature, we use the concept of emissive power. Emissive power, denoted as E and measured in W/m^2, is the total energy emitted per unit area in all directions over a given wavelength range within a unit of time. Any infinitesimal surface element is divided into two symmetrical hemispheres: one emitting radiation into the upper hemisphere and also receiving radiation from the same

hemisphere. The relationship between a blackbody's emissive power (E_b) and its thermodynamic temperature (K) is governed by the Stefan-Boltzmann law, expressed as:

$$E_b = \sigma T^4 = C_0 (T/100)^4$$

Where σ Stefan-Boltzmann constant, valued at 5.67×10^{-8} W/(m^2·K^4), C0 is a blackbody radiation coefficient, valued at 5.67 W/(m^2·k^4). The subscript b represents a blackbody.

While Max Planck formulated a law to describe the distribution of energy emitted by a blackbody as a function of wavelength. To understand this law, it's necessary to introduce the concept of spectral emissive power ($E_{b\lambda}$), referring to the power emitted per unit area of a surface per unit wavelength in a given direction. It is measured in watts per square meter per micron (W/(m²·μm)). Here, λ represents the wavelength, and the unit micrometer (μm) is often used instead of meter due to the typical range of thermal radiation wavelengths. Planck's law describes how the spectral emissive power of a blackbody varies with wavelength at a given temperature. The law is given by the formula[42]:

$$E_b = \frac{c_1 \lambda^{-5}}{e^{c_2/(\lambda T)} - 1}$$

Where $E_{b\lambda}$ is the spectral emissive power in watts per cubic meter (W/m³), λ is the wavelength in meters (m), T is the absolute temperature of the blackbody in kelvin (K), e is the base of the natural logarithm, c_1 is the first radiation constant ($3.7419\times10^{-16} W\cdot m^{-2}$), c_2 is the second radiation constant ($1.4388\times10^{-2} m\cdot K$). As show in Figure 2. 7, the peak of the spectral emissive power distribution curve shifts to shorter wavelengths with the increase of temperature.

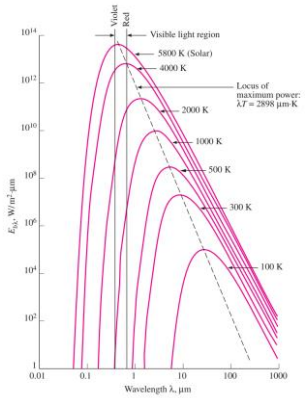

Figure 2. 7 The spectral emissive power curve of blackbody at different temperatures[36].

The area under the spectral emissive power curve shown in Figure 2. 7 represents the total emissive power of the blackbody at a given temperature. Thus, we have:

$$E_b = \int_0^\infty E_{b\lambda} d\lambda = \int_0^\infty \frac{c_1 \lambda^{-5}}{e^{c_2/(\lambda T)} - 1} d\lambda = \sigma T^4$$

It is evident that the spectral emissive power of a blackbody initially increases with wavelength, reaches a peak, and then decreases. The wavelength corresponding to the maximum spectral emissive power, denoted as λ_m, changes with temperatures. As temperature increases, the peak of the spectral emissive power distribution curve shifts to shorter wavelengths. The relationship between λ_m and T is given by Wien's Displacement Law:

$$\lambda_m \cdot T = 2.8976 \times 10^{-3} m \cdot K$$

The Wien's Displacement Law can also be derived by differentiating Planck's law with respect to λ and setting the derivative to zero.

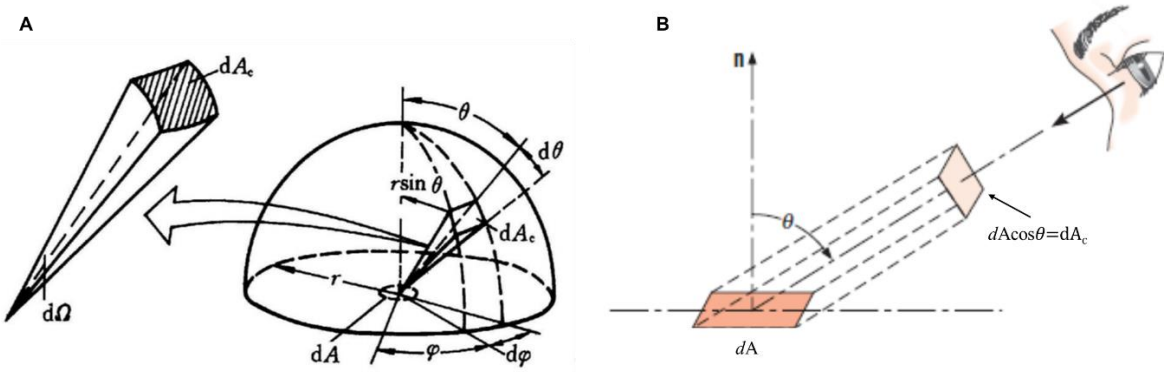

Figure 2. 8 (A) Schematic of the definition of solid angle. (B) Schematic of projected area[43].

Radiation is emitted by all parts of a plane surface in all directions into the hemisphere above the surface, and the directional distribution of emitted radiation is usually not uniform. Therefore, we need a quantity that describes the magnitude of radiation emitted in a specified direction in space. This quantity is radiation intensity, denoted by I, which is the a function of direction in a given wavelength. The direction in s space can be described using solid angle (marked as sr), as shown in Figure 2. 8A. According

to definition, the solid angle (Ω) refers to:

$$\Omega = \frac{A_C}{r^2}$$

Then we have the expression of differential solid angle:

$$d\Omega = \frac{dA_c}{r^2}$$

Based on Figure 2. 8A, the differential solid angle can be express in the form of longitudinal angle (φ) and latitudinal angle (θ) and we can also have:

$$dA_c = rd\theta \cdot r\sin\theta d\varphi$$

Thus, we have:

$$d\Omega = \frac{dA_c}{r^2} = \frac{rd\theta \cdot r\sin\theta d\varphi}{r^2} = d\theta \sin\theta d\varphi$$

Note that the area dA_c is normal to the direction of viewing direction (as shown in Figure 2. 8B). In general, the differential solid angle $d\omega$ can be subtended by a differential blackbody emitting area (dA). Obviously, we have:

$$dA_c = dA\cos\theta$$

Thus, we can have:

$$d\Omega = \frac{dA_c}{r^2} = \frac{dA\cos\theta}{r^2}$$

Then the intensity $I(\theta,\varphi)$ of the emitted radiation is defined as the rate at which radiation energy ($d\phi$) is emitted in a given direction per unit area normal to this direction (projected area) and per unit solid angle about this direction. Hence, we have:

$$I(\theta,\varphi) = \frac{d\phi}{dA_c d\Omega} = \frac{d\phi}{dA\cos\theta d\Omega} = \frac{d\phi}{dA\cos\theta d\theta \sin\theta d\varphi}$$

This equation can also be expressed as:

$$\frac{d\phi}{dAd\Omega} = I(\theta,\varphi)\cos\theta$$

and,

$$\frac{d\phi}{dAd\Omega\cos\theta} = I(\theta,\varphi)$$

Based on this equation, we can conclude that the intensity of the radiation by a surface varies with direction. But in practical use, many surfaces can be approximated as being diffuse. In this case, the intensity of the radiation by a diffusely emitting surface is

independent of direction, and thus $I(\theta,\varphi)$ is a constant, marked as I_b. Thus, we have

$$\frac{d\phi}{dAd\Omega} = I_b \cos\theta$$

and

$$\frac{d\phi}{dAd\Omega\cos\theta} = I_b$$

$\frac{d\phi}{dAd\Omega\cos\theta} = I_b$ indicates that the directional radiation intensity of a given blackbody diffuse surface is constant and is independent with the directions. This is known as Lambert's Law for blackbody radiation. It is important to note that directional radiation intensity is based on the unit projected area (see Figure 2. 8B, dA_c) as a reference. If the unit actual emitting surface area (see Figure x, dA) is used as the reference, then the result is $\frac{d\phi}{dAd\Omega} = I_b \cos\theta$, which demonstrates that energy emitted by a unit surface area of a blackbody is not uniformly distributed in different directions in space, but rather varies according to the cosine law of the latitudinal angle (θ). The radiation is maximal in the direction perpendicular to the surface and zero in the direction parallel to the surface. This is another expression of Lambert's Law, also known as the cosine law.

The relationship between the Lambert's Law and the Stefan-Boltzmann law can be described as follows:

While $\frac{d\phi}{dA}$ is the radiation flux for the emitted radiation, which is also knows as the emissive power (E). Therefore, we can have the differential form of the emissive power:

$$dE = \frac{d\phi}{dA} = I(\theta,\varphi)\cos\theta d\theta \sin\theta d\varphi$$

The hemisphere above the emitting surface will intercept all the radiation emitted by the surface, therefore, the emissive power from a given emitting surface can be determined by integration of dE . Thus, we have:

$$E = \int_{\Omega=2\pi} dE = \int_{\varphi=0}^{2\pi}\int_{\theta=0}^{\pi/2} I(\theta,\varphi)\cos\theta\sin\theta d\varphi d\theta$$

As mentioned before, the $I(\theta,\varphi)$ can be regarded as constant (I_b) as many surfaces

can be approximated as being diffuse. In this case, we have:

$$I(\theta,\varphi) = constant = I_b$$

Then we can have:

$$E = \int_{\varphi=0}^{2\pi}\int_{\theta=0}^{\pi/2} I(\theta,\varphi)\cos\theta\sin\theta d\varphi d\theta = I_b\int_{\varphi=0}^{2\pi}\int_{\theta=0}^{\pi/2}\cos\theta\sin\theta d\varphi d\theta$$

Noticing that $\int_{\varphi=0}^{2\pi}\int_{\theta=0}^{\pi/2}\cos\theta\sin\theta d\varphi d\theta = \pi$. Therefore, we can have:

$$E = I_b\int_{\varphi=0}^{2\pi}\int_{\theta=0}^{\pi/2}\cos\theta\sin\theta d\varphi d\theta = I_b\pi$$

For a blackbody, which is a diffuse emitter, we have:

$$E_b = I_b\pi$$

Where the E_b can be expressed as σT^4. Thus, the intensity of the radiation emitted by a blackbody at a given temperature (T) can be expressed as:

$$I_b(T) = \frac{\sigma T^4}{\pi}$$

Overall, we can conclude a few points for black radiation. (1) The emissive power of a blackbody is determined by the Stefan-Boltzmann Law, stating that the emissive power is proportional to the fourth power of the thermodynamic temperature. (2) The distribution of blackbody radiation energy over different wavelengths follows Planck's Law. (3) The directional distribution of blackbody radiation follows Lambert's Law. (4) The spectral emissive power of a blackbody exhibits a peak value. The wavelength λ_m corresponding to this peak value is determined by Wien's Displacement Law, which states that λ_m shifts towards shorter wavelengths as the temperature increases.

However, the real objective is not blackbody. The emissive power (E) of a real objective is always lower than that of blackbody (E_b). Here the concept of emissivity or emittance, referring to the ratio of the radiation emitted by the surface at a given temperature to the radiation emitted by a blackbody at the same temperature, was introduced. Obviously, the emissivity always varies from zero to 1and is a function of temperature (T), wavelength (λ), and direction (θ, φ). Consequently, the most fundamental emissivity of a real surface at a given temperature is the spectral directional emissivity. This is defined as the ratio of the radiation intensity emitted by the surface at a particular

wavelength and in a specific direction to the radiation intensity emitted by a blackbody at the same temperature and wavelength.

$$\varepsilon(\lambda,\theta,\varphi,T)=\frac{I(\lambda,\theta,\varphi,T)}{I_b(\lambda,T)}$$

By integrating the intensities over all wavelengths, we can have total direction emissivity:

$$\varepsilon(\theta,\varphi,T)=\frac{I(\theta,\varphi,T)}{I_b(T)}$$

Similarly, spectral hemispherical emissivity can be obtained by integrating the rate of radiation energy emitted at a specific wavelength per unit surface area over the entire hemisphere.

$$\varepsilon(\lambda,T)=\frac{E(\lambda,T)}{E_b(\lambda,T)}$$

Lastly, the total hemispherical emissivity, often referred to as the average emissivity, is defined as the radiation energy emitted across all wavelengths and in all directions.

$$\text{as: } \varepsilon(T)=\frac{E(T)}{E_b(T)}=\frac{\int_0^\infty \varepsilon(\lambda,T)E_b(\lambda,T)d\lambda}{\sigma T^4}$$

Overall, the emissivity of a surface depends on the type of material, surface temperature, and surface condition. This indicates that emissivity is related only to the radiating material itself and not to external conditions. This principle also provides ideas for the manipulation of surface emissivity in many reports.

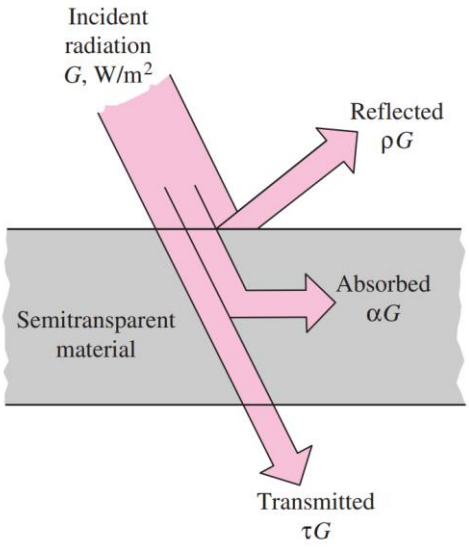

Figure 2. 9 The absorption, reflection, and transmission of the incident radiation by a semitransparent material[36].

When radiation encounters a surface, it is partially absorbed, partially reflected, and, if applicable, partially transmitted, as illustrated in Figure 2. 9The radiation flux that reaches the surface is known as irradiation and is represented by the symbol G. The absorptivity (α), reflectivity (ρ) and transmissivity (τ) were defined as follows:

$$\alpha = \frac{G_{abs}}{G}, \quad \rho = \frac{G_{ref}}{G}, \text{ and } \quad \tau = \frac{G_{tr}}{G}$$

Obviously, we can have:

$$G_{abs} + G_{ref} + G_{tr} = G$$

$$\alpha + \rho + \tau = 1$$

For an opaque surface, $\tau = 0$, we have:

$$\alpha + \rho = 1$$

While based on Kirchhoff's law, we can have:

$$\alpha(\lambda, T) = \varepsilon(\lambda, T)$$

For an opaque surface, we can have:

$$\varepsilon(\lambda, T) = \alpha(\lambda, T) = 1 - \rho(\lambda, T)$$

This equation is also the theoretical foundation of the emissivity data in many literatures that involving radiative cooling since the emissivity cannot be measured directly but calculated according to this equation. What we can obtained through FTIR spectrometer equipping with a golden integrating sphere is spectral hemispherical reflectivity. Then, the spectral hemispherical emissivity was calculated according to this equation. Overall, this section introduced the fundamental theory of blackbody radiation and radiative heat transfer, which is crucial to understand the physical mechanism of radiative cooling. Next, the thermal balance of one real terrestrial objective will be discusses to show the possibility of radiative cooling. The following section was also summarized from published literatures[44-52].

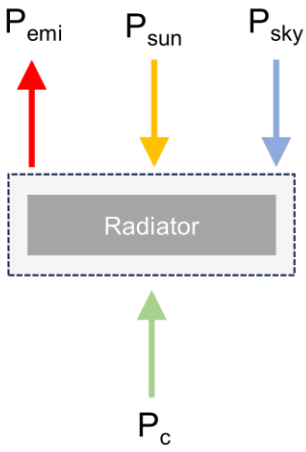

Figure 2. 10 Thermal balance of daytime radiative cooler.

However, the thermal balance of one real terrestrial objective not only involve emitting and absorbing radiation, but also non-radiative heat transfer process (as shown in Figure 2. 10). The energy balance process of a radiator in radiative cooling process can be expressed as[46]:

$$P_{cooling}(T) = P_{rad}(T) - P_c$$

Where $P_{cooling}(T)$ is the cooling power that the emitter can achieved, $P_{rad}(T)$ is the radiative thermal load of the emitter due to the radiative exchange with the surrounding environment. For daytime radiative cooling:

$$P_{cooling}(T) = P_{emi}(T) - P_{sky}(T_{amb}) - P_{sun}(T) - P_c$$

Where $P_{emi}(T)$ is the power emitted from the emitter, $P_{sky}(T_{amb})$ is the downwards radiation from the atmosphere that is absorbed by the emitter. $P_{sun}(T)$ is the incident solar power absorbed by the emitter. P_c is the heat load on the cooler due to the conductive and convective heat exchange with the environment.

$$P_{emi}(T) = A\int d\Omega \cos\theta \int_0^{\infty} d\lambda I_b(\lambda, T)\varepsilon(\lambda, \theta)$$

$$P_{sky}(T_{amb}) = A\int d\Omega \cos\theta \int_0^{\infty} d\lambda I_b(\lambda, T_{amb})\varepsilon_{sky}(\lambda, \theta)\varepsilon(\lambda, \theta)$$

$$P_{sun}(T) = A\cos\theta_{sun} \int_0^{\infty} d\lambda I_{sun}(\lambda)\varepsilon(\lambda, \theta_{sun})$$

$$P_c = Ah(T_{amb} - T)$$

Where Ω is the solid angle, θ denotes the angle between the direction of the solid

angle and the normal direction of the surface, $\varepsilon(\lambda,\theta)$ is the emissivity of the object at a wavelength λ and angle θ, $I_b(\lambda,T)$ spectral radiation intensity of a blackbody, $\varepsilon_{sky}(\lambda,\theta)$ is the emissivity of the atmosphere, $I_{sun}(\lambda)$ is the solar spectrum, θ_{sun} is the direction of the incoming sunlight and h is a combined non-radiative heat transfer coefficient that describes such conductive and convective heat exchange. Finally, the sub-ambient cooling can be achieved when the $P_{cooling}(T)$ is positive.

Despite well-established theoretical and practical demonstrations of sub-ambient cooling for various applications, two challenges remain: low performance efficiency in humid or highly cloudy climates, and the risk of overcooling. Weather significantly impacts the performance of radiative coolers due to reduced atmospheric transparency in the spectral windows caused by atmospheric component variations. The second limitation is the undesirable cooling during cold days and the heating season, which can be highly counterproductive in year-round assessments of energy savings due to temperature fluctuations in many climate zones. Although the heating penalty is not widely quantified in the literature, it is a well-acknowledged issue, and potential solutions have been identified. One possible solution is to use materials with temperature-dependent emissivity, allowing for controllable switching of emitted radiation to meet varying heating or cooling needs.

2.3 Building thermal management via radiation manipulation

2.3.1 Radiative cooling for building thermal management

Space cooling is almost indispensable for modern society, especially for building. It is also reported that nearly 40 % of the total energy consumption was related to buildings. Notably, cooling energy consumption can constitute 30% to 50% of the total energy usage in residential buildings, particularly during the summer months and in hot climates. Therefore, radiative cooling has found a clear value proposition in various building envelopes (roofs, walls, windows and coatings), alleviating the heavy cooling energy load of building thermal regulation system.

The significant potential of radiative cooling for buildings has been validated through numerical simulations. Joseph et al[53]. developed a comprehensive radiative cooling

assessment model that considers atmospheric factors such as precipitation, transparency, and wind-induced dynamic convective heat transfer coefficients. This model evaluates the global energy-saving potential of radiative cooling technology. Applying this model to single-family residential buildings, the study examined the impact of radiative cooling across all ASHRAE climate zones in the United States. The numerical analysis revealed that in warm climates, energy-saving rates exceeded 22% for high-efficiency buildings and 46% for typical buildings.

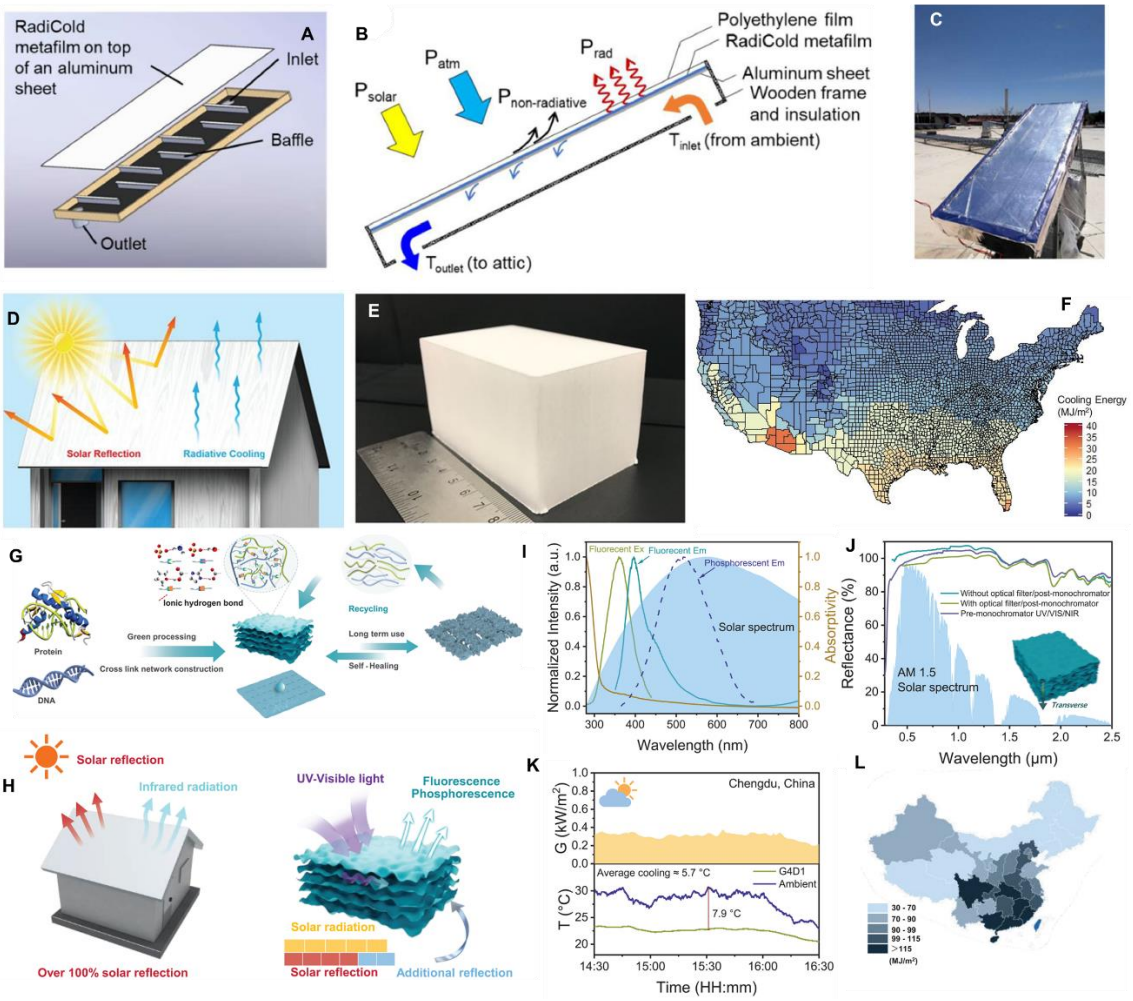

Figure 2. 11 (A-C) Demonstration of radiative air cooler [54]. (D-E) Illustration of the wooden radiative cooler (F) Energy saving potential of wood radiative cooler in US cities. [55]. (G-l) Demonstration of biomass aerogel radiative cooler. (I) [56].

Many practical demonstrations have also confirmed the effectiveness of radiative cooling for indoor space cooling. Zhao et al.[54] introduced a novel concept of a roof-integrated radiative air-cooling system (Figure 2. 11A-C) that combines radiative cooling with attic ventilation to reduce attic temperatures. They manufactured and

tested a radiative air cooler with a surface area of 1.08 square meters under outdoor conditions. During summer, the system achieved continuous day and night cooling of the air below ambient temperatures at three different flow rates—a result previously unreported. The maximum nighttime temperature reduction reached 8°C, while at noon, it was 5°C. Utilizing this roof-integrated cooling system, annual cooling energy savings ranged from 3.7 kWh/m² to 11.8 kWh/m² (26.5%–76.1%). Li et al.[55] developed a wooden daytime radiative cooling material (Figure 2. 11D-F) with excellent mechanical strength, intended for use as roof and wall coatings (Figure 2. 11 D-E). The material's efficient cooling performance is attributed to the aligned cellulose nanofibers, which strongly scatter sunlight and emit infrared radiation. This material demonstrated energy savings twice that of typical white roofs across the United States (Figure 2. 11F). More recently, Ma et al.[56], intrinsic photoluminescent biomass aerogel for building applications. The bio-based aerogel was made from DNA and gelatin, which are cross-linked by the strong ionic hydrogen bonds (Figure 2. 11G). The prepared shows great potential for building materials (Figure 2. 11H). Due to the photoluminescent effect, its "solar reflection" can exceed 100% (Figure 2. 11I&J). The outdoor test results demonstrate that an average cooling effect of 5.7°C can be achieved in cloudy conditions, and 2.9°C cooling under overcast weather (Figure 2. 11K). The energy saving simulation shows that considerable energy saving can be achieved across China by adopting this aerogel in buildings (Figure 2. 11L). Additionally, the prepared aerogel demonstrated outstanding repairability, recyclability, and biodegradability, resulting in minimal environmental impact throughout its lifecycle.

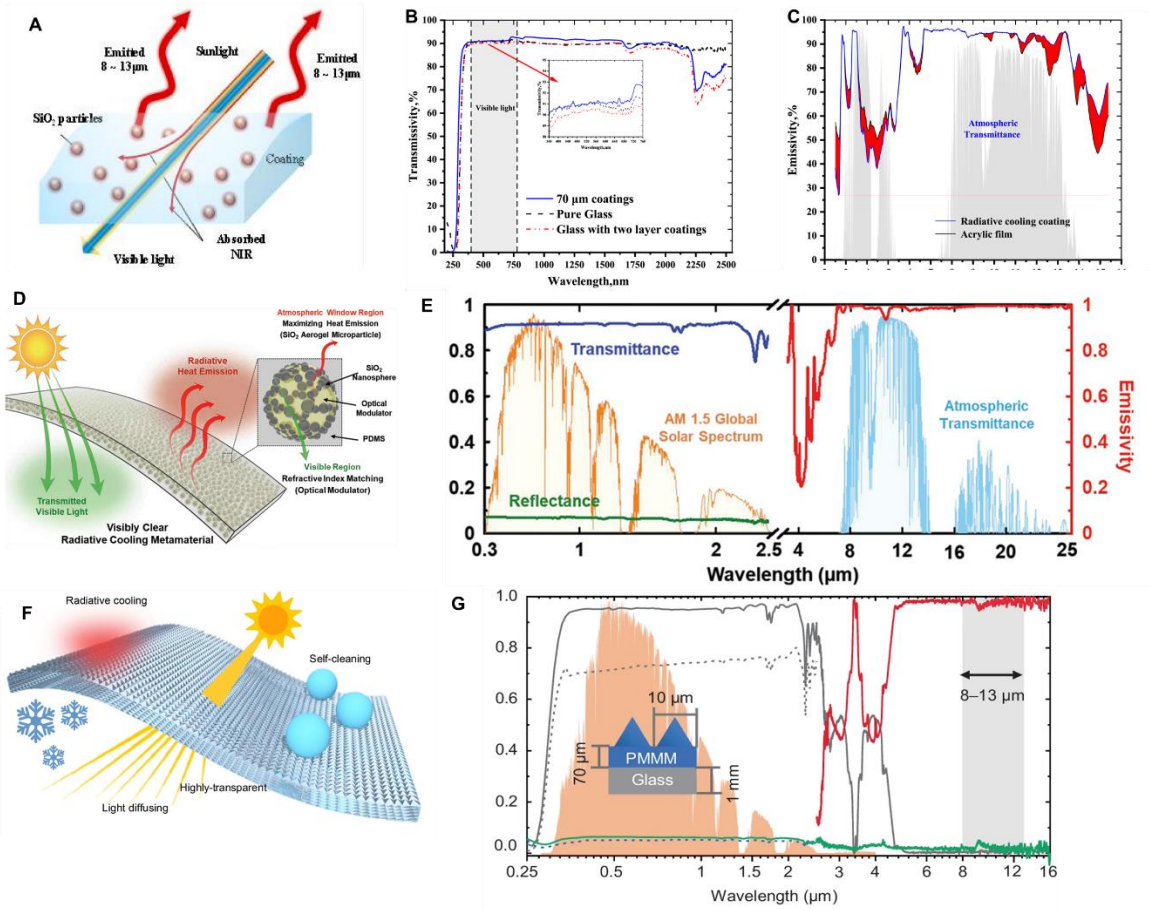

Figure 2. 12(A) Schematic of radiative cooling coating. (B) Solar transmittance of coating; (C) emissivity of acrylic film and radiative cooling coating[57]. (D) Working principle of the radiative cooling window. (E) Measured infrared transmittance and reflectance [58]. (F) Concept of PMMM integrated the functions of light diffusing, anti-reflection, self-cleaning and radiative cooling. (G) Optical properties of PMMM film on a 1-mm-thick soda-lime glass substrate. [59].

Apart from traditional roofs, radiative cooling also has applications for building windows, which are often the most energy-inefficient part of a building. Unlike roofs, radiative cooling windows require high visible transmittance and high emittance. Cheng et al. [57] employed an inexpensive, convenient, and scalable liquid blade coating method to achieve radiative cooling with exceptionally high visible light transmittance and excellent cooling performance (Figure 2. 12A). Spectral results showed an average visible light transmittance greater than 91.3%, significantly higher than previous reports, and an average emissivity within the atmospheric window exceeding 93.7% (Figure 2. 12B-C). Lee et al[58] proposed a visibly transparent

radiative cooling metamaterial that deploys light modulators in SiO2 aerogel microparticles within a polydimethylsiloxane (PDMS) matrix. The random distribution of a large quantity (40 vol.%) of SiO2 aerogel microparticles fully infiltrated with hexadecane achieves an integrated emissivity of over 98% within the atmospheric window while suppressing visible light scattering, resulting in a visible light transmittance of over 91% across wavelengths of 400–800 nm (Figure 2. 12D&E). Huang et al.[59] fabricated a polymer-based micro-photonic multifunctional metamaterial (Figure 2. 12F). This metamaterial scatters 73% of incoming sunlight, enhancing indoor comfort and privacy. Its visible light transmittance (95%, Figure 2. 12G) surpasses that of traditional glass (91%). The metamaterial exhibits high emissivity in the mid-infrared spectrum (~0.98, Figure 2. 12G), providing an estimated cooling capacity of ~97 W/m² at ambient temperature. It can maintain temperatures approximately 6°C cooler than the ambient temperature in humid Karlsruhe conditions.

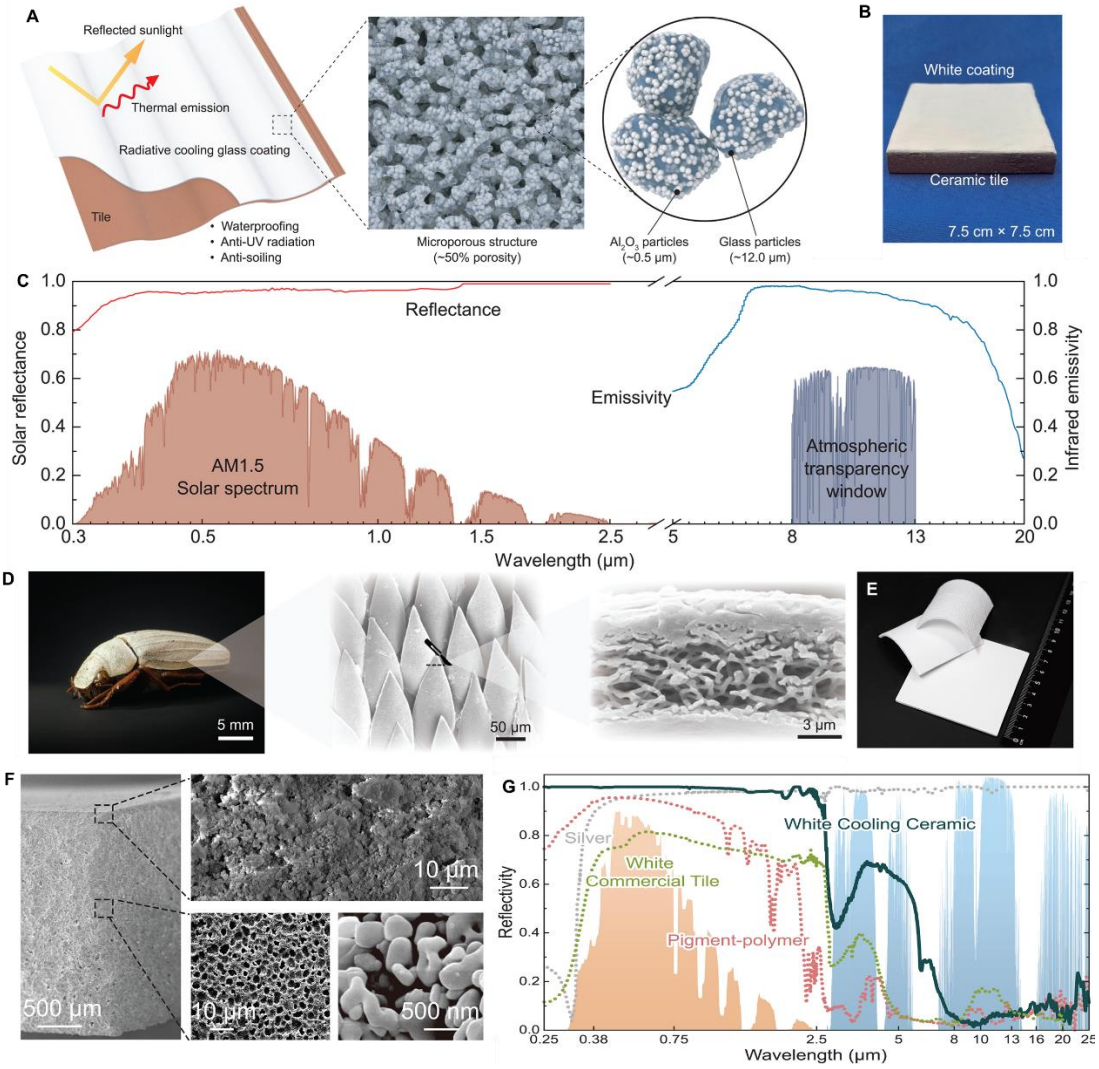

Figure 2. 13 (A) Schematic of the radiative cooling glass coating on a ceramic roofing tile. (B)The radiative cooling glass coating applied on a ceramic tile[60]. (C) The solar reflectance and infrared emissivity of the radiative cooling glass coating.(D) Photograph of the Cyphochilus specimen. (E) Photograph of the cooling ceramics with flat and curved shapes (F) The hierarchically porous structure of the cooling ceramic. (G) Comparison of the optical properties of the white cooling ceramic with white-pigmented polymer[61].

The most facile approach to apply radiative cooling technology in current buildings is coating. Many reports have explored the energy-saving potentials of radiative cooling coating in buildings. Radiative cooling can be applied onto walls or roofs, showing considerable energy saving potential in summers. Very recently, Zhao et al.[60] developed a randomized photonic composite composed of a microporous glass framework that selectively emits long-wave infrared radiation (LWIR) while maintaining high solar reflectance. The composite also incorporates aluminum oxide particles, which effectively scatter sunlight and prevent the porous structure from densifying during the manufacturing process. (Figure 2. 13A-B). The radiative cooling glass was fabricated by sintering a composite of low-melting glass particles and nano Al_2O_3 particles. During this process, the low-melting-point glass microparticles in the mixture quickly sinter to form an interconnected mesoporous structure. The radiative cooling glass coating (Figure 2. 13C, red line) demonstrates a high solar reflectance of 0.96 and significant emissivity (~0.95, blue line) within the atmospheric transparency window (8 to 13 μm). This combination effectively minimizes solar heating while radiating heat to the cold sink of outer space as long-wave infrared (LWIR) radiation. Another similar demonstration was proposed by Lin et al.[61] illustrating a cooling ceramic prepared from a phase reversion process followed by a sintering process. The hierarchical structure was inspired by the Cyphochilus, which exhibits strong bio-whiteness and porous structure (Figure 2. 13D-F). The prepared cooling ceramic (Figure 2. 13D) shows almost perfect solar reflection (99.6%, Figure 2. 13G) and excellent infrared emittance (0.965, Figure 2. 13G) the AW range. The cooling ceramic is capable of delivering continuous sub-ambient cooling in outdoor environments, with a cooling power exceeding 130 watts per square meter at midday, showcasing significant energy-saving potential on a global scale.

2.3.2 Radiative cooling modulation for building thermal management

Despite the great potential of radiative cooling for energy savings, continuous sub-ambient cooling can lead to a heating penalty during cold hours, increasing the heating load for space heating. Baniassadi et al. explored the energy implications of implementing high-performance radiative coolers, characterized by solar reflectance greater than 0.96 and emissivity over 0.97, as a rooftop strategy across eight U.S. cities[62]. Their findings revealed that sub-ambient surface temperatures were maintained throughout the year across all climates, leading to a negative average daily sensible heat flux of 30–40 $W \cdot m^{-2}$. While cooling energy savings were twice as high compared to conventional white roofs, the heating energy penalty also doubled due to the radiative cooling effect during colder hours. To address this issue, the radiative cooling power should be modulated dynamically according to the environmental temperature, catering to the fluctuating thermal needs of temperature-regulating systems. Since the net cooling power of radiative coolers is closely related to solar reflection, the heating penalty can be mitigated by increasing solar absorption during cold hours. Some studies have explored thermochromic radiative coolers, which exhibit high solar reflection during warm periods and lower solar reflection (increased solar absorption) during cold hours. This approach effectively modulates the net cooling power of a radiative cooler and is seemingly more effective than directly manipulating infrared emissivity, as the heating power provided by solar radiation is much greater than the cooling power resulting from infrared emission. However, this modulation is only applicable to outdoor and daytime environments, where solar irradiance is a critical factor in the heat transfer process.

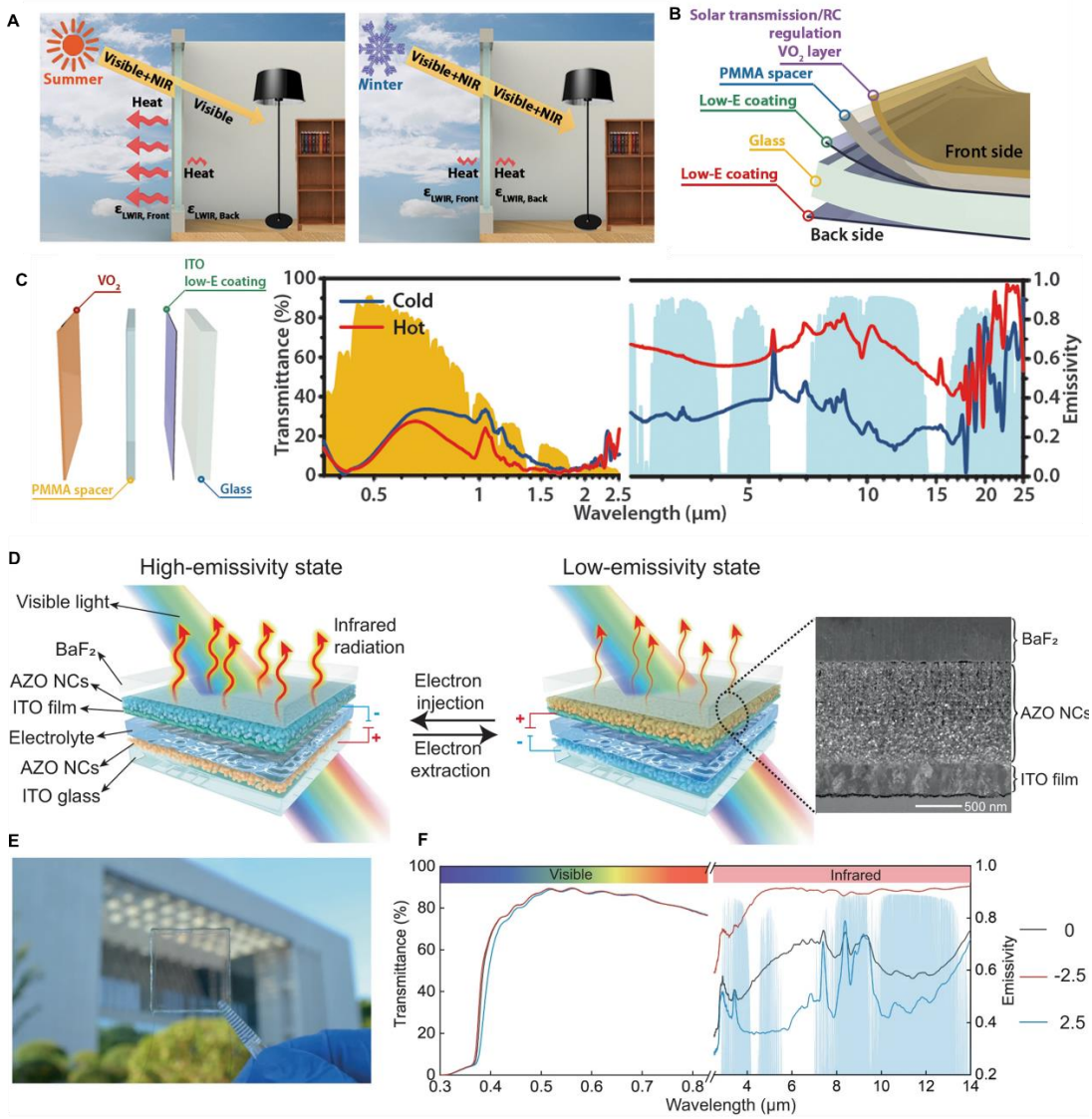

Figure 2. 14 (A-C) Demonstration of of RCRT window. [63]. (D-F) Demonstration of the TDIE regulator structure. [64].

Demonstrations of emissivity modulation have primarily focused on windows utilizing temperature-responsive infrared materials. For instance, Wang et al.[63] introduced a passive radiative cooling-regulating thermochromic (RCRT) smart window that utilizes near-room-temperature phase-change vanadium dioxide (VO_2) and doped VO_2. The RCRT smart window is designed to exhibit low emissivity during cold hours and high emissivity during hot hours (Figure 2. 14A). It comprises a layer of VO_2 nanocomposites, a poly(methyl methacrylate) (PMMA) lossless spacer layer, and a low-E coating (Figure 2. 14B). By forming a typical Fabry-Perot structure, the device achieved a maximum emissivity contrast of 0.4 (Figure 2. 14C). T The transition

temperature can be lowered to near room temperature through tungsten doping. Due to its self-adaptive emissivity modulation, the RCRT window demonstrated higher heating and cooling energy savings compared to commercial low-E glass across various climate zones. Another example is the transparent dynamic infrared emissivity regulator (DIE) proposed by Jia et al.[64], which utilizes electricity-induced localized surface plasmon resonance (LSPR). The operating mechanism of the DIE is shown in Figure 2. 14D. When the TDIE regulator is charged, electrons are injected into the aluminum-doped zinc oxide (AZO) nanocrystals (NCs), which enhances localized surface plasmon resonance (LSPR) absorption, leading to a high-emissivity state. Conversely, when the TDIE regulator is discharged, electrons are extracted from the AZO NCs, reducing LSPR absorption and increasing transmittance. Consequently, the TDIE regulator achieves high infrared reflectivity due to the upper indium tin oxide (ITO) layer, resulting in a low-emissivity state. The visible transmittance in both states is acceptable for window applications (Figure 2. 14E). The prepared TDIE regulators demonstrated maximum emissivity regulation ($\Delta_{\varepsilon MWIR}$ = 0.51, $\Delta_{\varepsilon LWIR}$ = 0.41, Figure 2. 14F) with a charge capacity of 0.27 ± 0.5 mC/cm². The adoption of the TDIE regulator is expected to result in considerable energy savings across different climate zones. Despite several demonstrations of emissivity regulation on conventional glazing substrates, emissivity regulation has not yet been reported on emerging glazing materials such as transparent wood.

2.4 Personal thermal management via radiation manipulation

2.4.1 Radiative cooling for personal thermal management

With its capacity for energy-free cooling, radiative cooling has also found applications in personal thermal management. Beyond HVAC systems, clothing made from various fabrics and textiles serves as a unique method to regulate core body temperature. However, traditional fabrics and textiles have limited insulation capabilities and are unable to achieve below-ambient cooling. Radiative cooling offers a promising approach by enabling fabrics to achieve sub-ambient cooling through strong infrared emissions within the atmospheric window.

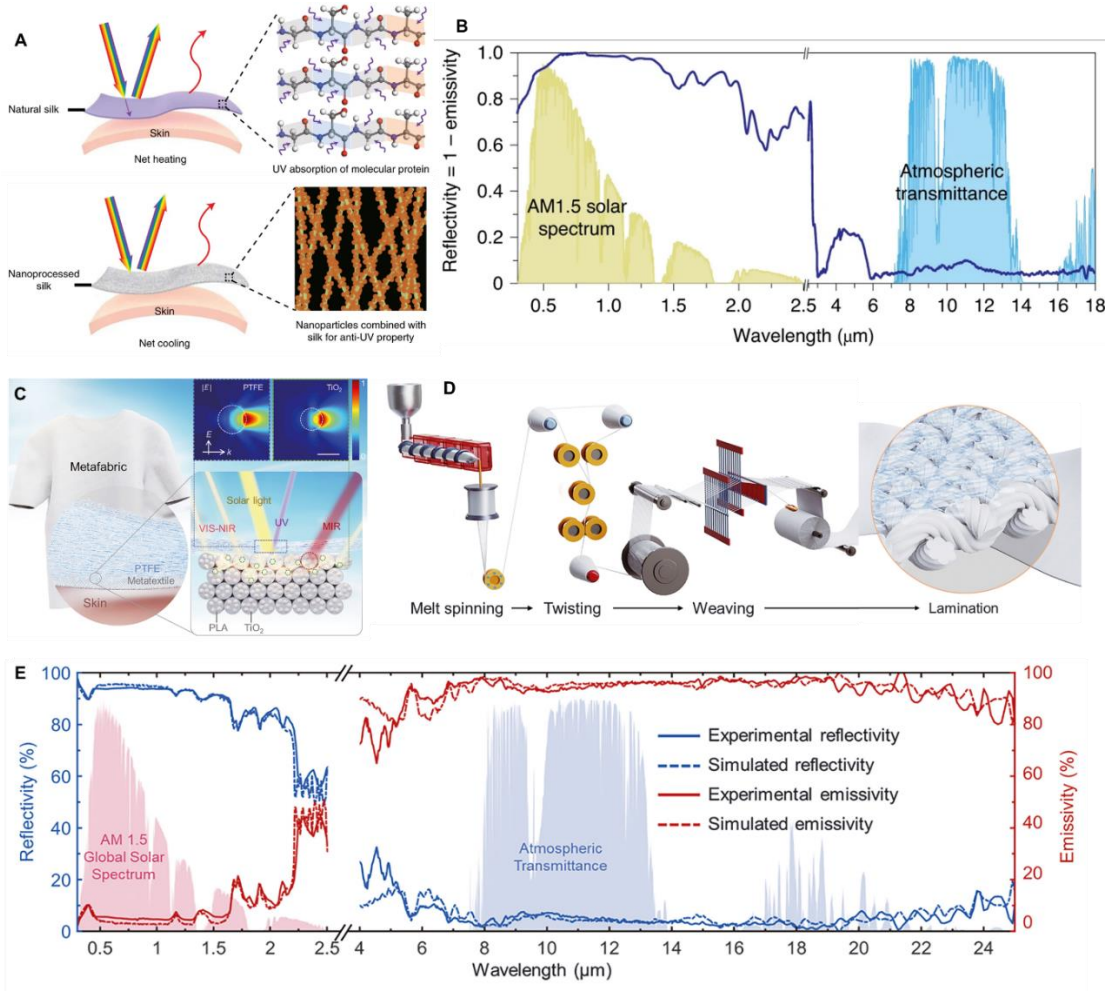

Figure 2. 15 (A-B) Schematic of the nano-processed silk [65]. (C-E) Schematic of the metafabric for daytime radiative cooling[66].

Based on the strong infrared emissions, radiative cooling textiles have been widely reported. For instance, Zhu et al.[65] developed nano-processed silk fabrics that overcome the inherent UV absorption through molecular bonding of Al_2O_3 nanoparticles (Figure 2. 15A). The nano-processed silk demonstrated a high solar reflectivity of approximately 0.95 and a significant emissivity of around 0.9 within the 8–13 μm wavelength range (Figure 2. 15B). This innovation allowed for an 8°C temperature reduction on simulated skin when coated with the nano-processed silk, compared to using natural silk. Zeng et al.[66] developed a passive daytime radiative cooling (PDRC) textile composed of multi-layer composite ultrafine fibers. This textile features a 500 μm TiO_2-PLA woven fabric covered with a PTFE layer. The design principles and fabrication process of the PDRC textile are shown in (Figure 2. 15C-D. The large-scale woven meta-fabrics offer high emissivity (94.5%) within the

atmospheric window and high reflectivity (92.4%) across the solar spectrum, owing to the hierarchical morphology design with randomly dispersed scatterers throughout the meta-fabric (Figure 2. 15E). Outdoor evaluations reveal that the PDRC textile can reduce the temperature of simulated skin by 4.8°C compared to cotton-covered textiles.

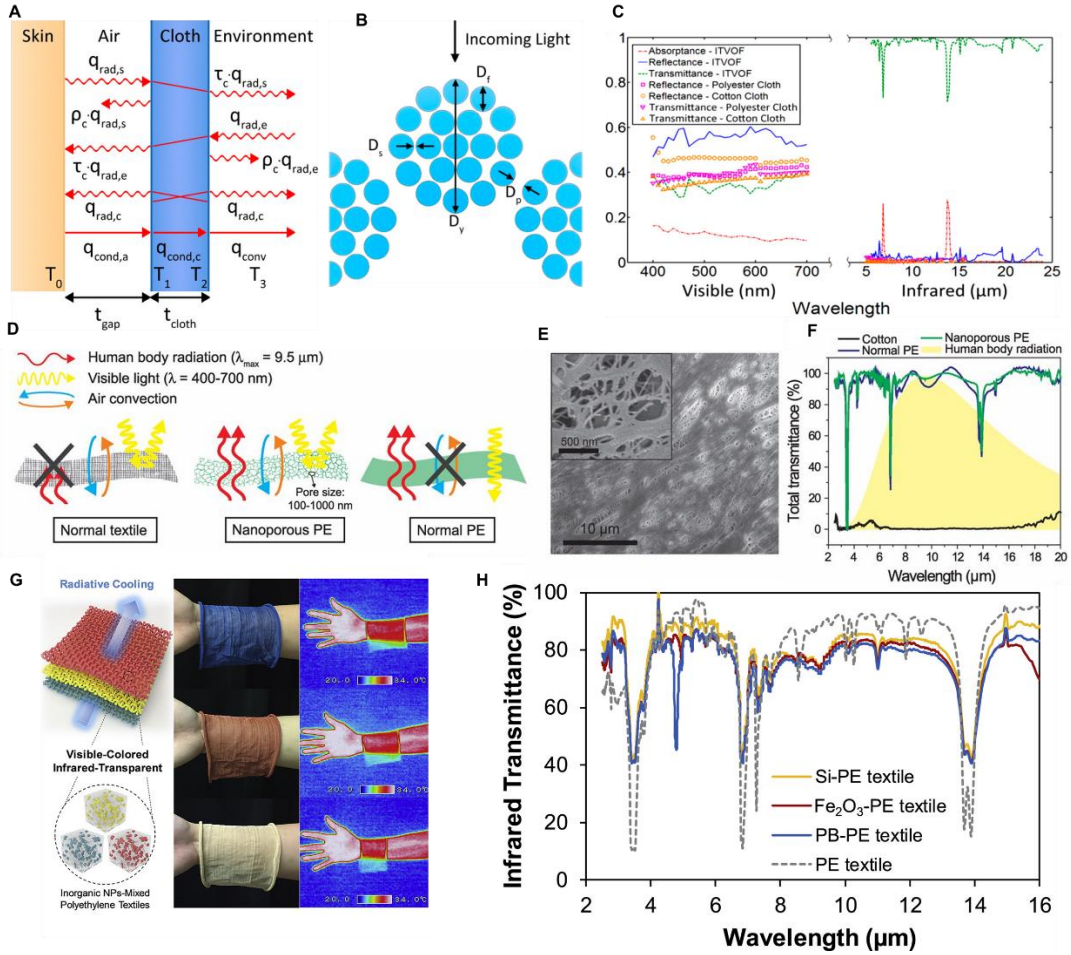

Figure 2. 16 (A-B) Heat transfer model, numerical simulation model from a clothed human body to the ambient environment. (C) Theoretical results of ITVOF[67]. (D-F) Demonstration of working principle, morphology and optical properties of NanoPE[68]. (G-H) Schematic illustration of a colored PE textile [69].

According to the heat transfer mode (Figure 2. 16A) developed by Tong et al.[67], clothing fabrics should allow transparency to mid-infrared and far-infrared radiation, which are the primary spectral ranges emitted by the human body. This is different from the radiative cooling concept mentioned before, which dissipates heat to the cold universe via strong emissions in the atmospheric windows. The investigated object here is the skin, not the radiative cooler itself. Building on this, they introduced the concept

of infrared-transparent, visible-opaque fabric (ITVOF), which enables passive cooling by allowing thermal radiation emitted by the human body to pass directly into the environment. They further suggested optimizing the cooling effect by adjusting parameters such as fiber diameter, yarn diameter, fiber separation distance, and yarn separation distance (Figure 2. 16B). The optimized optical properties (Figure 2. 16C) of ITVOF can be achieved by adopting a fiber diameter of 1μm, yarn diameter of 30 μm, fiber separation distance of 1 μm, and yarn separation distance of 5 μm. This concept (Figure 2. 16D) was experimentally proved by HSU et al. in the following year[68]. They demonstrated that nanoporous polyethylene (nanoPE) qualifies as one of the ITVO materials due to its specific pore size distribution (Figure 2. 16E). Then, an ITVO textile (ITVOT) was structured and fabricated based on nanoPE material, which exhibited excellent infrared transmittance (Figure 2. 16F). The experimental comparison showed that replacing traditional cotton with ITVOT could reduce skin temperature by 2.0°C. Additionally, a method for large-scale production of ITVOT was developed using NanoPE microfibers[70]. Cai et al. made further progress on the coloration issues, providing a facile coloration approach for nanoPE[69]. Different inorganic nanoparticles can act as coloration component for the infrared-transparent textiles (Figure 2. 16G). The fabricated composite textiles demonstrate high infrared transparency of approximately 80% (Figure 2. 16H) and achieve a passive cooling effect of around 1.6°C to 1.8°C. Additionally, they feature vibrant visible colors with excellent washing durability.

Similar to the overcooling effect observed in radiative coolers, the thermal needs of the human body fluctuate with environmental temperatures. Traditional radiative cooling methods, whether transmissive or emissive, cannot effectively respond to these dynamic thermal needs. Typically, human thermal comfort is regulated by adjusting clothing layers or frequently changing the thermostat. However, additional clothing may not always be accessible, and repeatedly altering thermostat settings is inefficient, energy-consuming, and often fails to satisfy the comfort needs of all occupants at once. Therefore, textiles with dynamic radiative cooling capabilities are needed to help the human body adapt to varying environmental temperatures and physiological conditions.

2.4.2 Radiative cooling modulation for personal thermal management

Until now, the conflicting requirements for infrared radiation control in heating and

cooling have restricted textiles to fulfilling only a single thermal function. Designing a textile that can simultaneously perform both heating and cooling functions remains a considerable challenge. While it is feasible to control heat transfer from external sources such as sunlight, wind, or sweat evaporation, these sources of heating or cooling are often inadequate, especially in indoor environments. Conversely, thermal radiation is a constant factor and serves as the primary mode of heat transfer for the human body. Therefore, textiles with the ability to dynamically regulate radiative heat transfer are crucial for maintaining human thermal comfort across different climates.

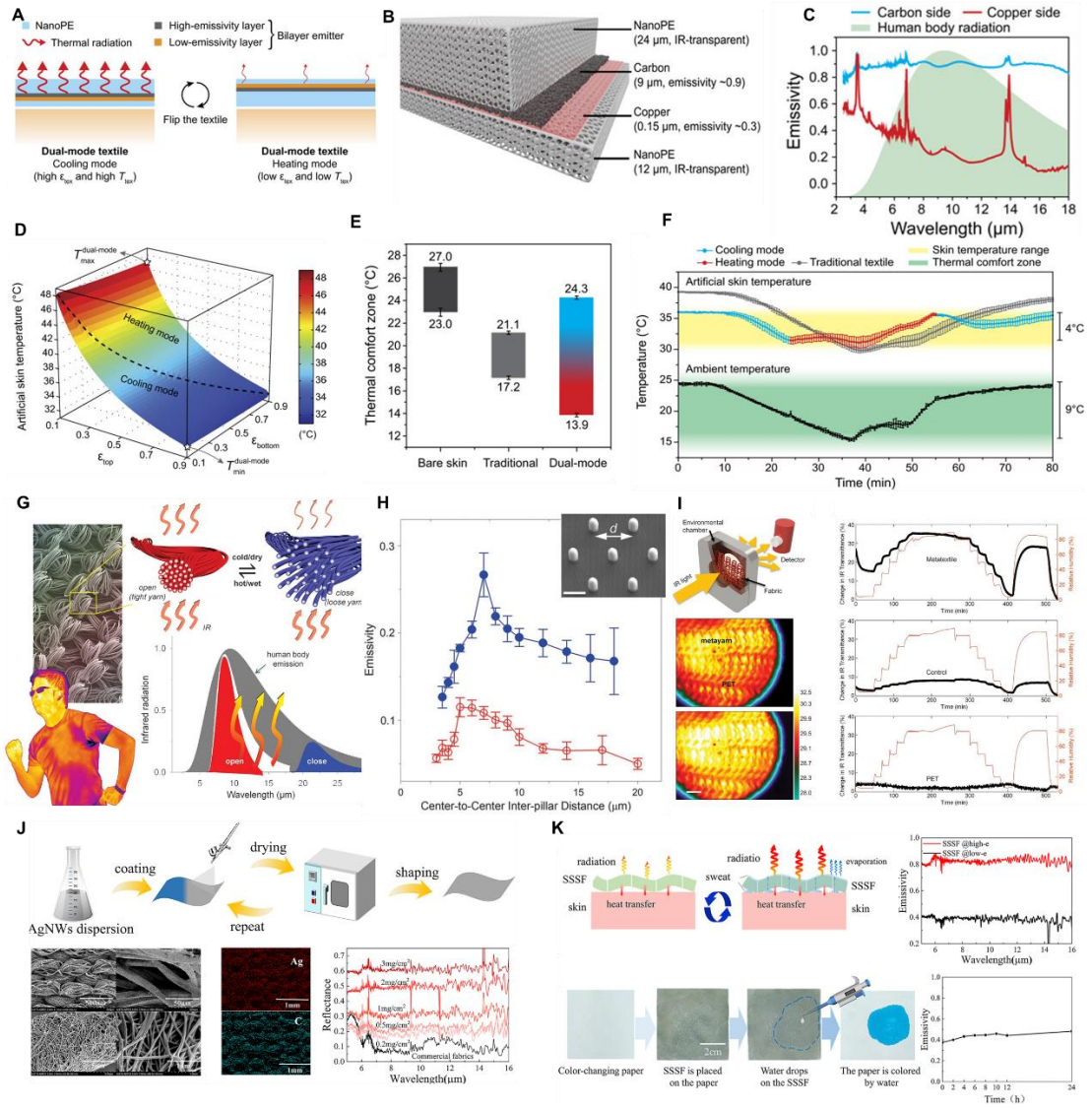

Figure 2. 17 (A-F)Demonstration of dual-mode textile [71]. (G-I) Design principles of an IR gating textile [72]. (J-K) Preparation, characterization and Spectral control mechanism of the SSSF [73].

The most facile approach to achieve this goal is through Janus structures, which were characterized by two surfaces with different optical properties. For example, Hsu et al.[71] proposed a dual mode (Figure 2. 17A) designed for both radiative heating and cooling of the human body. This textile is composed of a bilayer emitter embedded within an infrared-transparent nanoporous polyethylene (nanoPE) layer, shown in Figure 2. 17B. The weighted average emissivity based on human body radiation at 33°C is 0.894. In contrast, copper has a significantly lower emissivity, with a weighted average value of 0.303 (Figure 2. 17C). The thermal regulating capacity was firstly confirmed by numerical simulations. The skin temperatures when covered by textile with different emissivity (bottom and top) are show in Figure 2. 17D. The temperature differences between dual-mode textile and fixed emissivity textiles (low emissivity and high emissivity) can be up to 47.1 and 32.4 ºC. The field test also confirmed the temperature stabilization capacity of the dual-mode textile. For the dual-mode textile, with its two distinct heat transfer coefficients, the thermal comfort zone spans from 13.9°C to 24.3°C, covering a range of 10.4°C (Figure 2. 17E). This textile can maintain artificial skin temperature between 32°C and 36°C, even with a 9°C fluctuation in ambient temperature (Figure 2. 17F). This expanded thermal comfort zone is achieved by simply flipping the sides of the textile, without the need for any additional energy input. Many reports have also explored the dynamic thermal regulating capacity of the Janus structures. Despite the switching effectiveness of the mechanical flipping, frequent switching may lower the willingness of the adoption of such structures. Therefore, self-adaptive emissivity regulation which avoid the frequent mechanical flipping might be a better option.

To regulate the body radiation self-adaptively, Zhang et al.[72] developed a textile with dynamic gating of infrared radiation. The working principle of the IR gating textile was shown in Figure 2. 17G. Each yarn in the textile is composed of a bundle of ultra-fibers that operate through two key mechanisms: (i) the controlled incorporation of sub-elements, typically conductive materials, into the polymer textile fibers, and (ii) direct responses to changes in temperature and/or skin relative humidity. In hot and/or humid conditions, the yarn collapses, causing adjacent fibers to move closer together, which results in resonant electromagnetic coupling. This coupling modifies the textile's emissivity to more effectively align with the body's thermal radiation, thereby

enhancing heat exchange. Conversely, in cold and/or dry conditions, the yarn reacts in the opposite manner to minimize heat loss. This dynamic response enables the textile to effectively "gate" infrared radiation, either "opening" or "closing" it, depending on environmental changes. The electromagnetic coupling effect was highly dependent on the distance between the nanostructures (Figure 2. 17H). They wove cellulose-triacetate crystalline fibers into fabric, coated them with a solution of single-walled carbon nanotubes, and characterized their infrared response under controlled humidity levels. Using a humidity controller, we programmed the humidity levels within the environmental chamber (Figure 2. 17I). They visually captured the modulation of the ultra-textile's infrared emissivity with a calibrated high-resolution infrared camera (Figure 2. 17I)). As the relative humidity at room temperature increased from 10% to 75%, the yarns became brighter compared to knitted polyethylene terephthalate (PET) yarns used as side-by-side controls, due to increased thermal emissivity. The dynamic infrared response characteristics of the fabric were effective across a broad relative humidity range (5% to 90%), adequately covering the range of humidity levels typically experienced by the skin under varying environmental conditions. Overall, the IR gating textile can show different emissivity in response to humid, allowing dynamic regulation of human body radiation regulation. Note that though emissivity changes were caused by the distance changes between yarn’s fiber which was induced by humidity, the emissivity contrast was not related to the inherent high emissivity of moisture (mainly water).

Human sweat, primarily composed of water, can also initiate emissivity switching. Li et al.[73] proposed an adaptive fabric with emissivity regulation for personal thermal management. The self-adaptive smart fabric (SSSF) was fabricated by directly spraying silver nanowires (AgNWs) onto commercial polyester fabrics (Figure 2. 17J). The AgNWs adhered to the polyester fibers, exhibiting a mesh-like distribution (Figure 2. 17J). The reflectivity of the prepared SSSF depended on the mass concentration of AgNWs, with higher concentrations resulting in higher reflectivity. The emissivity modulation mechanism of SSSF, illustrated in Figure 2. 17K, leverages the high emissivity of water. Specifically, SSSF remains dry with a low emissivity surface due to the metallic properties of AgNWs, effectively suppressing radiative heat loss from the human body. However, during physical activity that induces sweating, the sweat permeates the fabric and coats the exterior surface of the SSSF. This leads to enhanced

radiative properties, as water has a high emissivity. As a result, the SSSF exhibits an emissivity of 0.39 when dry, which increases to 0.83 when wet, achieving an emissivity modulation of 0.44. (Figure 2. 17K).

Despite various attempts at emissivity modulation, temperature-adaptive emissivity for personal thermal comfort has not been explored, particularly the inherent emissivity modulation induced by temperature changes. Temperature-adaptive emissivity modulation presents a promising direction for the following reasons: Firstly, temperature is the most direct and important parameter for thermal sensation. Emissivity modulation induced by temperature can directly regulate a person's sensation of thermal comfort. Secondly, temperature-induced emissivity modulation is a passive, energy-free process that requires no external energy input. As the temperature changes, the emissivity will passively adjust in response to temperature fluctuations. Overall, temperature-induced self-adaptive emissivity modulation deserves more exploration and remains a challenging yet promising area of research.

2.5 Overview of transparent wood

2.5.1 Introduction

A green revolution of energy and materials consumption patterns is being undergone in almost every sector of global industry. Anthropomorphic overexploitation of natural resources and the resultant environmental problems associated with the use of petroleum-based chemicals and materials, as well as inefficient energy consumption patterns in contemporary industrial processes and materials, have resulted in a slew of global issues that must be presently addressed [65, 74, 75]. For example, residential building energy usage currently accounts for nearly 40% of the total energy consumption [76]. This, in turn, has motivated the development of new energy-saving building materials with good light transmittance and thermal insulating properties, offering substantial cost savings up-front, as well as a plethora of longer-term environmental benefits, contributing to a more carbon-neutral society (e.g., worldwide net-zero 2050 goals). In recent years, sustainable materials have reported unique and increasingly reliable materials properties (e.g., super plasticity, enhanced machinability, and superior strength and/or toughness) compared to established comparators (usually petroleum-based), combined with the increasing efficiency and variety of production technologies for mass production of these ‘green’ products. Such sustainable materials

and processes are critical for achieving the UN Sustainable Development Goals by the 2030 target [77-80].

Given its renewable and biodegradable nature, wood may play an essential role in this green revolution. Natural wood has been intensively used since the beginning of human civilization due to its ease of processing, broad availability, low thermal conductivity and excellent mechanical performance [81-83]. However, with developments of application requirements, natural wood has yet to be able to fully cater to contemporary human needs. This has contributed to the rise of petro-plastics, glass, metals, concrete and other industries – all of which are highly energy-intensive and environmentally damaging. If wood-based materials could realistically compete with modern industrial materials, it could once again offer a viable route to new industrial materials that are less costly to the environment and more beneficial to quality of life. To this end, various wood-based materials with additional or enhanced functionality have been developed in recent years via chemical or physical treatment, to better cater to the needs of different applications spanning energy saving, radiative cooling, energy harvesting, energy storage, electronic devices, hydrogel devices, and photonic devices [55, 84-88]. Among various wood-based materials, transparent wood (TW) has been intensively studied recently due to its unique performance.

TW is generally prepared via a discoloration process (i.e., delignification or lignin-modification) followed by polymer impregnation or a compressing process (top-down process). The primary TW prepared from the top-down process holds great potential for replacing traditional plastic materials due to the intrinsic high visible transparency and haze, low thermal conductivity, and excellent mechanical properties. TW can also derive from nanocellulose that originated from trees, plants, cotton and even bacterial (bottom-up process). A special TW (named transparent fiber wood) can be created by mixing wood nanofibers (obtained from the delignification of wood particles) and the refractive index (RI) matched polymers [89]. Another strategy for creating transparent composite of nanofibers and polymer is directly assembling the cellulose nanofibers (obtained from the fibrillation of wood pulp or bacterial) into a thin film, which was then impregnated by acrylic resin under vacuum [90, 91]. Although bottom-up processes have been implemented to achieve optical transparency, the resulting products have exhibited significant deviations in their microstructure from that of

natural wood. Cellulose based transparent composites prepared from such bottom-up process will not be addressed in this review. Thus, the focus of this review is limited to TWs obtained through top-down processes.

Though the original TW-substrates have been considered as good exploratory materials for many applications[92, 93], such substrates have yet to achieve sufficiently satisfactory properties for applications that required special functionalities. Functional TW with enhanced or added properties has been developed through various techniques, allowing TW to be utilized in a range of emerging applications, including smart buildings, smart windows, and optoelectronic devices. The functional TW can be prepared through either pre-functionalization or post- functionalization methods. Pre-functionalization refers to treatments before or during the impregnation, such as incorporating the functional component with the impregnating polymers, selecting impregnating polymers with special functions, special treatments on the wood scaffold [94-96]. Post-functionalization refers to treatments of TW after impregnation via surfacing engineering and coating [6, 7, 97]. Progress on TW has been comprehensively summarized, such as Berglund and coworkers for foundational transparent wood reports [98, 99], Zhang et al for processes and procedures [100], as well as specific architectural applications by Wang and Zhu [101]. Very recently, Zhu et al summarized transparent wood-based functional materials, emphasizing process-structure-property-application relationships [102].

This section systematically summarized the various TWs from a fabrication-functionality-application perspective. This chapter outlines the challenges and extraordinary opportunities afforded by TWs from the standpoint of coatings and/or composites. This will include the foundational literature from the nascent TW field, as well as associated literature from overlapping and adjacent fields. In cases where the topic falls outside the purview of the TW composites and coatings focus, we refer the readers to other excellent recent literature reviews for more information [86, 98-105].
TW and its various coatings and/or composites have been made optically transparent (i.e., highly optically transmissive over visible light wavelengths; ~350-780 nm), by impregnating the porous structure with various clear polymers and/or fillers that match the RI of the wood scaffold. Thus, at the fundamental level, TW composite combines the functional aspects of wood, with the optical aspects of a clear polymer. Although

TW was first reported in 1992 by Siegfried Fink[106], ostensibly to better understand wood anatomy – it was the more recent report in ~2016 by Li et al[3] and Zhu et al [4], that sparked the rush of interest in the area of functional TW composites and coatings. We will start with a brief overview of wood anatomy to provide a better overall understanding of TW substrates.

2.5.2 Wood Anatomy

Wood is the most used bio-based, renewable material in buildings, furniture, and a whole host of other applications (e.g., wearables and/or decorative) [107]. It is sustainable (including low energy input manufacturing practices), biodegradable and environmentally friendly [108]. Wood offers excellent mechanical properties, including reaction and alteration of the wood substrate's physico-chemical properties, when used for other applications. The architectures and compositions for natural wood (NW) at different levels of magnification are shown in Figure 2. 18, a typical tree trunk mainly includes pith, heartwood, sapwood (secondary xylem), and bark (secondary phloem and cork). NW typically exhibits a porous structure, aiding the chemical or physical modification, and all tracheids contain both primary, secondary walls, and middle lamella [109]. On the molecular scale, wood consists of the three natural biomacromolecules - cellulose, hemicellulose and lignin [110]. Generally, the cellulose microfibrils, containing both crystalline and amorphous regions, are embedded in the matrix of hemicellulose and lignin [111, 112]. Obviously, NW shows directional variance in terms of structural and chemical composition.

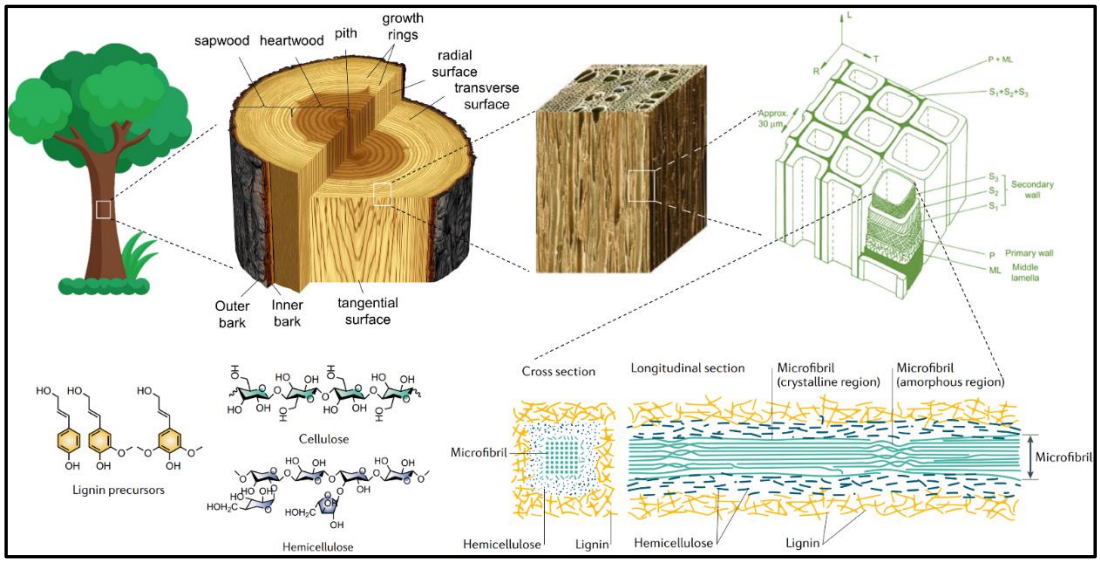

Figure 2. 18 A general overview of wood architectures and compositions at different levels of magnification. [113] [114].

Aside from being a natural material with intrinsic directional variance, wood is also an orthotropic-type of anisotropic material with marked variation in directional properties (e.g., strength) [115]. Briefly, the three main directions of wood property variance are; longitudinal (i.e., along the grain), as well as radial and tangential (both of which are perpendicular to the grain). For most purposes, the differences between the radial and tangential forms are considered minimal, although e.g., tangential shrinkage can be up to twice as high as radial shrinkage, due to reasons including variations in lignin presence, cell wall thicknesses, etc. [116]. Thus, the main differentiators in terms of physico-chemical properties tend to broadly be between parallel and perpendicular to grain. In addition, all woods have two broad zones: the inner core of darker heartwood hat contains the majority of living components of wood, and an outer ring of lighter sapwood, which is predominantly dead cells that only serve a supportive function [117].

In terms of material variation, the configuration and orientation between and even within species have marked influences on strength, and shrinkage, which is exacerbated by minor structural variations between different wood types, e.g., the longitudinal cells in softwood are usually shorter than those in hardwood. Because the longitudinal axes typically confer considerably higher strength than perpendicular axes – the strength of wood along the fibers is approximately ten times higher than the strength across the fibers, while the limiting strains across the fibers are significantly higher than along the fibers [118]. This anisotropy continues to be an issue after TW is formed, with

orientation having marked effects on optical and mechanical properties [4]. To a certain extent, multilayer TW could improve the mechanical strength and overcome some issues with material anisotropies, depending on element orientation and load direction [119, 120]. Further differences in property are due to the range of variations of compositional factors such as cellulose-hemicellulose-lignin compositions, the crystalline:amorphous character, the cellulose allomorphs present (cellulose I:cellulose II (α:β): cellulose IV), the presence of nodes, the arrangements of fibrils, the size of pores among many other factors [121, 122].

2.5.3 Preparation of Transparent wood

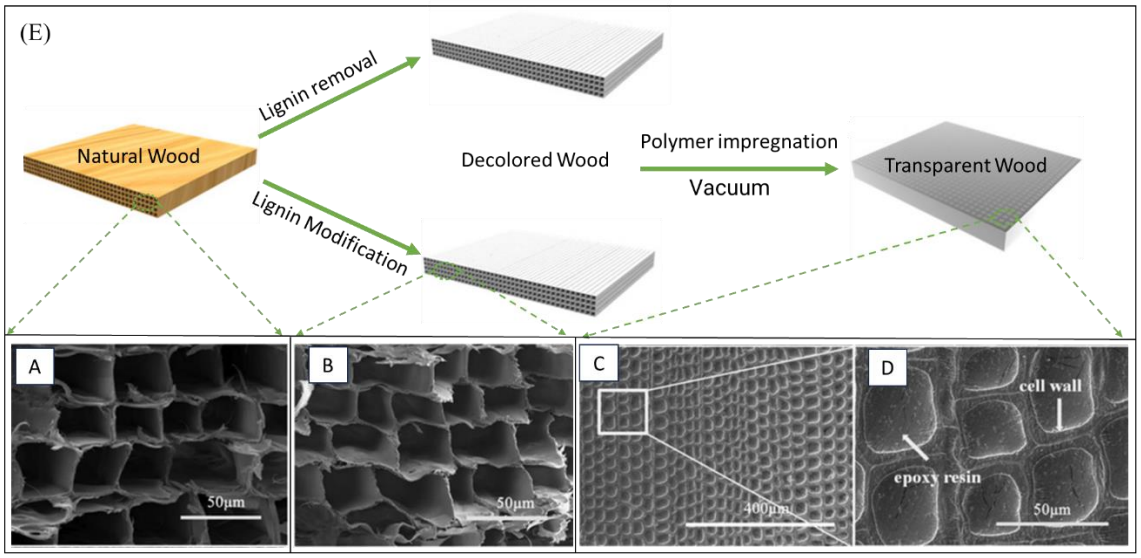

Figure 2. 19 A general fabrication process of TW and corresponding SEM images at different fabrication stages. [95].

The general fabrication process of TW involves two steps: wood discoloration and polymer impregnation (Figure 2. 19E). Discoloration can be achieved by two methods: lignin modification and/or delignification, which are quite similar to those used for chemical pulping, involving treating and compressing stages – most commonly by adopting the already proven bleaching chemicals and processes from such industries [123]. Though, enzymes are widely used in chemical pulping, there appear to be no reports of enzyme-based bleaching routes to TW to-date [124-126]. However, in addition to the decoloration effect resulted from delignification and lignin modification,

such treatments frequently result in some (usually undesired) loss of the hemicellulose components of wood. There are four different delignification recipes that are most frequently used to fabricate TW:

i) $NaOH$-Na_2SO_4-H_2O_2 system: Wood blocks or strips are immersed in boiling (80-100°C) aqueous solutions containing sodium hydroxide ($NaOH$) and sodium sulfite (Na_2SO_4) for ~12 hours, followed by boiling hydrogen peroxide (H_2O_2) for ~6 hours [4].

ii) $NaClO_2$-CH_3COOH system: The pH of $NaClO_2$ solution is adjusted to ~4.6 by CH_3COOH, then wood strips are immersed in the mixture at ~80^oC for several hours (until completely white, depending on the sample size) [3].

iii) $NaClO$ system: Wood strips are directly immersed in $NaClO$ solution for more than 12 hours [127].

iv) Peracetic acid (PAA)-NaOH system: Delignification is performed using an aqueous PAA solution (4 wt.%) at a pH of 4.8 (adjusted with sodium hydroxide) for several hours (until completely white, depending on the sample size) [128].

Partial or complete removal of the cell wall lignin-component leads to voids in the lignin-rich cell wall corner and a general thinning of cell walls[3]. It is worth noting that the natural porous structure of wood is generally reserved (at least at the micron level, Figure 2. 19A&B). Broadly, the loss of lignin has negative impacts on the mechanical properties of TW, but a positive impact on achieving a high level of transparency. While lignin removal is usually desirable for obtaining TW, in order to obtain the maximum value of visible transparency and mechanical performance simultaneously, alternative lignin modification processes have also been developed. In these processes, the chromophores of lignin are selectively eliminated while the aromatic skeleton remains intact. Li et al (2017) have reported a high lignin content TW (up to 80% lignin retention, TW-lignin) variant that exhibited transmittance of 83% (slightly lower than that (86%) of TW based on the delignified wood template (TW-delign) at the thickness of 1.5 mm) and a haze of 75% (an increase of 7% when compared to TW-delign at the thickness of 1.5 mm). [129]. Though a comparison of TW-lignin and TW-delign in terms of mechanical properties was not presented in this

study, the comparison of the mechanical properties of the two wood templates (delignification method and lignin modification method) were conducted. For both parallel and perpendicular direction of birch, pine, and ash, the wet strength of lignin modified samples was much higher than that of delignified samples.

Two lignin modification systems are commonly used for wood decoloration: thermal alkaline/H_2O_2 and ultraviolet-H_2O_2. The general recipe for alkaline/H_2O_2 lignin modification solution usually includes sodium silicate, sodium hydroxide, magnesium sulfate, diethylenetriaminepentaacetic acid (DPTA), and H_2O_2. Wood slides are immersed in such solution mixtures (usually below 100^oC) until they become completely white. Typically, this requires less processing time (1-2 hours) than the delignification process (usually more than 10 hours). Alternatively, Xia et al [130] also introduced an in-situ lignin modification method with the assistance of ultraviolet (UV). The natural wood was treated with a small quantity of a 10% NaOH solution prior to the addition of a 30% H_2O_2 solution. The pre-treated wood was then placed under UV light. This process also shows excellent patternability by directly brushing the H_2O_2 on the NaOH pre-treated wood surface [131]. This approach preserved the majority of the "binder," resulting in a durable wood scaffold suitable for polymer infiltration, while significantly reducing chemical and energy consumption, as well as processing time.

After wood discoloration, the decolored wood is usually stored in a low boiling point solvent (e.g., ethanol, acetone, etc.) to avoid densification. The water and chemicals remaining in the wood channel after the decoloration process will be displaced by the low boiling point solvent over time. In the final stage, an alternative polymer (e.g., epoxy, acrylic, poly (vinyl alcohol), polyvinylpyrrolidone, polyimide, thiol-ene, vitrimers, poly (limonene acrylate), melamine formaldehyde, etc.) is allowed to permeate into the wood matrix under vacuum (Figure 2. 19C&D). At this point, the substrate turns clear due to the reduced light scattering afforded by this new, interpenetrating, index-matched polymer [2, 95]. Such a configuration allows for the complete infiltration and long-term retention of the polymers as compared to conventional surface coating processes, in which only the surface cavity was impregnated with resin. One inconspicuous but very important point to ensure the decolored wood is fully immersed in the impregnation polymers. The density of decolored wood is even lower than that of natural wood, and it may float on the surface

of polymer mixtures during impregnation if proper precautions are not taken. Once floatation occurs, the infiltration process can fail, leading to the failure of the entire fabrication process.

2.5.4 Optical, mechanical and thermal properties of transparent wood

TW exhibits unique optical, mechanical, and thermal properties, which are derived from its intrinsic structural characteristics. These include the cellulose volume fraction, cellulose microfibril orientation, chemical interactions at cell wall interfaces, thickness, porosity, and the anisotropic structure of the TWs. Table 2. 1provides an up-to-date summary of all experimental reports of such structural variations and their effects on physical and optical properties.

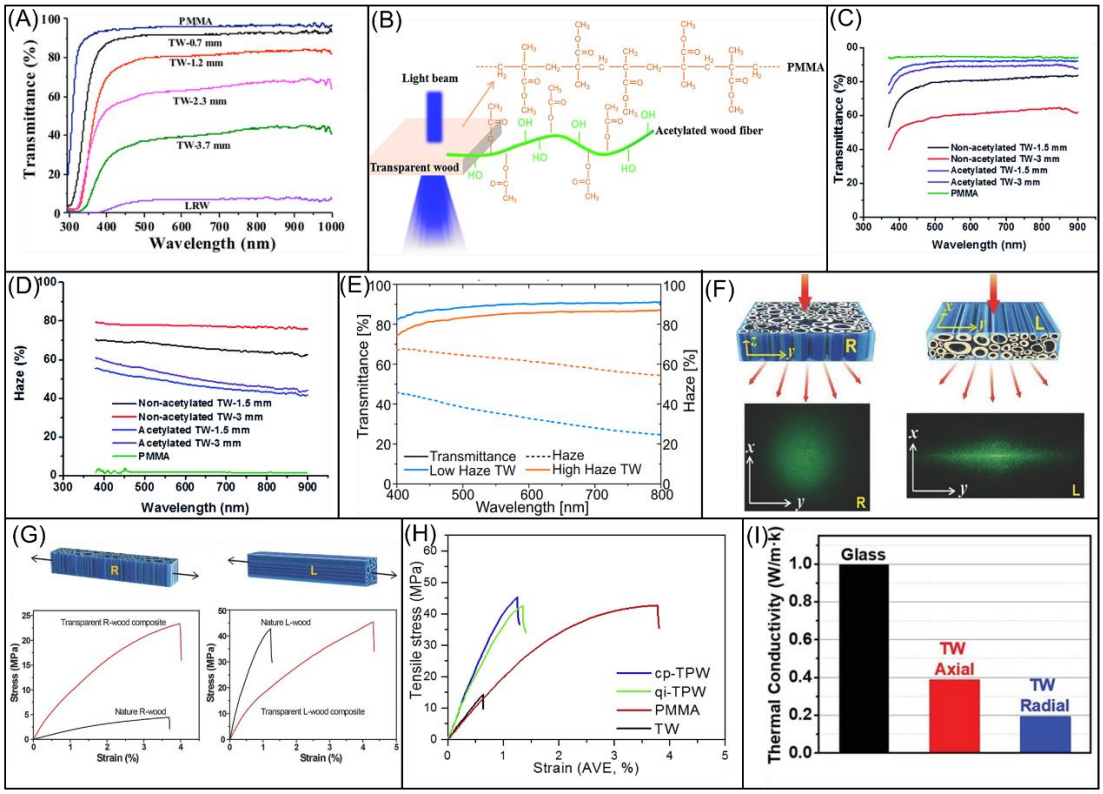

Figure 2. 20 General performance of TW. (A) Transmittance of transparent wood samples with different thicknesses [3]. (B) The Illustration showing the interactions between acetylated wood substrate and PMMA. (c & d) The transmittance(C) and haze(D) of acetylated TW and non-acetylated TW at the thickness of 1.5mm and 3mm[132]. (E) Optical transmittance and haze of TW specimens at the thickness of 1.2 mm [133]. (F) Photo images of scattering patterns from different direction. (G) Stress–

strain curves for the nature R/L-wood and transparent R/L-wood[4]. (H) Typical stress-strain curves of the tensile test in transverse direction [120]. (I) The thermal conductivity of the transparent wood was measured at the axial and radial heat transfer direction and the comparison with glass [134].

Table 2. 1 Summary of optical, mechanical, and thermal properties of TWs

Sample	Wood Species	[a]Decoloration Method	[b] Wood scaffolds Vol/%	Thick-ness /mm	Optical		Mechanical				Thermal	Direc tion	Ref
					T[c]/%	H[d]/%	E/Gpa	σ/Mpa	ε/%	Tn[e]/MJ·m^{-3}	Tc[f]/W·m^{-1}K^{-1}		
[g] DW/PMMA	Balsa	$NaClO_2$/Acetate	\	0.7	90	48	\	\	\				
			5	1.2	85	70	2.05	38	2.2				
			19	1.2	78	75	3.59	90.1	3.8	\	\	\	[3]
			65	1.2	34.	78	\	\	\				
			\	3.7	40	~80	\	\	\				
DW/EP	Basswood	NaOH-Na_2SO_4-H_2O_2	\	3	90	\	1.22	23.38	\	0.59	\	⊥	[4]
				3	~80		2.37	45.38		1.2		//	
DW/PVA	Balsa	NaClO	\	0.8	91	15	3.85	143	4.2	3.03	0.39	//	[134]
				0.8	\	\	3.1	67	3.7	1.06	0.19	⊥	
DW/EP	Balsa	$NaClO_2$/Acetate	\	2	77	\	\	69.13	\	\	\	//	[135]
				2	\			6.06				⊥	
	Basswood			2	64			75.12				//	
				2	\			8.17				⊥	
DW/PMMA	Balsa	$NaClO_2$/Acetate	\	1.5	86	68	\	\	\	\	\	\	[129]
[h] LMW/PMMA		Alkaline/H_2O_2[f]		1.5	83	75		100.7	2.18				
DW/thiol-ene	Balsa	$NaClO_2$/Acetate	5	1.2	85	63	3.2	53.7	2.1	\	\	\	[133]
LMW/thiol-ene		Alkaline/H_2O_2	4.3	1.2	90	36	3.4	59	2.5				
DW/LIMA	Birch	PAA-NaOH	26	0.7	88	49	12.6	146.6	1.2				[128]
SA-DW/LIMA	Birch			0.7	92	44	17.3	173.3	1.0				
DW/LIMA	Balsa		12	1.2	87	46							
SA-DW/LIMA				1.2	89	41							
DW/LIMA				2.0	80	62				\	\	\	
SA-DW/LIMA				2.0	87	45	\	\	\				
DW/LIMA				3.0	71	65							
SA-DW/LIMA				3.0	81	51							
DW/PMMA	Balsa	PAA-NaOH	6.4	2.0	70.6	76.3	4.8	41.4				//	[136]
DW/PMMA				2.0			2.9	11.4				⊥	
SA-DW/PMMA			6.2	2.0	83.8	66.9	4.5	61.7				//	
SA-DW/PMMA				2.0			2.9	12.8	\	\	\	⊥	
IA-DW/PMMA			6.5	2.0	76.6	76.2	4.3	54.9				//	
IA-DW/PMMA				2.0			3.3	33.2				⊥	
MA-DW/PMMA			6.0	2.0	79.5	73.6	4.3	46.2				//	

MA-DW/PMMA				2.0			3.1	18.0				⊥	

To be continued

Table 1 (continued)

DW/PEAG	Balsa	$NaOH-Na_2SO_4-H_2O_2$	\	\	93	98	2.2	153.6	\	\	\	//	[137]
DW/EP					82	\	\	\				//	
Compressed single DW/PVP (STW)	Balsa	$NaClO_2$/Acetate	40.25	0.48	70.4	31.9		99.5					[138]
Double layer-same direction laminated (DSTW)			41.15	\	59.6	41.4		\					
Double layer-same-direction laminated (DCTW)			40.75	\	50.0	58.1	\	88.3	\	\	\	\	
Trible layer-same-direction laminated (TSTW)			40.45	1.32	44.3	50.5		134.0					
Trible layer-cross-direction laminated (TCTW)			40.97	1.32	43.5	65.6		125.3					
DW/PMMA	Balsa	$NaClO_2$/Acetate	\	1.5	83	70	\	\	\	\		\	[132]
Acetylated-DW/PMMA			5%	1.5	92	50	4	78.9	2.2	1.0		⊥	
Acetylated-DW/PMMA			\	3	89	53	\	\	\	\	\	⊥	
Acetylated-DW/PMMA			\	7	71	74	\	\	\	\		⊥	
Acetylated-DW/PMMA			\	10	60	76	\	\	\	\		⊥	
DW/PMMA/PEG	Birch	$NaClO_2$/Acetate	\	0.5	84	74	\	\			\	\	[139]
DW/PMMA/PEG				1.5	68	77	14.9	70.5	\	\	0.3		
DW/EP(Clear)	Basswood	NaClO	2.54	0.7	90	10	\	43.39	19.14	6.10	0.35	//	[140]
DW/EP(Clear)		NaClO	\	\	\	\	\	33.29	16.30	3.96	\	⊥	
DW/EP(Haze)		$NaClO_2$/Acetate	\	\	90	80	\	\	\	\	0.24	\	
LMW/EP	Balsa	UV-H_2O_2-NaOH	\	1	90	60		46.2	3.4	1.64		//	[131]
LMW/EP				1.5	\	\	\	31.4	7.4	0.93	\	⊥	
DW/MF	Balsa	Alkaline/H_2O_2	11	1.1	65	92	\	\					[141]
LMW/MF	Balsa	$NaClO_2$/Acetate	8.5	1.2	68	90	\	\	\	\	\	\	
LMW/MF	Birch	Alkaline/H2O2	25	1.2	74	66	11.1	60					

[a] All decoloration recipes can be found in Section 2.2

[b] wood scaffold vol%: Depending on the decoloration methods, this value refers to the sum of cellulose vol%, hemicellulos vol%, and lignin vol% or cellulose vol%.

[c] Transmittance; [d] Haze; [e] Toughness; [f] Thermal conductivity; [g] Delignified wood; [h] Lignin modified wood

//: The direction of the light propagation applied stress and heat transferring is parallel to the wood channel. ⊥: The direction of the light propagation, applied stress and heat transferring is perpendicular to the wood channel.

The two most important measures of TW optical properties are transmittance and haze. As discussed in Section 2.4.4, the transmittance of transparent wood (TW) is determined by the ratio of transmitted light intensity—comprising both ballistically transmitted and diffusely transmitted light—to the incident light intensity. This transmittance is typically measured using an integrating sphere, which captures the total cone of scattered light, including both ballistic and randomly scattered photons. Though the transmittance can reach as high as 93%[137], the main contribution comes from diffusely transmitted light (forward scattering) rather than ballistic transmission. This also makes TW appear inconsistent with human's general perception to transparency. Another important parameter is haze, referring to the ratio of the ratio of diffused transmitted light intensity to the intensity of transmitted light (both ballistically transmitted and diffusely transmitted). Haze is measured according to ASTM D1003[142], and is defined as he percentage of transmitted light that is scattered at an angle deviating more than 2.5° from the direction of the incident beam. An insightful discussion about transmittance and haze measurements has been given by Li et al[99]. Although TW typically demonstrates high transmittance and high haze, a broad range of tunable transmittance (10-93%) and haze (10-98%) can be achieved by varying factors such as wood species, thickness, cellulose volume fraction, and microstructure. Based on the careful modulation of these factors, several strategies have been proposed to tailor the haze and transmittance of TW.

Thickness is a critical factor in on the optical properties of TW. The quantity of polymer/wood interface is highly thickness-dependent. The interfaces between the wood substrate and the polymer increases within the increase of sample thickness, thereby, resulting in a lengthened light propagation path. As a result, the transmittance will decrease and haze will increase. This trend has been observed for balsa-based (Figure 2. 20A)[3], beech-based[143] and birch-based[139] TWs. The quantitative relationship between the total transmittance (T_{total}) and the thickness of TW can be described by the anisotropic photon diffusion equation. This equation illustrates that T_{total} decreases exponentially as the thickness of the TW increases[144].

$$T_{total} = \exp(-\alpha d)$$

where α is the attenuation coefficient, and d is the sample thickness.

Interface tailoring is an effective strategy to control the optical properties of TW. Light scattering is primarily dominated by forward scattering, which results from the refractive index (RI) mismatch between the cell wall and the polymer. Nonetheless, if the air-filled voids caused by multiscale porous structural combination of micro, meso- and macropores and polymer shrinkage during polymerization cannot be minimized, such voids will completely dominate scattering in TW[145]. Thus, a good surface compatibility is crucial to the desired optical properties of TW. To date, surface manipulation (e.g., surface esterification and use of compatibilizer) has been explored to minimize the air-filled voids caused by the poor compatibility between the polymers and decolored scaffold[128, 132, 136, 146, 147]. By using compatibilizers, such as KH-550, epoxy resin and the decolored wood scaffold can be successfully coupled, resulting in an improved interfacial compatibility, consequently, improved optical performance [147]. Another approach involves grafting acetyl groups onto the cellulose microfibrils to enhance the interfacial compatibility between the wood scaffold and PMMA (Figure 2. 20B). Thanks to the improved interfacial compatibility, acetylated TW shows higher transmittance (92%) and lower haze (50%) than non- acetylated TW (transmittance ~83% and haze ~70%) at a thickness of 1.5 mm due to the improved interfacial compatibility (see Figure 2. 20C&D). Compatibility issues can also be caused by polymer shrinkage during polymerization. This can be resolved by selecting polymers with smaller shrinkage ratios. A novel impregnating system (i.e., thiol–ene) with a low volume shrinkage ratio (~4%) was introduced for the preparation of TW [133, 148]. Compared to normal PMMA based TW, the scattering from air voids and the corresponding haze are significantly reduced due to the low polymer shrinkage, resulting in improved optical performance (high transmittance and low haze, Figure 2. 20E).

The optical properties of transparent wood (TW) are strongly direction-dependent due to its anisotropic structure. Wood fibers can either guide light along the axial direction or induce significant anisotropic scattering, depending on the alignment between the

material direction and the incident light. When light travels parallel to the wood fiber direction, the polymer-filled lumen acts as a broadband waveguide, but with high propagation scattering losses. [2], showing an isotropic scattering (Figure 2. 20F, left). When light propagates perpendicular to the wood fiber direction (Figure 2. 20F, right), the x-direction-aligned wood fibers are expected to affect the light scattering in the y-direction. This interaction leads to a nonsymmetric intensity distribution across the two perpendicular planes. Anisotropy influences the transmittance and haze, based on the orientation of the incident beam relative respect to the direction of wood fibers. The transmittance and haze of R-wood are both higher than that of L-wood due to the high propagation scattering as light travelling in the vertically aligned channels of R-wood[4, 149, 150]. Despite the special advantages of anisotropic light scattering, the even distribution of light is often desired. Lamination is an effective way to turn the optical properties of TW from anisotropic to isotropic. Fu et al. [120] studied a five-layer structure of transparent plywood with varying fiber orientations. In contrast to the compressed, parallelogram-shaped scattering pattern seen in single-ply TWs, the quasi-isotropic transparent plywood displayed a nearly circular scattering pattern, with approximately 75% transmittance and 80% haze. The laminated fibers within the transparent plywood structure confined the light, leading to isotropic light scattering behavior. Similar anisotropic-to-isotropic transition has been reported by Wu et al [119, 151].

Berglund's group[3, 132, 133, 136, 144, 145, 150, 152, 153], has provided excellent illustrations of the relationship between the optical properties, the nano- and microscale structure, and the decoloration process and light-TW interaction. We refer the readers to these works for more detailed information about the TW substrate. However, the functional fillers and coting for TW are likely to introduce uncertainty to the current models. Further investigations about the impact of functional filler and coting on optical properties of TW should be conducted in future to better understand and control the optical properties of functional TW from a synthesis-structure-property perspective.

Mechanical properties are crucial to many practical applications of TW. Similar to the optical properties, the mechanical properties are highly dependent upon the wood species, wood scaffold volume, decoloration methods, polymer identities, sample thickness and microstructure (corresponding summary can be found in Table 2. 1). Several strategies can effectively enhance the mechanical performance of TW, including interface manipulation, densification of the wood scaffold and lamination.

The presence of air voids between the wood scaffold and polymers not only influence the optical properties, but also contribute to the formation and propagation of cracks under stress. Reduction of air voids through improvement of interfacial compatibility can enhance the mechanical properties of TW. For example, Montanari et al. prepared bio-based TW by impregnating cyclic anhydrides esterified delignified wood scaffold with PMMA[136]. Esterification of the delignified wood scaffold allows molecular-scale interface manipulation with tunable interfacial adhesion, improved optical transmittance and enhanced mechanical strength. Compared to the TW prepared from un-esterified wood scaffold, TW from succinic anhydride esterified wood scaffold shows improved tensile strength (from 41.4 MPa to 61.7 MPa, Table 2. 1). Similar to the control of optical properties, higher mechanical performance can also be achieved by selecting impregnating polymers with lower polymerization shrinkage[133]. Other interface design based on the surface modification of wood scaffold, such as acetylation, also permit improved control of the wood/polymer interfacial compatibility, achieving improved mechanical performance[132].

Another strategy to improve the TW mechanical properties is to adjust the wood scaffold volume fractions (V_f), which can be controlled by compressing the wood scaffold prior to impregnation. Compression increases the V_f accordingly, leading to enhanced mechanical performances. Densification by compression was reported by Li et al[3]. TW from the compressed wood scaffold shows much higher mechanical properties ($V_f = 19\%$, $E = 3.59$ GPa and $\sigma = 90$ MPa) than TW from un-compressed

wood scaffold (V_f = 19%, E = 2.05 GPa and σ = 38 MPa). Similar results can be found in Yu et al.'s and Wang et al.'s reports[94, 154]. The enhanced mechanical properties can be attributed to the hierarchical and longitudinally oriented cellulose nanofiber structure, which not only increases the modulus but also provides a significant synergistic improvement in strength. Some researchers also attributed these enhancements to the formation of additional hydrogen bonds between the cellulose microfibrils of the densified wood cells after compression[102]. The mechanical properties of TW are also anisotropic due to the intrinsic anisotropic structure of wood. As shown in Figure 2. 20G, the tensile strength (45.4 MPa) of L-wood is twice that of transverse TW (23.4 MPa, R-wood). However, in many cases, the isotropic mechanical performance is desirable. Similar to the methods for regulating optical properties, lamination is an effective method to obtain TW with isotropic mechanical properties. Transparent balsa veneer plies were laminated with control over the wood fiber direction and thickness to create an isotropic TW. The resulting transparent plywood exhibited an increase in ultimate strength from 15 MPa to 45 MPa (Fig. 4h) under transverse loading[120]. The resultant elastic moduli and tensile strengths after lamination might be predicted by classical lamination plate theory and simple rule of mixtures, respectively [138].

One significant justification for the potential of TW to replace common glasses is its toughness (~3.2 MJ/m^3), which can be 30 times higher to that of common glass (~0.1 MJ/m^3)[155]. Unlike common silica-based glass, TW will not shatter into sharp pieces in case of strong sudden impact, eliminating potential safety issues. The high toughness of TW might relate to the identity of the impregnating polymer and the wood structure[99]. Though the toughness of TW is crucial for practical applications, especially for building applications, little research has been expended on this topic. Recently, Jungstedt et al.[156] investigated the transverse fracture toughness of TW. Their results indicated that the fracture toughness of TW might be highly related to the intercellular peeling energy, which may decrease during the delignification process (removal of the lignin-rich middle lamella between fibers). Therefore, two possible

strategies for improving the fracture toughness were proposed[156]. One is impregnating polymers into the delignified interfiber region. Another is selecting other methods for selectively degrading the chromophores rather than delignification. These strategies might require additional validation in future research.

Thermal insulation is an essential component of buildings, particularly those designed for energy conservation, with its efficacy primarily dependent on thermal conductivity. The thermal conductivity of a material is influenced by various factors, including pore structure (pore size and porosity), the volume fraction of the solid wood scaffold, and the anisotropy of the wood structure. The thermal conductivity of transparent wood (TW) is anisotropic, with values such as 0.357 W/(m·K) in the axial direction and 0.190 W/(m·K) in the radial direction (Figure 2. 20H), primarily due to the alignment of wood cellulose fibers. This anisotropy can be explained by the fact that heat propagation perpendicular to the highly aligned lumens (Figure 2. 20I, radial) encounters greater phonon scattering compared to heat propagation along the lumens (Figure 2. 20I, axial). The nanoscale pores in the wood scaffold also against the heat propagation, leading to the low thermal conductivity of TW. This thermal conductivity is lower than conventional silica glass, implying that it is more thermally insulating. As a result, TW can inherently help maintain a more consistent temperature within a building, even without the use of coatings or additives, thereby facilitating higher energy efficiency. For example, TW glazing could reduce space conditioning energy consumption by ~25-33% in medium and large office spaces [157]. A further potential TW benefit stems from this thermal conductivity anisotropy; thin electronic devices require efficient heat dissipation and TW's directional dependence properties imply that TW is a potential substrate for dense loading of multiple devices with thermal interference between heat sources in close proximity being minimized due to the directional heat dissipation effects [158, 159].

The thermal conductivity of TW is also affected by the wood scaffold volume fraction. The thermal conductivity of haze wood (prepared from $NaClO_2$/acetate decoloration

method, 0.24 $W \cdot m^{-1}K^{-1}$) is lower than that of clear wood (prepared from NaClO decoloration method, 0.35$W \cdot m^{-1}K^{-1}$) [140]. The reduction in thermal conductivity can be attributed to the fact that the $NaClO_2$/acetate decoloration method (V_f~18.4%) provides higher wood scaffold volume fraction than the NaClO system (V_f~2.9%), resulting in more nanoscale pores. The increased nanoscale pores may pose more blocking or confinement (i.e., the increased phonon scattering) to heat propagation when phonons travel through the wood cell walls [2]. Therefore, manipulation of the wood scaffold volume fraction and heat transfer direction offers a potential method for achieving the desired thermal insulating performance.

2.5.5 Transparent wood for Building application

Since its inception, transparent wood (TW) has been developed as a structural material for building applications, owing to its exceptional mechanical, optical, and thermal properties. The use of nature-based materials intrinsically reduces the impacts of manufacturing on the broader environment. Green building materials enable construction of energy-efficient structures that could help decarbonize urban areas and achieve net-zero carbon buildings, whilst also producing sustainable structures that are stronger, more functional and longer-lasting (often outlasting their established counterparts) [160-162]. Intriguingly, such new materials will also enable the exploration of new design, architecture and construction directions, most likely for light discrimination purposes in the first instance [163, 164].

Conventional building materials and their often energy-inefficient nature make the building industry (both commercial and residential) one of the most energy-intensive sectors on this planet. For example, siliceous glass is the established material for use in building windows for light transmission. However, it suffers from high thermal conductivity (~1.0 W/(m·K)) and is brittle in the event of failure, resulting in unwanted substantial energy loss/gain and potential safety issues. The reflecting and glazing effect of glass not only causes visual discomfort but also results in lower working

efficiency, poor emotional well-being, and even occasional traffic accidents [2]. Moreover, the glass manufacturing industry is estimated to emit more than 60 million tons of CO_2 per year [165]. Thus, it is of great significance to promote the green transition of the building industry in terms of materials and energy consumption. Functional TW may play an important role in this anticipated transition due to its optical, mechanical and thermal properties as well as greater sustainability.

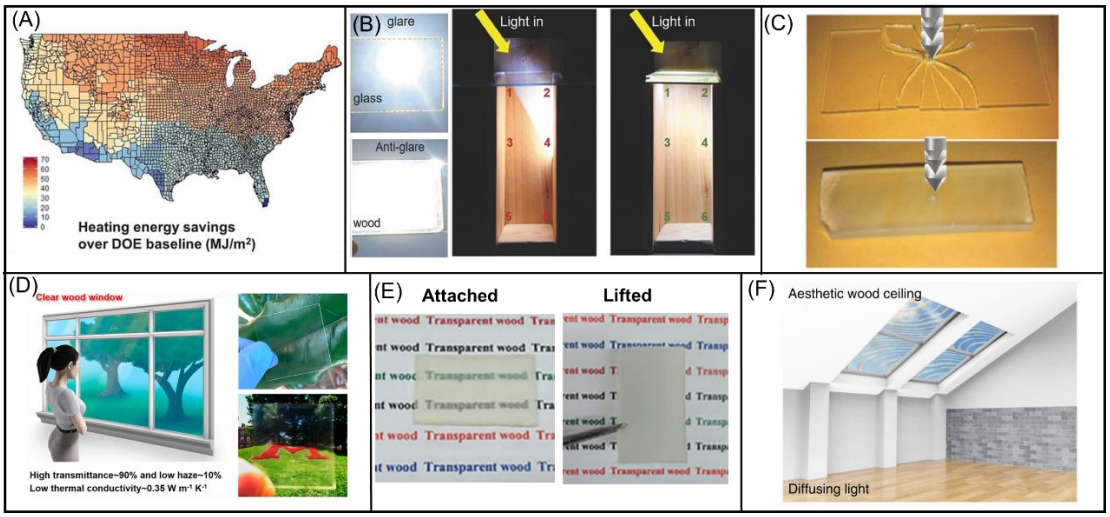

Figure 2. 21 (A) The heating energy savings pattern for the continental U.S. over the DOE baseline [134]; (b & c) [2]: (B) Photographic showing the anti-glare effect and light guide effect of TW; (c) The impact test of a piece of standard glass and a transparent wood composite of similar thickness; C) Photographic showing the anti-glare effect and light guide effect of TW; (D) Schematic illustration of the clear wood and its digital images [140]; (E) Digital photo showing the privacy protection potential of TW [129]; (F) The schematic scene shows the light distribution and aesthetic appeal inside a building [166].

TW has been considered one of the most promising green building material candidates for the following reasons: (1) The thermal insulating properties. (2) The ability of visible light guiding and high haze. (3) High toughness. (4) Sustainability. The inherent low thermal conductivity (~0.19 W/(m·K)) of TW makes it a promising candidate for energy saving applications, allowing for lower energy consumptions than conventional

glass. The energy saving simulation suggests that TW, when used in double-pane windows with air filling the intervening gap, can provide energy savings compared to the baseline set by the US Department of Energy (DOE). The savings are estimated to be 38 and 23 $MJ \cdot m^{-2}$ per year in old and new buildings, respectively (Figure 2. 21A) [134]. TW can be used for glazing materials in buildings for visual clarity (low haze) or privacy protection (high haze). The light guide effect of TW enables uniform illumination with enhanced visual comfort (Figure 2. 21B), while avoiding the glaring effect of common glass (Figure 2. 21B). Moreover, the potential safety issues of common glass arising from intrinsic brittleness can be avoided due to the high ductility of TW. As shown in the Figure 2. 21C, after a sudden impact, common glass break into shattered pieces, posing serious safety concerns. Due to its high toughness, transparent wood only bends and splits rather than shattering into sharp pieces, dispelling the safety concern associated with common glass [2]. TW can serve dual purposes as windows, providing both visual clarity and privacy protection, depending on the level of haze. Low-haze TW can be achieved by complete delignification (NaClO) and interfacial design [133, 134, 140]. TW with a 10% haze was obtained from NaClO delignification process, indicating a great potential of replacing common glass for visual clarity (Figure 2. 21D). While the high-haze TW with a haze of 75% and a transmittance of 83%, obtained from alkaline/H_2O_2 lignin modification, allows for normal lighting and personal privacy protection (Figure 2. 21E) [129]. The aesthetic appeal of building envelopes is also a fundamental cultural need for human beings. This can be accomplished through structural design and lamination. As discussed in section 3.7, TW with various patterns, such as letters and the symbol of TaiJi, can be obtained via the solar-assisted chemical (H_2O_2) brushing method[131]. By taking advantage of the gradient distribution of lignin between late and early natural wood, aesthetic TW with visually appealing patterns resembling the natural growth rings of trees can be obtained[166, 167]. More complicated patterns can be obtained by laminating several layers of TW. Such aesthetically pleasing TWs were showcased as a patterned ceiling installation in a museum or gallery, creating a uniformly illuminated indoor environment (Figure 2. 21F). From the point view of sustainability, the wood scaffold

can be regarded as renewable and biodegradable, and the fabrication process involves less energy consumption as compared to glass making. It is more promising to note that impregnated resins and functional components are transitioning towards more environmentally friendly materials, such as biomass-derived PLIMA, biodegradable PVA and renewable 1-dodecanol[128, 134, 168, 169]. According to the cradle-to-gate life-cycle assessment, the fully bio-based TW system offers higher sustainability benefits (approximately 40% lower environmental indicator metrics) when compared to conventional transparent panels like PMMA and PC [169].

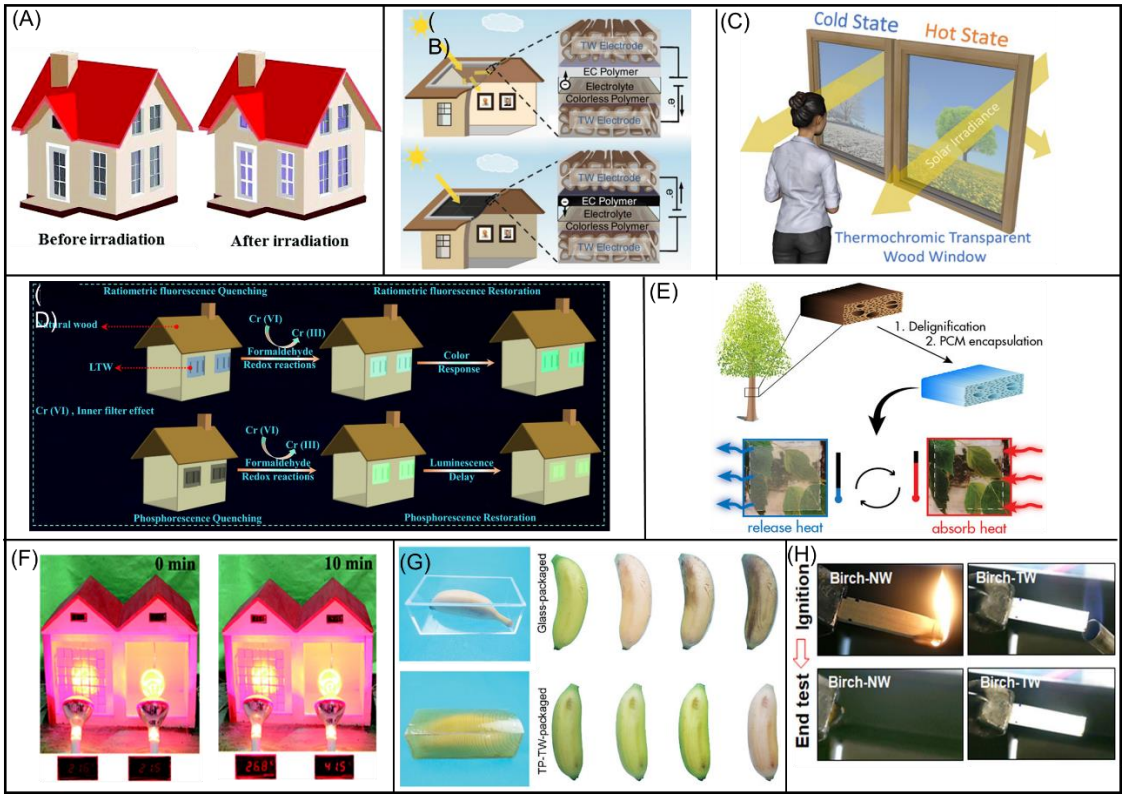

Figure 2. 22(A) Schematic of TW windows on building before irradiation and after irradiation[170]; (B) Demonstration of electrochromic TW for smart windows and roofs [155]; (C) The schematic illustration of thermochromic TW for smart windows [171]; (D) Schematic of the TW based gas sensor for detection of FA gas [172]; (E) Schematic illustration of TW for energy storage and release at different temperatures [139]; (F) Images of model houses to show the temperature change after 10 min's simulate solar radiation[94]; (G) Photo of glass-packaged (upper) and TP-TW-

packaged (lower) banana after different treatment durations of solar radiation [167]; (H) Flammability test snapshots in horizontal and vertical direction [141].

Extra functionalities boost the potential of TW in building application. Photochromic- [170], electrochromic- [173], thermochromic- [95, 174], luminescent- [172, 175, 176], thermal energy storage/release- [139, 177], NIR shielding- [94, 96], and UV-protective-TW [167, 175] both have enhanced its the application value in some aspects. Specifically, the implementation of photochromic TW as windows would enhance the aesthetic appeal by introducing color changes (Figure 2. 22A), while also reducing total light exposure through UV absorption[170]. Similarly, the electrochromic TW also shows unique color changes behaviors and holds great promise for energy-efficient smart windows and roofs (Figure 2. 22B) [155]. Thermochromic TW, enabled by VO_2, allows for low/high NIR transmissions at high/low temperatures, providing considerable solar modulation [95, 171]. This enables the use of TW as smart windows (Figure 2. 22C), providing improved indoor temperature control and, consequently, reduced indoor energy consumption. Luminescent TW, obtained from impregnating multicolor lignin-derived carbon dots (CDs) and poly(vinyl alcohol) (PVA) into wood scaffold, provides dual-channel, real-time, and visual detection of formaldehyde gas (Figure 2. 22D) when used as windows [172]. Thermal energy storage TW absorbs heat at high temperatures (above the melting temperatures of the polyethylene glycol (PEG) polymers), and releases heat at low temperature (below the crystallization temperature of PEG polymers), allowing TW better to regulate indoor temperature when used as energy-saving windows (Figure 2. 22E) [139]. By blocking the majority of near infrared, NIR shielding TW reduces the indoor temperature increase caused by solar radiation (as shown in Figure 2. 22F). Therefore, NIR shielding TW is expected to further enhance the energy efficiency of buildings by reducing the cooling loads during hot hours [178]. UV radiation is imperceptible to the human eye, yet it poses a potential hazard and can inflict damage to various indoor items, including furniture and interior displays. Consider the common glass packaged banana, which showed signs of rotting on the exterior after 3 h of simulated solar radiation [167]. In

contrast, the banana packaged with UV protective TW remained relatively fresh due to its thermal management and UV-blocking capabilities (Figure 2. 22G). The use of UV-protective TW creates a relatively UV-free environment, which is advantageous for prolonging the service life of indoor items. Despite the promising potential of TW in building applications, the issues of fire safety must be resolved before practical implementation can be achieved. The flammability of TW raises safety concerns regarding its practical application. To address these concerns, flame retardants or intrinsic flame-retardant polymers can be impregnated into wood scaffolds to increase the fire safety of TW [137, 141, 178-181], but this may compromise the optical properties. For example, by selecting melamine formaldehyde as the impregnating polymer, the MF based TW showed excellent self-extinguishing performance (Figure 2. 22H).

2.6 Conclusion and summary of the identified research gaps

2.6.1 Summary

In this chapter, the basic principle for building and personal thermal management, an overview of radiative cooling, radiative cooling modulation, and transparent wood is presented, with a focus on fundamental physics, working principles, applications, and performance. First, basic model and fundament design principle for building and personal thermal management is presented. The thermal management concept in the burning process was also proposed. Then, the fundamental physics of radiative cooling is discussed from the perspective of radiative heat transfer, covering basic concepts such as black body radiation, the fundamental mechanism of radiative cooling, and the overcooling effect associated with it. Third, examples of radiative cooling and radiative cooling modulation applications for building and personal thermal management are explored, including implementations in walls, roofs, windows, coatings, and textiles. Finally, a detailed introduction to transparent wood is provided, discussing its basic fabrication process, the mechanism behind its transparency, its various properties, and potential applications.

2.6.2 Summary of knowledge gaps

Integrating radiative cooling and its modulation into novel thermal management systems, such as building and personal thermal management, holds great promise for significant economic and environmental benefits. However, the development of these technologies faces several challenges. This literature review discusses the advancements in radiative cooling, its modulation, and transparent wood, highlighting the following research gaps in the field of novel thermal manipulation systems:

(1) Integration of Radiative Cooling and Transparent Wood: The combination of radiative cooling and window materials could significantly improve the energy-saving performance of the entire building. The integration of radiative cooling into transparent wood has not yet been explored. Thus, fabricating and exploring the energy-saving potential of transparent wood with radiative cooling capabilities is warranted.

(2) Transparent Wood with Emissivity Modulation: While transparent wood with radiative cooling offers considerable energy savings for novel thermal regulation systems, its continuous cooling power during cold hours may offset the energy savings achieved during hot hours. Therefore, it is crucial to develop methods to modulate the radiative cooling of transparent wood in response to the external environment.

(3) Self-Adaptive Radiative Cooling in Personal Thermal Management Via Emissivity Modulation: Radiative cooling has been widely explored in personal thermal management systems to enhance thermal comfort and save space cooling energy. However, temperature fluctuations can adversely affect human thermal regulation due to the fixed radiative cooling capacity. Therefore, self-adaptively modulated radiative cooling is essential to achieve thermal comfort in environments with significant temperature variations.

(4) Fire Safety of Transparent Wood: Despite the great potential of transparent wood for building thermal management, its fire safety limitations hinder widespread adoption. Current methods to improve the fire safety of transparent wood often compromise its transparency and mechanical properties. Therefore, it is imperative to enhance the fire performance of transparent wood without sacrificing these critical properties.

By addressing these gaps, we can advance the development of effective thermal management systems that leverage radiative cooling and its modulation, providing substantial benefits for both buildings and personal applications.

Chapter 3 Research Methodology

3.1 Transparency mechanism

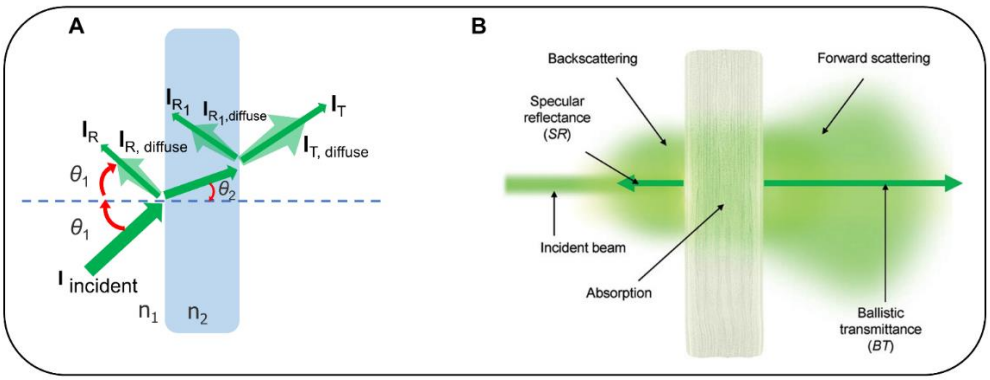

Figure 3. 1 A) Sketch Illustration of light-solid object(RI, n_1) interaction in a medium (RI, n_2), where $I_{incident}$ (incident light intensity), I_R (intensity of specular reflection) $I_{R,\ diffuse}$ (diffusely reflected light intensity), I_T (ballistically transmitted light intensity), $I_{T,diffuse}$(diffusely transmitted light intensity), θ_1(incident angle) and θ_2 (refracted angle) are presented. B) Measurable photon budget components[145].

The light-solid object interaction is crucial to comprehending the mechanism of transparency. As shown in Figure 3. 1A, when light interacts with a solid object (n_1) in a medium (n_2), it may be reflected backwards at the solid-medium interface, or it may propagate forwards for refraction and/or absorption, and the refraction is governed by Snell's law:

$$n_1 \sin\theta_1 = n_2 \sin\theta_2$$

Where n_1 is the RI of the medium, n_2 is the RI of solid object, θ_1 is the angle of incidence, θ_2 is the angle of refraction. Generally, the bigger the difference between n_1 and n_2, the stronger the light scattering. The transmittance of this solid object can be determined by the ratio of transmitted light intensity (both ballistically transmitted and diffusely transmitted) to incident light intensity. Haze is calculated using the ratio of diffused transmitted light intensity to the intensity of transmitted light (both ballistically transmitted and diffusely transmitted). Wood is usually composed of cellulose (RI of 1.52), hemicellulose (RI of 1.53), and lignin (RI of 1.61) – a light-absorbing (accounting for 80–95% of the light absorption) structural polymer that serves as a 'glue'

for the wood framework[106, 182]. Wood naturally possesses a multiscale porous structure (both micro- and nanoscale), with its lumen spaces fully filled with air (refractive index, RI of 1.00). Consequently, the RI contrast between the wood cell walls (1.52-1.61) and the air-filled lumen (1.00), along with the presence of lignin (which absorbs light), leads to significant scattering and absorption when light interacts with the wood at the air-cell wall interfaces. To render wood transparent, it is essential to reduce or eliminate both the absorption caused by lignin and the scattering effects due to the RI contrast.

Therefore, the preparation of TW usually involves two steps: decoloration (removing/modifying lignin) and impregnation (reducing the light scattering). The air-filled lumen is filled with RI-matched polymers. Such impregnating polymers subsequently enables the production of TW. As shown in Figure 3. 1B, the light scattering is dominated by forward scattering if there are no voids within the sample (e.g., nano-voids inside wood cell wall or air gaps between cell wall and polymer). In other words, the majority of the photons can pass through TW, despite the fact that the ratio of ballistically transmitted photons to total transmitted photons (forwards scattering and ballistically transmitted) varies with different sample thickness. Therefore, the resultant composite appears “transparent” after impregnation. The resultant material is also less frequently (but perhaps more correctly), as ‘translucent wood’.

3.2 Delignification of natural wood

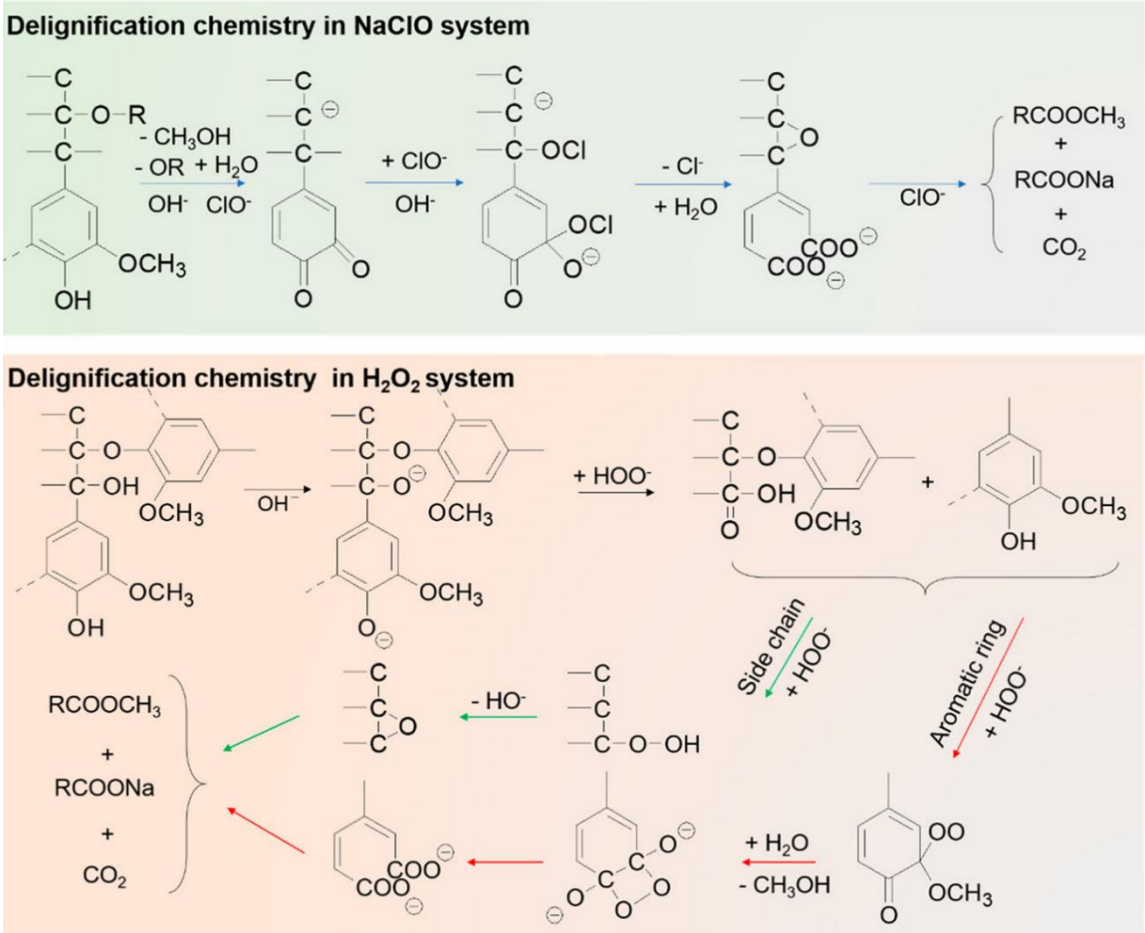

Figure 3. 2 Chemistry in NaClO and H_2O_2 system[104].

In order to make the wood transparent, it is essential to remove or modify the light-absorbing content (i.e., lignin) in the natural wood. Two delignification approaches were adopted in this thesis: NaClO and H_2O_2 system[104].

For the NaClO system (Figure 3. 2), lignin, with its anionic phenol groups and cleaved β-ether bonds, is targeted by hypochlorite ions, resulting in the formation of hydrochloride ester structures within the lignin. Through the release of hypochlorite ions, lignin undergoes oxidation and hydrolysis, breaking down into carboxyl- and carbonyl-containing fragments, as well as CO_2. During the NaClO-based delignification process, cellulose also experiences chemical changes, primarily involving the transformation of hydroxyl groups into carbonyl and subsequently carboxyl groups. Additionally, the polysaccharides degrade into oligosaccharides and related saccharic and organic acids.

The chemistry for the H_2O_2 system is even more complicated (Figure 3. 2)). Within the H_2O_2 system, various reactive anions and radicals are generated, including hydroperoxide (HOO^-) ions, superoxide ($O_2^{-}\bullet$) radicals, and hydroxyl ($HO\bullet$) radicals. Among these, HOO^- ions play a predominant role in reacting with lignin by cleaving the bonds between aromatic rings and side chains (Figure 4c). These ions also disrupt unsaturated bonds in lignin's side chains, such as carbonyl groups and olefin aldehyde structures, leading to the formation and subsequent breakdown of oxirane intermediates into small aliphatic compounds. Concurrently, the aromatic rings are attacked by HOO^- ions, forming epoxide intermediates that are eventually oxidatively decomposed into carbonyl and carboxyl compounds. Additionally, HO^- ions, $HO\bullet$ radicals, and $O_2^{-}\bullet$ radicals contribute to the oxidation, hydrolysis, and degradation of lignin, further facilitating the delignification of wood. The fragmentation of lignin macromolecules and the breakdown of conjugated lignin structures demonstrate the effectiveness of these chemical processes in modifying wood structure at the micro- and nanoscale. However, it is important to note that transition metal ions can catalyze the decomposition of H_2O_2 into O_2, which negatively impacts the overall delignification rate. To counteract this, chelating agents such as ethylenediaminetetraacetic acid (EDTA) and diethylenetriaminepentaacetic acid (DTPA) are often added to the H_2O_2 system to prevent metal-catalyzed decomposition. Additionally, earth-metal-based chemicals like $MgSO_4$ and Na_2SiO_3 can act as stabilizers, suppressing H_2O_2 decomposition and thereby enhancing the rate and efficiency of delignification.

3.3 Sonochemical deposition

Sonochemical deposition is a process that leverages the extreme conditions generated by ultrasound-induced acoustic cavitation to deposit materials onto substrates[183, 184]. When high-intensity ultrasound waves propagate through a liquid containing precursor materials, they create alternating compressive and expansive waves, leading to the formation, growth, and collapse of bubbles (Figure 3. 3). This phenomenon, known as acoustic cavitation, results in the generation of transient hot spots with temperatures exceeding 5000 K, pressures over 1000 atmospheres, and extremely rapid heating and

cooling rates. The collapse of bubbles also produces microjets that offer distinct make the directed deposition possible.

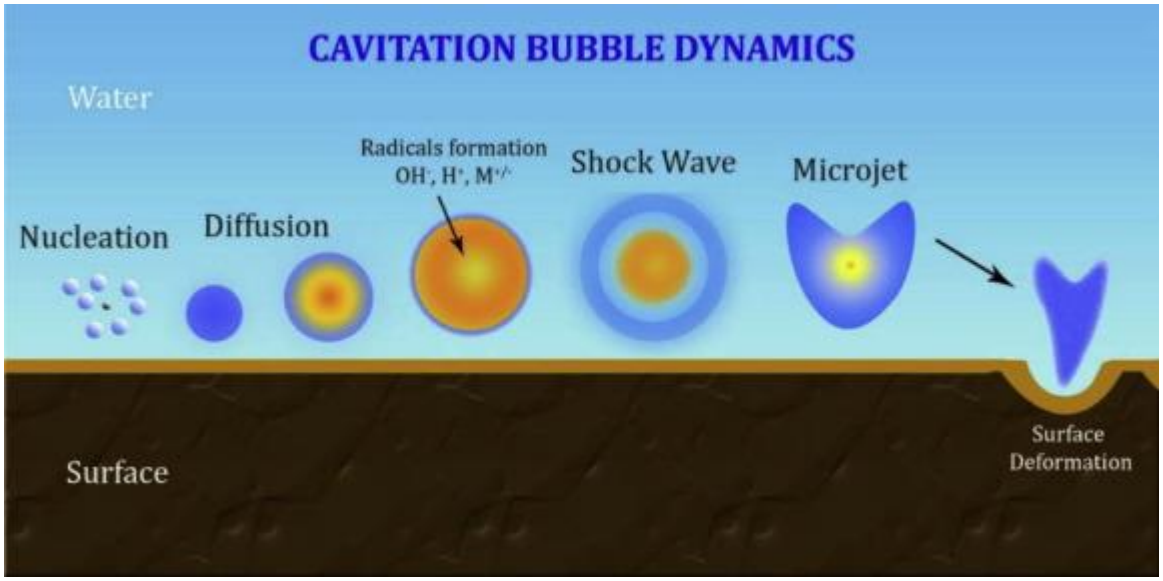

Figure 3. 3 The process of acoustic cavitation and its effect[184].

These extreme conditions are capable of initiating and accelerating chemical reactions within the liquid medium, leading to the deposition of the resulting material onto a substrate. The ZnO nanocoating on transparent wood was fabricated via sonochemical deposition technique. The preparation process created uniform ZnO coatings at lower bulk temperatures.

3.4 Spinning coating

Spin coating is a widely utilized technique in material science and nanotechnology for applying uniform thin films onto flat substrates. The process involves depositing a liquid solution onto the center of a substrate, which is then rapidly rotated at high speeds. The centrifugal force generated during spinning spreads the liquid evenly across the surface, forming a thin, uniform film. The film's thickness can be precisely controlled by adjusting parameters such as spin speed, solution viscosity, and concentration. Spin coating is valued for its efficiency, reproducibility, and ability to produce smooth, homogeneous films. Here, we use this technique to construct Fabry-Perot structures on transparent wood.

3.5 Energy saving simulation

TRNSYS 18 is a versatile and highly flexible simulation software package designed for modeling and analyzing the performance of transient systems, particularly in the fields of building energy simulation and renewable energy systems. Developed by the Solar Energy Laboratory at the University of Wisconsin-Madison, TRNSYS stands for Transient System Simulation Tool and has been widely used in academia, research, and industry for over four decades. In this thesis, TRNSYS 18 was adopted to simulate the energy saving potential of ZnO coated transparent wood.

Energy Plus is a widely used, open-source building energy simulation software developed by the U.S. Department of Energy. It is designed to model and simulate the energy performance of buildings, including heating, cooling, lighting, ventilation, and other energy-related aspects. Energy Plus provides detailed analysis by integrating complex algorithms that account for various factors such as weather conditions, building materials, HVAC systems, and occupant behavior. In this thesis, Energy Plus V22-2 was adopted to simulate the energy saving potential of emissivity regulation transparent wood in various climates.

3.6 Thermal imaging

Infrared imaging, also known as thermal imaging, is a technology used to visualize and measure temperature variations on the surface of objects. This technique captures infrared radiation, which is emitted by all objects based on their temperature and converts it into a thermal image or thermogram. The resulting images reveal temperature differences that are not visible to the naked eye, making infrared imaging an essential tool in various fields such as building diagnostics, electrical inspections, industrial maintenance, and research. Infrared imaging and emissivity are closely related, as emissivity is a key factor in the accuracy and interpretation of thermal images. The camera detects the infrared radiation emitted by the surface of an object to determine its temperature. The accuracy of this temperature measurement depends on the emissivity setting of the camera. If the emissivity is not correctly accounted for, the

temperature readings may be inaccurate. For instance, a material with low emissivity, such as shiny metals, will reflect more of the surrounding infrared radiation, potentially leading to an underestimation of its actual surface temperature in the thermal image. This relationship makes it possible to compare the emissivity of different objects using infrared imaging, provided the effect of surrounding radiation is minimized. When two objects are at the same actual temperature, differences in their apparent infrared temperatures can reveal variations in their emissivity. In this thesis, FLIR E95 IR camera (working wavelength~7-14 μm) was used for thermal imaging.

3.7 Outdoor and indoor measurement

To thermal performance of SARCF, indoor and outdoor experiments were conducted using self-made setups and skin simulator. To simulate human skin, a layered structure comprising a Kapton heater, thermally conductive silicone grease, a copper plate, and 3M tape was employed. The Kapton heater, powered by a direct current source, delivered a heat flux of approximately 150 W/m², equivalent to the metabolic heat generation of the human body. The silicone grease and the 1.5 mm thick copper plate functioned as a thermal connector and heat diffuser, respectively, ensuring uniform temperature distribution across the surface. To minimize external thermal influences during testing, aluminum foil and EPS foam were integrated into the device. Temperature data was continuously recorded every second using a M2100 Series (Samcq) Temperature Acquisition Remote IO Module, which was connected to a laptop and equipped with PT100 resistance thermometers to monitor the temperature.

3.8 Thermal properties

3.8.1 Thermal conductivity

The thermal conductivity of building envelope plays a significant role in building energy efficiency and energy savings. Thermal conductivity indicates a material's ability to conduct heat. For windows, this property directly affects how much heat is transferred between the interior and exterior of a building, influencing both heating and cooling demands. Windows with high thermal conductivity allow more heat to pass

through, leading to higher heat loss in the winter (heating season) and more heat gain in the summer (cooling season). This results in increased energy consumption for heating and cooling systems to maintain comfortable indoor temperatures. Conversely, windows with low thermal conductivity act as better insulators, reducing heat transfer between the inside and outside of the building. This minimizes the demand on heating and cooling systems, leading to significant energy savings. Int this thesis, all the thermal conductivity of TW was measured by a thermal conductivity meter equipped with Hot Disk Kapton sensor.

3.8.2 Differential Scanning Calorimetry (DSC)

Differential Scanning Calorimetry (DSC) is particularly useful for characterizing the phase transition of materials like Vanadium Dioxide (VO_2). VO_2 exhibits a well-known phase transition from a monoclinic (insulating) phase to a tetragonal (metallic) phase at around 68°C (341K). This phase transition is reversible and is accompanied by a significant change in electrical conductivity and optical properties. The phase transition is also associated with a change in enthalpy, making DSC an ideal tool to study this thermal behavior. The DSC curve will show a characteristic peak at the transition temperature, which can be analyzed to determine the onset temperature, peak temperature, and the enthalpy change (ΔH) associated with the phase transition. The phase transition temperature of VO2, determined by DSC, is also an effective indicator for the doping effectiveness. Here, we use PerkinElmer DSC 8000 to measure the enthalpy of VO2 associated with the phase transition.

3.9 Tensile test

Tensile test is a fundamental mechanical test used to determine the mechanical properties of a material, particularly its strength and ductility. During the test, a sample material is subjected to a controlled, uniaxial tensile force until it fails. The test provides valuable data on how the material behaves under tension, including its ability to withstand pulling forces and its capacity to deform before breaking. It yields important data on strength, ductility, and elasticity, making it essential for material selection, product design, and quality assurance in various industries. Here, we use tensile test to

evaluate the mechanical performance of TW.

3.10 Spectral characterization

3.10.1 UV-Vis-NIR Spectroscopy (UV-Vis-NIR)

UV-Vis-NIR Spectroscopy is a powerful analytical technique used to measure the absorbance, reflectance, and transmission of light across the ultraviolet (UV), visible (Vis), and near-infrared (NIR) regions of the electromagnetic spectrum. With the integrating sphere, UV-Vis-NIR spectrometer allows the measurement of transmittance and reflectance quantitatively in the range of 200-2500nm. The UV-Vis-NIR is adopted to measure the reflectance and transmittance of the samples mentioned in this thesis. The haze was also measured and calculated based on the ASTM D1003 using the same UV-Vis-NIR spectroscopy.

3.10.2 Fourier Transform Infrared (FTIR)

Fourier Transform Infrared (FTIR) Spectroscopy is an analytical technique used to obtain an infrared spectrum of absorption, emission, or photoconductivity of a solid, liquid, or gas sample. It works by passing infrared light through a sample and measuring how much of the light is absorbed at different wavelengths. The resulting spectrum represents the molecular fingerprint of the sample, with distinct absorption bands corresponding to specific molecular bonds and functional groups. We can measure reflectance and transmittance of one objective quantitatively by equipping a Mid-IR integrating sphere (Figure 3. 4) with an existing FTIR spectrometer. The s optical geometry of the Mid-IR integrating sphere was shown in Figure 3. 4.

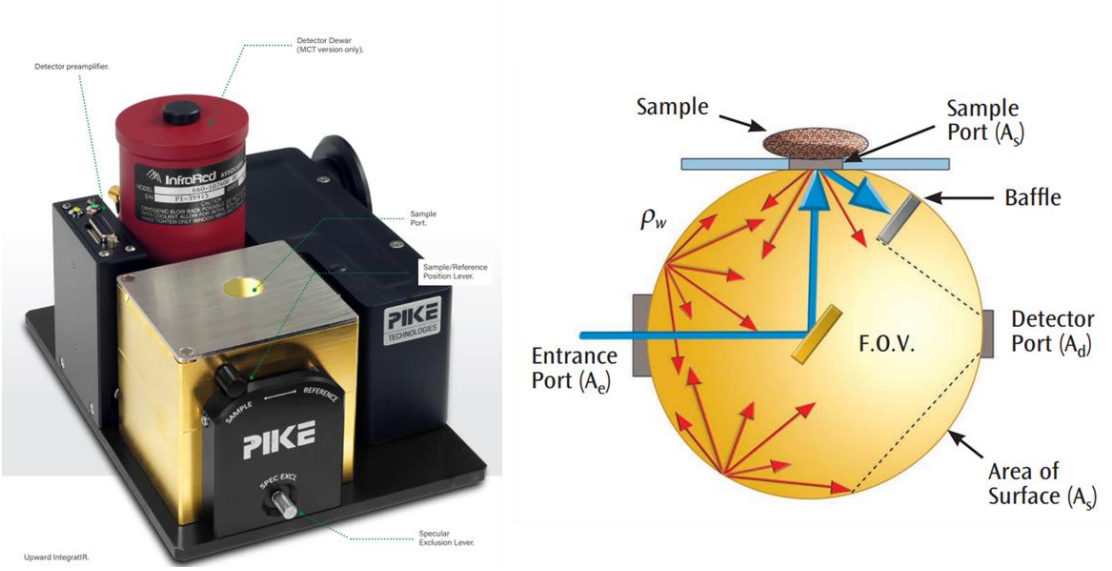

Figure 3. 4 Mid-IR integrating sphere from PIKE and its optical geometry.

For the reflectance mode, the sample is placed at the sample port (labeled as A_s) on the surface of the integrating sphere. Infrared light from the FTIR source enters the sphere through the entrance port (labeled as A_e) and illuminates the sample. When the light strikes the sample, part of it is reflected diffusely. This means that the reflected light is scattered in many directions rather than just one. The diffusely reflected light is captured by the integrating sphere. The internal reflective coating of the sphere ensures that the light is uniformly scattered within the sphere. Then, the detector, positioned at the detector port, measures the light that has been diffusely reflected and evenly distributed within the sphere. The baffle inside the sphere helps in minimizing direct specular reflection from the sample to ensure that only diffuse reflectance is measured.

For the transmittance mode, the sample is typically placed at the entrance port or another designated port within the sphere that allows light to pass through the sample. The light enters the sphere through the entrance port and passes through the sample. As light transmits through the sample, it may scatter due to the material properties. This scattered, transmitted light then gets diffused within the integrating sphere. Similar to the reflection mode, the internal coating of the integrating sphere ensures that the transmitted light is uniformly scattered within the sphere. The detector, located at the detector port, measures the light that has been diffusely transmitted through the sample

and evenly distributed within the sphere.

Note that the emissivity (ε)/or absorbance (σ) cannot be directly measured by integrating sphere. The emissivity (ε(λ)) can be calculated according to Kirchhoff's law:

$$\varepsilon(\lambda) = \sigma(\lambda) = 1 - R(\lambda) - T(\lambda)$$

Where $\sigma(\lambda)$, $R(\lambda)$ and $T(\lambda)$ are the absorbance, reflectance, and transmittance spectrum of the surface. All quantitative MID infrared data was obtained or calculated according to above text.

3.10.3 Raman Spectroscopy

Raman Spectroscopy is a non-destructive analytical technique used to study the vibrational, rotational, and other low-frequency modes in a material. It works by shining a monochromatic light source, typically a laser, onto a sample and measuring the scattered light. Most of the scattered light has the same wavelength as the incident light (Rayleigh scattering), but a small portion is scattered at different wavelengths due to interactions with the molecular vibrations of the material—this is known as Raman scattering. The shift in wavelength provides a unique molecular fingerprint that can be used to identify chemical structures, study molecular interactions, and analyze material compositions. In this thesis, a Renishaw Micro-Raman Spectroscopy System equipped with a LTS120T-P Electrical & Probe Temperature Control System was used to acquire the Raman spectra. The LTS120T-P was used to control the temperature, in case heating or cooling is needed.

3.10.4 X-ray diffraction (XRD)

X-ray Diffraction (XRD) is a fundamental technique used for characterizing the crystalline structure of materials. The principle behind XRD is based on the constructive interference of monochromatic X-rays and a crystalline sample. When X-rays are directed onto a crystalline material, they interact with the atoms in the crystal lattice. Depending on the arrangement of atoms, the X-rays are diffracted in specific

directions. For the measurements of ZnO coating on TW, a Rigaku SmartLab X-ray diffractometer at Grazing angle mode is adopted. In this mode, the incident X-ray beam strikes the sample surface at a very shallow angle, typically just a few degrees relative to the surface plane, rather than the more typical higher angles used in standard XRD. In this thesis, a glancing angle of 2º was applied. For powder sample, a normal mode (θ-2 Theta) was applied. In case of the need of heating and cooling, an Anton PAAR TTK 600 temperature control system was involved.

3.10.5 . X-ray Photoelectron Spectroscopy (XPS)

X-ray Photoelectron Spectroscopy (XPS) is a highly sensitive surface analysis technique used to investigate the elemental composition, chemical state, and electronic state of the materials' surfaces. It works by irradiating a sample with X-rays, typically from an aluminum or magnesium source. When the X-rays hit the surface, they cause the emission of photoelectrons from the atoms within the material. The kinetic energy of these emitted photoelectrons is measured, and from this data, the binding energy of the electrons in the atoms can be calculated. The binding energy is characteristic of specific elements and their chemical states, allowing for precise identification and quantification of the elements present at the surface of the sample, typically within the top 1-10 nanometers. X-ray Photoelectron Spectroscopy wad adopted to characterize the ZnO coating and W-VO_2 in this thesis.

3.11 Morphology and element distribution

3.11.1 Scanning Electron Microscopy (SEM) and Energy Dispersive X-ray Spectroscopy (EDS)

Scanning Electron Microscopy (SEM) is a powerful imaging technique used to obtain high-resolution images of the surface of a material. In SEM, a focused beam of high-energy electrons is scanned across the surface of the sample. When these electrons interact with the atoms in the sample, they generate various signals that can be detected and used to produce detailed images of the sample's surface topography and composition. Energy Dispersive X-ray Spectroscopy (EDS) is an analytical technique

often coupled with SEM to provide elemental analysis of a sample. When the electron beam in SEM strikes the sample, it can eject inner-shell electrons from the atoms. This creates vacancies that are filled by electrons from higher energy levels, resulting in the emission of characteristic X-rays. EDS detects these X-rays and uses their energies to determine the elemental composition of the sample. It can provide qualitative and quantitative information about the elements present and their distribution within the sample. EDS is particularly useful for identifying the composition of small features observed in SEM images, allowing for a comprehensive analysis of the material's structure and composition. In this thesis, SEM and EDS technique was applied to observe and analyze the sample morphology and element composition when needed.

3.11.2 Transmission Electron Microscopy (TEM)

Transmission Electron Microscopy (TEM) is a powerful imaging technique that allows for the visualization of the internal structure of materials at an atomic or nanometer scale. Unlike Scanning Electron Microscopy (SEM), which images the surface of a sample, TEM involves transmitting a beam of high-energy electrons through an ultra-thin sample. As the electrons pass through the sample, they interact with the material's atoms, and these interactions produce a variety of signals that can be used to form an image. The transmitted electrons are focused by magnetic lenses to create highly detailed images that reveal the internal structure of the sample, including the arrangement of atoms, crystallographic information, and defects within the material. In this thesis, TEM was adopted to confirm the morphology and crystal structure of W-VO_2.

3.12 Fire performance

3.12.1 Thermogravimetric Analysis (TGA)

Thermogravimetric Analysis (TGA) is an analytical technique used to measure the change in mass of a material as a function of temperature or time under a controlled atmosphere. The technique involves heating a sample in a controlled environment (either in the presence of an inert gas like nitrogen or in an oxidative environment like

air) and recording the mass loss or gain as the temperature increases. It provides information about the thermal stability and composition of materials, as different materials will decompose, oxidize, or lose volatiles at different temperatures. In this thesis, TGA was adopted to evaluate the thermal stability of FRTW.

3.12.2 Limited Oxygen Index (LOI)

The Limited Oxygen Index (LOI) is a standardized test method used to determine the minimum concentration of oxygen, expressed as a percentage, that is required to support the combustion of a material. It provides a quantitative measure of a material's flammability, with higher LOI values indicating better resistance to burning in an oxygen-enriched environment.

3.12.3 UL-94 Vertical Burn Test

The UL-94 flammability standard provides specific ratings that categorize the flammability of plastic materials based on their burning behavior when exposed to a flame. These ratings help manufacturers and engineers select materials that meet the required safety standards for their applications. Below are the details of the UL-94 ratings: In this test, the material is subjected to a flame for 10 seconds in a vertical orientation. The ratings are determined by the time it takes for the material to stop burning and whether flaming drips occur. The rating details are shown in Table 3. 1.

Table 3. 1 Flammability rating UL 94

Test Criteria	V-0	V-1	V-2
Burning time of each individual test specimen (s) (after first and second flame applications)	≤ 10	≤ 30	≤ 30
Total burning time (s) (10 flame applications)	≤ 50	≤ 250	≤ 250
Burning and afterglow times after second flame application (s)	≤ 30	≤ 60	≤ 60
Dripping of burning specimens (ignition of cotton batting)	No	No	Yes
Combustion up to holding clamp (specimens completely burned)	No	No	No

3.12.4 Cone Calorimeter

The Cone Calorimeter Test, commonly referred to as the CONE test, is a widely used

method for evaluating the fire behavior of materials under controlled conditions. It is named after the conical shape of the radiant heater used in the test. The CONE test provides quantitative data on key fire properties such as heat release rate, time to ignition, mass loss rate, and smoke production, making it an essential tool in fire safety research and material development. The CONE test was adopted to evaluate the fire safety of FRTW in this thesis.

3.12.5 Thermogravimetry-Infrared Spectroscopy (TG-IR)

Thermogravimetry-Infrared Spectroscopy (TG-IR) is an analytical technique that combines thermogravimetric analysis (TGA) with infrared (IR) spectroscopy to study the thermal decomposition of materials and simultaneously identify the evolved gases. This integrated approach provides both quantitative and qualitative data, making it a powerful tool for understanding material behavior under thermal stress. In TG-IR, the material is first subjected to TGA, where it is heated in a controlled atmosphere (such as air or nitrogen) while the mass of the sample is continuously recorded. This step provides information about the material's thermal stability, decomposition temperatures, and mass loss at different stages of heating. The gases evolved during thermal decomposition are then transferred to an infrared spectrometer. The IR spectrometer detects and identifies the functional groups present in the evolved gases based on their characteristic absorption bands in the IR spectrum. This allows for the identification of the chemical composition of the decomposition products. In this thesis, TG-IR was adopted to further understand the thermal decomposition process of FRTW, providing better understanding about the flame mechanism.

Chapter 4 Sonochemically-Coated Transparent Wood for Energy Saving Applications

4.1 Introduction

Growing global energy consumption has attracted attention over the exhaustion of energy resources and environmental problems related to energy dissipation. Globally, the building sector accounts ~40% of total energy usage, with indoor temperature management accounting for a significant proportion [67]. Recent estimates project that the changing climate together with continuing worldwide socioeconomic development, will significantly increase monthly electricity demand; by up to ~89% for the residential sector in the 2090's compared with 2018 levels [185]. Green buildings based on new building materials that improve energy efficiency are therefore crucially needed for reducing energy consumption in the residential sector and broader built environment, worldwide [186, 187].

Many methods have been developed to reduce the cooling energy usage, including radiative cooling (RC), in which heat is dissipated from the substrate via irradiating long wavelength infrared to the ultracold outer space through the atmospheric transparent window (8-13 μm)[188-193]. Daytime sub-ambient RC is more challenging than night-time RC, due to the presence of incident solar radiation. To achieve sub-ambient temperatures in daytime, high reflectance in the solar spectrum and high emissivity in the range of the atmospheric window are required simultaneously, which leads to complicated cooling structures involving more than two layers [194-198]. For example, Zhai et al [198] achieved a noon-time radiative cooling power of 93 $W \cdot m^{-2}$ under direct sunlight by embedding resonant polar dielectric microspheres in a polymeric matrix. But in most cases, the cooling structure as a whole is non-transparent across the visible range, which is unacceptable for glazing material requirements, especially for windows. Although sub-ambient temperature RC for a whole building in daytime seems impossible to achieve, integration of RC structures with building envelopes such as roofs and windows could result in substantial energy savings [199].

Transparent wood (TW) is a wood-based material known for its high optical transmittance and clarity. It is produced by selectively removing a significant portion of lignin (delignification, up to an ideal limiting concentration) and replacing it with a suitable polymer that matches the refractive index [200]. Recent studies suggest that TW holds significant potential for contributing to energy-efficient buildings, offering a viable alternative to established materials due to its high transmittance, excellent thermal insulation, and low cost [66, 201-203]. Mi et al [201]. developed a clear, strong, and thermally insulated transparent wood (TW) for energy-efficient windows by nearly completely removing the lignin content from the wood. Xia et al[66]. fabricated patternable TW using solar irradiance, resulting in a material with high optical transmittance of over 90%, adjustable optical haze of 60-80%, and desirable mechanical properties. However, research on the functionalization of TW, such as through coatings, is still limited. For instance, Qiu et al [204] produced anti-ultraviolet and infrared heat shielding TW by infiltrating pre-polymerized methyl methacrylate (PMMA) with modified antimony-doped tin oxide (ATO) nanoparticles. Other functionalities for wood have been reported, such as flame retardancy [205], superhydrophobicity [206], photochromic [207] and electroluminescent [208]. However, most of such functionalization were based on pre-treatment, introducing functional components into the impregnation polymers, or coating of NW itself. Post-functionalization of TW has not been well investigated, e.g., thin film coating methods, and are otherwise an effective and established route to achieving value-added function (e.g.; in the glass, steel and plastics industries).

Conventional high temperature (high-T) processes for nanoparticle synthesis and coating are intrinsically incompatible with temperature-sensitive substrates, including wood, textiles and paper. Sonochemical synthesis methods use ultrasonic (i.e.; sound) frequencies larger than 20 kHz to effect acoustic cavitation in a liquid medium, for the excitation of chemical reactions in solution, instead of the more common heat, pressure, light and/or catalyst. The generation and subsequent collapse of the bubbles formed by

the process, generates extremely high temperatures and pressures within a highly localised region [209]. This allows effective coating with high-formation temperature inorganic materials, achieving crystalline formation, often generated and deposited in situ, durably incorporated into the substrates, absent the use of binders, for high-quality coatings on TW [210, 211]. Such routes are attractive as fast, convenient, energy-efficient methods for the controlled growth of NPs, as it enables chemical reactions to be carried out under ambient conditions with shorter reaction times, also minimises waste outputs and by-products, while also possessing the ability to be easily integrated into processing lines [212-215]. For example, both Suslick and coworkers, and Gedanken and coworkers have reported on ultrasonic ZnO coatings on polymeric substrates [216, 217].

In this study, we present the formation of polycrystalline thin-film ZnO-coated transparent wood (TW), marking the first known instance of TW being coated with functional metal oxide layers. The TW was initially fabricated through delignification, followed by infiltration with epoxy resin. Subsequently, a continuous, solid, pure-phase polycrystalline ZnO coating was achieved via a silver (Ag)-mediated seeding process using a sonochemical deposition method. This sonochemically coated transparent wood (CTW) demonstrated favorable optical transmittance, excellent mechanical and thermal insulation properties, and high emissivity in the long-wavelength infrared region, making it a promising candidate for energy-saving applications. According to our simulation results based on the CTW empirical data inputs, as applied to Hong Kong, Shanghai and Chongqing, highly desirable and meaningful energy saving results can be achieved.

4.2 Materials and Methods

4.2.1 Materials and chemicals

Balsa wood sheet (purchased from Zhuhai DeChi Co., Ltd.) was used to prepare the transparent wood substrate. The natural wood was cut into slices of different sizes along the longitudinal growth direction (i.e.; parallel to the fiber/grain); only samples of

longitudinal orientations were explored in this study, not perpendicular (i.e.; radial or tangential) orientations[218, 219]. The sodium hypochlorite (NaClO; Shanghai Macklin Biochemical Co., Ltd) solution with 5% available chlorine (~0.35 mol/L) was used for delignification. The epoxy resin (GC135) and curing agent (D230) used for infiltration were purchased from Kunshan Jiulimei Electronic Materials Co., Ltd. Silver nitrate ($AgNO_3$; Alfa Aesar) and Ethylene glycol (EG; Sigma-Aldrich), Polyvinylpyrrolidone (PVP, M_w=58000, Acros Organic) and ammonia (25%, VWR-CHEM), Zinc acetate dihydrate ($Zn(Ac)_2 \cdot H_2O$, Acros Organic) and ethanol (99.7%, Anaqua) were used for the sonochemical process. All chemicals were used as bought and deionized (DI) water (18 MΩ) used, in all cases.

4.2.2 Delignification of natural wood (NW)

The balsa wood was cut into slices with thickness 1 mm along the growth direction. Then the wood slices were completely immersed into NaClO solution (5% available chlorine). In order to ensure the completely immersion of wood slices, a NaClO-resistant plastic net was sunk to the bottom of the beaker. After 48h of bleaching, the delignified wood (DW) was washed with ethanol and DI water to remove any residual chemicals and the resultant substrates stored in ethanol for further use.

4.2.3 Fabrication of transparent wood (TW)

The epoxy and curing agent were mixed at a ratio of 10:3 via vigorous stirring, then DW was immersed into the mixture. The entire mixture was transferred into a vacuum dryer and degassed to below 0.1 atm for 30 min, then released to atmosphere pressure, allowing impregnation of epoxy resin. The above vacuum-release process was repeated three times, to ensure the complete infiltration of epoxy. After this, the epoxy impregnated wood slices were taken out cured at room temperature for at least 36h. After curing, the epoxy impregnated transparent wood (TW) slices were peeled off from the laser photocopying film and used without further treatment.

4.2.4 Fabrication of coated transparent wood (CTW)

All coating was done on an automated ultrasonic probe mixer was purchased from (CY Scientific Instrument Co., Lit, Zhengzhou, China). In all cases, a flat-tipped, stainless steel ultrasonic horn (16 mm, 20 kHz, 750 W at 70% efficiency) was immersed into the solution mixture, with a horn tip-substrate distance of 2 cm. As shown in Fig.1a, the manufacturing process of CTW can be divided into two steps: 1) Ag seeding process and; 2) ZnO deposition. For the first step, $AgNO_3$ (0.3394g) and PVP (0.3g) were dissolved in a mixed solvent (100 ml) of EG and DI at the ratio of 9:1. Following this procedure, the transparent wood (TW) was placed at the bottom of a beaker, and 300 μL of 25 wt% ammonia was added to the mixture within 15 seconds of initiating sonication. After 210 seconds of sonication, the TW was removed, washed three times with deionized water (DI) and ethanol to eliminate any residual chemicals, and then allowed to dry in air. In the second step, 1.0974 g of $Zn(Ac)_2 \cdot H_2O$ was dissolved in a mixed solvent of ethanol and DI at a 9:1 ratio (100 mL total volume). Then, 1250 μL of 25 wt% ammonia was added to the mixture within 15 seconds of initiating sonication. After 20 minutes of sonication, the sample was removed, washed three times with DI and ethanol to remove any residual chemicals, and then dried in air. The resulting sonochemically coated transparent wood (CTW) was then used for testing without any further processing.

4.2.5 Characterization

The morphology of NW, TW and CTW were imaged by Field-Emissing Scanning Electron Microscope (Tescan VEGA3) at acceleration voltage of 20 kV. The granular morphology of ZnO was characterized via atomic force microscopy (AFM, Bruker Multimode 8, USA) in tapping model using silicon nitride probes (SNL-10, Bruker). The scanning area is 10 × 10 μm with the scan rate of 0.4 Hz, for each direction 256 lines of profiles were collected. The XRD patterns of NW, DW, EP and TW were characterized by X-ray diffraction (XRD) θ–2θ scans using a Rigaku SmartLab X-ray diffractometer with Cu Kα1 radiation (λ = 1.5406 Å), while the Grazing Incidence XRD pattern of CTW thin film was obtained in the glancing angle configuration at an incidence angle of 2°. All measurements were conducted in the range of 10-80° with a

step size of 0.02° and scan rate of 4°/min. X-ray photoelectron spectroscopy analysis (XPS) was conducted by using ThermoFisher-nexsa with a monochromatic Al Kα X-ray source. The XPS survey spectrum as collected in the range of 0-1350 eV under the pass energy of 100 eV with the energy step size of 1 eV, while the high-resolution spectra of Zn 2p, Ag 3d, O 1s and Zn LMM were obtained at a pass energy of 50 eV with the step size of 0.1 eV. For all XPS collection, the spot size of the x-ray is 400 μm. All data was collected absent any sputtering and all analysis was done on the Advantage software (Version 5.952) using C 1s (284.8 eV) as reference. The transmittance and reflectance across 200-2500 nm were recorded by PERKIN ELMER_UV-vis-NIR LAMBDA 1050+ spectrometer equipped with a 150 mm integrating sphere at a data interval of 2 nm. The reflectance (R(λ)) across 2.5-15 μm was measured by Fourier Transform Infrared (FT-IR Spectrometer, Spectrum 100, PerkinElmer) with a diffuse gold integrating sphere. The scanning range is 650 cm^{-1} to 4000 cm^{-1} at the resolution of 4 cm^{-1}, and 16 scans were collected in total. The emissivity (ε(λ)) was calculated according to Kirchhoff's law (equation 1):

$$\varepsilon(\lambda) = \sigma(\lambda) = 1 - R(\lambda) - T(\lambda)$$

where $\sigma(\lambda)$, $R(\lambda)$ and $T(\lambda)$ are the absorbance spectrum, reflectance and transmittance spectrum of the surface. The FTIR spectra of DW, EP and TW were obtained from a FT-IR Spectrometer, Spectrum 100, PerkinElmer with an ATR accessory. The scanning range is 650 cm^{-1} to 4000 cm^{-1} at a resolution of 4 cm^{-1}, and 16 scans were collected in total, for each sample. The chemical composition of NW and DW were measured according to previous reports[220]. Briefly, 1g dried small particles of NW and DW were extracted in ethanol for 4h, and then dried in oven at 80ºC for 8h. Then the dried particles were added to 15 ml of sulfuric acid (72%), stirring for 2h at room temperature. The mixed solution was subsequently diluted with 560 ml of DI water and boiled at 110ºC for 4h. Upon cooling to room temperature, the diluted solution was filtered to remove the soluble content in the mixture, and washed until the pH of filtrate ran neutral by sand core funnel (G3) and dried in oven for 24h. The lignin content was calculated according to equation 2:

$$P_l(\%) = \frac{m_{s+l} - m_s}{m_0} * 100\%$$

where the m_{s+l} is the dried weight of insoluble particles and sand core funnel; m_s is the dried weight of sand core funnel before use; m_0 is the weight of the dried wood or delignified particles before any treatment. The mechanical properties were obtained from an Instron 5566 universal testing machine with the sample size of 50 mm × 10 mm × 1 mm (length x width x thickness). The tensile stress was applied to the longitudinal direction. The thermal-mechanical properties were measured by DMA Q800 under single cantilever mode at a heating rate of 3.0°C.min^{-1} at frequency of 1 Hz from 0-80°C. The thermal conductivity was obtained from a thermal conductivity meter equipped with a Hot Disk Kapton sensor, at a power of 200 mW and measuring time of 40s.

4.2.6 Simulation method

To validate the energy-saving potential of CTW for window glazing applications, the annual energy-saving performance was simulated using TRNSYS 18 software. In the simulation, a single-story small office building was created, of dimensions 30 m (L) × 10 m (W) × 5 m (H). The glazing system had a gross window glass area of 200 m^2 and was evenly distributed across all four walls, with a window to wall ratio of 50%. The building parameters were all set according to the local building energy efficiency standards[221]. Only the HVAC system was considered for space cooling in this simulation and no heating. Three typical metropolises of Hong Kong, Shanghai and Chongqing were selected as case studies. In addition, conventional glass and commercial low-emissivity (Low-E) glass (based on reports from Wang et al)[222] were used as comparators to CTW.

4.3 Results and Discussion

4.3.1Fabrication of ZnO Coated Transparent Wood

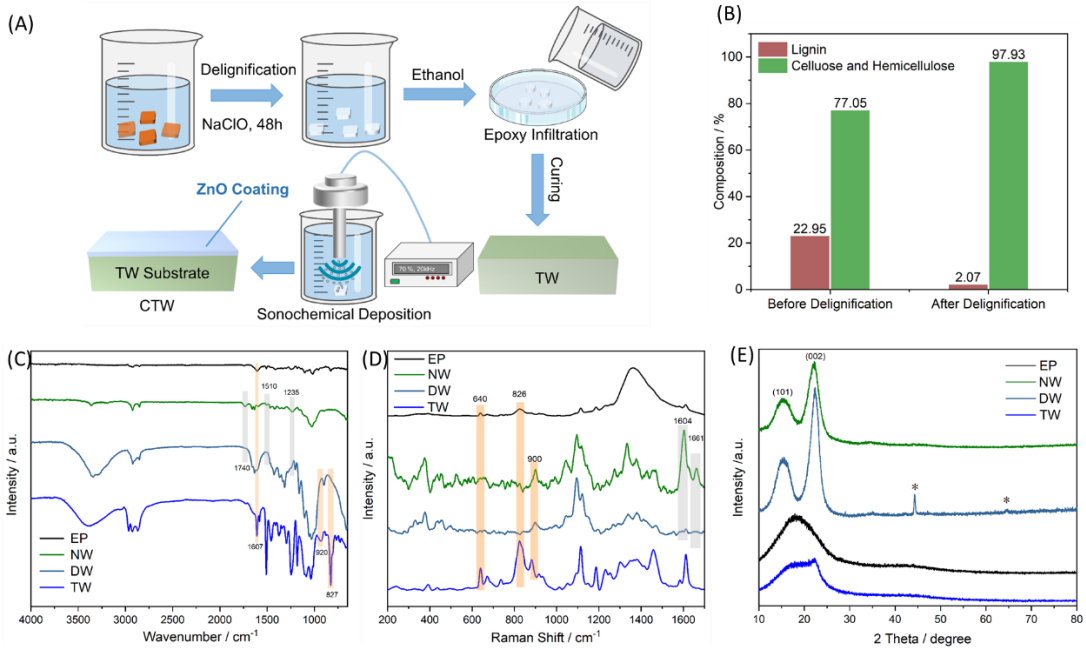

Figure 4. 1 (A) Schematic manufacturing procedures of CTW; (B): chemical compositions of NW and DW; (C): FTIR spectra of NW, DW, EP and TW; (D): Raman spectra of NW, DW, EP and TW; (E): XRD patterns of NW, DW, EP and TW. * Signals for the aluminum holder.

This study investigated the coating of a transparent wood substrate. A natural balsa wood substrate (NW) was delignified (DW), then impregnated with an epoxy to form the transparent wood substrate (TW). Then, a ZnO coating was obtained via an Ag-seed mediated process, to achieve a coated transparent wood (CTW) output (Figure 4. 1A). Seeded control and growth of thin film coatings in general, as well as silver-seeded growth of ZnO have been reported previously, for alternative substrates[223, 224].

The tannish color of the wood is due to its chemical polymer composition of cellulose, hemicellulose, and primarily, lignin. Much of the absorption and scattering that makes wood opaque is predominantly due to lignin (i.e., 80-95%). Delignification allows almost complete removal of lignin, to fabricate the TW substrate, upon impregnation with a suitable, refractive-index matched polymer (e.g.; epoxy). XRD, FTIR and Raman spectra of NW, DW, TW and CTW are investigated. Figure 4. 1B, shows that the lignin content of NW is 22.95%, which dramatically decreased to 2.07% after

delignification. The near-complete removal of lignin is also confirmed by the Raman and FTIR spectra. Figure 4. 1C-D exhibit the peak at 1740 cm^{-1} (δ (C=O), stretching vibration), which corresponds to the xylan in hemicelluloses, which is undetectable after delignification. This indicates not only lignin but also partial hemicellulose degradation, as the delignification process is extended. Similar to 1740 cm^{-1} (δ (C=O), stretching vibration), the peak at 1510 cm^{-1} (skeletal vibration of δ(C=C) in phenolic ring of lignin) almost disappears after delignification. Furthermore, removal of lignin is also characterized by the decreasing intensity of 1235 cm^{-1} (C_{ar}-O originating from coupled OH bending and C–O stretches vibrations) [225, 226]. For Raman spectra, the band at 1661 cm^{-1}, corresponding to C=C in coniferyl alcohol or C=O in coniferaldehyde, disappeared after delignification, indicating the deterioration of coniferaldehyde and/or coniferyl alcohol structures [227, 228]. Likewise, there is a decreasing intensity of 1604 cm^{-1} which is related to the symmetric stretch of aromatic ring. The absence of 1600 cm^{-1} and 1668 cm^{-1} bands in Raman spectra is in total accordance with the vanishing of 1510 cm^{-1} and 1235 cm^{-1} in the IR spectra. Thus, by comparing Raman and IR spectra, it is rational to conclude that most of lignin content in the balsa has been removed, and partial hemicelluloses have also been destroyed, while celluloses are well-reserved. Detailed Raman and FTIR spectra for the entire delignification process are shown in Figure 4. 2.

4.3.2 Delignification process of natural wood

The structural changes of wood during the entire delignification process were monitored by ATR-FTIR and Raman spectroscopy. The wood pieces were taken out from the NaClO solution at different time intervals over a 48 hr period, and washed with distilled water for 3 times prior to freeze-drying for 24h. At different stages of delignification, the IR spectra show some differences in regions concerning lignin, cellulose and hemicellulose. The broad peaks at 3360 cm^{-1} and 1630 cm^{-1} are assigned to the stretching vibration of OH-groups and the absorbed water. The peaks at 2920 cm^{-1} and 2850 cm^{-1} reveal the contribution of the C-H stretching vibration in -CH_2. In all spectra, the band at 1105 cm^{-1} (δ(C-O-C)) is indicative of glycosidic ring in

carbohydrates. It is worth noticing that the intensity of 1660 cm^{-1}, corresponding to δ(C=O) in quinone or p-quinone, can be detected in all samples and gets stronger within the delignification process, indicating the oxidation of the lignin fraction. While the peak at 1740 cm^{-1} (δ (C=O), stretching vibration), which corresponds to the xylan in hemicelluloses, cannot be detected after ~6h delignification. This indicates not only lignin but also partial hemicellulose degradation, as the delignification process is extended. Similar to 1740 cm^{-1} (δ (C=O), stretching vibration), the peak at 1510 cm^{-1} (skeletal vibration of δ(C=C) in phenolic ring of lignin) almost disappears after ~12h delignification, indicating removal of the lignin[225, 226]. Furthermore, the removal of lignin also characterized by the decreasing intensity of 1235 cm^{-1} (C_{ar}-O originating from coupled OH bending and C–O stretches vibrations). The peaks at 1460 cm^{-1} (δ(CH_2) asymmetric bending), 1427 cm^{-1} (δ(CH_2) symmetric bending in crystallized cellulose I and amorphous cellulose), 1315 cm^{-1} (δ(CH_2) in crystallized cellulose I), 1160 cm^{-1} (δ(C–O–C), asymmetric stretch vibration in cellulose and hemicelluloses), 1030 cm^{-1} (δ(C–O–C), skeletal vibration of polysaccharides ring) and 898 cm^{-1} (stretching vibration of C_1–O–C of β-(1–4)-glycosidic linkages in cellulose I and amorphous fraction) reveal the presence celluloses. For further understanding of the delignification process, Raman spectra was obtained under the excitation of 785 nm laser. Considering the natural difference of wood, the same samples were used for both FTIR and Raman spectroscopic analysis. The bands around 2890 cm^{-1} and 1381 cm^{-1} are assigned to the C-H stretch and bend, respectively, in different groups. The Raman contribution of CH_3 bending occurs at 1466 cm^{-1}. The bond at 1122 cm^{-1} is primarily due to the presence of cellulose, which is also characterized by the band at 1096 cm^{-1} (cellulose skeletal mode), 1330 cm^{-1} (Aliphatic O-H bend). The peaks, including 900 cm^{-1}, 520 cm^{-1}, 432 cm^{-1} and 378 cm^{-1}, reveal the Raman contribution of skeletal deformation in cellulose. These characteristic bonds for celluloses almost remain unchanged in terms of Raman intensity during the delignification process, implying the well reserved celluloses structure in delignified wood. The peak at 1668 cm^{-1}, corresponding to C=C in coniferyl alcohol or C=O in coniferaldehyde, cannot be detected after ~12h delignification, indicating the deterioration of coniferaldehyde

and/or coniferyl alcohol structures in lignin. The destruction of lignin is also characterized by the decreasing intensity of 1600 cm^{-1}, which is related to the symmetric stretch of aromatic ring. The absence of 1600 cm^{-1} and 1668 cm^{-1} after ~12h delignification is in total accordance with the vanishing of 1510 cm^{-1} and 1235 cm^{-1} in the IR spectra[227]. By comparing Raman and IR spectra, it is rational to conclude that most of the lignin content in the balsa has been removed, and partial hemicelluloses have also been destroyed, while celluloses are well reserved.

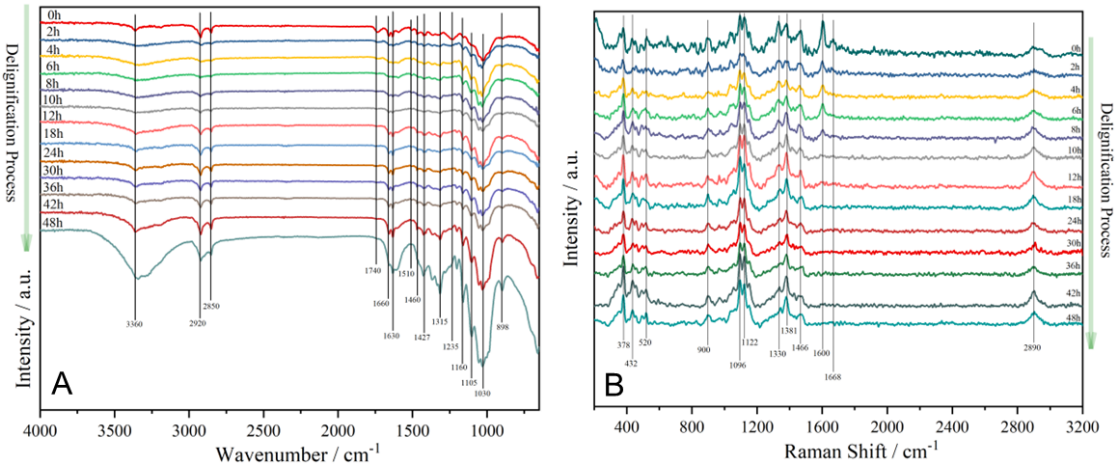

Figure 4. 2 FTIR (A) and Raman (B) spectra of DW within the delignification process.

The XRD patterns (Figure 4. 1E) show almost no change between the NW and DW; both exhibiting the cellulose crystalline planes of (101) and (002) [229]. The epoxy polymer infiltration process was also investigated by XRD, FTIR and Raman. Successful infiltration of epoxy is characterized by the presence of several peaks 827 cm^{-1}, 920 cm^{-1} and 1607 cm^{-1}, which corresponds to stretching of C-O-C in oxirane group, C-O in oxirane group and C=C in aromatic ring, respectively [24]. Peaks corresponding to aromatic C-H out-of-plane deformation (640 cm^{-1}), substituted aromatic (826 cm^{-1}) and oxirane group (900 cm^{-1}) in Raman spectra, as well as overlapping amorphous peaks of cellulose and epoxy in XRD patterns also confirmed the impregnation of epoxy [230].

4.3.3 Characterization of ZnO coated transparent wood

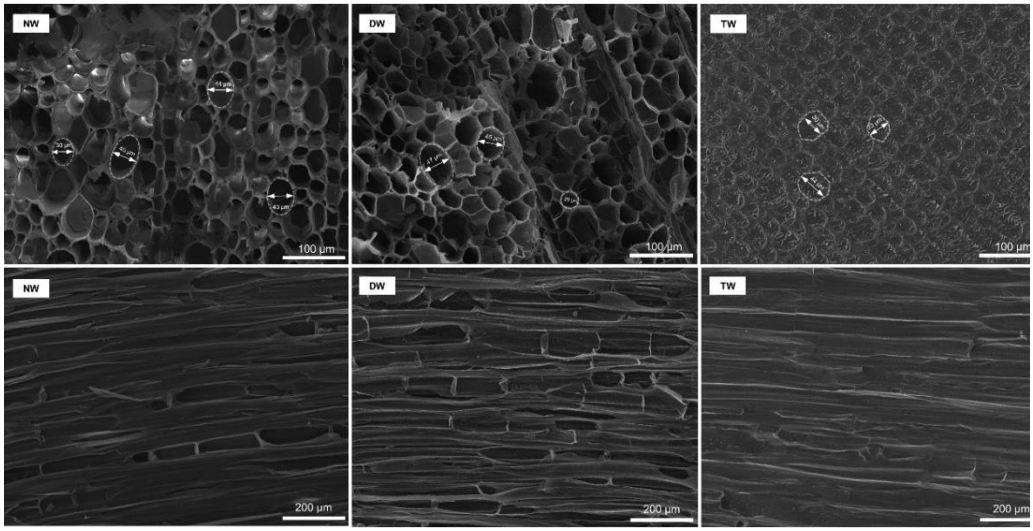

Figure 4. 3 SEM images of NW, DW and TW from the top view and side view.

In Figure 4. 3, highly aligned microchannels, approximately 20-50 μm in size, are visible in both the cross-sectional and top views of the original balsa natural wood (NW). After delignification, these aligned microchannels are well preserved in the delignified wood (DW), although the cell walls become significantly thinner due to the removal of lignin. For the TW, the microchannels were completely filled with epoxy resin, with no gaps observed between the epoxy and the cell walls. Strong interactions, such as hydrogen bonding or van der Waals forces, are expected between the wood cellulose and epoxy. Following this, a polycrystalline ZnO coating was applied to the TW, resulting in the fabrication of the sonochemically coated transparent wood (CTW).

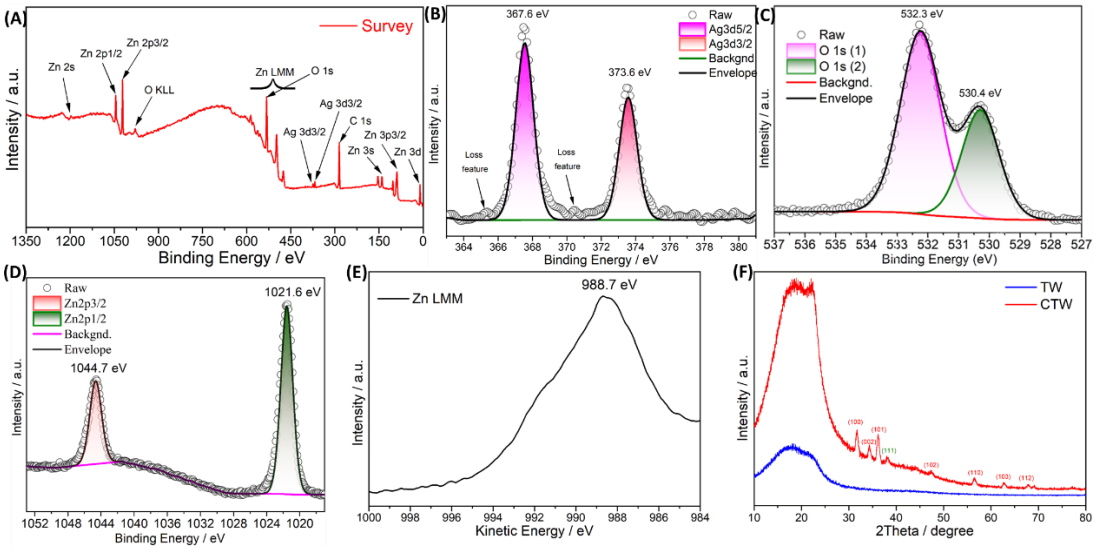

Figure 4. 4 (A): XPS survey spectra of CTW; (B-E): high-resolution scan of Ag-3d, O-1s, Zn-2P and Zn-LMM; (F): Grazing Incidence XRD pattern of TW and CTW.

The structure of the polycrystalline coating on CTW was studied by XPS and glancing angle XRD. Figure 4. 4 show the XPS survey, Zn 2p, O 1s, Ag 3d, Zn LMM and glancing XRD pattern of CTW. Peaks in the XPS survey spectrum (Figure 4. 4B) can be assigned to Zn, Ag, O and C, among which C (high-resolution spectrum of C1s) is the contamination introduced by exposure to air. The high-resolution spectra of Ag 3d (Figure 4. 4B) shows two peaks (367.6 eV and 373.6 eV) corresponding to Ag $3d_{5/2}$ and Ag $3d_{5/2}$, respectively. Obvious loss feature was detected between Ag $3d_{5/2}$, Ag $3d_{5/2}$ and high binding energy region, suggesting the formation of silver metal rather than Ag cations. In the case of O1s (Figure 4. 4C), the peak at 530.4 eV is ascribed to the O^{2-} ions in the crystal structures encircled with Zn^{2+} ions, while another peak at 532.3 eV reveals the contribution of chemisorbed oxygen or excess oxygen such as H_2O or O_2 [231]. High-resolution spectra of Zn 2p (Figure 4. 4D) shows peaks cantered at 1021.6 eV and 1044.7 eV corresponding to doublets Zn $2p_{3/2}$ and Zn $2p_{1/2}$, respectively. However, such peaks can often suffer from overlap with the pure Zn metal. Fortunately, chemical state determination can be made clear by comparing the modified Auger parameter, which can be defined as following [232]:

$$\alpha' = E_B(Pho) + E_K(Aug)$$

where α' is the modified Auger parameter; $E_B(Pho)$ is the Binding energy of Zn $2p_{1/2}$ photoelectron; $E_K(Aug)$ is the kinetic energy of Auger electron related to Zn LMM. The high-resolution spectrum of Zn LMM (Figure 4. 4E) shows that the kinetic energy of Auger electron related to Zn LMM peaks is at 988.7 eV, while the binding energy of Zn $2p_{1/2}$ photoelectron is 1021.6 eV. In this case, the modified Auger parameter is 2010.3 eV, which is perfectly consistent with previous reports of Zn(II) [233]. GIXRD patterns of the thin films indicate the presence of wurtzite ZnO. The broad peak around 20° can be ascribed to cellulose in the TW substrate, while peaks

centered at 2θ = 31.7° (100), 2θ = 34.6° (002), 2θ = 36.2° (101), 2θ = 47.4° (102), 2θ = 56.4° (110), 2θ = 62.7° (103) and 2θ = 67.8° (112) correspond to the hexagonal crystal structure of ZnO, showing good agreement with previous literature (JCPDS card no.36-1451) [234]. A single discernible peak at 2θ =38.0° indicates presence of metallic Ag (111), which acts as the nucleus during the formation of ZnO hexagonal crystal. Combined with the XPS analysis, it is rational to conclude that a layer of pure phase polycrystalline ZnO coating was deposited on top the TW surface, and that this nucleation and coating density was enhanced by the presence of the sparse Ag seeding layer.

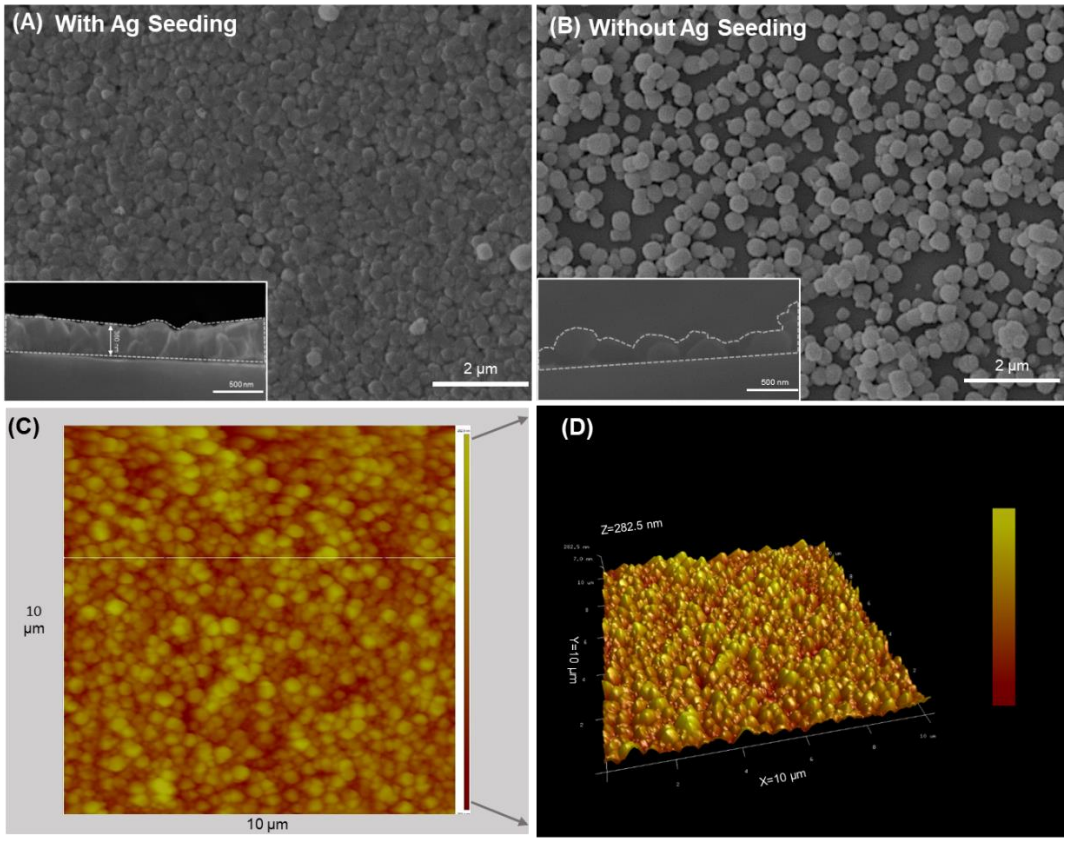

Figure 4. 5 (A): SEM image of ZnO coating (with Ag seeding) on TW substrate from top and cross-sectional view; (B): SEM image of ZnO coating (without Ag seeding) on TW substrate from top and cross-sectional view; (C): 2D-AFM image of ZnO coating (with Ag seeding) on the surface of CTW; (D): 3D-AFM image of ZnO coating (with Ag seeding) on the surface of CTW.

The morphology of Ag-seeded TW and CTW was characterized by SEM. The top views of Ag-seeded TW (Fig.4.6A) show that small silver particles of 20-50 nm were evenly distributed on the substrate, acting as nuclei for ZnO growth in the subsequent sonochemical deposition.

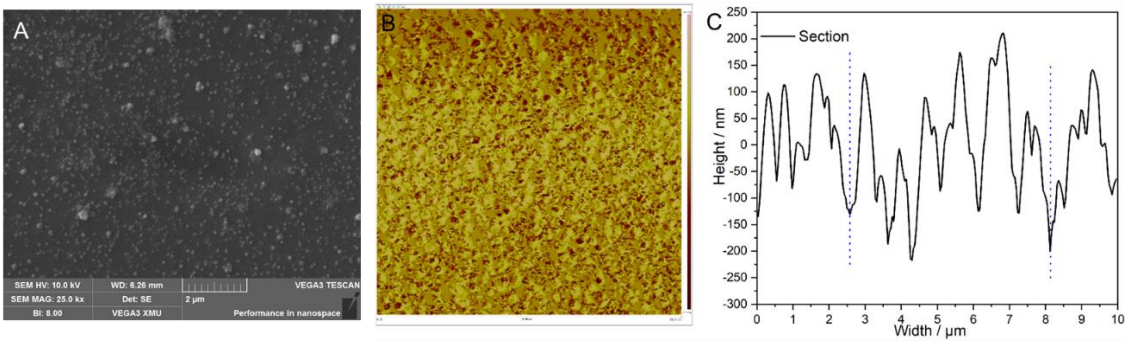

Figure 4. 6 (A)SEM image of Ag-seeded transparent wood from the top view. (B) Phase image of ZnO coating on CTW and sectional profile (C).

In Figure 4. 5A-B, the deposited ZnO nanoparticles (NP) were spherical, with average sizes of 300-400 nm, although smaller (<200 nm) and larger spheres (>400 nm) were also present. The morphology of Ag-seeded TW and CTW was characterized by SEM. The top views of Ag-seeded TW (Figure 4. 6A) show that small silver particles of 20-50 nm were evenly distributed on the substrate, acting as nuclei for ZnO growth in the subsequent sonochemical deposition. In all cases, ZnO NP were in relatively even distribution. But the seeding process significantly alters the quality of ZnO film. Without Ag-seeding, the ZnO N are in discrete distribution, implying that close stacking cannot be achieved. With Ag seeding, no discontinuities, cracks, pores, or defects can be observed due to the close stacking of ZnO particles. Thus, Ag-seeding plays a significant role in controlling film formation, the Ag nuclei heterogeneously inducing the formation and growth of ZnO particles. Cross-sectional SEM images of CTW show that ZnO particles were vertically well-aligned over the surface, with coating thicknesses of ~360 nm, showing a compact structure without any delamination or defects. Without Ag seeding, ZnO particles are in a looser distribution, which is consistent with the top view. The granular morphology of ZnO coating was investigated by AFM, 2D-AFM and 3D-AFM images are shown in Figure 4. 5C-D. The ZnO is

homogeneous and uniformly coated on the surface, consistent with SEM images. The root mean square average roughness for this whole area is 82 nm, implying the uniformity of the ZnO coating. From the sectional profile (Figure 4. 6C) of a random line, the thickness of the ZnO coating is approximately 400 nm, close to the thickness of what observed in SEM images (~360 nm). Meanwhile, the phase image (Figure 4. 6B) of AFM also shows no obvious phase angle changes, indicating that this area has very similar surface properties, again in line with the SEM images.

4.3.4 Optical, thermal, and mechanical properties of ZnO coated transparent wood

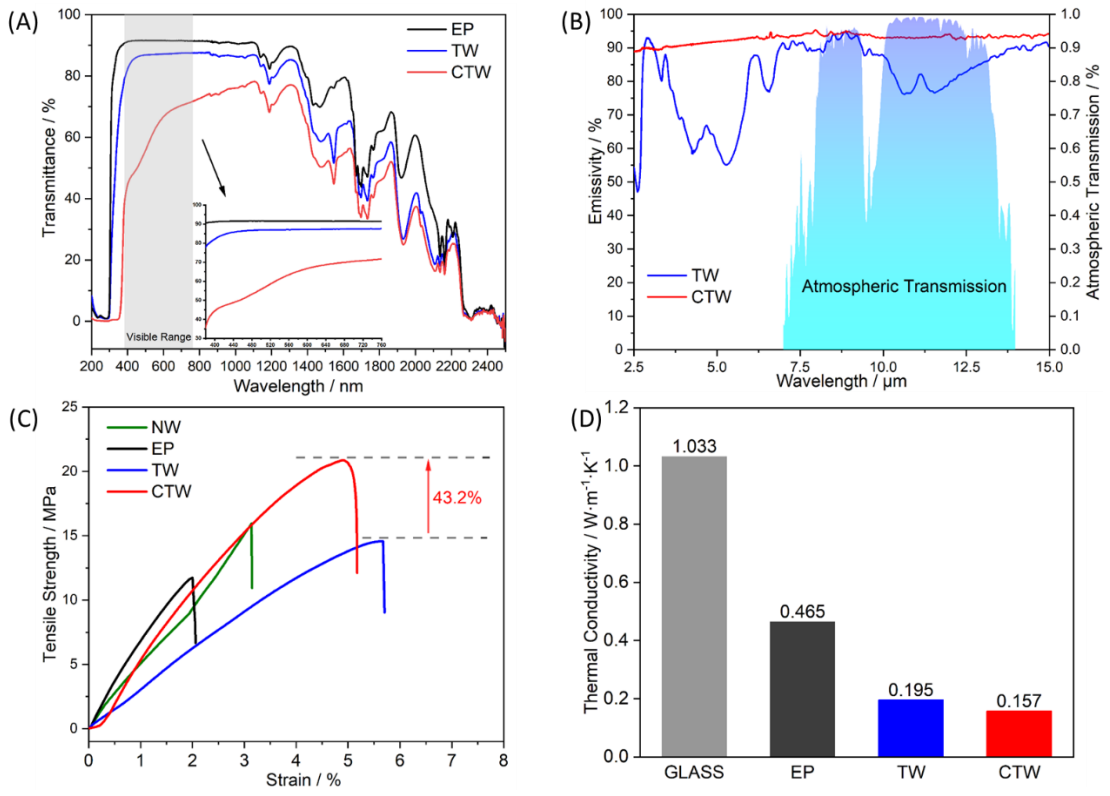

Figure 4. 7 (A)The transmission of EP, TW and CTW cross the solar irradiance; (B): emissivity spectrum of TW and CTW cross the long wavelength infrared; (C): stress–strain curves of natural wood, EP, TW and CTW; (D): thermal conductivity of glass, EP, TW and CTW. The thermal conductivity of glass was cited from previous report [203].

The mechanical properties are fundamental to any building material. To date, and for TW to be realistically used in real-world applications, marked improvements in properties are required. As presented Figure 4. 7C, the measured tensile strength of CTW experienced a significant increase due to localized high temperature during the sonication process, which further improved the crosslinking density of epoxy[235]. The sonochemical coating also endows TW with unique optical properties, showing great potential for solar control and radiative cooling. Specifically, TW exhibits a high luminous transmittance (T_{lum}=87.16%), while that of CTW decreases after the ZnO deposition, falling to ~ T_{lum}=66.04% (Figure 4. 7A). The T_{lum} still remains at a reasonable level for both visual comfort and luminous purposes, despite the decrease. Even more noteworthy is that the ZnO coating also changed the emitting spectrum in the wavelengths of infrared (2.5 μm to 15 μm). TW has fluctuating emissivity (Figure 4. 7B) within 2.5-15 μm, the average emissivity is 0.76, which is not desired for cooling energy savings. The irradiating capability of CTW is significantly improved compared to TW, especially in the region of the atmospheric window (8-13 μm). The CTW shows high emissivity~0.914 in the infrared range, implying that substantial heat flux in the form of infrared will be irradiated to the cold outer space through atmospheric window (8-13 μm). Another important parameter for energy-efficient buildings is the thermal conductivity of building materials. Figure 4. 7D shows that CTW has the lowest thermal conductivity ~0.157 $W \cdot m^{-1} \cdot K^{-1}$ compared to EP (0.465 $W \cdot m^{-1} \cdot K^{-1}$), TW (0.195 $W \cdot m^{-1} \cdot K^{-1}$) and glass (1.033 $W \cdot m^{-1} \cdot K^{-1}$), implying higher energy efficiency compared to traditional glass.

4.3.4 Energy saving potential of ZnO coated transparent wood

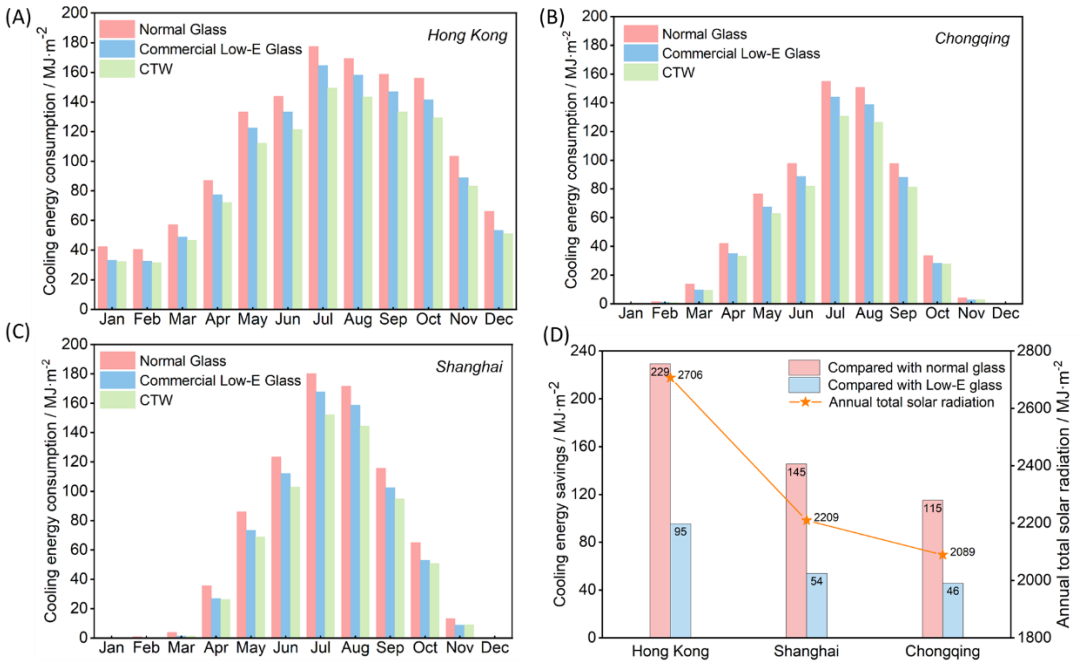

Figure 4. 8 Monthly cooling energy consumption in Hong Kong (A), Chongqing (B), Shanghai (C); and annual cooling energy saving compared with the other two types of windows (D).

The outstanding performance of CTW, such as reasonable visible transmittance and solar reflectance, desirable mechanical performance, excellent thermal insulation and high emissivity, make it a promising candidate for window glazing applications. A simple simulation was carried out to validate the energy-saving potential of CTW for window glazing applications using TRNSYS 18. Figure 4. 8 shows the monthly and annual cooling energy consumption/savings in Hong Kong, Shanghai and Chongqing with the different window materials. It is clear that CTW shows great cooling energy-saving potential compared with normal glass and commercial Low-E glass in the three cities. The cooling energy savings mainly resulted from 1) high emittance; 2) lower solar radiation transmission, and 3) lower thermal conductivity. These three parts correspond to the high emissivity within 8-13 μm, lower solar transmittance, as well as low thermal conductivity of CTW. As shown in Figure 4. 8A-C, the largest monthly energy saving of CTW compared with normal glass and commercial Low-E glass is 28.06 $MJ \cdot m^{-2}$ and 15.14 $MJ \cdot m^{-2}$, respectively, both appearing in July, in Hong Kong. July also affords the largest savings for Shanghai, the comparison values being 28.14

$MJ \cdot m^{-2}$ and 15.71 $MJ \cdot m^{-2}$, respectively. For Chongqing, the corresponding values are 24.17 $MJ \cdot m^{-2}$ and 13.21 $MJ \cdot m^{-2}$. The peak energy saving in July can be attributed to high solar radiation in July; it is generally the hottest month of the year in both Hong Kong and Shanghai, while for Chongqing, it is August [28]. Additionally, in Hong Kong, there are energy savings every month, but for Shanghai and Chongqing, there are no energy savings in winter. This is due to the fact that the climate temperature in Hong Kong is relatively high all year round, with an accompanying cooling load. However, cooling is not needed in Shanghai and Chongqing in winter. In Figure 4. 8D, the CTW window shows a reduced cooling energy consumption of 229 $MJ \cdot m^{-2}$ and 95 $MJ \cdot m^{-2}$ annually compared with normal glasses and Low-E glasses in Hongkong. In Shanghai and Chongqing, the CTW window also shows considerable cooling energy savings, although less than that for Hong Kong. This is due to the difference in annual total solar radiation; Hong Kong exhibiting the highest value, so Hong Kong sees the largest cooling energy savings. In addition, the simulations indicate that the annual energy-saving rate of the CTW window achieved approximately 17.2% and 7.9 % compared with normal glasses and Low-E glasses, respectively, in Hong Kong. Thus, the monthly and annual simulation results illustrate the great energy-saving potential of CTW as one of the most promising windows for zero energy consumption buildings.

4.4 Conclusions

We demonstrate the functionalized ZnO-based coating of TW using a purely solution-based sonochemical coating method without the need for external temperature and vacuum application. The sonochemically coated transparent wood exhibits impressive performance in terms of optical selectivity, thermal insulation and mechanical properties due to the presence of a layer of pure-phase polycrystalline ZnO coating, enabling it to be a promising material for energy saving applications. CTW features reasonable T_{lum} (~66.04%) for both visual comfort and luminous purposes, enhanced mechanical properties (43%) compared to untreated transparent wood, low thermal conductivity (0.157 $W \cdot m^{-1} \cdot K^{-1}$), and high emissivity (~0.914) across the long-wavelength infrared, making it a promising candidate of windows materials. Energy-

saving simulations show that CTW can provide considerable cooling energy savings, specifically 95 $MJ \cdot m^{-2}$, 54 $MJ \cdot m^{-2}$ and 46 $MJ \cdot m^{-2}$ of annual cooling energy saving can be achieved in Hongkong, Shanghai and Chongqing, respectively, when compared to commercial Low-E glass. All these results position CTW as a promising candidate for energy-efficient building materials, as well as demonstrating the feasibility of the functionalization of TW using sonochemical coating methods.

Chapter 5 Transparent Wood with Self-Adaptive Emissivity Modulation for Energy Saving Applications

5.1 Introduction

Buildings account for 40% of total energy consumption and more than 30% of greenhouse gas emissions[236]. The growing active thermal regulating demand (i.e., air conditioning and central heating usage) has raised concerns over the exploitation of energy resources and heavy environmental loads (ozone layer depletion, global warming, extreme climates, etc.)[237]. As a passive route for thermal regulation systems, radiative cooling (RC) has attracted the interests of many researchers and industrialists [238-241].

Radiative cooling occurs spontaneously on highly emissive surfaces by emitting thermal radiation to the cold outer space through the atmospheric window [46] (typically defined as 8-13μm [242]) , using the sky as a 'heat sink'. The applications of radiative cooling to regulate energy ingress (i.e., via high solar reflection and strong thermal emission) across windows [243], walls [244], electronic skin [46], roofs [245], fabrics[246], and textile[247, 248], have demonstrated significant cooling effect and energy-saving potentials. However, the environmental temperature is always changing. Therefore, cooling is not always the top priority for thermal regulation systems, especially for year-round applications. Radiative cooling materials emit thermal radiation consistently regardless of temperature fluctuations, thus providing a continuous cooling effect even during cold hours [249]. The continuous cooling may lead to over-cooling during colder periods, resulting in an increase in heating loads and potentially offsetting the energy savings achieved during hot periods.

Therefore, for effective, extended, real-world operation, the emissivity of RC materials is expected to be self-adaptive, providing favourable cooling power at different temperatures throughout the year [240, 250]. Take the RC window materials as an

example[240], its ideal spectra within the mid infrared (MIR, 2.5-25 μm) should be characterized by low emissivity (ε_{MIR}) at low temperature (restraining the radiative heat dissipation) and high emissivity at high temperature (promoting the radiative heat dissipation, see Figure 5. 1B). For the goal of self-adaptive emissivity modulation at near-room temperature, vanadium dioxide (VO_2) is considered the most promising candidate material (in its doped form) [251]. However, the intrinsic emissivity contrast of VO_2 particles is negative [252, 253] (i.e., emissivity decreases with the increase of temperatures), which contradicts the radiative cooling modulation concept (i.e., positive emissivity contrast). Constructing Fabry-Perot (FP) multi-layered structure, which includes a lossless dielectric spacer, a VO_2 top layer, and a reflective bottom layer [254-260], provides a chance for positive emissivity contrast. The VO_2 insulating layer and spacer allow thermal radiation to pass through directly at low temperatures. The reflective substrate reflects most of the thermal radiation, resulting in low thermal absorption (i.e., low thermal emissivity) for the F-P resonator. Once VO_2 transitions into a metallic state above the transitional temperature, it acts as an infrared mirror for the Fabry-Perot (F-P) resonator. Thermal radiation now fluctuates between the metallic VO_2 layer and the opaque substrate, leading to an eventual enhancement of thermal absorption/emissivity[19]. Though positive emissivity contrast of VO_2 had been demonstrated experimentally, the fabrication processes adopted to-date have been relatively costly and complicated, involving inapproachable and expensive technologies or instruments, such as high-power impulse magnetron sputtering [261], enhanced chemical vapor deposition [262], magnetron sputtering [263], and pulse laser deposition [264]. Moreover, these routes are usually exclusive for expensive and/or difficult-to-source substrates (usually opaque e.g., sapphire, wafer, Au, and Al). Many established materials, such as cement, are not suitable for above processes. Therefore, an affordable, facile, and widely-applicable fabrication process to achieved emissivity modulation on any potential materials is still required.

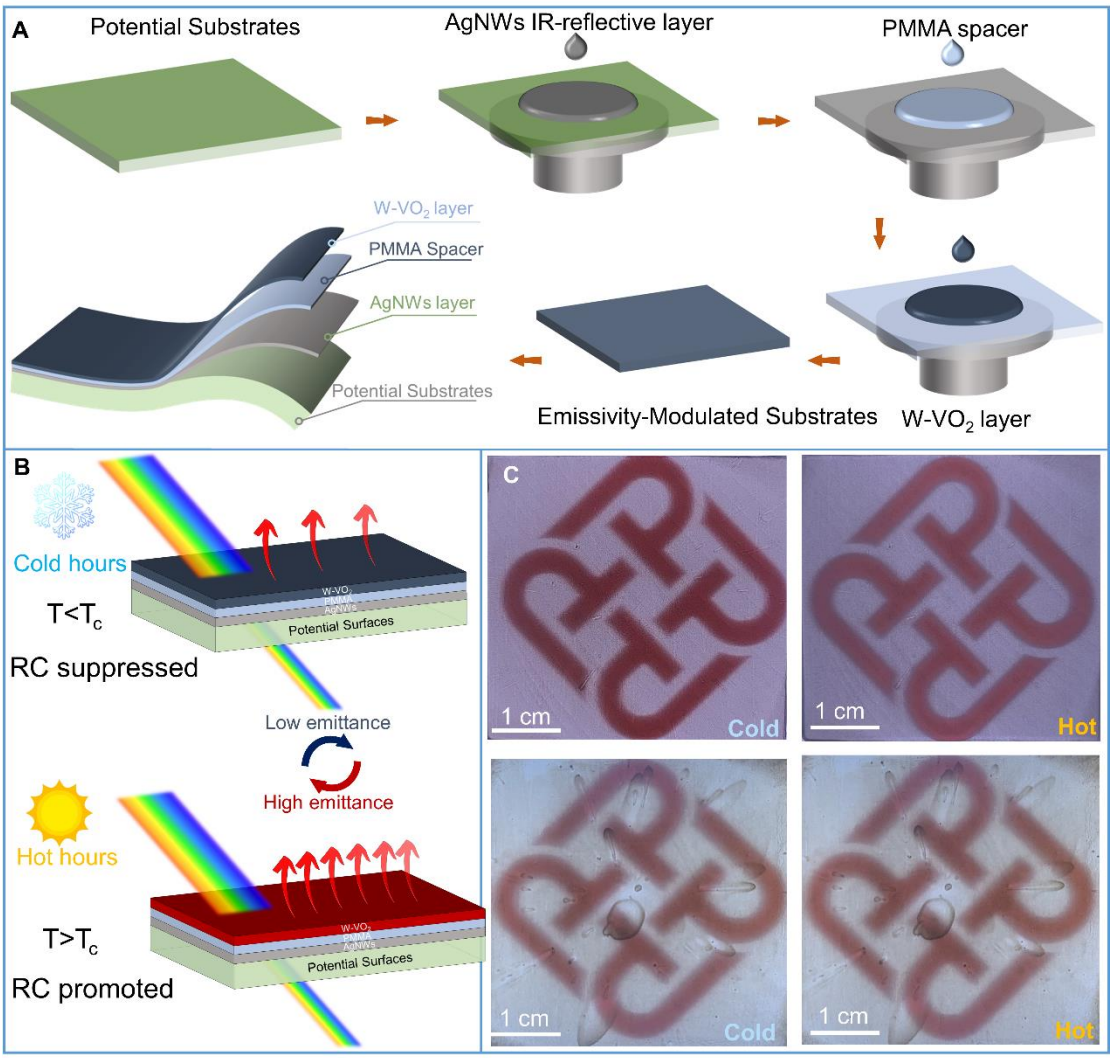

Figure 5. 1 (A) Schematic illustration of the fabrication process of EMTW. (B) Schematic illustration of the RC regulating process. (C) Digital photos of TW with emissivity modulation (bottom) and without emissivity modulation (top) at low temperatures and high temperatures. The sample size is 5 cm × 5 cm.

Here, we propose to achieve positive emissivity contrast on various potential substrate via e a facile and widely applicable route, in which a typical Fabry-Perot structure was assembled. (Figure 5. 1A). A promising window-replacement material (transparent wood[3-5, 99, 166, 265], TW) was choose as the substrate for the first demonstration of this route. The emissivity-modulated TW (EMTW) gives an emissivity contrast of 0.44 ($\varepsilon_{8\text{-}13\text{-}L}$ ~0.19 and $\varepsilon_{8\text{-}13\text{-}H}$ ~0.63) within atmospheric window due to the phase transition of W-VO_2. EMTW also shows acceptable luminous transmittance (T_{lum}, 20.3%

at 20 °C and 19.6% at 60 °C) at different temperatures (Figure 5. 1C). Due to the self-adaptive emissivity changes, EMTW offers considerable energy saving across a variety of climate zones. To demonstrate the wide applicability of this route, we also applied the proposed method to established industrial materials, such as normal glass, cement, and PET films. The stacking design on these three substrates also results in a positive emissivity contrast, indicating the great significance of this route for the promotion and adoption of the RC modulation concept in various potential fields.

5.2 Experiment Section

5.2.1 Materials and chemicals

Vanadium pentoxide (AR, V_2O_5), hydrazine hydrate (AR, $N_2H_4 \cdot HCl$), and sodium tungstate dihydrate ($Na_2WO_4 \cdot 2H_2O$) were purchased from Aladdin chemical reagent corporation. Polymethylmethacrylate (PMMA, Mw ~120,000) and hydrogen peroxide (30 wt%) were supplied by Sigma-Aldrich. Acetone (99%) and ethanol (99.7%) were obtained from Anaqua. Sodium silicate, sodium hydroxide (NaOH), magnesium sulfate ($MgSO_4$), hydrogen peroxide (30wt%), and diethylenetriaminepentaacetic acid (DTPA) were bought from Macklin. Silver nitrate ($AgNO_3$, Alfa Aesar) and Ethylene glycol (EG, Sigma-Aldrich), Polyvinylpyrrolidone (PVP, Mw=58000, Acros Organic) were used to prepared silver nanowires (AgNWs). Aero-Marine epoxy resin (#300 and #21) was used for polymer impregnating. Balsa wood (longitudinal) was supplied by Zhuhai DeChi Co., Ltd. All chemicals were used without further purification and deionised (DI) water (18 MΩ) used, in all cases. Green Island Portland cement (52.5N) was used for the preparation of cement specimens. Normal quartz glass with the dimensions of 30 × 30 × 1.5 mm was provided by DongHong Glass Co., Ltd. The PET film with the size of 210 × 297 mm was supplied by XinCan Co., Ltd.

5.2.2 Fabrication of transparent wood (TW)

The balsa wood was cut into 3 cm × 3 cm and 5 cm × 5 cm slices with the thickness of 1.5 mm. The preparation of lignin-modified wood refers to section 3.2. Aero-Marine

epoxy resin (#300 and #21) was used for polymer impregnation. The Epoxy resin #300 and curing agent #21 were mixed at a ratio of 2:1. Lignin-modified wood strips were submerged in the epoxy precursor in a petri dish. Then, a vacuum of 0.1 atm was applied to the mixture for 15 mins, allowing the infiltration of epoxy into the wood scaffold. The vacuum was repeated three times to ensure complete impregnation, after which, wood strips were sandwiched between two PET film sheets, and the samples cured at room temperature for 48 hours. Finally, the formed transparent wood (TW) was peeled off from the PET film.

5.2.3 Preparation of tungsten doped VO_2 nanoparticles (W-VO_2)

The W-VO_2 was prepared broadly in accordance with previous reports, with a slight modification [266]. First, 1.82 g V_2O_5 was added into 30 ml H_2O with stirring. Then hydrazine monohydrochloride (0.52 g) was added into the obtained brownish precursor with stirring until the mixture turned blue-black. Then, the doping element (sodium tungstate dihydrate) was added. The doping concentration set as 2%, which is calculated based on to the atom ratio of tungsten and vanadium. Finally, the mixture was transferred into a 50 mL PPL liner and sealed in a steel autoclave. The hydrothermal reaction was performed at 285 ^oC for 48 hours. After the mixture was cooled to room temperature, the black solution was washed with DI three times under centrifugation. Finally, the obtained black powder was dried for 24 hours in a vacuum oven at 80^oC.

5.2.4 Synthesis of silver nanowires (AgNWs)

The preparation of AgNWs was synthesized broadly in accordance with previous reports with slight modification [267]. Silver nitrate ($AgNO_3$) and PVP were dissolved in 100 ml of EG with stirring. Then 1.6 ml of $CuCl_2 \cdot 2H_2O$ (3.3 mM) EG solution was added under mild stirring. Finally, the mixture was transferred in to preheated silica oil bath at 130^oC for 6 hours. Upon cooling to room temperature, the resultant grey solution was washed with acetone and ethanol three times under centrifugation of 3000 rpm for 5 min. Then, the obtained AgNWs were dispersed in ethanol at a concentration of 10 mg/ml for further use.

5.2.5 Fabrication of transparent wood with and without RC regulation

The prepared TW was used as the substrate. The preparation of TCTW was divided into three steps: the deposition of AgNWs, the deposition of PMMA spacer, and the deposition of VO_2 layer. The PMMA solution was prepared by dissolving the PMMA in acetone at concentration of 10 wt% under stirring. To prepare W-VO_2-PMMA solution, different weight (0.25 g, 0.5 g, 1 g) of W-VO_2 and 0.1 g PMMA were dissolved in 5g of acetone under stirring overnight. Before use, AgNWs solution and VO_2-PMMA solution were sonicated in the ultrasonic bath for 5 mins to obtain uniform solution. Before conducting the coating process, the TW substrates (3 cm × 3 cm for general measurement, 5 cm×5 cm for the scale-up production) was washed with ethanol, DI, and acetone under ultrasound for 5 mins. Then a certain layer of AgNWs was spin-coated on the TW substrate with a fixed spinning speed of 1000 rpm for 20 s. For every layer of AgNWs, 200 μL of the prepared solution was applied. Then a layer of PMMA was spin-coated above the AgNWs with a certain spinning speed of either 2000, 3000, and 4000 rpm for 20 s using 1000 μL of the prepared PMMA solution. Lastly, an overcoat of W-VO_2 was spin-coated over the PMMA layer at different concentrations (5 wt%, 10wt%, and 20 wt%) with a fixed spinning speed of 3000 rpm. For the deposition of W-VO_2, 500 uL of the prepared solution was used every time. For the TW without RC regulation, the W-VO_2 solution was directly spin-coated on TW substrate at a fixed spinning speed of 3000 rpm.

5.2.6 Fabrication of cement/PET/glass with and without RC regulation

To demonstrate the versatility of the proposed route, we choose cement, PET, and glass as alternative substrates for the RC design. The PET film was cut into 3 cm × 3 cm pieces, while the glass with the size of 3 cm × 3 cm was used. The cement samples were prepared with a water/cement ratio (W/C) of 0.38. The mixtures were mixed by vigorous stirring. Then the paste was cast into a petri dish, forming a cylinder with a diameter of 3 cm and a thickness of 3 mm. The sample was cured at 40 ºC for 24h. Finally, the specimen was demolded and the cured at room temperature for another 48h.

The multi-layer structure was spin-coated on PET/cement /glass using the same procedures as the preparation of TCTW, while the spinning speed of PMMA spacer was fixed to 4000 rpm.

5.2.7 Energy saving simulation

The energy consumption simulation of the TCTW was conducted on Energy Plus V22-2, where a medium office prototype building model was used[268]. The façade of the model and HVAC parameters are presented in Table 5. 1. The building has a total area of 4982.19 m^2 with a 33% window to wall ratio. The glazing system has a total window area of 652.83 m^2.

Table 5. 1 Information of building model and HVAC system used for the simulation

Information of building model and HVAC system used for the simulation

Items	Parameters
Window fraction	33 %
Total floor area	4982 m^2
Floor-to-Floor Height	3.96 m
Floor-to-Ceiling Height	2.74 m
Aspect Ratio	1.5
Window locations	Evenly distributed on four walls
Exterior walls	Heavy-weight concrete + Steel frame wall insulation + gypsum
Window	See Table S3
Roof	Roof membrane + roof insulation + metal decking
HVAC	Cooling: Packaged air conditioning unit, direct expansion (DX) cooling Heating: Packaged air conditioning unit, gas furnace Air distribution system: multi-zone VAV with damper-controlled terminal boxes and electric reheating coils Service water heating: Storage tank, natural gas water heater
Thermostat[269]	Setpoint 24 °C for cooling with a setback of 26.7 °C, and 21 °C for heating with a setback of 15.6 °C

The transition of the optical properties of TCTW was achieved by the built-in

thermochromic function of glazing materials. The transition temperature was set to 33.5 °C. The optical properties of TCTW, low-E glass, and normal glass are shown in Table 5. 2(parameters for low-E glass and normal glass are cited from Wang's report[240]). Considering the variation of site-to-source conversion factor in different regions, we adopted the same site-to-source conversion factor (2.40 for electricity and 1.04 for natural gas) as Wang's report[240].

Table 5. 2 Optical parameters used in simulation

Optical parameters used in simulation

Optical properties	TCTW	Low-E glass	Normal glass
ε_{MIR-L}	0.40	0.84	0.84
ε_{MIR-H}	0.71	0.84	0.84
$\Delta\varepsilon_{MIR}$	0.31	0	0
$\varepsilon_{MIR-back}$	0.85	0.1	0.84
T_{Vis-L} / %	19.6	85	88.1
T_{Vis-H} / %	20.3	85	88.1
$R_{vis\ front-L}$ /%	7.1	5.6	8.0
$R_{vis\ front-H}$ /%	7.2	5.6	8.0
$R_{vis\ back}$ /%	11.4	7.9	8.0
$R_{sol\ front-L}$ /%	6.7	19.0	7.1
$R_{sol\ front-H}$ /%	6.8	19.0	7.1
$R_{sol\ back-L}$ /%	10.8	22.0	7.1
$R_{sol\ back-H}$ /%	10.8	22.0	7.1
T_{sol-L} / %	21.6	63.0	77.5
T_{sol-H} / %	21.1	63.0	77.5

The building energy saving performance values are obtained by comparing the annual and monthly energy consumption between different window materials including TCTW, commercial low-E glass, and normal glass. Three typical cities from each climate zone classification as used for the simulation are presented in Table 5. 3. The heating/cooling energy consumption per unit area is calculated based on the total building area, while the heating/cooling energy savings per unit area is calculated based on the total window areas. Besides, the annual energy savings benchmarked by a commercial low-E glass across all different climate zones was calculated by averaging the energy saving

performance in three cities from each climate zone.

Table 5. 3 Cities from each climate zone for the simulations.

Cities from each climate zone for the simulations.

Zones	Features	Cities		
0A	Extremely Hot Humid	Bangkok (Thailand)	Singapore (SGP)	Manila (Philippines)
0B	Extremely Hot Dry	AbuDhabi (Emirate of Abu Dhabi)	Karachi (Pakistan)	Ahmedabad (India)
1A	Very Hot Humid	Honolulu (USA)	Rio de Janeiro (Brazil)	Veracruz (Mexico)
1B	Very Hot Dry	New Delhi (India)	Richmond (Australia)	Yuanjiang (China)
2A	Hot Humid	Hong Kong (China)	Sao Paulo (Brazil)	Tunis (Tunisia)
2B	Hot Dry	Cairo (Egypt)	LIMA (Peru)	Makindu (Kenya)
3A	Warm Humid	Auckland (New Zealand)	Chongqing (China)	Roma Ciampino (Italy)
3B	Warm Dry	Adelaide (Australia)	Cozzo Spadaro (Spain)	Melilla (Spain)
3C	Warm Marine	Nairobi (Kenya)	Cape Town (South Africa)	Kunming (China)
4A	Mixed Humid	Beijing (China)	Brussels (Belgium)	Lyon (France)
4B	Mixed Dry	Madrid (Spain)	Tabriz (Iran)	AnYang (China)
4C	Mixed Marine	Vancouver (Canada)	Seattle (USA)	San Francisco (USA)
5A	Cool Humid	Birmingham (UK)	Bremen (Germany)	Hamburg (Germany)
5B	Cool Dry	Denver (USA)	Salt Lake City (USA)	Lanzhou (China)
5C	Cool Marine	Comox (Canada)	Sandspit (Canada)	Ketchikan (USA)
6A	Cold Humid	Stockholm (Canada)	Helsinki (Finland)	Moskva (Russia)
6B	Cold Dry	Alamosa (USA)	Kaunas (Lithuania)	Skagway (USA)
7	Very Cold	Tampere (Finland)	Cordova (USA)	Ostersund (Sweden)

8	Subarctic/Arctic	Tanana Ralph (USA)	Yakutsk (Russia)	Inuvik (Canada)

5.2.8 Characterization

Temperature dependent XRD measurements were conducted on Rigaku SmartLab 9kW-Advance X-ray diffractometer equipped with an Anton PAAR TTK 600 temperature control system. XRD patterns within a heating-cooling (25-95-25ºC) circle were obtained to show the phase change of VO_2. For each temperature point, signals were collected in the range of 20-80° with step size of 0.02° and scan rate of 10°/min using a HyPix-3000 Hybrid Pixel Array Detector. The remaining XRD patterns (i.e., with no temperature variation) were collected using the Rigaku SmartLab 9kW. For powder samples, the powder was dispersed in ethanol, then the solution was dropped onto the cover slip until full coverage. For the PET, glass, cement, and TW, the samples were directly placed on the sample holder for measuring. The sample alignment was conducted by the system automatically. Then the patterns were collected in the range of 20-80° with step size of 0.02° and scan rate of 10°/min under the 2 Theta mode with the glancing angle configuration at an incidence angle of 2°. Temperature-dependent Raman was also used to reveal the phase change process of W-VO_2. Raman spectra at different temperatures were obtained from a Renishaw Micro-Raman Spectroscopy System equipped with a LTS120T-P Electrical & Probe Temperature Control System. A 780 nm laser with a laser power of 10 mW were selected for all measurements. The transition temperature of W-VO_2 was measured by differential scanning calorimetry (DSC) on PerkinElmer DSC 8000. The sample (< 5 mg) was sealed in an aluminum pan and placed in the furnace. The sample and the reference pan were heated/cooled under nitrogen atmosphere (50 $mL \cdot min^{-1}$) with the heating/cooling rate of 20 $°C \cdot min^{-1}$ from -10 to 100 °C. The transition temperature was determined by averaging the corresponding temperatures of the two DSC peaks. Scanning electron microscope (SEM) images were obtained from TESCAN VEGA. The reflectance (R(λ)) and transmittance (T(λ)) across 2.5-15 μm were measured by Fourier Transform Infrared (FT-IR Spectrometer, Spectrum 100, PerkinElmer) with a diffuse gold integrating

sphere. The scanning range is 650 cm^{-1} to 4000 cm^{-1} at the resolution of 4 cm^{-1}, and a total of 16 scans were collected. The reflectance and transmittance at high temperatures were obtained using a self-made silicone rubber heating plate. The emissivity (ε(λ)) was calculated according to Kirchhoff's law:

$$\varepsilon(\lambda) = \sigma(\lambda) = 1 - R(\lambda) - T(\lambda)$$

where $\sigma(\lambda)$, $R(\lambda)$, and $T(\lambda)$ are the absorbance spectrum and reflectance spectrum of the surface. The $\varepsilon(\lambda)$ of TW and cement was directly determined by the following formula:

$$\varepsilon(\lambda) = \sigma(\lambda) = 1 - R(\lambda)$$

due to the negligible transmission $T(\lambda)$ over the spectra of interest. The integrated emissivity was calculated by averaging the absorbance spectrum $\varepsilon(\lambda)$ within the corresponding wavelength. The emissivity contrast was determined by the following formula:

$$\Delta\varepsilon_{x-y} = \varepsilon_{x-y,\text{high temperature}} - \varepsilon_{x-y,\text{low temperature}}$$

where the x and y refer to specific waveband. The in-situ transmittance T(λ) and reflectance R(λ) across 200-2500 nm were obtained from SHIMADZU UV-3600 Plus with a 150 mm integrating sphere at 20°C and 60°C.

The T_{sol}, R_{sol}, and T_{lum} were determined by the following formula:

$$\text{Tsol} = \int_{200}^{2500} \varphi_{sol}(\lambda) \cdot T(\lambda)\, d\lambda \Big/ \int_{200}^{2500} \varphi_{sol}(\lambda)\, d\lambda$$

$$\text{Rsol} = \int_{200}^{2500} \varphi_{sol}(\lambda) \cdot R(\lambda)\, d\lambda \Big/ \int_{200}^{2500} \varphi_{sol}(\lambda)\, d\lambda$$

$$\text{Tlum} = \int_{380}^{800} \varphi_{lum}(\lambda) \cdot T(\lambda)\, d\lambda \Big/ \int_{380}^{800} \varphi_{lum}(\lambda)\, d\lambda$$

The solar modulation was determined by the following formula:

$$\Delta T_{sol} = T_{sol,\text{low temperature}} - T_{sol,\text{high temperature}}$$

where the φ_{sol} (λ) is the solar irradiance spectrum distribution for AM 1.5 (corresponding to the sun standing 37° above the horizon with 1.5 atmosphere thickness

and the presence of a solar zenith angle of 48.2°); $\varphi_{lum}(\lambda)$ is the standard luminous efficiency function of photopic vision for the wavelength of 380–800 nm[270]. $T(\lambda)$ and $R(\lambda)$ are the transmittance spectrum and reflectance spectrum. The IR images were collected by an FLIR E95 (working wavelength ~7-14 μm, reference emissivity ~0.90) with a background ($\varepsilon_{7\text{-}14}$~0.46). The sample and the background were placed on a heating stage with temperature control. To avoid the effect of surrounding radiation, the whole set up was surrounded by an acrylic box. Note that the color in the IR images only represents the emissivity difference between the background and the sample due to the huge emissivity difference between the measuring objects and the built-in emissivity reference (0.90) of the IR camera[271].

5.3 Results and discussion

5.3.1 Phase transition behaviors of the prepared vanadium dioxide

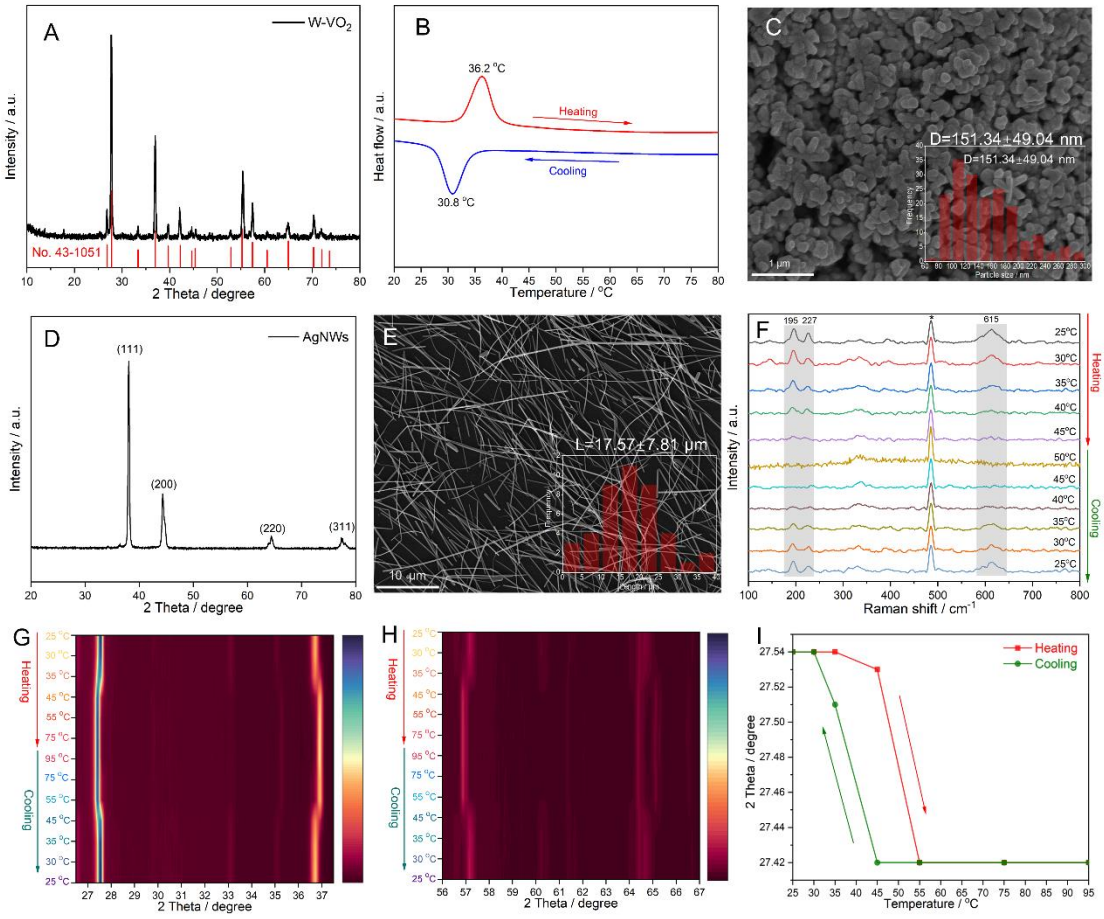

Figure 5. 2(A-C) XRD pattern, DSC curve and SEM image of the prepared W-VO_2. (D-E) XRD pattern and SEM image of the prepared AgNWs. (F) Temperature dependent Raman spectra of W-VO_2 during a heating and cooling cycle (* Raman band of the cover plate for the temperature control module). (G-H) Temperature dependent XRD patterns of W-VO_2 within 26.5-37.5^o and 56-67^o. (I) The peak location of the (011) orientation changes versus temperature during the heating /cooling cycle.

Tungsten-doped VO_2 (W-VO_2) was synthesized by a one-step hydrothermal process [252]. The sharp and strong diffraction peaks in the XRD pattern (Figure 5. 2A) not only confirm the monoclinic VO_2(M) phase (JCPDS No. 43-1051) but also suggest a high level of crystallinity. DSC results (Figure 5. 2B) reveal that the phase transition temperature (T_c) of the prepared W-VO_2 is much lower than pure M phase VO_2 (~68^{o}C) due to the tungsten doping. The transition temperature (~33.5^{o}C, obtained by averaging the exothermal and endothermic peaks) is much closer to room temperature, which makes it suitable for window applications. The morphology of the prepared W-VO_2 is that of small particles with average diameter of 151.34 nm (Figure 5. 2C). The AgNWs were chosen as the bottom layer of the stacking design and were prepared using a solution process [267, 272]. As shown in Figure 5. 2D, the XRD pattern of the prepared AgNWs is nearly identical to the standard fcc patterns of JCPDS No. 04-0783. The prepared AgNWs have an average length of 17.57 μm (Figure 5. 2E) and an average diameter of 145.45 nm (Figure 5. 3A).

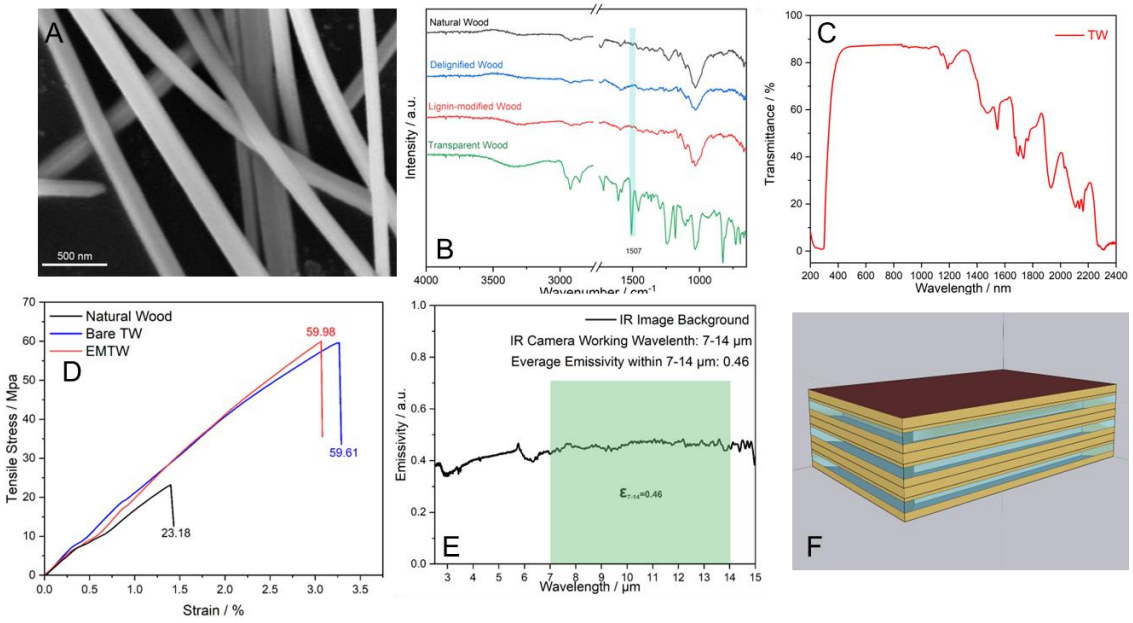

Figure 5. 3(A)The SEM image of the prepared AgNWs. (B) FTIR spectra of natural wood, delignified wood, lignin-modified wood, and transparent wood. (C) The UV-vis-NIR transmittance of pure TW across the range of 200 nm to 2400 nm. (D) Tensile strength of natural wood, bare TW and EMTW. (E) The absorbance(emittance) spectrum of the background used for the IR imaging. (F) Model of the Medium Office prototype building for the simulation.

The phase transition behaviors of as-prepared W-VO_2 were characterized by temperature-dependent Raman and XRD analyses. The Raman resonance band intensities of W-VO_2 are highly temperature-dependent. The intensity of scattering peak intensities (e.g., 195cm^{-1}, 227cm^{-1} and 615 cm^{-1}) decreases as temperature rises and vice versa (Figure 5. 2F) [273]. This is primarily due to the changes in lattice symmetry caused by the phase transition from insulator state to metal state [274, 275]. The phase transition was also confirmed by in situ XRD measurement. A distinct peak shift (Figure 5. 2G-H) from monoclinic VO_2(M) to rutile VO_2(R) phase transition was observed over a broad temperature range (30-45°C) as shown in Figure 5. 2I. The transition behaviors are consistent with the Raman spectra [276], suggesting the phase transition is a gradual process rather than an abrupt one from a macro point of view. Indeed, a mixed phase of VO_2(M) and VO_2(R) occurs during the heating/cooling cycle of Raman and XRD measurements. Overall, the temperature-dependent XRD and Raman measurements

confirmed the reversible phase transition of W-VO_2 at low temperatures, paving the way for emissivity modulation.

5.3.2 Characterization of EMTW

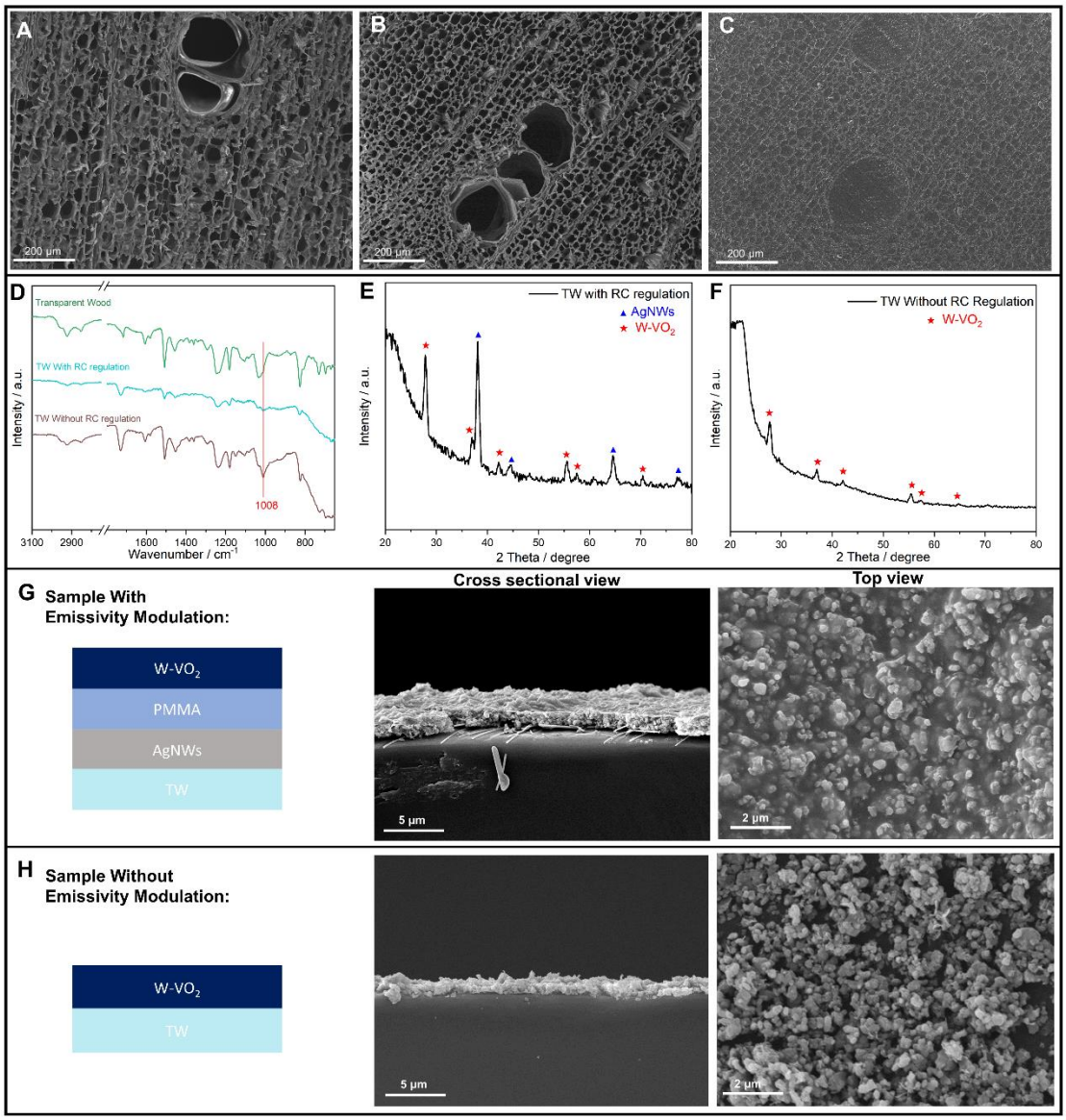

Figure 5. 4 Cross-sectional SEM image s of natural wood (A), lignin-modified wood (B) and transparent wood (C). (D)FTIR spectra of TW, TW without emissivity modulation, and TW with emissivity modulation. XRD patterns of TW with (E) and without (F) emissivity modulation. (G) Schematics structure of EMTW and its SEM images from cross-section and top view. (H) Schematics structure of TW without emissivity modulation and its SEM images from cross-section and top view.

The self-adaptive emissivity modulation design typically includes a AgNWs layer due to its considerable visible transmittance and high IR reflectivity, a lossless dielectric spacer (PMMA) due to its infrared transparency, and a thermochromic layer (W-VO_2) due to its phase change nature that allows for self-adaptive modulation of emissivity. TW substrates were prepared via lignin modification followed by epoxy impregnation. The FTIR spectra of natural wood (NW), delignified wood (DW), lignin-modified wood (LMW) and TW are shown in Figure 5. 3B. The characteristic peak of lignin (1507 cm^{-1}) was observed in the NW and LMW spectra, indicating preservation of the lignin skeleton [7, 277]. The cross-sectional SEM images of NW (Figure 5. 4A), LMW (Figure 5. 4B), and TW (Figure 5. 4C) suggest that the highly aligned microchannels were well reserved after lignin modification, providing the space for subsequent polymer impregnation. Then the microchannels were fully impregnated with epoxy, showing no gaps between polymer and wood scaffold. The resultant TW shows high transmittance (~87% at 550 nm) across the visible range (Figure 5. 3C). The assembling of the coating shows little impact on the mechanical properties of TW (Figure 5. 3D).

The structural difference between TW with and without emissivity modulation can be partially demonstrated by FTIR peak at 1008 cm^{-1}, representing the stretching vibration V=O ((Figure 5. 4D) [137]. The XRD patterns provide further confirmation of the structural difference between the samples with ((Figure 5. 4E) and without ((Figure 5. 4F) emissivity modulation design. Diffraction peaks corresponding to W-VO_2 are present in both samples. However, peaks corresponding to AgNWs are exclusively present in the sample with emissivity modulation. For samples with emissivity modulation ((Figure 5. 4G), the cross-sectional images showed that the AgNWs were located underneath the W-VO_2 layer, while top-view images confirmed the presence of a continuous W-VO_2 film on top.

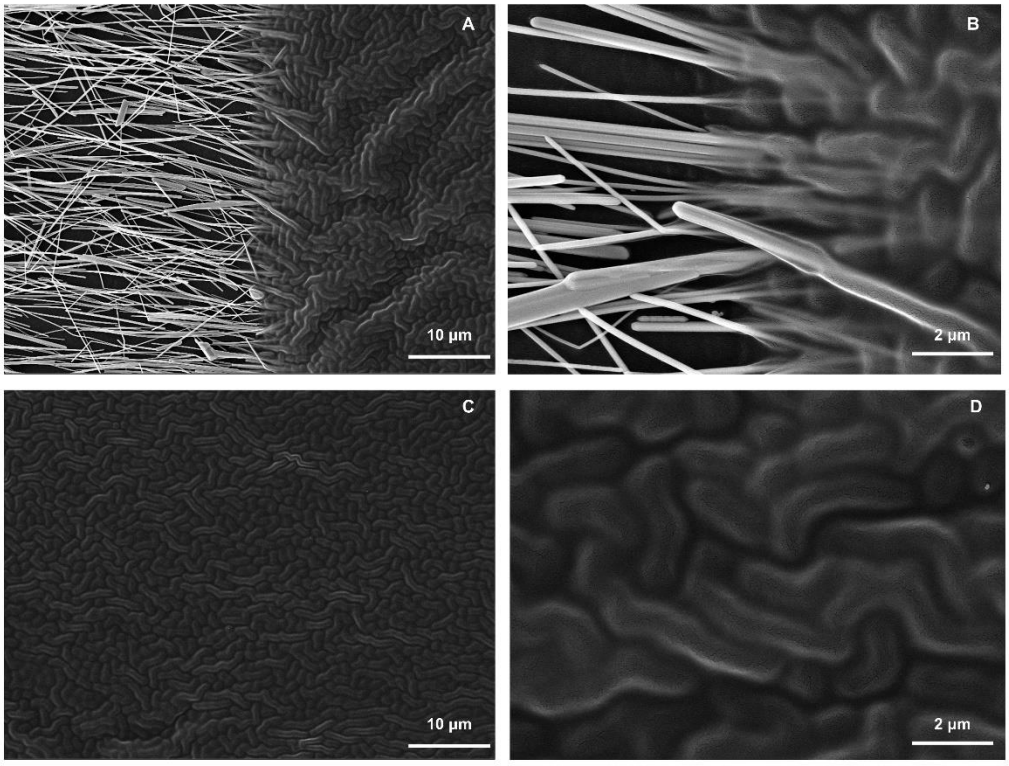

Figure 5. 5 SEM images of the sample coated with AgNWs (Before W-VO_2 coating).

To verify the presence of the PMMA spacer, we directly observed the sample after PMMA coating (Figure 5. 5), which clearly showed that the AgNWs were covered by a layer of PMMA. Although not immediately apparent, a middle layer (PMMA spacer) can be identified to a broad approximation. The lack of a clear boundary between the two layers (AgNWs and W-VO_2) is most likely due to the fact that the PMMA spacer layer can be partially dissolved by the acetone used during the W-VO_2 spin coating process, and/or interpenetration within the AgNWs structures. While this may obscure the PMMA layer in cross-sectional imaging, AgNWs are clearly covered by a layer of PMMA the top-view images. Thus, we believe that the PMMA component can still be considered as a spacer for the photonic Fabry-Perot resonator, as evidenced by the optical properties. For the sample without emissivity modulation, W-VO_2 was directly spin-coated on TW. However, the resulting film is not continuous, as seen from the top view SEM image (Figure 5. 4H). This may be attributed to the wettability of TW to acetone used for the PMMA-WVO_2 solution [278].

5.3.3 Optical properties of EMTW

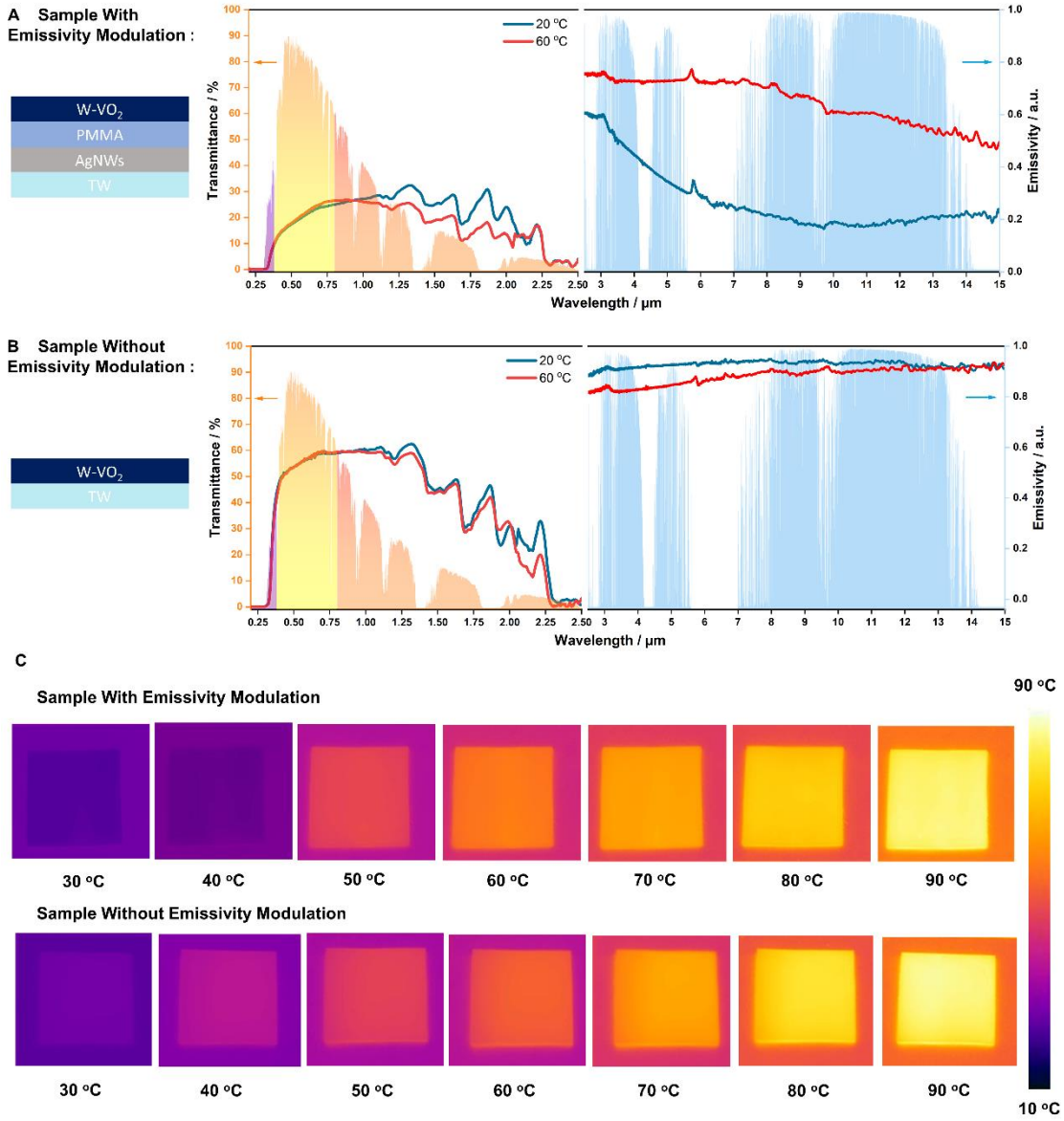

Figure 5. 6 The experimental optical spectra of samples with (A) and without (B) emissivity modulation design in the visible-NIR and MIR ranges (2.5-15 μm) at 20°C (blue line) and 60°C (red line) against a normalized AM1.5 solar spectrum (purple, yellow and orange shaded areas) and MIR atmospheric transmittance window (blue shaded areas). Schematics structures of each sample are shown on the left. (C) The IR camera images of the EMTW (top) and the sample without emissivity modulation (bottom) as the temperature increased from 30 °C to 90 °C. The emissivity of the background in 7-14 μm ($\varepsilon_{7\text{-}14}$) is 0.46.

The optical spectra of the prepared TW with and without emissivity modulation at various temperatures were investigated (Figure 5. 6A &B). The sample without emissivity modulation shows a T_{lum} of 55.7% under 20 ^oC and 55.6% under 60^oC, respectively. EMTW shows a very close T_{lum} at two different temperatures (20.3% at 20^oC and 19.6% at 60^oC). This can be attributed to the fact that the coating for the sample without emissivity modulation is discontinuous (Figure 5. 4H), allowing more visible light to pass through. EMTW exhibits a limited solar modulation capacity (ΔT_{sol}~0.5%), with a T_{sol} of 21.6% at 20 ^oC and a T_{sol} of 21.1% at 60 ^oC. The limited solar modulation capacity of EMTW may be attributed to the relatively high absorption in the NIR range of the TW substrate. The emissivity of EMTW within 2-15μm (ε_{2-15}) is 0.4 when the temperature is below T_c (33.50 ^oC) but increases to 0.71 when the temperature exceeds T_c. EMTW shows a more impressive emissivity contrast of 0.44 (ε_{8-13}=0.19 at 20 ^oC, ε_{8-13}=0.63 at 60 ^oC). As a comparison, the sample without emissivity modulation shows a negative $\Delta\varepsilon_{2.5-15}$ of -0.07 (0.92 at 20 ^oC and 0.85 at 60 ^oC), which is consistent with previous report [252]. This suggests that the stacking design of EMTW, which includes the Fabry-Perot resonance structure, is responsible for the desired positive emissivity contrast.

The IR images were collected using a FLIR E95 (working wavelength ~7-14 μm, emissivity reference ~0.90), where a background with a ε_{7-14} of 0.46 (Figure 5. 3E) was employed. At the same temperature, the colour of the IR image indicates the emissivity in the working wavelength of the IR camera; darker colours suggest lower emissivity and vice versa[271]. For samples with emissivity modulation, the colour of the EMTW was darker than the background before 40 ^oC, indicating a lower emissivity (ε_{7-14}~0.2) compared to the background (ε_{7-14} ~0.46). When the temperature exceeded 50 °C, the colour of the EMTW became brighter than the background, suggesting a higher emissivity (ε_{7-14}~0.65) compared to the background (ε_{7-14} ~0.46). In comparison, the colour of the sample without emissivity modulation remained consistently brighter than the background, confirming that it is incapable of modulating RC capacity in response to changes in temperature without AgNWs/PMMA/W-VO_2 stacking design.

Table 5. 4 Spinning speed of the PMMA spacer and the W-VO_2 concentration used to adjust the emissivity and emissivity contrast

ε-cold				
W-VO_2 concentration / wt%	Wave band /μm	PMMA spin speed / rpm		
		4000	3000	2000
5	2.5-15	0.35	0.44	0.60
	8-13	0.20	0.21	0.31
10	2.5-15	0.36	0.49	0.62
	8-13	0.20	0.27	0.35
20	2.5-15	0.40	0.51	0.61
	8-13	0.19	0.27	0.36
ε-Hot				
W-VO_2 concentration / wt%	Wave band /μm	PMMA spin speed / rpm		
		4000	3000	2000
5	2.5-15	0.46	0.50	0.65
	8-13	0.28	0.30	0.42
10	2.5-15	0.55	0.59	0.68
	8-13	0.39	0.38	0.48
20	2.5-15	0.71	0.74	0.75
	8-13	0.63	0.60	0.60
Δε				
W-VO_2 concentration / wt%	Wave band /μm	PMMA spin speed / rpm		
		4000	3000	2000
5	2.5-15	0.11	0.06	0.06
	8-13	0.08	0.09	0.11
10	2.5-15	0.19	0.10	0.06
	8-13	0.19	0.11	0.13
20	2.5-15	0.31	0.23	0.14
	8-13	0.44	0.33	0.24

The tunability of emissivity contrast was investigated by varying the spinning speed of PMMA layer and the concentration of W-VO_2, which in turn determining the thickness and arrangement of the multi-layered stack (Table 5. 4). By fixing the W-VO_2 concentration, both ε_{-cold} and ε_{-hot} increased gradually, despite few exceptions. This can be attributed to the introduction of PMMA and W-VO_2. Additionally, it was observed

that there was a decrease in emissivity contrast as the PMMA spinning speed decreased, despite few exceptions. This indicates that the modulation capacity is highly related to the spacer thickness, which is in line with previous studies [279, 280]. However, the thickness of PMMA spacer can influenced by the solvent of W-VO_2 solution. It might be difficult to obtain the accurately quantified thickness for PMMA spacer and W-VO_2 layer for now. The detailed relation between the PMMA spacer thickness and emissivity contrast deserves further exploration in the future.

5.3.4 Global Energy saving potential of EMTW

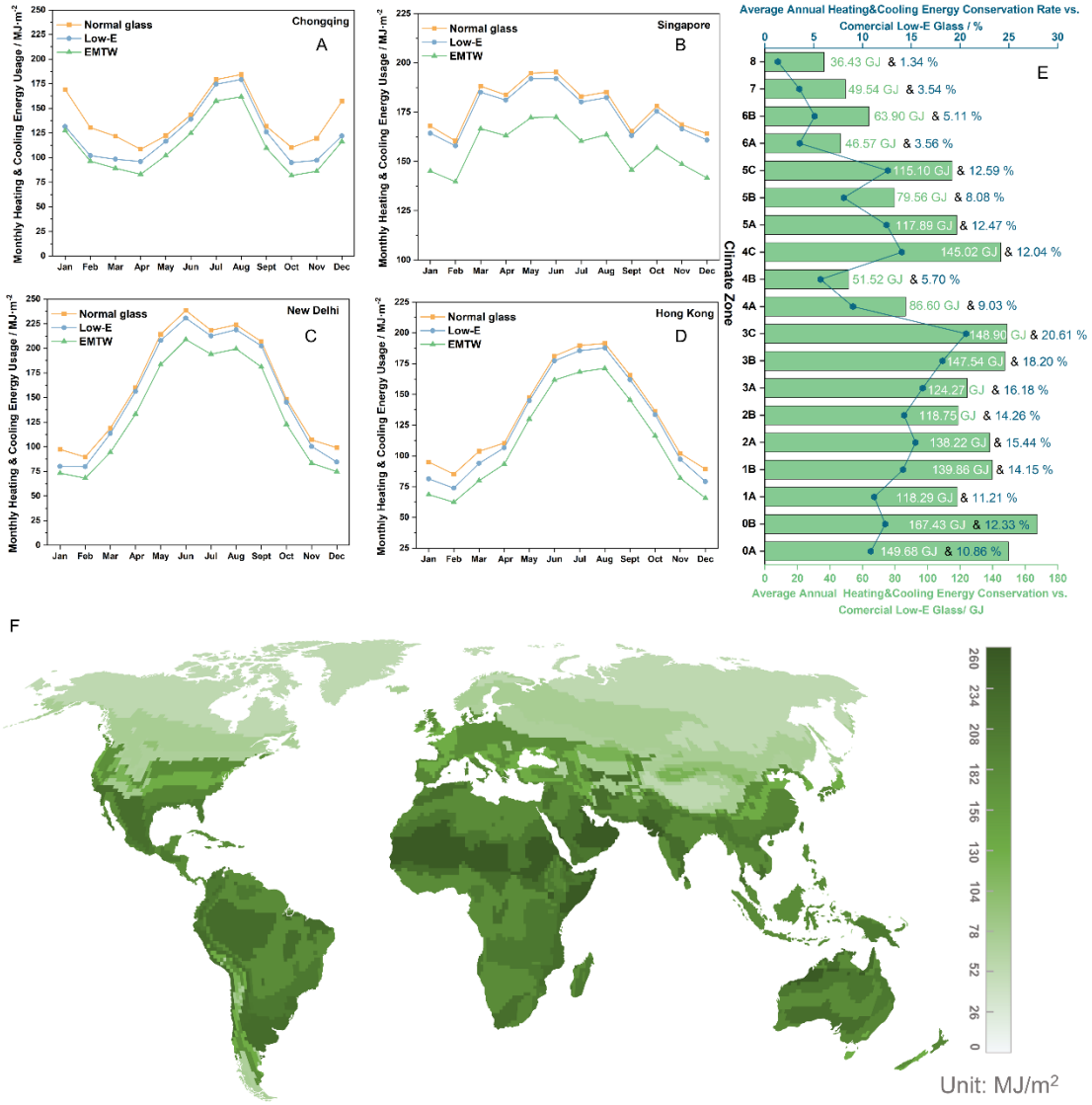

Figure 5. 7 (A-D) Monthly heating/cooling energy usage in four typical cities (Hong Kong, Chongqing, Singapore, and New Delhi) (E) Simulated average annual

heating/cooling energy conservation and conservation rate of EMTW compared to commercial low-E glass across different climate zones. (F) Mapping of the simulated average heating/cooling energy conservation of EMTW compared commercial low-E glass across various climate zones.

Energy simulations were conducted on a medium office prototype building with a total area of 4982 m^2 (Figure 5. 3F) to validate the energy saving potential of the as-prepared EMTW. Three representative cities (57 in total, Table 5. 3) from each climate zone were selected for the simulation. The optical properties (Table 5. 2) for the simulation were extracted from the experimental sample with the maximum $\Delta\varepsilon_{2\text{-}15}$. We adopted the same principle as Wang's report[240] in terms of selecting emissivity for the simulation. We choose $\varepsilon_{2\text{-}15}$ to represent the broadband emissivity for the simulation due to two facts [52, 240]: 1) The broadband cooler has higher net cooling power than the selective one (8-13 μm) when the temperature is above or close to the surrounding temperature; 2) The exterior surface temperature of window is usually higher than the ambient temperature. The monthly heating/cooling energy consumption of EMTW was compared against with both glass and commercial low-E glass (Figure 5. 7A-D) in four typical cities (Singapore, zone 0; New Delhi, zone 1; Hong Kong, zone 2; Chongqing, zone 3;), which are usually considered as building/population-dense areas. EMTW exhibited the lowest monthly heating/cooling energy usage not only in the four selected cities, but also in the other selected cities (spanning a range of climate zones) when compared to normal glass and low-E glass. Consequently, EMTW had lower annual heating/cooling energy consumptions compared to normal glass and commercial low-E glass. An average energy savings up to 167.43 GJ and an energy saving rate up to 20.61% can be realised in zone 0B and zone 3C, respectively (Figure 5. 7E). EMTW exhibits higher energy conservation benchmarked by commercial low-E glass across all climate zones (Figure 5. 7F) with a heating/cooling energy saving per unit area up to 256.46 $MJ \cdot m^{-2}$, further revealing the critical role of radiative cooling modulation. Despite the fluctuation in energy conservation performance, it seems that EMTW shows higher energy saving potential in hot areas than cold areas. This is possibly caused by

the lower temperatures, which are too low to induce the optical transition of EMTW. Take Yakutsk as an example, the warmest month (July) has the average temperature of 20 °C [281], which is not capable of inducing the optical transition of EMTW (33.5 °C) in our current system architecture. The calculated energy saving performance of EMTW across different climate zones reveals the significance and validity of adaptive emissivity modulation for all-weather, year-round applications, which is in good agreement with Wang's report [240].

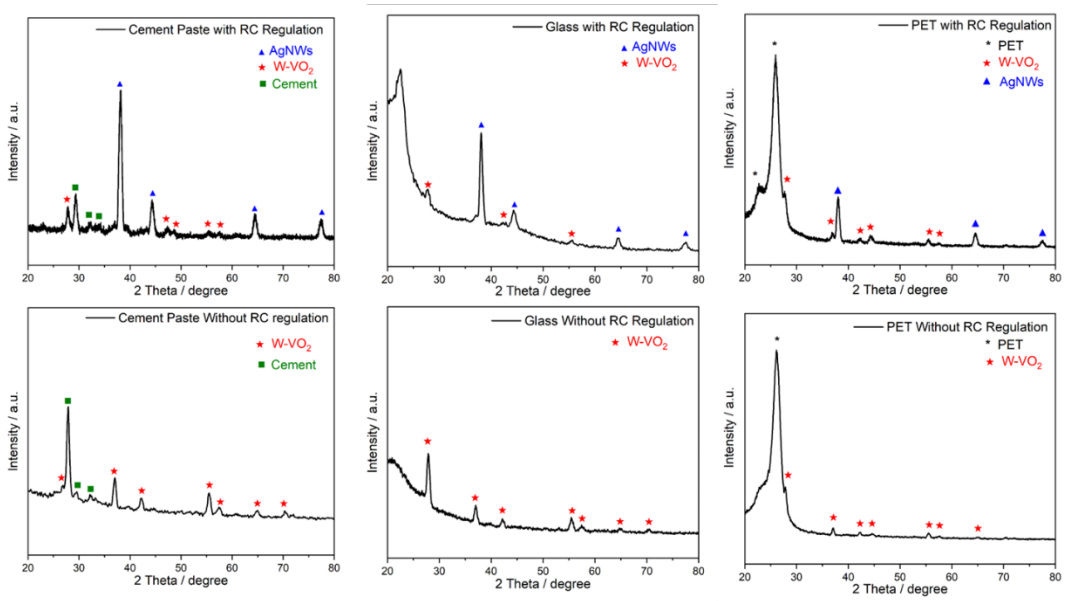

Figure 5. 8 XRD patterns of cement/PET/glass with (Top) and without (Bottom) RC regulation.

The adopted route above has the potential for a wide range of established materials. We alternatively applied this route to PET film, glass and Portland cement paste to create emissivity modulator. The XRD pattern (Figure 5. 8) confirmed their different structures. Without F-P structure design, PET ($\Delta\varepsilon_{8\text{-}13}$~-0.03, from 0.84 to 0.81), glass ($\Delta\varepsilon_{8\text{-}13}$~-0.02, from 0.80 to 0.78), and cement ($\Delta\varepsilon_{8\text{-}13}$~-0.07, from 0.91 to 0.84) all exhibited a negative emissivity contrast (Figure 5. 9B), suggesting the failure of emissivity modulation. However, it is promising to note that the emissivity modulation can be achieved on both PET ($\Delta\varepsilon_{8\text{-}13}$~0.14, from 0.61 to 0.75), glass ($\Delta\varepsilon_{8\text{-}13}$~0.21, from 0.48 to 0.69) and cement ($\Delta\varepsilon_{8\text{-}13}$~0.17, from 0.58 to 0.75) due to the stacking F-P design

(Figure 5. 9A), despite the limited emissivity contrast. The limited emissivity contrast compared to the case of TW is possibly due to the different surface properties of each substrate[282], which then results in the different thickness for each layer. The established coting processes for emissivity modulation are usually substrate-dependent (usually opaque substrates) and generally require high temperatures and vacuum, which are unfavorable for wide adoptions. Our method only involved simple spin coating and does not require any expensive or inapproachable instruments. Overall, the method we proposed can provide a facile, widely adoptable and affordable way to achieve a degree of radiative cooling modulation for many established materials spanning various industrially relevant materials across built environment fields.

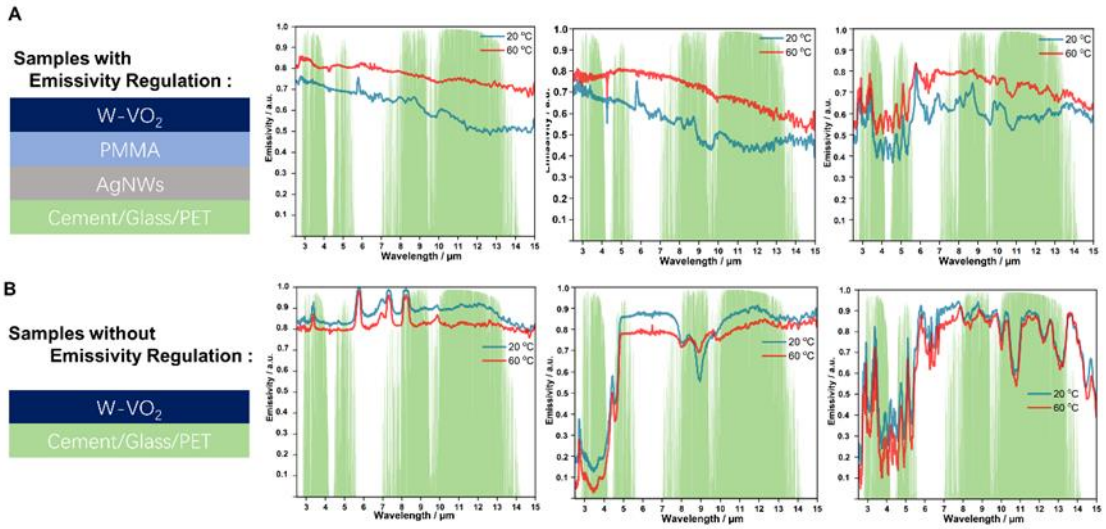

Figure 5. 9 Experimental optical spectra of PET/Glass/Cement with (A) and without (B) emissivity modulation within MIR range at 20 °C (blue line) and 60 °C (red line) against the atmospheric transmittance window (green shaded areas).

5.4 Conclusion

Radiative cooling modulation capability on TW was obtained through a facile and widely applicable solution processing route. An emissivity contrast of 0.44 (0.19 for low temperatures and 0.63 for high temperatures) within the atmospheric window (8-13μm) was achieved on TW. The emissivity contrast can be altered by adjusting the spinning speed of the PMMA layer and the concentration of W-VO_2 during fabrication. The emissivity modulation capability also accompanied by considerable luminance

transmittance (approximately 20%) and low transition temperature (~33.5 ºC), which lends the structure towards feasible and effective real-world applications. Energy consumption simulations demonstrated that the EMTW outperformed commercial low-E glass in terms of energy savings across a variety of climate zones. Importantly, this approach is facile, widely applicable, and substrate independent. Theoretically, radiative cooling modulation can be achieved on any potential surfaces, including roofs, walls, and textiles, through this approach with few modifications. Positive emissivity contrasts were also successfully demonstrated on three different widely used materials (PET, glass, and cement). The wide applicability and approachability of this approach are of great significance in promoting the concept of radiative cooling modulation, which is expected to enhance the efficiency of various smart, passive thermal-regulating systems across relevant applications.

Chapter 6 Self-Adaptive Emissivity-Regulated Fabrics for Personal Thermal Management

6.1 Introduction

Body thermal comfort crucial to safety and health due to a narrow normal temperature range (36-38^{o}C) of the delicate physiological metabolism system. Extreme temperatures will have adverse effects on people's psychological state and labor productivity, ultimately affecting social development[283]. Therefore, tremendous energy was consumed to provide thermal comfort for human in indoor environments annually via conventional heating, ventilation, and air conditioning (HVAC) systems, contributing to the global energy crisis and sustainability issues[5, 284]. Passive personal thermal management concept, focusing on the manipulation of the human body local environment, was considered as a promising method to alleviate the massive energy consumption for building temperature regulation system[65, 69, 285]. Studies indicate that increasing the cooling and heating set-points by 4°C each can result in significant energy savings, with reductions of up to 45% and 35%, respectively[28, 68]. Conventional textiles serve merely as insulation against thermal conduction and convection, ignoring the importance of infrared (IR) radiation for human thermal comfort.

Human skin is an excellent IR emitter, with an emissivity of 0.98[286]. Consequently, the human body emits thermal radiation primarily in the mid-IR wavelength range of 7–14μm, with peak intensity at around 9.5μm[24]. IR radiation also accounts for 40% of heat exchanges between human body and indoor environment. Some reports have explored the personal thermal management via manipulation of body IR radiation[287-291]. For example, textile for radiative cooling and radiative heating, have been developed to provide localized thermal control of the immediate environment around the human body[292, 293]. Tong et al. proposed a theoretical design for an IR-transparent, yet visibly opaque fabric (ITVOF) made from synthetic polyethylene fibers[67]. Based the concept of IR-transparent fabrics, Cai et al. proposed a spectrally

selective nanocomposite textile for radiative outdoor cooling[24]. In addition to IR-transmissive radiative cooling textiles, IR-emissive radiative cooling textiles have also been developed by Zhu et al., proposing a nano-processed silk with high emittance and solar reflection for radiative cooling purposes[65]. As for radiative heating purpose, fabrics with strong IR reflection were fabricated for human body to remain warming. Pure metallic yarns (steel fibers) were reported by Larciprete et al[294]. Metal-polymer composite yarns (core spun yarns and blended yarns) were also developed to maintain skin temperature. The most common approach to prepare high IR reflective fabrics is surface medication (i.e., depositing IR reflective materials on the surface of normal fabrics). For example, Hsu et al. developed a radiative heating fabric by embedding normal cotton with silver nanowires (AgNWs) using a dip-coating method[288].

While these studies have demonstrated excellent performance in either single-mode heating or cooling, they lack the ability to respond to changes in ambient environment. This may lead to thermal discomfort in some circumstances (radiative cooling in cold environment or radiative heating in hot environment). Therefore, dynamic reflectivity/emissivity regulation has attracted many researchers' attention[8]. Few reports have explored dynamic IR radiation modulation via electricity or mechanical actuation[71, 295-298]. Chen et al. proposed a kirigami-enabled electrochromic wearable device with variable-emittance (i.e., variable reflectivity) for adaptive personal thermoregulation. The maximum emissivity contrast of 0.27 (0.38 at -1V, 0.65 at 0.4V) was obtained by changing voltage, showing potential for skin temperature stabilization. Zhang et al. achieved modulation of infrared (IR) radiation in response to changes in the relative humidity of underlying skin [72]. They engineered triacetate-cellulose bimorph fibers, incorporating a thin layer of carbon nanotubes to make the polymer fibers electrically conductive. A maximum IR transmittance contrast of 35 % can be achieved due to the resonant electromagnetic coupling effect induced by mechanical actuation, which was also triggered by sweating. Li et al. developed a spectrally self-adaptive smart fabric by coating polyester fabric with silver nanowires[299]. The resulting fabric autonomously adjusts its emissivity based on the

body's condition, seamlessly transitioning between dry and wet states. An emissivity contrast of 0.44 (0.39 in the dry state and 0.83 in the wet state) was demonstrated due to wetting effect of sweat, primarily composed of water, which is characterized by high emissivity. Overall, despite a few attempts at dynamic IR emissivity/reflectivity/transmissivity modulation for bidirectionally regulating of both heating and cooling, achieving temperature-dependent IR emissivity manipulation in textiles without any energy input remains challenging.

Figure 6. 1Schematic illustration of SARCF

In this chapter, we developed a self-adaptive radiative cooling regulation fabric (SARCF) capable of dynamically manipulating infrared (IR) radiation (Figure 6. 1). SARCF was prepared by depositing VO_2 nanoparticles onto low-e fabrics, supplemented by the stitching of an IR-transparent nonporous polyethylene layer on top to provide the solar reflection and passageway for infrared. At low temperatures, SARCF exhibited a high solar reflection of 84.24% and a low IR emissivity of 39.38%, suppressing the radiative cooling effect. As the temperature increased, the IR emissivity shifted to 74.20%, enhancing the cooling effect. Such temperature-dependent emissivity regulation can help human to stay thermal comfort against temperature fluctuations. In addition. the passive transition of IR emissivity is an energy-free process, which was induced by ambient temperature. Overall, this study introduces a facile approach for dynamic manipulation of radiative cooling power and body radiation via emissivity modulated fabrics, showing great potential in providing thermal comfort in various environments.

6.2 Methods

6.2.1 Materials

Tungsten doped vanadium dioxide (W-VO_2) was purchased from Hangzhou Jikang New Materials Co., Ltd. The particle size of the W-VO_2 nanoparticles (NP) was approximately 30-50 nm. Low-e fabrics with Cu-Ni coating were purchased from Guangzhou Jiujing electronic materials Co., Ltd. The thickness of the low-e fabrics is 0.06mm with a surface resistance of <1 Ω. The bare polyester fabrics were obtained from corroding the Cu-Ni via diluted nitric acid (Sigma-Aldrich, 60%). Nanoporous polyethylene (Nano-PE, 25 μm) was bought from SK Innovation. Polydimethylsiloxane (PDMS, SYLGARD 184) was bought from Dow Co., Ltd.

6.2.2 Fabrication of self-adaptive radiative cooling regulation fabric

The self-adaptive radiative cooling regulation fabric (SARCF) was prepared by decorating low-e fabrics with randomly distributed W-VO_2 NP and then stitching this coated fabric together with nanoPE. The VO_2 NP were coated onto low-e fabrics via dip coating with sonication. Specifically, various amounts of W-VO_2 were added to an isopropanol solution (50 ml) containing 1 g of PDMS with sonication. The mixture was sonicated for 5 hours to ensure complete and even dispersion of the W-VO_2 NP. Subsequently, 0.1 g of curing agent was added to the mixture, which was then sonicated for an additional 30 minutes. The Low-e fabrics were immersed in the mixed solution for 15 minutes under ultrasound. The W-VO_2 coated fabrics was obtained after drying in a vacuum oven at 80°C for 24 hours. Finally, the SARCF was obtained by assembling the W-VO_2 coated fabrics and NanoPE together via ultrasonic wielding.

6.2.3 Thermal measurement

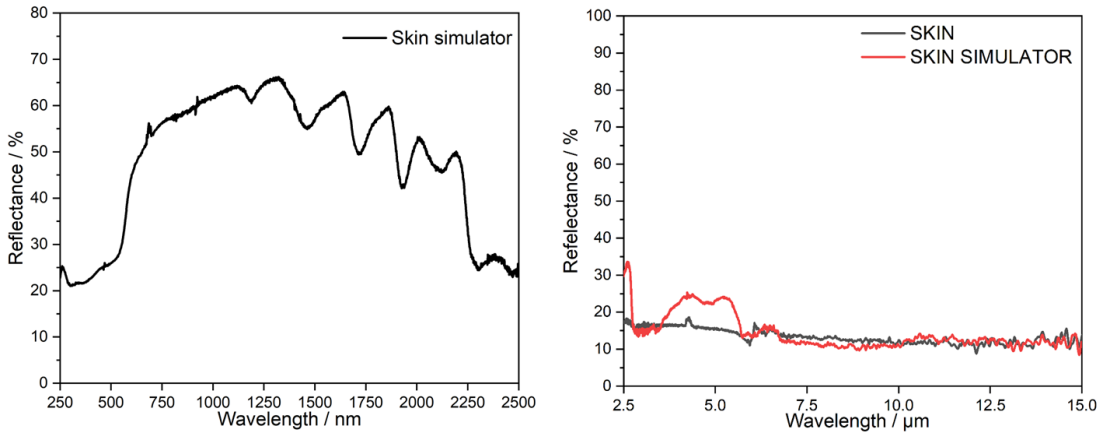

Figure 6. 2 Solar and infrared reflectance of skin simulator.

The thermal regulating capacity of the prepared SARCF was assessed using the experimental setup depicted in Figure 6. 10A. To simulate human skin, a layered structure comprising a Kapton heater, thermally conductive silicone grease, a copper plate, and 3M tape was employed. The infrared properties of this skin simulator closely mimic those of real human skin (Figure 6. 2). The Kapton heater, powered by a direct current source, delivered a heat flux of approximately 150 W/m², equivalent to the metabolic heat generation of the human body. The silicone grease and the 1.5 mm thick copper plate functioned as a thermal connector and heat diffuser, respectively, ensuring uniform temperature distribution across the surface. To minimize external thermal influences during testing, aluminum foil and EPS foam were integrated into the device. Temperature data was continuously recorded every second using a M2100 Series (Samcq) Temperature Acquisition Remote IO Module, which was connected to a laptop and equipped with PT100 resistance thermometers to monitor the temperature. The thermal evaluations were conducted in both hot and cold environments. For the hot environment, tests were performed at noon in Hong Kong, where the ambient temperature exceeded 35°C. In contrast, the cold environment tests took place inside a refrigerator, maintaining an ambient temperature of 5°C.

6.2.4 Infrared imaging

The IR images were collected using a FLIR E95 (working wavelength ~7-14 μm, emissivity reference ~0.98), where a cupper background with a $\varepsilon_{7\text{-}14}$ of 0.1was

employed. Four samples, white cotton, low-e fabric, heat-shielding fabric, and SARCF were placed on the cupper plate, which is sitting on a heater with temperature control. Note that environment radiation, especially human body radiation, has huge impact on the imaging of low-e stuffs due to its high infrared reflectance. Therefore, the whole setup was put in an acrylic that insulating the external radiation. The heater was kept at every temperature point for 5 min to avoid possible error caused by the different thermal conductivity of each sample. At the same temperature, the colour of the IR image indicates the emissivity in the working wavelength of the IR camera; darker colours suggest lower emissivity and vice versa[271].

6.2.5 Characterization

Temperature dependent XRD measurements were conducted on Rigaku SmartLab 9kW-Advance X-ray diffractometer equipped with an Anton PAAR TTK 600 temperature control system. XRD patterns within a heating-cooling (10-50-10ºC) circle were obtained to show the phase change of W-VO_2. For each temperature point, signals were collected in the range of 10-90° with step size of 0.02° and scan rate of 10°/min using a HyPix-3000 Hybrid Pixel Array Detector. To ensure the accurate sample temperature, the XRD patterns were collected five minutes later when the instrument temperature reaches set temperature point. The transition temperature of W-VO_2 was measured by differential scanning calorimetry (DSC) on PerkinElmer DSC 8000. The DSC curve was treated by subtracting baseline and smoothing in Origin Pro 2022. The sample (< 5 mg) was sealed in an aluminum pan and placed in the furnace. The sample and the reference pan were heated/cooled under nitrogen atmosphere (50 $mL \cdot min^{-1}$) with the heating/cooling rate of 20 $°C \cdot min^{-1}$ from -10 to 100 °C. The transition temperature was determined by averaging the corresponding temperatures of the two DSC peaks. Scanning electron microscope (SEM) images were obtained from TESCAN VEGA. Transmission electron microscopy (TEM) and high-resolution TEM (HRTEM) were conducted on JEOL 2100F, Japan (operating voltage = 200 kV). X-ray photoelectron spectroscopy analysis (XPS) was conducted by using ThermoFisher-nexsa with a monochromatic Al Kα X-ray source. The XPS survey spectrum as

collected in the range of 0-1350 eV under the pass energy of 100 eV with the energy step size of 1 Ev. The reflectance (R(λ)) and transmittance (T(λ)) across 2.5-15 μm were measured by Fourier Transform Infrared (FT-IR Spectrometer, Spectrum 100, PerkinElmer) with a diffuse gold integrating sphere. The scanning range is 650 cm^{-1} to 4000 cm^{-1} at the resolution of 4 cm^{-1}, and a total of 16 scans were collected. The reflectance and transmittance at high temperatures were obtained using a self-made silicone rubber heating plate. The emissivity (ε(λ)) was calculated according to Kirchhoff's law:

$$\varepsilon(\lambda) = \sigma(\lambda) = 1 - R(\lambda) - T(\lambda)$$

where A(λ) and R(λ) are the absorbance spectrum and reflectance spectrum of the surface, respectively, while T(λ) is the transmission spectrum. The ε(λ) of SARCF was directly determined by the following formula:

$$\varepsilon(\lambda) = \sigma(\lambda) = 1 - R(\lambda)$$

due to the negligible transmission T(λ) over the spectra of interest. The integrated emissivity was calculated by averaging the absorbance spectrum ε(λ) within the corresponding wavelength. The emissivity contrast was determined by the following formula:

$$\Delta\varepsilon_{x-y} = \varepsilon_{x-y,\text{high temperature}} - \varepsilon_{x-y,\text{low temperature}}$$

where the x and y refer to specific waveband. The temperature of the sample was controlled by self-made heating unit with temperature controller. The in-situ reflectance R(λ) across 200-2500 nm were obtained from SHIMADZU UV-3600 Plus with a 150 mm integrating sphere at 20°C and 60°C.

$$\text{Rsol} = \int_{200}^{2500} \varphi_{\text{sol}}(\lambda) \cdot \text{R}(\lambda)\, \text{d}\lambda \Big/ \int_{200}^{2500} \varphi_{\text{sol}}(\lambda)\, \text{d}\lambda$$

where the φ_{sol} (λ) is the solar irradiance spectrum distribution for AM 1.5 (corresponding to the sun standing 37° above the horizon with 1.5 atmosphere thickness and the presence of a solar zenith angle of 48.2°). Other spectrum over solar range without temperature control were collected from LAMBDA 1050+ UV/Vis/NIR spectrophotometer using a calibrated diffuse reflectance standard (Spectralon®

reflectance standard, Labsphere) as a reference. It should be noted that the solar reflectivity reported in this work is a relative value to the reference. When the reflectivity of a sample exceeds that of the reflectance standard, the measured spectral reflectivity value is greater than one. To not overestimate the reflectivity of the sample, any measured spectral reflectivity that exceeded one was truncated to 1 during data processing. When nanoPE was involved, it can be noted that the reflectivity over UV range is greater than one, therefore, the reflectivity was truncated to 1 in this range.

Optical Simulation

The optical characteristics of the fabricated structure (Figure 4A) within the 7-15 μm spectral range were numerically investigated through finite-difference time-domain (FDTD) simulations implemented in Lumerical FDTD Solutions. The computational model comprises a copper-coated polyethylene terephthalate (PET) fiber substrate overlaid with a vanadium dioxide (VO2)-polydimethylsiloxane (PDMS) composite layer, where VO2 nanoparticles were stochastically dispersed within the PDMS matrix. A parametric study was conducted to examine the influence of VO2 filler concentration, with volume fractions varying systematically at 10%, 20%, 40%, and 60%. Notably, the simulation protocol permitted particle aggregation and overlap effects to approximate real-world composite morphologies. The numerical domain was constructed by applying periodic boundary conditions along the x- and y-axes to simulate an infinite array configuration, while perfectly matched layer (PML) boundary conditions were implemented in the z-direction to mitigate artificial reflections. A normally incident plane wave excitation was imposed at the upper boundary of the computational space. Material optical constants were derived from established references: VO2[300], PET[301], Cu[302], and PDMS[301], with all constituent materials assumed to exhibit ideal surface morphology and chemical purity in accordance with common simulation practice. Surface roughness effects and impurity-related scattering mechanisms were intentionally excluded from the model to isolate the fundamental structure-property relationships.

The scattering characteristics of VO_2 particles embedded within a polydimethylsiloxane (PDMS) matrix were numerically investigated via finite element simulations (COMSOL Multiphysics 6.3). A parametric study was conducted by varying the radius r of the spherical VO_2 inclusions. To ensure computational efficiency while maintaining accuracy, the PDMS domain was bounded by a Perfectly Matched Layer (PML) to truncate the simulation space. This PML configuration effectively suppresses artificial boundary reflections without perturbing the electromagnetic solution within the region of interest, thereby ensuring consistency with results obtained from an unbounded domain. The total scattered energy was quantified through flux integration across a designated monitoring surface. The incident wavefront was modeled as a transverse electromagnetic (TEM) wave propagating along the positive x-axis, with electric field polarization aligned parallel to the z-axis. Symmetry boundary conditions were strategically applied to reduce computational complexity: Perfect Magnetic Conductor (PMC) conditions were enforced on the x-z symmetry plane, while Perfect Electric Conductor (PEC) conditions governed the x-y symmetry plane. These boundary treatments enabled efficient simulation of the periodic scattering system. As schematically illustrated in Figure. S3, the geometric model incorporates randomly distributed VO_2 particles approximated as equivalent spherical scatterers within the PDMS host medium, establishing a representative volume element for analyzing effective scattering responses.

6.3 Result and Discussion

6.3.1 Design Concept and Fabrication of SARCF

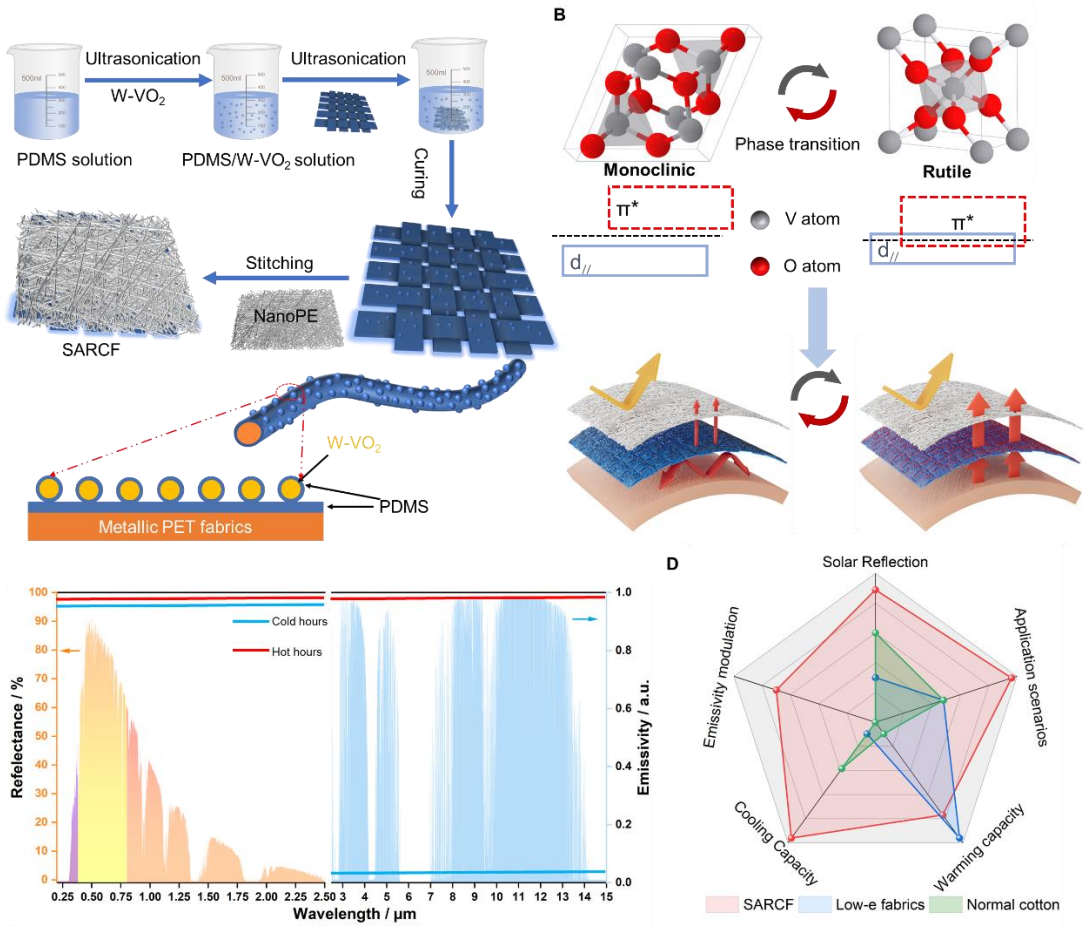

Figure 6. 3 (A) Schematic for fabrication process of SARCF. (B) Schematic for mechanism of the phase induced emissivity modulation process. (C) The ideal spectrum of radiative cooling regulation fabrics. (D) Radar chart for comparison in terms of solar reflection, application scenarios, cooling capacity, warming capacity, and emissivity modulation, among SARCF, low-e fabrics, and normal cotton.

The human body is a significant infrared emitter, radiating energy at an intensity of 70-200 W/m². Effectively managing this radiation is crucial for maintaining thermal comfort. In cold environments, fabrics with low infrared emissivity (high reflectivity) are essential, as they reduce radiative heat loss, helping to keep the body warm. Conversely, in warmer settings, fabrics with high infrared emissivity (low reflectivity) facilitate heat dissipation, keeping the body cool. Given the body's varying thermal

needs across different environmental conditions, fabrics that can adjust their emissivity in response to ambient temperatures are highly advantageous. Ideally, a self-adaptive radiative cooling fabric should maintain high solar reflection regardless of temperature changes, while offering temperature-responsive infrared emissivity—low emissivity in cold conditions and high emissivity in hot conditions (Figure 6. 3C). To achieve this, we propose a straightforward strategy for developing fabrics with self-adaptive radiative cooling regulation (SARCF). SARCF consistently reflects solar radiation while adjusting its emissivity according to temperature changes, thereby catering to the body's dynamic thermal needs in both cold and hot environments. SARCF is fabricated by combining a solar-reflective and infrared-transparent layer (NanoPE) with an emissivity regulation layer (W-VO_2-coated metallic PET fabrics), as illustrated in Figure 6. 3A. The emissivity regulation layer (ERL) is created by depositing W-VO_2 nanoparticles onto metallic PET fabrics using ultrasonication and a PDMS binder. These W-VO_2 nanoparticles undergo a metal-insulator phase transition (Figure 6. 3B), which alters their infrared properties, enabling radiative cooling modulation. With its high solar reflectance and emissivity modulation capability, SARCF outperforms low-emissivity fabrics and conventional cotton in providing thermal comfort across varying conditions (Figure 6. 3D).

6.3.2 Temperature Induced Phase Transition of W-VO_2(M)

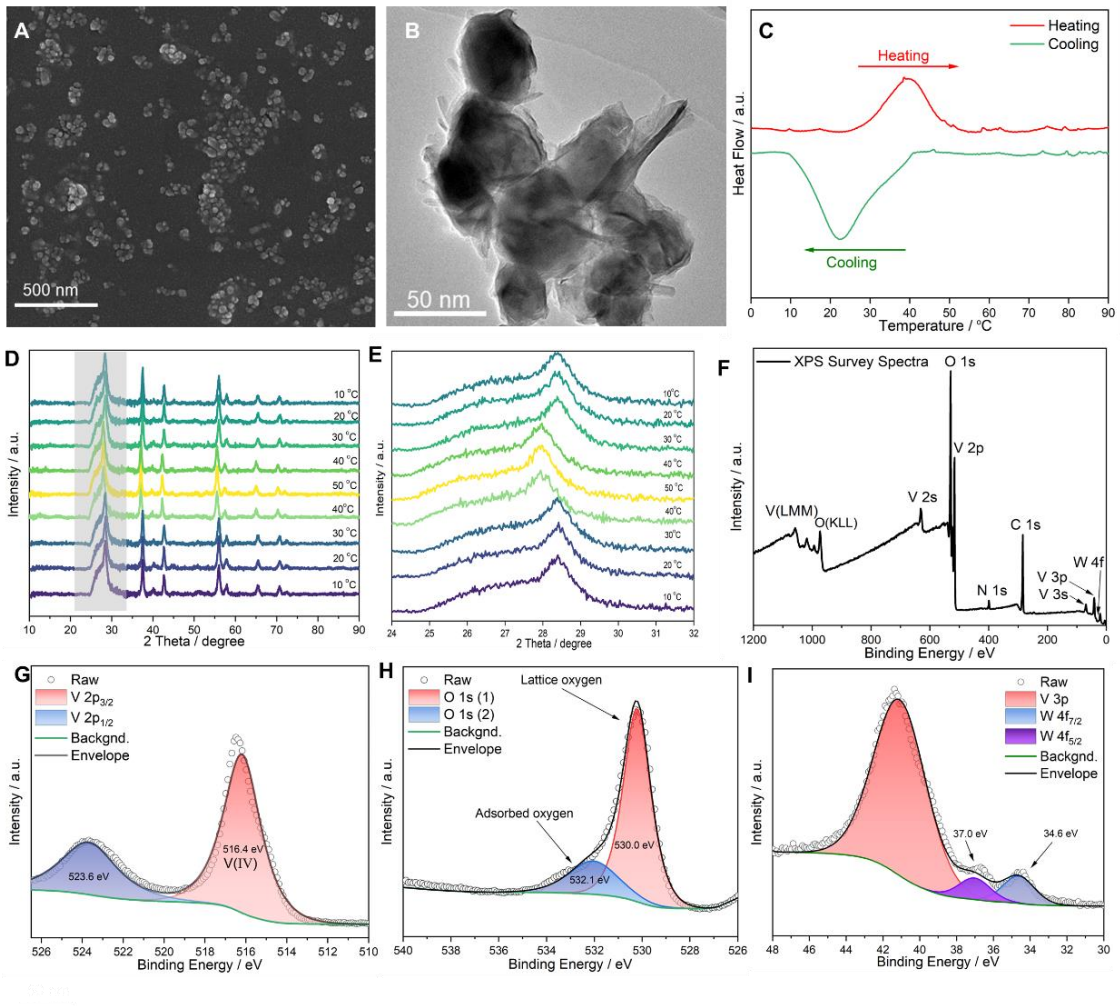

Figure 6. 4 (A)SEM and TEM (B) image of W-VO_2 nanoparticles. (C) DSC curve of W-VO_2 nanoparticles. (D)Temperature-dependent XRD patterns of W-VO_2 nanoparticles in 2 Theta of 10-90^o. (E) Enlarged temperature-dependent XRD patterns of W-VO_2 nanoparticles from 24-32^o. (F) XPS survey W-VO_2 nanoparticles. (G-I) High-resolution scans for V2p, O1s, and W 4f.

Vanadium oxide (VO_2) is a promising candidate for temperature-responsive emissivity modulation due to its metal-insulator phase transition behavior. Notably, its transition temperature can be lowered to near room temperature (~30°C) through element doping, such as with tungsten, fluorine, or magnesium, which is critical for practical applications[251, 266, 303, 304]. As shown in SEM and TEM image (Figure 6. 4A&B), the tungsten-doped vanadium oxide (W-VO_2) nanoparticles have a size range of

approximately 30-50 nm. The DSC curve of W-VO_2 shows endothermic peaks at 39.2°C during heating and exothermic peaks at 21.8°C during cooling (Figure 6. 4C). The transition temperature (~30.5°C) was determined by averaging the temperatures at these exothermic and endothermic peaks, significantly lower than that of undoped VO_2 (~68°C). The near room-temperature transition is considered more suitable for real-world applications. Additionally, the apparent thermal hysteresis observed in the DSC curves indicates the reversible transition of W-VO_2 [305-308]. The XRD patterns (Figure 6. 4D) are well-matched with the standard monoclinic phase (JCPDS No. 43-1051, VO_2(M)). The peak around 28.4°, corresponding to the (011) plane, is a key feature of the monoclinic phase[309]. All other peaks can also be assigned to the standard VO_2(M), no other additional phases were observed. The temperature-dependent XRD (Figure 6. 4D&E) patterns also confirmed the reversible phase transition (from the monoclinic VO_2 (M) phase to the rutile VO_2 (R) phase, as shown in the Figure 6. 3B). A shift of the strongest peak from 28.4° to 27.9° clearly indicates this structural phase transition, where VO_2(M) (011) transitions into VO_2(R) (110)[276]. This is a clear indication of such structural phase transition, in which a VO_2 (M) (011) transit into VO_2 (R) (110). The effect of tungsten doping on the chemical composition of VO_2 was investigated using XPS. All the spectra were calibrated based on the binding energy of 284.8 eV for C1s. As shown in Figure 6. 4F, O1s, V3s, V3p, V2s, V2p, W4f, C1s, and N1s peaks were found in the XPS survey. Despite the binding energy of C1s was used as the reference for calibration, C1s and N1s peak are the contaminates introduced in the measurement process. V2p, O1s, and W4f peak were further deconvoluted in high-resolution spectra for detail analysis, as shown in Figure 6. 4G-I. The fitting process was only conducted on the spin orbital splitting peaks of V2p, despite the scan range spans the O1s (overlapped with the V2p). Due to the O1s was not involved in the fitting process, the peak intensity ratio of $V2p_{3/2}$ and $V2p_{1/2}$ was manually set to 3:1. Consequently, the full width at half maximum (FWHM) of $V2p_{1/2}$ was manually fixed to 1.5 times of that for $V2p_{3/2}$. As shown in Figure 6. 4G, the two spin orbital splitting peaks of V2p ($V2p_{3/2}$ and $V2p_{1/2}$) can be observed, the binding energy of $V2p_{3/2}$ (516.4 eV) was perfectly matched with V(IV). The splitting value

observed (7.2 eV, 523.6-516.4 eV) was also different from that of V metal, which usually exhibited a splitting value of 7.6eV. Therefore, the V(IV) can be confirmed. Two fitting peaks can be found in O1s spectra, one is adsorbed oxygen (532.1 eV, surface contamination), another is attributed to lattice oxygen (530.0 eV, V-O). In the case of W4f, the two orbital splitting peaks of W4f occur at 34.6 ($W4f_{7/2}$) and 37 eV($W4f_{5/2}$), respectively, with a splitting value of 2.4 eV, which is inconsistent with the known splitting value of W metal (2.17eV). This indicates that the existing form of W in the sample is W(VI)[221, 310-312]. Combining the DSC, DSC, XRD, and XPS results, we can rationally conclude that the transition temperature of monoclinic phase VO_2 (M) was successfully lowered to 30.5 ^oC by tungsten doping.

6.2.3 Morphology of SARCF

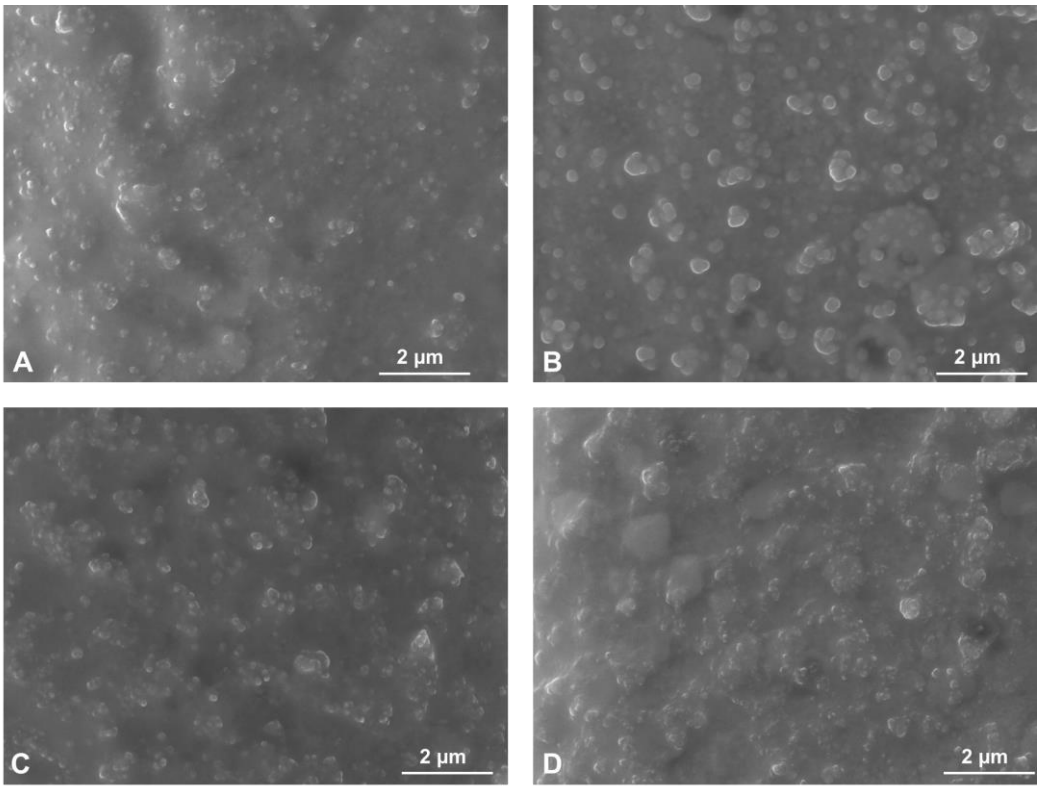

Figure 6. 5 SEM image of ERL1 (A), ERL2 (B), ERL3 (C) and ERL4 (D).

The SARCF is primarily composed of two parts: the emissivity regulation layer (ERL) at the bottom and the solar-reflective yet infrared-transparent NanoPE shelter on top. Digital images of these two layers are shown in Figure 6. 7F. The NanoPE appears

white, indicating its high solar reflectivity. The incorporation of W-VO_2 nanoparticles onto the low-emissivity fabric changes its color to light black. SEM images of NanoPE and ERL are presented in Figure 6. 7A-C, commonly used as a separator in lithium-ion batteries to prevent short circuits, features interconnected porous structures on the nanoscale (50-1000 nm), resulting in over 50% pore volume. These porous structures cause strong Mie scattering in the visible range, leading to high solar reflection while maintaining nearly perfect infrared transmittance. This ensures that the infrared properties of the ERL beneath the NanoPE are preserved, enabling effective radiative cooling. The ERLs were prepared by simple dip coating with the assistance of ultrasound. The SEM images of ERL3 were shown in Figure 6. 7B, continuous coating consisting of W-VO_2 nanoparticles were observed. The particle density of W-VO_2 nanoparticles increased with the increase of W-VO_2 concentrations (Figure 6. 5). However, increasing the concentration of W-VO_2 may cause agglomeration, which leads to the deterioration of emissivity regulation capacity. Elemental analysis via EDS mapping EDS mapping images (Figure 6. 7D-E) detected Si, C, O, Cu, Ni, and V, with Cu and Ni originating from the low-emissivity coating on PET fabrics, Si, C, and O from the PDMS binder, and V and O from the W-VO_2 nanoparticles. Tungsten was not detected in the EDS mapping due to its low doping concentration, though its presence is confirmed by XPS spectra. The cross-sectional image clearly shows low-e-W-VO_2-PDMS coating, which exhibits a thickness of ~3.5 μm (Figure 6. 7C). The EDS mapping of the cross-sectional image was shown Figure 6. 6. Si, C, O, Cu, Ni, and V were found in the EDS mapping, indicating the successful W-VO_2-PDMS coting on low-e fabrics. Due to the strong adhesion of PDMS and limitation on sample preparation for SEM imaging, the boundary between low-e coating and PDMS-W-VO2 is not clear. But the EDS mapping has clearly shown this boundary by the distribution of V and Cu elements. Then SARCF was then fabricated by assembling the ERL and nanoPE via ultrasonic wielding.

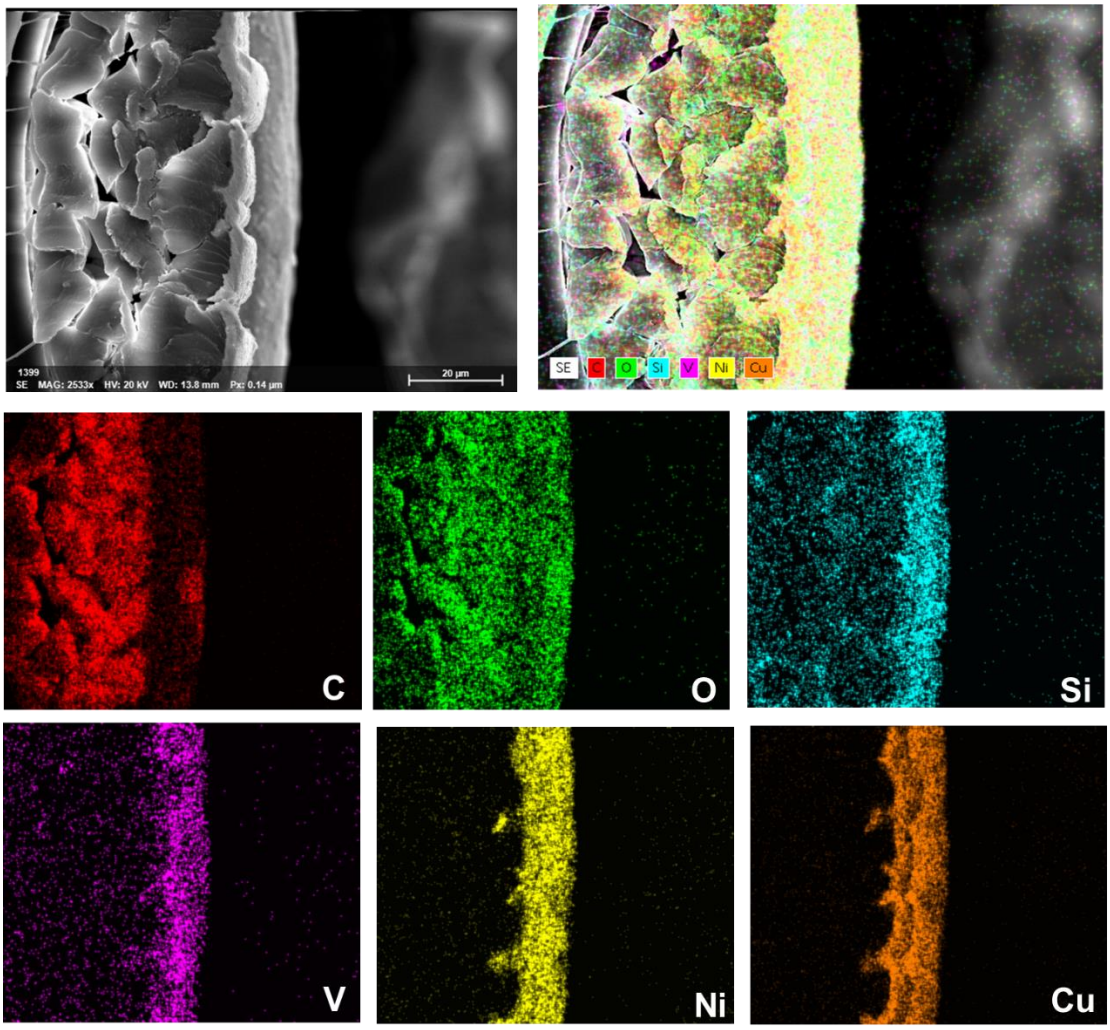

Figure 6. 6 EDS mapping of ERL from side view.

The infrared (IR) properties of SARCF were first demonstrated through IR imaging. For comparison, we selected normal cotton, low-e fabrics, and commercial heat-shielding fabrics (with an emissivity of ~0.56 within the 7-14 μm range). To ensure uniform heating, all samples were placed on a copper plate, which was heated using a temperature-controlled heater. The scale bar was manually set between 20-60°C, with the reference emissivity set to 0.98. One image was taken at room temperature (21°C) without the heater on, followed by IR images taken at 30, 40, 50, and 60°C by adjusting the heater accordingly. As shown in Figure 6. 7G, although the four samples are barely visible at room temperature, normal cotton appears brighter than the other samples. This indicates that the emissivity of cotton (~0.87 within 7-14 μm) is much higher than the other three samples. At 30°C, both the low-e fabrics and SARCF are visibly brighter

than cotton and heat-shielding fabric, indicating lower emissivity. It's worth noting that SARCF appears darker than the heat-shielding fabric, which has an emissivity of 0.56. This suggests that the emissivity of SARCF is lower than 0.56. As the temperature rises to 40°C, SARCF becomes slightly brighter than the heat-shielding fabric but remains darker than cotton, indicating that its emissivity has surpassed that of the heat-shielding fabric while still being lower than cotton. The emissivity changes of SARCF are further confirmed in the IR images at 50°C, where SARCF is clearly brighter than the heat-shielding fabric, revealing its higher emissivity. The same trend is observed at 60°C. Throughout all temperature ranges, the low-e fabrics and cotton remain the darkest and brightest, respectively, indicating their lowest and highest emissivity among the four samples. The relative brightness of SARCF compared to the heat-shielding fabric demonstrates its emissivity modulation capability as the temperature increases. Based on the IR imaging, we conclude that the emissivity contrast induced by the phase change occurs as a gradual process rather than an abrupt one. This transition involves a continuous adjustment from the monoclinic phase to the rutile phase, rather than a sudden change under specific conditions, which aligns with the temperature-dependent XRD patterns. We will further quantify phase-transition-induced emissivity changes in the following section. While this study serves as a proof of concept, SARCF shows potential for scale-up, as demonstrated by the spray-coating process shown in Figure 6. 7H.

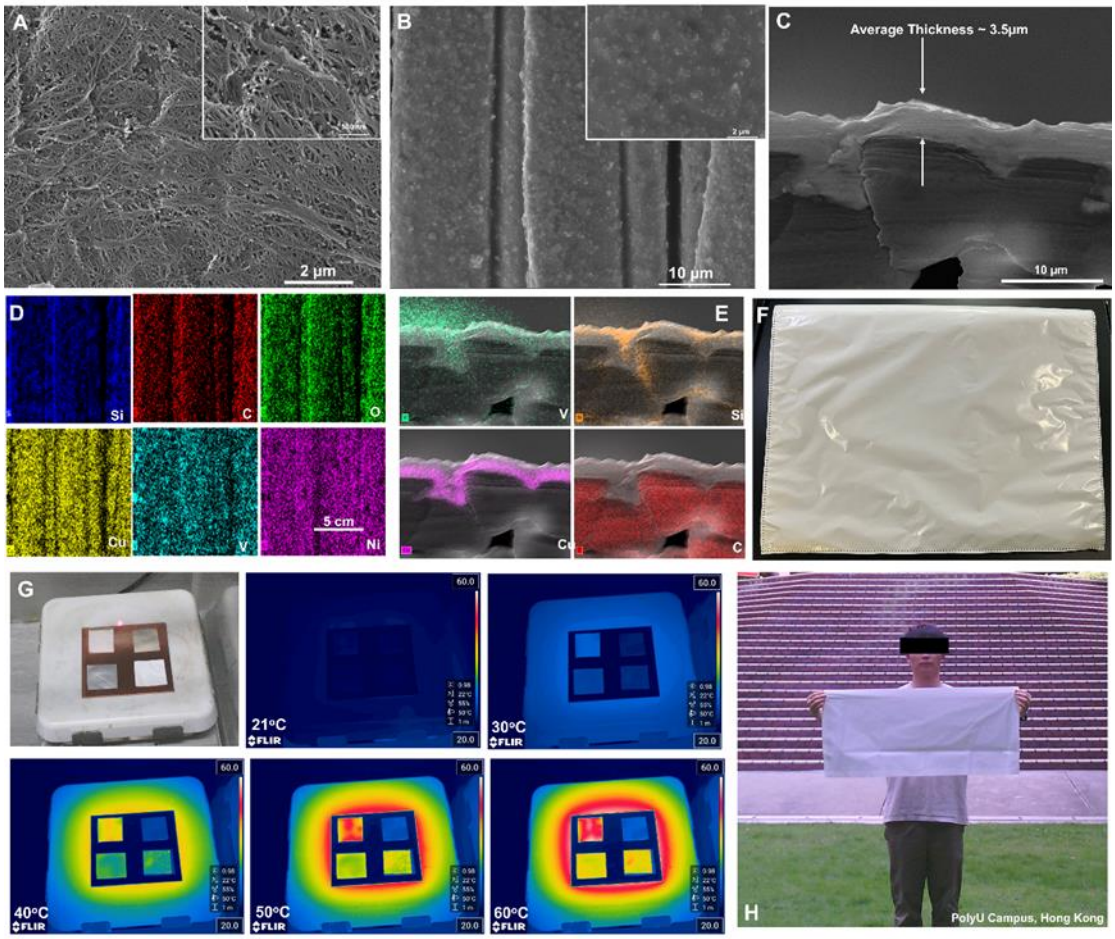

Figure 6. 7 (A-B) SEM images of the front side (NanoPE side) and back side (ERL)of the SARCF. (C) SEM images of ERL from cross-sectional view. (D-E) EDS mapping of ERL. (G) Digital image showing positions of cotton (top right), low-e fabrics (top left), heat-shielding fabrics (low left) and SARCF (low right), and IR images of these four samples at different temperatures (21, 30, 40, 50, and 60oC). (H) Digital image showing the scaling up potential of SARCF.

6.2.4 Temperature-Dependent Optical Properties of SARCF

As discussed before, Nanoporous PE was adopted to provide high solar reflection and thoroughfare for the emission from the ERL. NanoPE exhibited the typical absorption peaks of -CH_2- at 3.44μm (2920 cm^{-1}), 6.8μm (1460 cm^{-1}) and 13.9μm (720cm^{-1}). Apart from these peaks, NanoPE showed high transmittance within other wavelengths. More importantly, these peaks are all outside of the atmospheric window. Such high infrared

transmittance poses little impact on the infrared performance of materials below the NanoPE, thereby, facilitating the observation of emissivity modulation. The NanoPE also functions as the solar shelter for SARCF, providing considerable solar reflectance. The W-VO2 nanoparticle coated low-e fabrics were the key emissivity regulating layer (ERL) for SARCF. Here, we assume that W-VO2 nanoparticles were randomly distributed in the PDMS matrix and coated on the low-e fabrics (Figure 6. 9A, top). The MIR (7-15μm) properties of this structure were simulated at different filling ratio of W-VO2 nanoparticles. The simulation model was shown in Figure 6. 9A (bottom). The simulated MIR reflectance at insulating and metallic states were shown in Figure 6. 9B. It is clear that the emissivity contrast is highly related to the filling ratio. The simulated emissivity contrast increased as the rise of filling ratio. The experimental results (ERL3) seemingly confirmed the simulated results (Figure 6. 9C). The measured solar reflection of ERL experienced a considerable reduction, which is not favorable for radiative cooling applications, compared to the bare low-e fabrics. As shown in Figure 6. 8A, the solar reflection gradually decreased as the increase of W-VO2 content. In visible range, the reflectance of ERLs almost remain unchanged. Meanwhile, ERLs showed temperature-adaptive reflectance in NIR band(1250 nm-2500 nm), where the reflectance decreased when temperature rose up. However, the soar irradiance in 1250-2500nm only accounts for about ~10.9% of the total solar energy, making the solar regulation efficiency limited. In the MIR range, the reflectance of ERLs decreased compared to the initial low-e fabrics due to the introduction of PDMS binder. Importantly, both ERL1, ERL2, and ERL3 showed negative reflectance differences, i.e. positive emissivity contrast (Figure 6. 9D). A broad absorption within the MIR was observed for ERLs at high temperature (Figure 6. 8B), indicating higher emissivity regulation capacity. A maximum emissivity contrast of 36.24% (65.85% of infrared reflectance at 20^{o}C and 29.61% at 60^{o}C) can be achieved for ERL3. It should be noted that the high infrared reflectance of low-e fabric substrate is crucial to achieve negative reflectance difference (i.e., positive emissivity contrast) that meets the concept of radiative cooling regulation. Even though the same fabrication process of ERL3 was applied to bare PET fabrics, negative reflectance difference cannot be obtained (Figure

6. 8C).

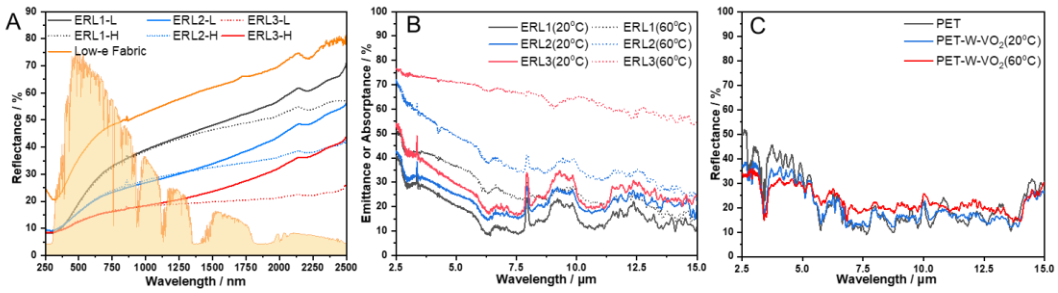

Figure 6. 8 Infrared reflectance of bare PET and PET-W-VO2 at 20 °C and 60 °C.

After the preparation of ERLs, four layers of NanoPE ultrasonically wielded onto the ERLs to construct SARCF. Similar to ERLs, the solar reflection of SARCF decreased with the increase of VO2 content(Figure 6. 9C). Meanwhile, the solar reflection of SARCF1 was 86.80% at 20°C , while this value decreased to 84.78% when W-VO2 transitions to rutile state at 60°C (Figure 6. 9E). SARCF2 and SARCF3 also experienced similar reduction as the rise of temperatures. The limited solar modulation s is due to two fact that 1) the self-adaptive reflectance of ERLs mainly occurred in 1250-2500nm band and 2)NanoPE film is highly solar reflective in this waveband. These will then cause any changes in solar reflectance on ERLs will be invisible for the detector of the spectrometer. Though the solar modulation of SARnoPE. The infrared reflectance of SARCF1, SARCCF is limited, the decent modulation on infrared properties can be reserved due to the high MIR transmittance of NaF2, and SARCF3 at different 20 and 60 °C were shown in Figure 6. 9F. All the SARCFs exhibited different levels of infrared reflectance modulation. Specifically, SARCF1 shows an infrared reflectance of 71.21% at 20°C, while its infrared reflectance falls to 55.29% at 60°C, corresponding to an emissivity contrast of 15.92%. The emissivity contrast increases to 26.51% (an infrared reflectance of 68.50% at 20°C and 41.99% at 60°C) for SARCF2. The maximum emissivity contrast was achieved by SARCF3, which exhibits an infrared reflectance of 60.62% at 20°C and 25.80% at 60°C, corresponding to an emissivity contrast of 34.82%. When focus was put on atmospheric window (8-13μm)

range, the emissivity contrast can be more impressive, reaching up to 38.46%. Further increase in the content of W-VO2 cannot result in high emissivity contrast. The infrared properties of ERL4 and SARCF4 were shown in Figure 6. 9G. Detailly, ERL4 shows an emissivity contrast of 21.93%, which is lower than that of ERL (36.24%). Similarly, the emissivity contrast of SARCF4 was also lower than that of SARCF3, falling from 34.82% to 18.01%. The bottom face of SARCF3 can be considered as ERL3, showing high infrared reflectance (65.85%) at low temperatures and avoiding body heat loss. While it exhibits low infrared reflectance (29.61%) at high temperatures, promoting body heat dissipation. The upper face of SARCF3 were characterized by high solar reflection as well as temperature-dependent infrared optical properties. The solar reflection reaches 85.19% at 20ºC and then decreases to 84.24 % at 60ºC, which makes the daytime radiative cooling possible. More importantly, its infrared emissivity is 39.38% at 20ºC (i.e., infrared reflectance of 60.62%), which is beneficial to maintain the body temperature at cold environment. However, its infrared emissivity then rises to 74.20% at 60ºC (i.e., infrared reflectance of 25.80%), promoting the body heat dissipation. The optical properties of SARCF meet the requirements of wearables in both cold and hot environments, and the transition is induced passively by the ambient temperature without energy input.

Explanation for the modulation

Despite the decent emissivity modulation capacity demonstrated in this study, the detailed mechanism behind this still remains unclear. First of all, there is no doubt that modulation is induced by the temperature. However, the detailed physics of the temperature-induced phase transition still remains unclear. We will not explore the detailed physics about the phase transition, but a brief explanation for the experimental results obtained in the study. From previous research, the most widely accepted one is a multilayer model, i.e., Fabry-Perot resonator, which consists of a bottom reflective layer (usually metal), a dielectric layer and VO_2 layer. Specifically, the infrared property of the F-P structure was determined by the bottom reflective layer when the temperature is below the phase transition temperature as the VO2 layer is transparent to infrared at

this phase. While the temperature is above the phase transition temperature, the bottom reflective layer, and the dielectric layer and the top metallic VO_2 layer can be considered as a typical F-P cavity, which leads to strong absorption enhancement at certain wavelengths due to interference. Tang's work has clearly demonstrated constructive interference and destructive interference at certain wavelengths in a VO_2 based F-P resonator theoretically and experimentally. It should be noted that VO2 was considered a pure thin film their demonstration. However, randomly distributed VO_2 particles in PDMS matrix might be the most appropriate model to describe the real situation in this study. The broadening of the absorption peaks in the metallic W-VO_2/PDMS composite film at elevated temperatures may arise from the size-dependent localized surface plasmon resonance (LSPR) characteristics of the embedded W-VO_2 particles. As evidenced by the extinction cross-section analysis (Figure 6. 9H), the LSPR peak of metallic VO_2 particles exhibits a pronounced redshift with increasing particle size, transitioning from 600 nm (near-infrared, NIR) for 50 nm-radius particles to 7.5 μm (mid-infrared, MIR) for 1000 nm-radius particles. This polydispersity in particle dimensions within the composite system leads to spectral overlap of resonant absorption bands across distinct size populations, consequently resulting in a broadened absorption profile spanning both NIR and MIR regions under thermal activation conditions. We can also observe the increased absorption and scattering within 7-15 μm when the temperature was elevated (Figure 6. 9I). The amplified scattering events induce multiple light-particle interactions, effectively elongating the optical path length and promoting energy dissipation through cumulative optical losses. Critically, the PDMS matrix exhibits intrinsic strong absorption across this spectral range, ensuring efficient capture of the scattered radiation. Concurrently, the metallic VO_2 particles themselves demonstrate intrinsic absorption in the MIR region due to their characteristic electronic and lattice vibrational transitions. The combined effects of (1) PDMS-mediated absorption of scattered photons and (2) direct MIR absorption by metallic VO_2 collectively drive a pronounced broadband absorption enhancement in the 7–15 μm range. The amplified scattering and absorption mechanism and red shift of LSPR peak under thermal activation led to the considerable emissivity contrast

achieved in this study.

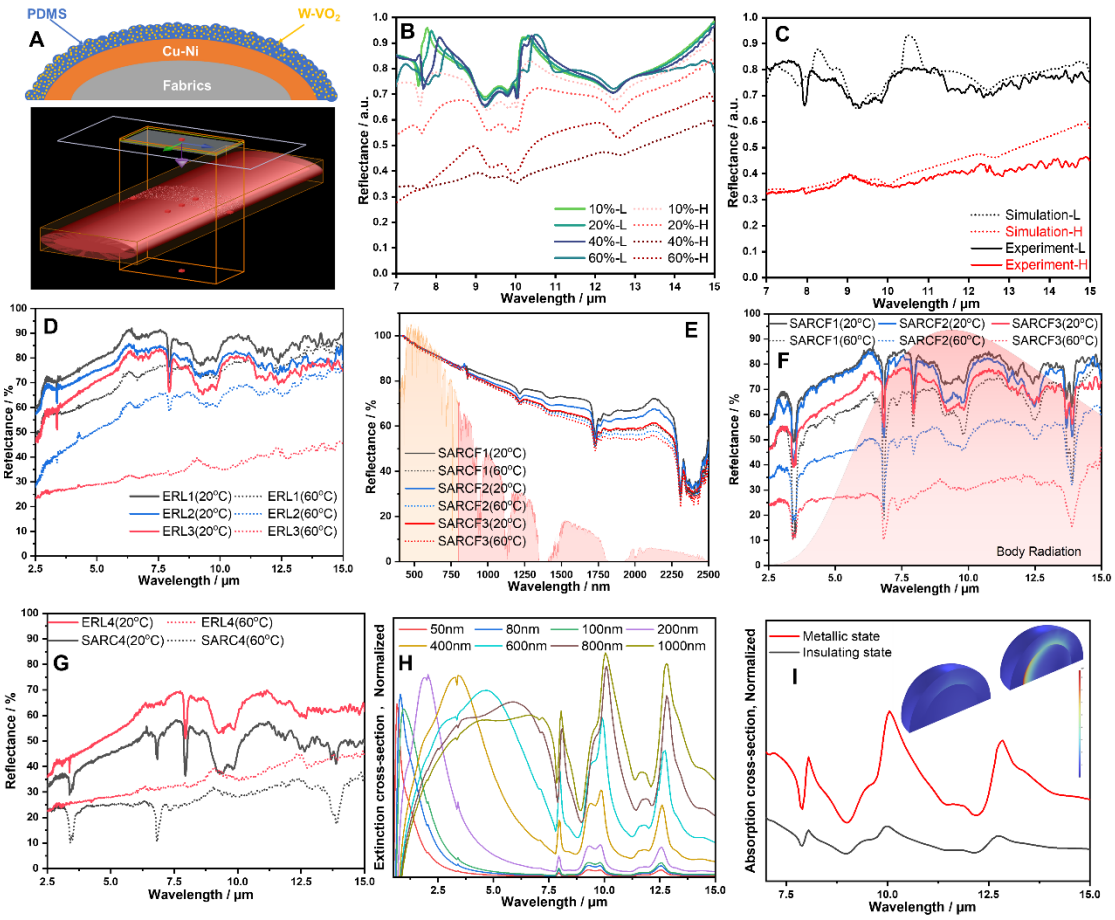

Figure 6. 9 (A) Schematic of the ERL model for FDTD simulation. (B)simulated MIR reflectance at different fill rate of W-VO_2. (C) Simulated(dash line) and experimental (solid line)reflectance of ERL3 at 20°C (black) and 60°C (red) . (D) The infrared reflectance of ERL1, ERL2 and ERL3 at 20°C (solid lines) and 60°C (dash lines). (E) The solar reflectance of SARCF1, SARCF2, and SARCF3 at 20°C (solid lines) and 60°C (dash lines). (F) Infrared reflectance of SARCF1, SARCF2, and SARCF3 at 20°C (solid lines) and 60°C (dash lines). (G) Infrared reflectance of ELR4 at 20°C (solid lines) and 60°C (dash lines). (H) Normalized Extinction cross section of W-VO_2 particles at different radius. (I)Normalized absorption cross section of W-VO2 (800nm)in PDMS matrix(inserted figure, loss power density at insulating and metallic state).

6.2.5 Thermoregulatory Performance of SARC in Different Environments

The optical properties of SARCF suggest strong thermal management potential in both cold and hot environments. To evaluate its thermal performance, tests were conducted in two typical environments: outdoor and indoor, using custom-built devices (Figure 6. 10A&B). For comparison, two common textiles were selected: commercial white cotton and low-e fabrics. The low-e fabrics exhibit a solar reflectance of 47.05%, nearly zero solar transmittance, and an infrared reflectance of 99.23%. In contrast, the commercial white cotton shows a solar reflectance of 67.62%, a solar transmission of 27.08%, and an infrared emissivity of 77% within the 2.5-15 μm range. SARCF3 was chosen for thermal measurements due to its maximum emissivity contrast. All textile samples were integrated into similar measurement setups, which included a skin simulator, a PT100 temperature sensor (adhered to the upper surface of the skin simulator to monitor its temperature in real-time), and insulating foam. The skin simulator was carefully designed, with a copper plate used as the heat diffuser and thermal grease filling the space between the copper plate and the heater to ensure effective heat transfer. To simulate the optical properties of human skin, a 3M skin-color tape was applied to the copper plate. The final skin simulator exhibited a solar reflectance of 47.58% and an infrared emittance of 87.84% (Figure 6. 2), closely matching the properties of real skin. To simulate the metabolic heat production rate of human skin, a constant input power of 150 W/m² was applied to the heater. The electrical resistance of the heater was strictly controlled at 17.5±0.1Ω to ensure that any temperature differences were due to the optical properties of the textiles rather than variations in input power. The PT100 temperature sensors were calibrated before use to ensure accurate temperature readings.

As shown in Figure 6. 10B, the outdoor test was conducted in 24, July 2024, a cloudy day in Hong Kong. During the test, moisture levels around the experimental setups were recorded (Figure 6. 10C). The peak solar irradiance reached 1199 W/m², and the highest ambient temperature recorded was 39.5°C at 11:45 AM and 11:50 AM, respectively. The average ambient temperature during the monitoring period was 35.7°C. As shown in Figure 6. 10D&E, As illustrated in Figures 6.10D&E, the skin simulator covered with

SARCF exhibited the lowest surface temperature among the three textiles tested. The surface temperature of the skin simulator was closely related to the solar irradiance, indicating that the solar reflectance of the fabrics played a dominant role in determining the localized thermal microenvironment.

The low-e fabrics, with the lowest solar reflectance (47.05%), resulted in the highest surface temperature, exceeding 100°C with a peak of 102.3°C. This extreme temperature was due to the fabric's high solar absorption (52.95%) and high infrared reflectance, which together caused significant solar heating while also preventing the loss of infrared radiation from the simulator. Such performance is unsuitable for wearable applications, even without considering the body's natural cooling mechanisms like sweating. In comparison, the skin simulator covered with white cotton had a much lower surface temperature than that covered with low-e fabrics. This difference is attributed to white cotton's lower solar absorption (5.3%), with a solar reflectance of 67.62% and solar transmission of 27.08%. However, the solar transmission through the cotton also contributed to photothermal effects on the skin simulator's surface, raising the temperature. Despite this, the peak surface temperature for the cotton-covered simulator still reached 73.2°C, suggesting that white cotton may not be the best option for outdoor daytime wear. The SARCF-covered simulator exhibited an even lower surface temperature than the white cotton throughout the test, primarily due to its high solar reflectance (85.19%) under sunlight. Given that the ambient temperature was consistently above 30°C, SARCF was in a high-emissivity state, promoting body heat loss through infrared radiation. The peak surface temperature for the SARCF-covered simulator was 65.3°C, significantly lower than those for low-e fabrics (102.3°C) and white cotton (73.2°C). Despite the average surface temperatures of all simulators being higher than the ambient temperature (35.74°C), the SARCF-covered simulator maintained the lowest average surface temperature at 51.60°C, compared to 76.67°C for low-e fabrics and 56.27°C for white cotton (Figure 6. 10F). This indicates that SARCF may be a superior choice for maintaining thermal comfort during outdoor daytime conditions compared to low-e fabrics and commercial white cotton.

Similar setups were used to further evaluate the thermal performance of SARCF during cold hours. The skin simulators were covered with SARCF, low-e fabrics, and white cotton. Initially, the surface temperature of each skin simulator was stabilized at room temperature (22°C). The entire setup was then transferred to a refrigerator with an ambient temperature of 5°C to simulate cold conditions. As shown in the Figure 6. 10G, the surface temperatures of the skin simulators covered by SARCF, low-e fabrics, and white cotton stabilized at 37.8°C, 34.8°C, and 33°C, respectively, in the room environment. In the absence of solar irradiance indoors, the surface temperature of the skin simulators was primarily determined by the infrared properties and thermal conductivity of the fabrics. The skin simulator covered by white cotton stabilized at 33.1°C, while the one covered by low-e fabric stabilized at 34.8°C, which is 1.7°C higher than the cotton-covered simulator. This difference is due to the higher infrared reflectance of the low-e fabrics, which prevents radiation loss to the environment. In contrast, commercial white cotton, an emissive radiative cooling textile, promotes heat loss from the skin simulator. The thermal conductivity is also a crucial factor. The low-e fabric can be considered as an excellent conductor for heat, as a result, the heat generated by the skin simulator can be easily transfer to the upper surface. Then such heat can be dissipated into ambient through thermal convection. Thermal conductivity is another critical factor. The low-e fabric, an excellent heat conductor, easily transfers heat from the skin simulator to its upper surface, where it dissipates into the ambient environment through convection. White cotton, with lower thermal conductivity, provides better warmth compared to low-e fabrics by reducing heat loss through conduction and convection. Consequently, the warming effect of low-e fabrics via infrared reflection is offset by the cooling effect from thermal conduction and convection. Similarly, SARCF's warming effect is enhanced by its lower thermal conductivity, which results from air gaps between the emissivity regulation layers (ERLs) and the NanoPE, as well as the nanopores within the NanoPE. As a result, the stabilized surface temperature of the SARCF-covered simulator was higher than that of the low-e fabrics at room temperature (22°C), reaching 37.8°C. When the setups were

transferred to the refrigerator, the ambient temperature quickly dropped to 5°C. However, the temperature detected inside the thermal insulation foam box stabilized at 11°C. This discrepancy is likely due to the insulation foam acting as a thermal barrier, creating a thermal equilibrium between the box and the refrigerator's ambient temperature. After being transferred to the refrigerator, the surface temperatures of all skin simulators gradually decreased, reaching 23.4°C (low-e fabrics), 22.3°C (SARCF), and 21.2°C (cotton). These results initially seem to conflict with the previous conclusion that SARCF's warming effect is enhanced by its lower thermal conductivity. However, the reduced final stabilized temperature of the SARCF-covered simulator compared to the low-e fabrics is likely due to stronger thermal convection in the room environment, which is less pronounced in the refrigerator. In the confined space of the refrigerator, infrared radiation becomes the dominant heat transfer mechanism. Thus, the skin simulator covered by low-e fabrics exhibited a higher final stabilized surface temperature due to its high infrared reflectance. Despite this, SARCF still outperformed white cotton under these conditions.

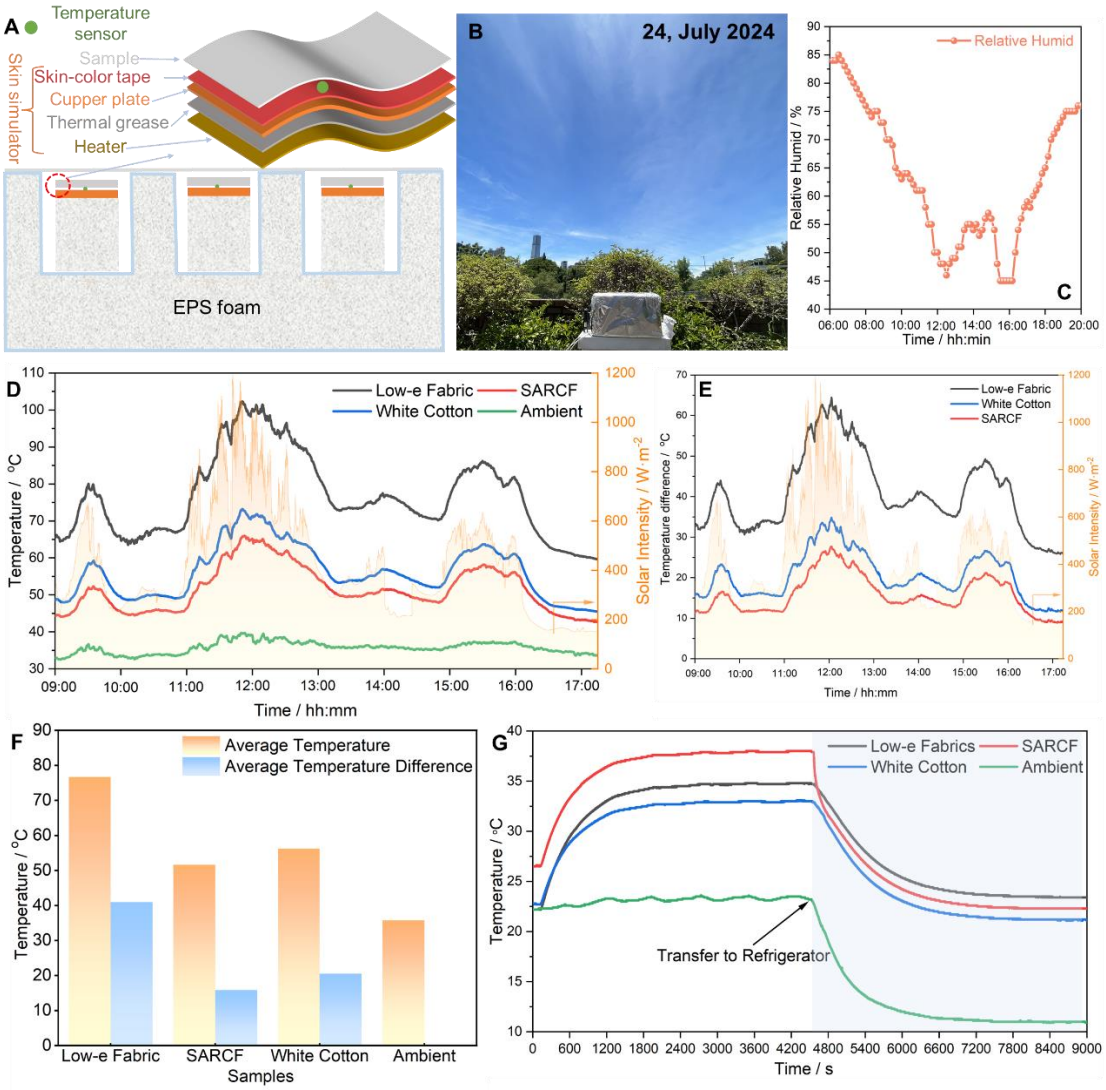

Figure 6. 10 (A) Schematic of setups for the outdoor test indoor test and the multilayer structure of the skin simulator. (B) Sky images when conducting the outdoor test. The test was conducted on 24, July 2024. (C) Relative humidity when conducting the outdoor test. (D) The real-time surface temperature of the skin simulator during the outdoor test.

6.4 Conclusion

In this study, we introduced the novel concept of self-adaptive radiative cooling fabrics. As a proof of concept, we developed emissivity regulation layers (ERLs) by depositing W-VO_2 nanoparticles onto low-emissivity fabrics. The ERL3 sample achieved a maximum emissivity contrast of 36.24%, driven by the phase transition of W-VO_2. At 20°C, ERL3 exhibited an infrared reflectance of 65.85%, effectively reducing body heat loss through radiation. However, at 60°C, this reflectance decreased to 29.61%, promoting heat dissipation via radiation. Thus, ERL3 (the skin-facing side of SARCF3) meets the infrared properties required for textiles in both hot and cold conditions. After integrating ERL3 with NanoPE, SARCF3 demonstrated both high solar reflectance and temperature-dependent emissivity. Specifically, SARCF3 achieved a maximum solar reflectance of 85.19% and an emissivity contrast of 34.82%, enabling effective manipulation of radiative cooling through emissivity modulation. In both outdoor and indoor tests, SARCF3 outperformed low-emissivity fabrics and white cotton in terms of warming and cooling performance. Under strong solar irradiance, the average surface temperature of the skin simulator covered by SARCF3 was 25.07°C, which is 4.67°C lower than that of low-emissivity fabrics and white cotton. In cold environments, the skin simulator with SARCF3 reached a stabilized surface temperature of 37.8°C, 3.0°C higher than low-emissivity fabrics (34.8°C) and 4.8°C higher than white cotton (33.0°C). Overall, this study demonstrates the feasibility of applying self-adaptive radiative cooling regulation to textiles, paving the way for more intelligent personal thermal management solutions. However, biosafety of the vanadium, washing durability and wearing comfort deserves further exploration in the future.

Chapter 7 Flame-Retardant Transparent Wood with Enhanced Mechanical Performance via Bio-Based Co-Curing Agent

7.1 Introduction

Nearly every sector of global industry needs a green revolution in energy and material consumption to address current sustainability challenges, i.e., the overexploitation and excessive use of nonrenewable resources, along with the resulting environmental impact and inefficient energy consumption patterns in modern industrial processes [162, 313]. In this context, wood, a renewable natural resource with a long history of use, has garnered significant interest from researchers worldwide. Wood has been extensively utilized for structural, aesthetic, and energy purposes throughout human history due to its ease of processing, wide availability, low thermal conductivity, excellent mechanical performance, and combustibility. Recent advancements in wood research have led to the development of transparent wood (TW), presenting a promising opportunity for smart and energy-efficient building construction that fulfils global net-zero targets[7, 8, 166, 170].

TW is a composite material that is typically prepared through a discoloration process (such as delignification or lignin modification), followed by impregnation with a polymer that matches the refractive index of wood[3-5]. The use of wood as the base material affords an energy-saving potential, that makes it a more environmentally friendly option compared to other glazing materials[4]. While initial TW substrates have shown promise as candidates for energy-saving applications, the inherent flammability of wood-based systems as well as the impregnating polymer, poses significant fire risks that could cause potential injury and fatalities[314]. Therefore, it is critical to develop additives that can mitigate these inherent flammability risks for TW to be viable for future mass adoption in real-world applications. One approach to create flame-retardant TW (FRTW) is by adopting fire-resistant polymers. For instance, Chen et al.[179] incorporated polyimide (PI) into delignified wood (DW) slices to fabricate FRTW, while Samanta et al.[141] used melamine formaldehyde (MF) resin as the impregnating polymer. However, most current polymers, including polymethyl

methacrylate (PMMA) and epoxy resin (EP)—the commonly used polymers for TW fabrication—are combustible[30]. There is still considerable room for improvement in enhancing flame retardancy for TW made from such combustible polymer additives. Another approach to improve the fire safety of TW is the incorporation of flame retardants (FRs), typically added to a liquid monomer mixture and impregnated into the wood structure, followed by polymerization. Samanta et al.[178] prepared FRTW with silica nanoparticle (SiNP; ~30 nm, carrying positive charge) infused into nanostructured cell walls at pH 8.5. The prepared FRTW also showed improved fire safety. However, challenges with this method include inhomogeneous particle distribution and agglomeration, which can deteriorate mechanical properties[130]. Additionally, poorly-matched refractive indices of the FR additives to the TW substrate can significantly reduce visible transparency of the system[153]. Physical embedding of FRs into the TW matrix may also lead to leaching problems. Therefore, integrating FRs into the TW matrix through chemical bonding, rather than physical mixing, could offer a more effective solution to avoid issues such as incompatibility, agglomeration, and leaching[315].

Grafting FR into the TW matrix via chemical bonding requires active sites to form covalent bonds. Among the polymers used in fabricating TW, EP stands out as one of the most promising candidates for integrating FR components due to its epoxy functional groups, which provide ample active sites for chemical binding. Therefore, incorporating environmentally friendly and highly efficient phosphorus containing FRs into the EP crosslinking network represents a promising approach to enhance the fire safety of TW prepared from EP.

DOPO-ITA is a bio-based phosphorus-containing FR synthesized through the Michael addition reaction of bio-derived ‘itaconic acid’ (ITA) with ‘9,10-dihydro-9-oxa-10-phosphaphenanthrene 10-oxide’ (DOPO). DOPO-ITA, with its combination of carboxyl and phosphaphenanthrene groups, can thus serve as a potential FR co-curing agent for EP systems[316, 317]. Additionally, the presence of a biphenyl group in the

DOPO-ITA structure suggests the likelihood of π-π interactions, which may act as sacrificial bonds, providing in-situ strengthening and toughening effects[318]. The integration of DOPO-ITA into the TW matrix is also a solvent-free process[319]. All these attributes together not only position DOPO-ITA as a promising candidate for fabricating high-performance, fire-retardant TWs but also ensure a more facile and sustainable manufacturing process.

In this study, we report a facile and solvent-free process to prepare FRTW by integrating DOPO-ITA into the TW matrix. DOPO-ITA was successfully grafted onto epoxy molecular chains through solvent-free polymerization. FRTW was then fabricated by lignin-modified wood, followed by impregnation with the DOPO-ITA modified epoxy precursor. We investigated the optical, mechanical, and fire performance properties of the prepared FRTW. The potential FR and strengthening mechanisms of DOPO-ITA were also proposed, involving the introduction of phosphorus-containing groups and π-π stacking interactions within the matrix. Overall, the prepared FRTW demonstrated excellent performance, combining high fire safety with significantly improved mechanical properties. This study provides a facile and environmentally friendly approach to fabricating TW with enhanced fire safety, directly addressing the fire safety concerns associated with normal TW compositions.

7.2 Experimental Section

7.2.1 Materials and chemicals

Balsa wood with average density of 180-230 kg/m^3 was purchase from Zhuhai DECHI Technology Co.,Ltd. The wood was cut into 3 cm × 3 cm × 1 mm strips alongside the growth direction. E51 epoxy and D230 curing agent were offered by Jiangsu LvXun Co.,Ltd. 9,10-Dihydro-9-oxa-10-phosphaphenanthrene 10-Oxide (DOPO) and Itaconic acid (ITA) were provided by Aladdin. Sodium silicate, sodium hydroxide (NaOH), magnesium sulfate ($MgSO_4$), hydrogen peroxide (30wt%), and diethylenetriaminepentaacetic acid (DTPA) were bought from Macklin. All chemicals were used without further purification and deionized (DI) water (18 MΩ) used, in all

cases.

7.2.2 Preparation of DOPO-ITA

The synthesis of DOPO-ITA was conducted using a modified procedure based on previous reports[316]. Briefly, DOPO (0.1 mol, 216.7 g), itaconic acid (0.1 mol, 130.1 g), and xylene (500 mL) were heated and stirred in a three-necked flask at 130°C under a nitrogen atmosphere for approximately 6 hours, then allowed to cool to room temperature. The resulting DOPO-ITA product was washed three times with acetone. Finally, the solid DOPO-ITA powder was obtained by drying in a vacuum oven at 80°C for 24 hours, with a yield of approximately 72%.

7.2.3 Preparation of flame-retardant transparent wood (FRTW)

The flame-retardant epoxy precursor was produced through a straightforward, solvent-free polymerization method. The DOPO-ITA and E51 were added into a 3-necked round-bottomed flask under continuous stirring. The detailed formulas of the reaction are listed in Table 7. 1. Then the mixture was reacted under N_2 for 20 min at 160ºC. The disappearance of white powder indicates the complete integration of DOPO-ITA into the epoxy precursor. The balsa wood was cut into 3 cm × 3 cm slices with the thickness of 1.5 mm. The preparation of TW follows previous reports with few modifications[7, 320]. The lignin modification solution (DI water as solvent) was prepared by mixing following chemicals: sodium silicate (3.0 wt%), sodium hydroxide (3.0 wt%), magnesium sulfate (0.1 wt%), and diethylenetriaminepentaacetic acid (0.1 wt%), hydrogen peroxide (8.0 wt%). The balsa strips were immersed in the prepared solution and maintained at 70 ºC for around 2 hours. Then the white wood strips (lignin modified wood, LMW) were washed several times with DI water before being stored in ethanol for further use. The lignin modified wood strip was immersed into the above mixture under vacuum for 10 mins. To ensure the complete infiltration, the gassing-degassing process was repeated three times. After this, the fully infiltrated wood strips were sandwiched between two slices of PET film and allowed to cure at room temperature for 48 hours. For brevity, the cured flame-retardant transparent wood was

marked as FRTW“X”, where X indicates the addition of content of DOPO-ITA. The prepared formulas for TW and FRTWs are listed in Table 7. 1. Note that the amount of D230 curing agent was slightly modified since the integration of DOPO-ITA slightly changed the content of the active hydrogen content in the epoxy precursor. The addition of D230 curing agent was calculated based on principle that there should be a 1:1 molar ratio between the epoxy and the active hydrogen in a curing system[321]

Table 7. 1 The total preparation formulas EP, FREP, TW and FRTWs

Samples	E51 / g	D230 / g	DOPO-ITA / g	Wood framework (Y^b/N^c)
EP	80.00	24.00	\ [a]	N
FREP	80.00	18.14	16.00	N
TW	80.00	24.00	\	Y
FRTW5	80.00	22.13	4.00	Y
FRTW10	80.00	20.80	8.00	Y
FRTW20	80.00	18.14	16.00	Y

[a]: Not appliable

[b]: Lignin modified wood involved.

[c]: Lignin modified wood not involved.

7.2.4 Characterization

The morphologies of the samples were observed by Field Emission Scanning Electron Microscope (SEM, Tescan MAIA3). All the samples were sputtered with a thin layer of gold before observation. The transmittance spectra of samples across 200 nm to 800 nm were collected by Cary 300 Conc UV-Vis Spectrometer with a 150 mm of integrating sphere at a step size of 1 nm. The haze was also measure by Cary 300 Conc UV-Vis Spectrometer based on ASTM D 1003:2007. XRD patterns were acquired using the Rigaku SmartLab 9kW instrument, spanning a range of 20-80° with a step size of 0.02° and a scan rate of 10°/min in 2 theta mode, while maintaining a glancing

angle of 2°. The cone calorimeter (cone) test adhered to ISO 5660 standards and was conducted using equipment from Fire Testing Technology. Samples sized at 100 × 100 × 3 mm^3 were subjected to an external heat flow of 35 kW/m^2. For the vertical burning test, a laboratory-assembled UL 94 vertical flame chamber was utilized in accordance with ASTM D3801 guidelines. Samples measuring 130 × 13 × 3.2 mm^3 were evaluated. The limiting oxygen index (LOI) was measured using a JF-3 type instrument from Jiangning Analysis Instrument Co., China, following ASTM D2863 specifications. Specimens with dimensions of 100 × 6.5 × 3.0 mm^3 were used for these measurements. The vertical burning test was performed in a laboratory-assembled UL 94 vertical flame chamber according to ASTM D3801, with sample sizes of 130 × 13 × 3.2 mm^3. Thermogravimetric analysis (TGA) was carried out using the PerkinElmer TGA 4000 System, where samples weighing 1-5 mg were heated from 25°C to 800°C at a rate of 10°C/min under an airflow of 50 mL/min. Fourier-transform infrared spectroscopy (FTIR) was performed using a Thermo-Scientific Nicolet IS50 Spectrometer in ATR (Attenuated Total Reflectance) mode, with a resolution set to 4 cm^{-1}, and 32 scans were collected in total. Raman spectra were obtained using the Renishaw Micro-Raman Spectroscopy System. The laser (785 nm) power was set to 10 mW, and a total of 3 scans were collected. Any cosmic rays were removed before the fitting. The multiple-peaks fitting was conducted based on Gauss model by Original Pro 2021. The tensile strength was measured on INSTRON 5566 with a stretching rate of 10 mm/min. The sample size was 15 × 100 × 1.5 mm. Thermogravimetric analysis/infrared spectrometry (TG-IR) was performed using a TGA 4000 thermogravimetric analyzer (PerkinElmer), which was connected to a Spectrum Two FT-IR spectrophotometer (PerkinElmer) via a stainless-steel transfer pipe. The samples were heated from 30°C to 800°C at a heating rate of 20°C/min under a nitrogen flow of 20 mL/min.

7.3 Results and Discussion

7.3.1 Fabrication and characterization of FRTW

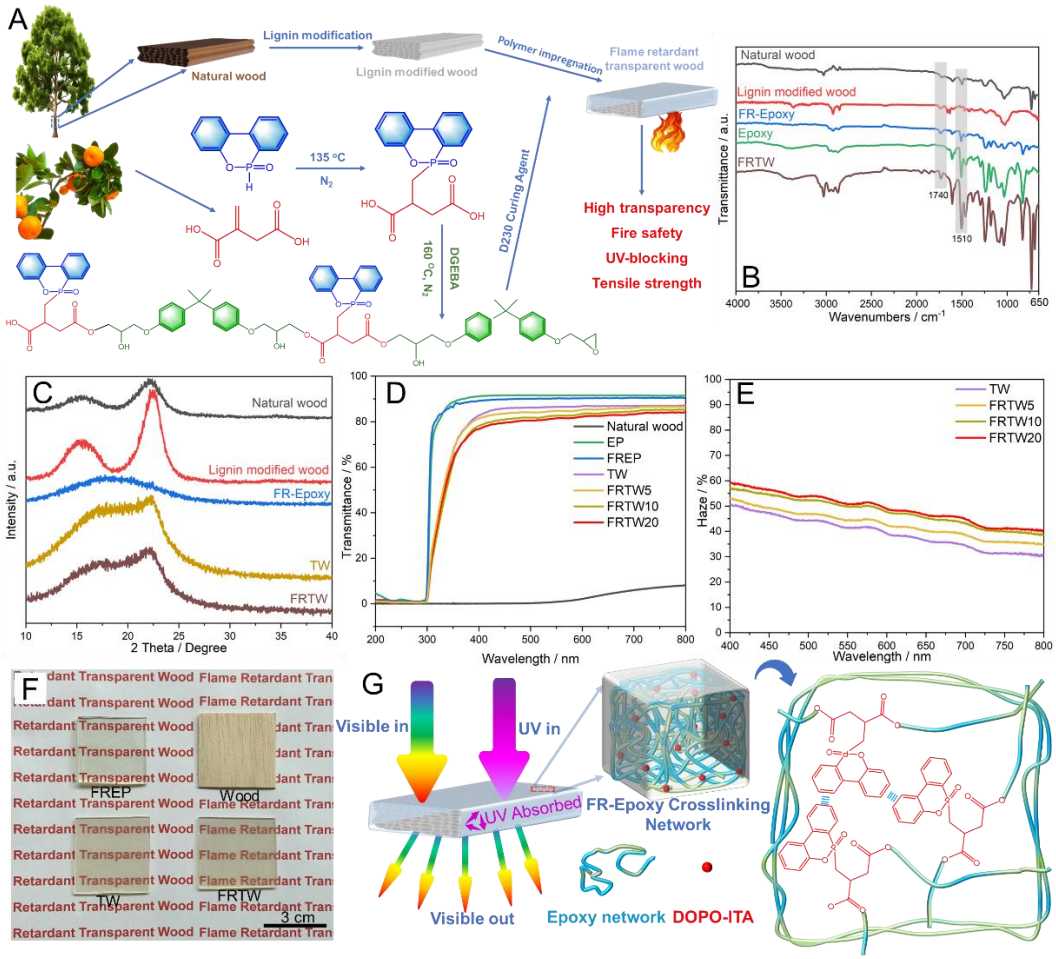

Figure 7. 1 A) Schematic illustration of the preparation of FRTW. B) FTIR spectra of natural wood, lignin modified wood, EP, FREP, and FRTW. C) XRD patterns of wood, lignin modified wood, FREP, and FRTW. D) Transmittance of Natural wood, EP FREP, TW, FRTW5, FRTW10 and FRTW20 crossing 200-800 nm. E) Haze of TW, FRTW5, FRTW10 and FRTW20 crossing the visible range (400-800 nm). F) Digital photo of FREP, wood, TW, and FRTW20. G) Schematic illustration of the chemical bonding of DOPO-ITA into epoxy crosslinking network.

The typical preparation process of FRTW was illustrated in Figure 7. 1A. The flame retardant co-curing agent (DOPO-ITA) was prepared from the Michael addition reaction between DOPO and ITA. It can be considered as FR co-curing agent for epoxy curing system due to the existence of carboxyl and phosphaphenanthrene groups[322]. Also, the biphenyl group in the structure of DOPO-ITA is also thought to provide a

strengthening effect due to the π-π interactions[323]. DOPO-ITA also shows a limited effect on the inherent transparency of epoxy due to the fact that it is chemically bound to the epoxy crosslinking network. Therefore, the DOPO-ITA shows great potential to prepare transparent FRTW with enhancement on mechanical properties. Frequently, FR additives result in a significant decrement in TW optical properties. Notably, the bonding process of DOPO-ITA is a solvent-free polymerization, which can be regarded as a "green chemistry" process[324]. FTIR analysis of the different composite conditions highlights the resultant differences.

The peak at 1740 cm-1 ((δ (C=O), stretching vibration) cannot be observed in the original epoxy, while this peak occurs in the spectra of FREP (Figure 7. 1B). This indicates the successful chemical integration of DOPO-ITA into the epoxy crosslinking network. Then, the DOPO-ITA integrated epoxy was used to prepared TW. The natural wood was decolored by a lignin modification process, during which most of chromophore in lignin structure were destroyed, while the benzene-based structure in the lignin was reserved[320, 325]. This can be indicated by the reservation of the peak at 1510 cm^{-1} (skeletal vibration of δ(C=C) in phenolic ring of lignin) in the FTIR spectra (Figure 7. 1B).

The XRD patterns of natural wood, lignin modified wood, FREP, TW, and FRTW are shown in Figure 7. 1C. There are no significant changes after lignin modification for natural wood. The XRD pattern of FREP shows no crystalline peak, indicating an amorphous structure. TW and FRTW also show an amorphous character, with only two broadband diffraction peaks at 2θ = 17° and 22º observable. Apparently, DOPO-ITA shows limited effect upon the amorphous structure of EP, which is also the main reason for retention of the high optical transparency[326]. As shown in Figure 7. 1D&E, the transmittance and haze of TWs prepared from EP and FREP were characterized by UV–visible spectrophotometry. Natural wood shows a close-to-zero transmittance at 550 nm (T_{550}) based on lignin absorption of light. The EP alone shows the highest recorded transmittance (91.6%) at 550 nm, while the transmittance of FREP was slightly

decreased, down to T_{550} of 90.3%. TW prepared from the original EP shows a T_{550} of 86.5%, while T_{550} of FRTW5, FRTW10, and FRTW20 fell to 84.7%, 82. 7%, and 81.6% respectively. These figures are higher than reports from previous works indicating greater optical clarity from this alternative additive composition[178, 179, 181]. With the increase of DOPO-ITA content, the transmittance of FRTW slightly decreased. This might be attributed to the changes in refractive index after chemically bonding of DOPO-ITA. Notably, FRTWs shows a near-zero transmittance in the UV range, demonstrating its excellent UV (A and B) blocking effect. The haze of FRTW5, FRTW10, and FRTW20 are 44.3%, 49.7, and 50.9%, respectively, which are slightly higher than that of TW (41.4%). This might be attributed to the changes in refractive index after chemically bonding of DOPO-ITA into epoxy, as well as discontinuities contained in the mixture therein, which therefore led to enhanced light scattering in the structure[3, 153]. The digital photographs of natural wood, FREP, TW, and FRTW are shown in Figure 7. 1F, the characters below the TW and FRTW can be both seen clearly. The transmittance difference between these two samples is difficult to distinguish with the naked eye. Overall, DOPO-ITA hold very limited impact on optical properties of FRTW, which exhibits high transmittance and excellent UV blocking effect (Figure 7. 1G). This is due to DOPO-ITA being bonded to the epoxy crosslinking network via covalent bonding at least party via the carbonyl groups.

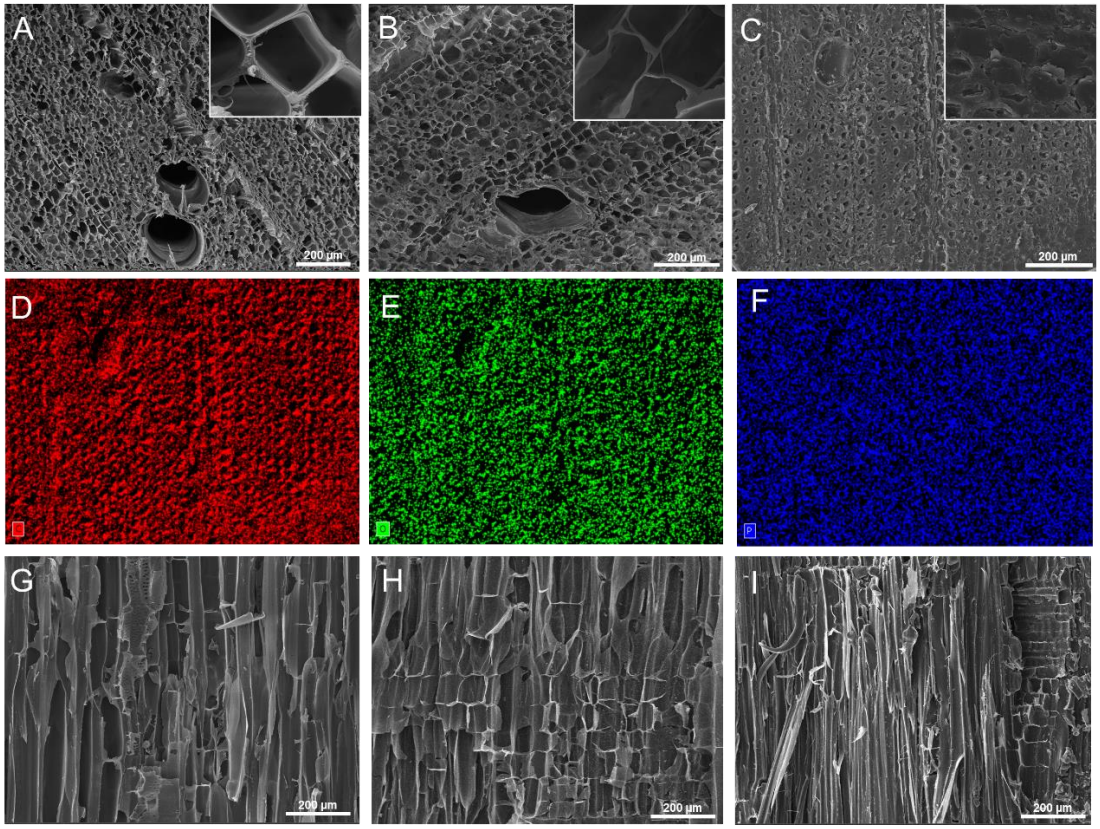

Figure 7. 2 A-C) Cross sectional SEM images of natural wood, lignin modified wood, and FRTW20. D-E) C, O, and P Energy Dispersive Spectroscopy (EDS) images of FRTW20. G-I) SEM images of natural wood, lignin modified wood, and FRTW20 along the longitudinal direction.

The highly aligned microchannels measuring approximately 20-50 µm can be observed in both the cross-sectional and top views of the natural wood (Figure 7. 2A&G). Following lignin modification, these microchannels remain well-preserved, although the cell walls become significantly thinner (Figure 7. 2B&H)[325, 327]. In the FRTW20, the microchannels are filled with epoxy resin, leaving no gaps between the epoxy and the cell walls (Figure 7. 2C&I). This suggests strong interactions, such as hydrogen bonding or van der Waals forces between the wood cellulose and the epoxy. From the EDS images of FRTW20 (Figure 7. 2D-F), both C, O, and P are evenly distributed in the matrix. This indicates that the FR components (DOPO-ITA) were evenly bonded to the epoxy crosslinking network. The mass and atom ratio of P obtained from the EDS is approximately 3.01% and 1.29, respectively, which is what ensures its excellent

flame retardancy.

7.3.2 Thermal stability and physical properties of FRTW

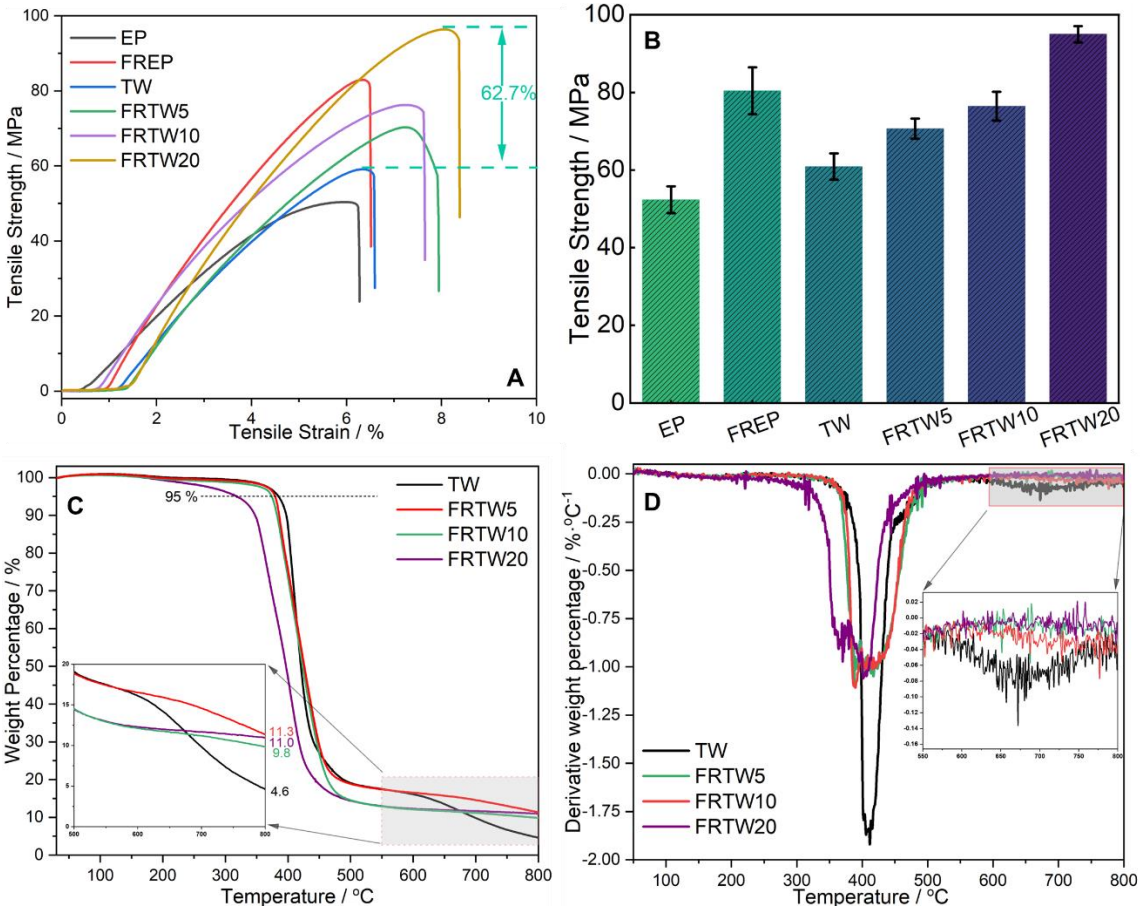

Figure 7. 3 A) Tensile strength-strain curves of EP, FREP, TW, FRTW5, FRTW10, and FRTW20 for each median sample. B) Average tensile strength of P, FREP, TW, FRTW5, FRTW10, and FRTW20. C &D) TG and DTG curves of TW, FRTW5, FRTW10, and FRTW20.

The mechanical properties of epoxy thermosets and TWs were investigated. The tensile strength-strain curves of each median sample and tensile strength in average were shown in Figure 7. 3A & B. For pure EP thermosets, virginal EP shows the lowest tensile strength (52.35 MPa), while the average tensile strength was increased by 153.5%, reaching 80.38MPa after introduction of DOPO-ITA. The tensile strength of TW (60.88MPa) is also higher that of EP. This is further enhanced by the increase of

DOPO-ITA content; the tensile strength of FRTW gradually increased, reaching 94.98 MPa for the sample of FRTW20. The introduction of DOPO-ITA significantly increased the tensile strength for both pure EP thermosets and FRTWs. The possible reasons for the enhancement in mechanical performance may include following: 1) the phosphate phenanthrene group, which is usually considered a rigid component, may increase the rigidity of the final epoxy crosslinking network, and therefore, yield an increased tensile strength[328]; 2) the biphenyl group in DOPO structure may exert in-situ reinforcing effect via π-π stacking, which has proven effective in improve mechanical performance[329].

The thermal stability of transparent woods (TWs) was investigated using thermogravimetric analysis (TGA). The TG and DTG curves for TW, FRTW5, FRTW10, and FRTW20 are shown in Figure 7. 3C&D. The temperature at 5% weight loss (T5%) for FRTW5 (379°C) and FRTW10 (372°C) is almost identical to that of TW (385°C). However, T5% for FRTW20 significantly decreased by 69°C, dropping to 316°C. This reduction is likely due to the catalytic decomposition effect of DOPO-ITA[330]. As a result, while the thermal stability of FRTW5 and FRTW10 remains largely unchanged, FRTW20 shows decreased thermal stability due to this catalytic effect. Similarly, the temperature at maximum weight loss rate (Tmax) for FRTW5, FRTW10, and FRTW20 (389°C, 389°C, and 402°C, respectively) is slightly lower than that of TW (411°C), again attributed to the catalytic decomposition effect. However, the maximum weight loss rates of FRTW5, FRTW10, and FRTW20 are significantly reduced compared to TW. The char residue at 800°C for FRTW5 (11.3%), FRTW10 (9.8%), and FRTW20 (11.0%) is notably higher than that of TW (4.6%), suggesting that DOPO-ITA facilitates the carbonization of TW at high temperatures. Notably, the char residue yields for TW and FRTW5 show further decomposition after 550°C, indicating initially unstable char layers. In contrast, the char residues for FRTW10 and FRTW20 remain stable beyond 550°C, as evidenced by the DTG curve in Figure 7. 3D. This stability suggests that DOPO-ITA contributes to the formation of more stable char layers at high temperatures, despite its early catalytic decomposition effect. This

indicates a critical additive loading threshold is required for optimal performance. These new and more stable char layers are believed to play a key role in the excellent fire resistance observed in FRTW.

7.3.3 Flame retardancy of FRTW

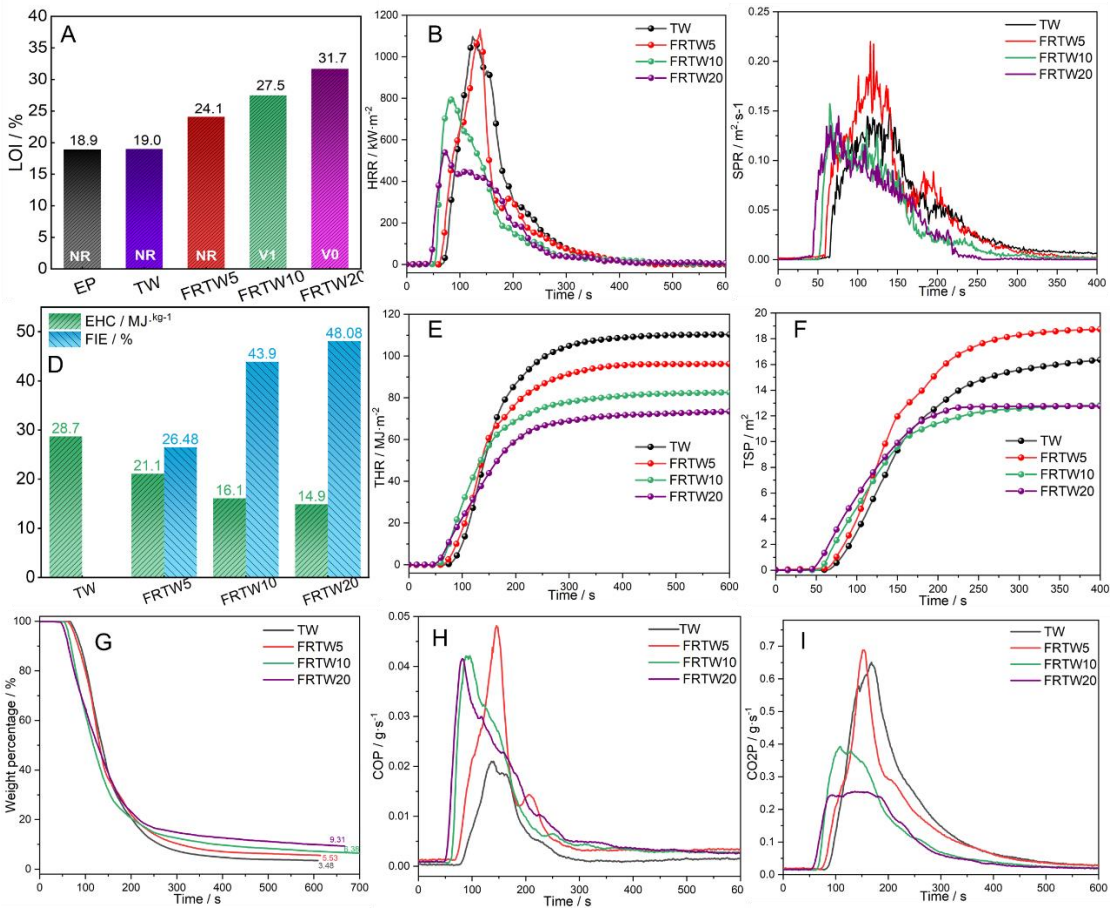

Figure 7. 4 A) LOI and UL-94 test for EP, TW, FRTW5, FRTW10, and FRTW20. B&C) HRR and SPR curves of TW, FRTW5, FRTW10, and FRTW20. D) EHC and FIE (unavailable for TW) index for TW, FRTW5, FRTW10, and FRTW20. D&F) THR and TSP curves of TW, FRTW5, FRTW10, and FRTW20. G) Mass loss curves of TW, FRTW5, FRTW10, and FRTW20 during the combustion. H&I) COP and CO2P curves of TW, FRTW5, FRTW10, and FRTW20.

The fire safety of TW composites was evaluated using the limiting oxygen index (LOI), which indicates the level of oxygen needed to sustain combustion—a higher LOI value

generally signifies greater flame retardancy—and the UL-94 test. As shown in Figure 7. 4A, the combination of lignin-modified wood and epoxy resin does not alter the flammability properties of either material, resulting in LOI values of 18.9% for TW and 19.0% for EP. Both TW and EP also failed the UL-94 test, further confirming their flammable nature. However, integrating DOPO-ITA significantly enhanced the fire safety of all TW systems. Specifically, the LOI values of FRTW5, FRTW10, and FRTW20 gradually increased to 24.1%, 27.5%, and 31.7%, respectively, indicating a progression from slow burning to self-extinguishing. FRTW10, with a DOPO-ITA mass ratio of ~7%, achieved a UL-94 V1 rating, and FRTW20, with a ~14% mass ratio, reached the highest UL-94 V0 rating. Compared to other phosphorus-based flame retardants, the additive loading of DOPO-ITA in this study is not low[331, 332], but it does not compromise the mechanical properties of the material, making this a significant advancement over previous reports. This approach could also be used to fabricate epoxy thermosets that require fire safety, transparency, and mechanical performance.

The cone calorimeter test was employed to further evaluate the fire performance of the prepared fire-retardant transparent woods (FRTWs). The heat release rate (HRR), total heat release (THR), smoke production rate (SPR), and total smoke production (TSP) curves are presented in Figure 7. 4B, C, E, & F. Consistent with the UL-94 results, TW released a large amount of heat and smoke after ignition, while the heat and smoke release of FRTW10 and FRTW20 were significantly suppressed due to the DOPO-ITA structure bonded within the epoxy crosslinking network. Notably, the peak HRR of TW was 1097.3 kW/m², while FRTW5 exhibited a slightly higher peak HRR of 1125 kW/m². This could be attributed to the increased flammability caused by the catalytic decomposition effect of DOPO-ITA during the early combustion stage and the fact that the critical loading threshold for DOPO-ITA had not been reached, resulting in unstable char layers with a weak protective effect at low loadings. Another possible explanation could be machine errors in the cone calorimeter. However, as expected, the peak HRR for FRTW10 was reduced by 27.3% compared to TW, falling to 797.5 kW/m², and

FRTW20 exhibited an even lower peak HRR of 539.3 kW/m², a reduction of 50.3% compared to TW. Unlike the peak HRR results, FRTW5, FRTW10, and FRTW20 all showed various degrees of THR reduction. At 600°C, the THR values for FRTW5, FRTW10, and FRTW20 were 96 MJ·m^{-2}, 82 MJ·m^{-2}, and 73.1 MJ·m^{-2}, respectively, all significantly lower than the 101.6 MJ·m^{-2} recorded for TW, indicating a decreased fire hazard for the FRTW systems. Smoke behavior was also monitored during combustion. As with other phosphorus flame retardants, DOPO-ITA had little effect on SPR; the SPR of FRTW10 and FRTW20 remained relatively unchanged compared to TW. However, like the peak HRR results, the SPR of FRTW5 was slightly higher than that of TW. Due to the increased peak SPR, the TSP of FRTW5 was also higher than that of TW, which can be explained by the previously mentioned reasons. Nevertheless, the TSP values for FRTW10 and FRTW20 decreased to 12.8 m² and 12.7 m², respectively, representing reductions of approximately 22.0% and 22.5% compared to TW (16.4 m²).

The average effective heat of combustion (EHC) is an important parameter for evaluating the degree of combustion of gas-phase volatiles[333]. As shown Figure 7. 4B, the EHC gradually dropped from 28.7 MJ/kg for TW to 14.9 MJ/kg for FRTW20, suggesting that the combustion of volatiles in the gas phase was suppressed by the pyrolytic components of DOPO-ITA. Another calculated parameter from the cone test results that describes the flame retardant mechanism in the gaseous phase is the flame inhibition effect (FIE) [334], which is presented in Figure 7. 4B. The FIE value for FRTW gradually increased with higher DOPO-ITA content, reaching 48.08 for FRTW20. This suggests that DOPO-ITA can inhibit flame initiation and propagation during combustion through gas-phase effects. As discussed in the TG section, DOPO-ITA also provides a protective effect in the condensed phase. Thus, it offers a dual approach, both passively guarding against fire and actively extinguishing flames once they arise. The mass loss curve of TW and FRTWs samples are shown in Figure 7. 4G. The remaining char residue after TW combustion was only 3.48%, while that of FRTW samples gradually increased, reaching a maximum of 9.31% for FRTW20. This

suggests that DOPO-ITA promotes the formation of stable carbon layers during combustion. These stable carbon layers provide a protective effect in the condensed phase, separating the flammable gases (fuels resulting from the decomposition of epoxy and lignin-modified wood) from oxygen. In this way, the fire safety of FRTW is significantly enhanced. However, the production of toxic gas (CO) during combustion appears to increase, as shown in Figure 7. 4H. This might be due to the reduced oxygen availability caused by the protective effect of the stable carbon layers, leading to incomplete combustion[335, 336]. On the other hand, the peak CO2 production rate for FRTW10 and FRTW20 decreased compared to TW (Figure 7. 4H), likely due to the catalytic carbonization effect of DOPO-ITA during thermal pyrolysis, which allows more carbon to remain in the condensed phase rather than entering the gas phase. Overall, the LOI and UL-94 results demonstrate that the fire safety of FRTW is significantly improved compared to TW. The cone calorimeter test also confirms that the combustion process is significantly suppressed.

7.3.4 Flame retardancy mechanism of FRTW

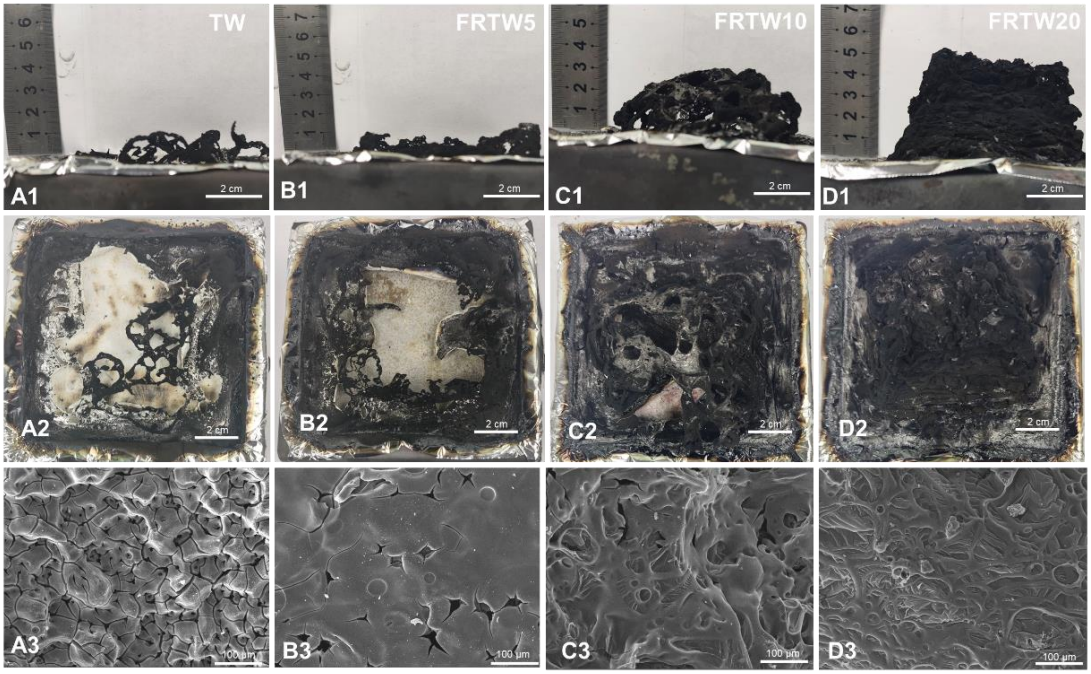

Figure 7. 5 A1 & A2) Side view and top view of TW after Cone test. A3) SEM images of the char residues of TW after Cone test. B1 & B2) Side view and top view of

FRTW5 after Cone test. B3) SEM images of the char residues of FRTW5 after Cone test. C1 & C2) Side view and top view of FRTW10 after Cone test. C3) SEM images of the char residues of FRTW10 after Cone test. D1 & D2) Side view and top view of FRTW20 after Cone test. D3) SEM images of the char residues of FRTW20 after Cone test.

The macro- and micro-morphology of char residues provide strong evidence for the condensed phase effect of the flame retardant (FR). Digital photos of the remaining char residues after the cone calorimeter test were recorded. As shown in the Fig. 5A1 & A2, almost nothing remains of the TW after the test, with a residual mass of only around 3.48% (Figure 7. 4G). Additionally, no intumescence was observed in TW, indicating the absence of an effective FR mechanism during combustion. Further evidence of this failure is visible in the SEM images of the remaining carbon layers (Figure 7. 5A3), which are fragile, fragmented, and riddled with cracks. These cracks provide ample pathways for fuel and oxygen to contact each other, allowing the complete combustion of TW. The micromorphology of char residues of FRTW5 is similar to that of TW. No intumescence was observed (Figure 7. 5B1 & B2), despite the remining mass rate increasing to 5.53% (Figure 7. 4G). The micro-structure of the char residues is different from that of TW, showing some wrinkles and cracks on the surface (Figure 7. 5B3). but the number of cracks is significantly reduced compared to TW. This suggests that DOPO-ITA contributes to the formation of more stable carbon layers, though the flame-retardant efficiency at this additive loading level is insufficient to achieve satisfactory fire performance. With increased additive loading, the macro- and micro-morphology of FRTW10 and FRTW20 show significant improvements compared to TW and FRTW5. As shown in Figure 7. 5C1-3 & D1-3, noticeable intumescence is observed after burning, with the char residue height reaching approximately 3 cm for FRTW10 and 5 cm for FRTW20. The micro-morphology of FRTW10 and FRTW20 is also significantly improved. While very small cracks and pores are present in FRTW10, the carbon layer remains broadly intact and continuous. In the case of FRTW20, no cracks or pores are observed in the carbon layers. Thus, at

sufficient additive loading, the carbon layers of FRTW20 are much more intact and continuous than those of TW, providing a strong protective effect in the condensed phase. These intact and continuous carbon layers protect the inner matrix from oxygen, resulting in excellent fire performance [337, 338].

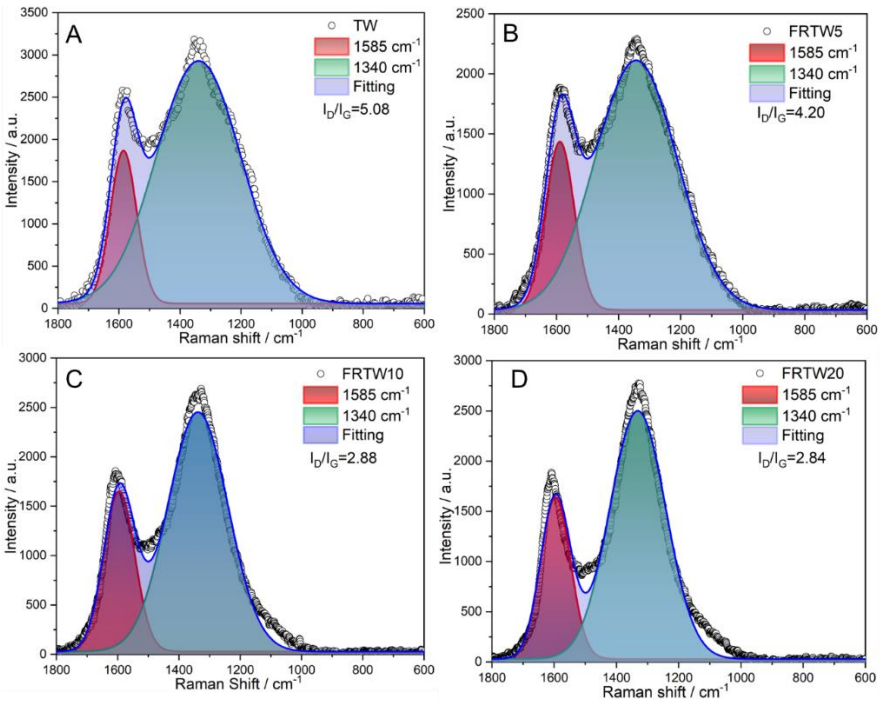

Figure 7. 6 A-D) Raman spectra of TW, FRTW5, FRTW10, and FRTW20

Raman spectral analysis of the char residues after the cone test can provide insights into the stability of the formed carbon layers. All char residues displayed D and G bands at 1340 and 1585 cm^{-1}, corresponding to amorphous carbon and orderly graphite structures, respectively [339]. The integral area ratio of the D to G bands (ID/IG) is used to assess the graphitization degree of residual chars[340, 341], with a lower ID/IG value indicating a higher degree of graphitization. A higher graphitization degree is associated with greater stability of the carbon layers. As displayed in Figure 7. 6A-D, the ID/IG ratio gradually decreases as the DOPO-ITA content increases. Specifically, the ID/IG of TW is 5.08, suggesting low graphitization and unstable carbon layers. This ratio decreases to 4.20 for FRTW5, 2.88 for FRTW10, and 2.84 for FRTW20, indicating that the stability of these carbon layers improves with higher DOPO-ITA content. The

enhanced stability of the carbon layer is also supported by the TG results and the microstructure of the char residues. Overall, the Raman spectra demonstrate a higher degree of graphitization and increased stability of FRTWs after combustion, which enhances the protective effect for the substrate in the condensed phase.

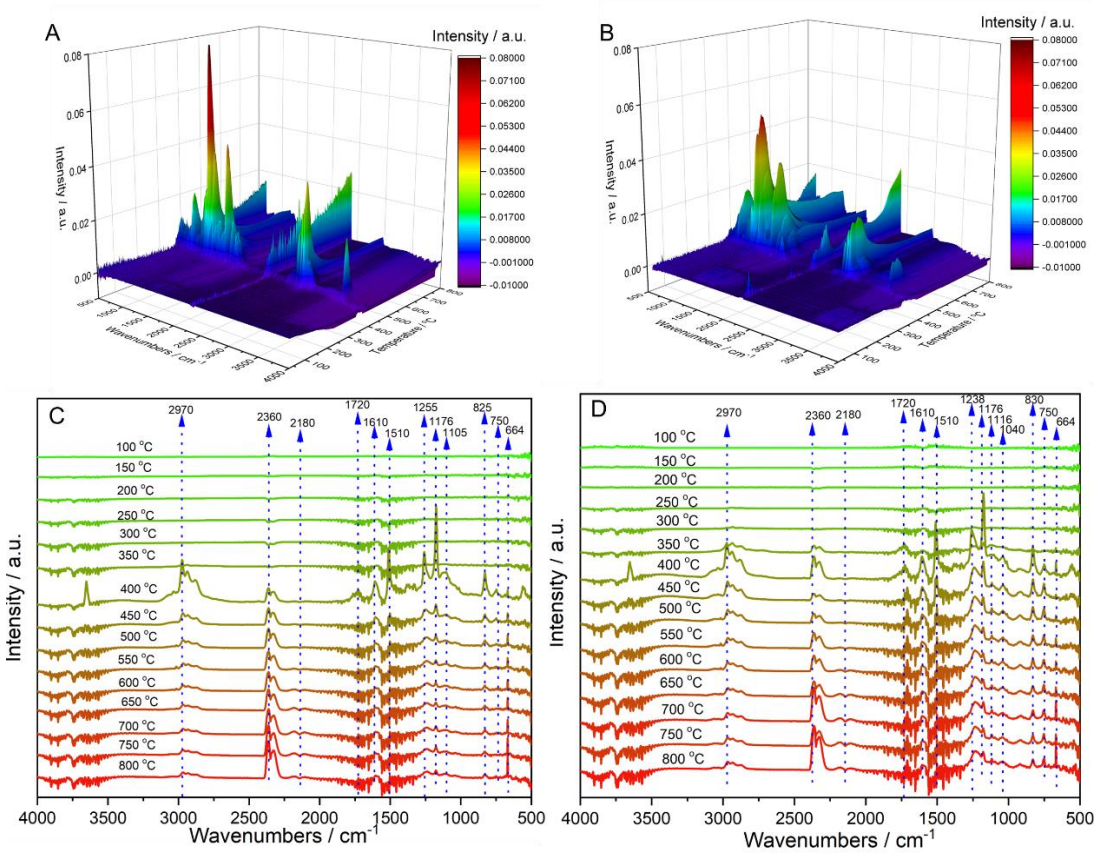

Figure 7. 7 A) 3D TG-IR spectra of TW. B) 3D TG-IR spectra of FRTW20. C) FTIR spectra of the pyrolytic products at different temperatures. D) FTIR spectra of the pyrolytic products at different temperatures.

Combustion is an extremely complex process involving both chemical and physical reactions in the condensed and gas phases [342]. To better understand the flame-retardant mechanism, TG-IR analysis was used to monitor the thermal decomposition process of TW and FRTW20. The 3D TG-IR images of TW and FRTW20 are shown in the Figure 7. 7A & B. The absorption intensity of the pyrolysis products for both TW and FRTW20 increases with temperature and then decreases in the final stage,

indicating that the combustion process releases a large amount of gas into the gas phase. These released gases include flammable components, non-flammable compounds, and some phosphorus-containing substances, which are fragments and by-products from the flame retardant (FR) additive. These gases play a crucial role in the subsequent cross-linking that occurs during char formation in the combustion process. The 3D images further reveal that the peak gas release for FRTW20 is significantly lower than that of TW, suggesting a reduced total gas release, although the compositional differences are not immediately clear. The FTIR spectra of the pyrolytic products for TW and FRTW20 at different temperatures are shown in Figure 7. 7C & D, identifying the specific compositions. The IR signals for FRTW20 appear earlier than those for TW, indicating an earlier decomposition onset due to the DOPO-ITA structure. The detected IR signals for TW include peaks at 2970 cm^{-1} (hydrocarbons), 2360 cm^{-1} (CO_2), 2180 cm^{-1} (CO), 1720 cm^{-1} (carbonyl compounds), 1610 cm^{-1} (aromatic ring compounds), 1510 cm^{-1} (aromatic ring compounds), 1255 cm^{-1} (C-O), 1176 cm^{-1} (ether compounds), 1105 cm^{-1} (ether compounds), 825 cm^{-1} (aromatic ring compounds), 750 cm^{-1} (ether compounds), and 664 cm^{-1} (CO_2) [343-347]. Similarly, these peaks are observed in the pyrolysis FTIR spectra of FRTW20, with some slight shifts in peak locations. The peaks for FRTW20 include 2790 cm^{-1}, 2360 cm^{-1}, 2180 cm^{-1}, 1720 cm^{-1}, 1610 cm^{-1}, 1510 cm^{-1}, 1238 cm^{-1}, 1176 cm^{-1}, 1116 cm^{-1}, 1040 cm^{-1}, 810 cm^{-1}, 750 cm^{-1}, and 664 cm^{-1}. All these peaks, except the one at 1040 cm^{-1}, are also found in TW. The exclusive peak at 1040 cm^{-1} is assigned to the P-O-C vibration, indicating the presence of phosphorus-containing compounds in the gas phase, which are a critical component of the FR mechanism[29].

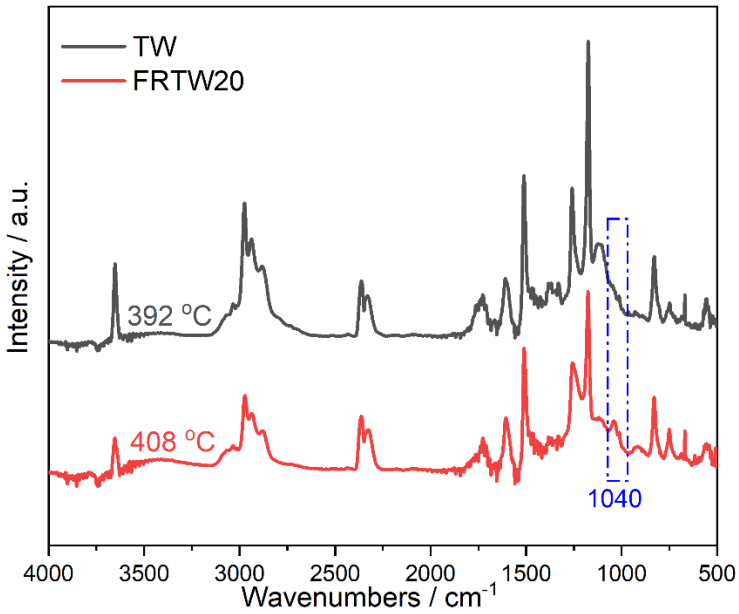

Figure 7. 8 FTIR spectra of pyrolysis products for TW and FRTW20 at the maximum evolution rate

To highlight this peak more clearly, the FTIR spectra of the pyrolysis products for TW and FRTW20 at the maximum evolution rate are shown in Figure 7. 8. As observed, this peak is exclusive to the spectra of FRTW20. The presence of phosphorus-containing compounds suggests that P· or PO· radicals may form during combustion, quenching OH· or H· free radicals, which inhibits flame spread and contributes to the material's self-extinguishing properties [348]. Overall, the thermal degradation process of both TW and FRTW is accompanied by the release of a large amount of gaseous products, which serve as fuel for combustion. The detection of phosphorus-containing compounds confirms their role in providing flame retardancy in the gas phase.

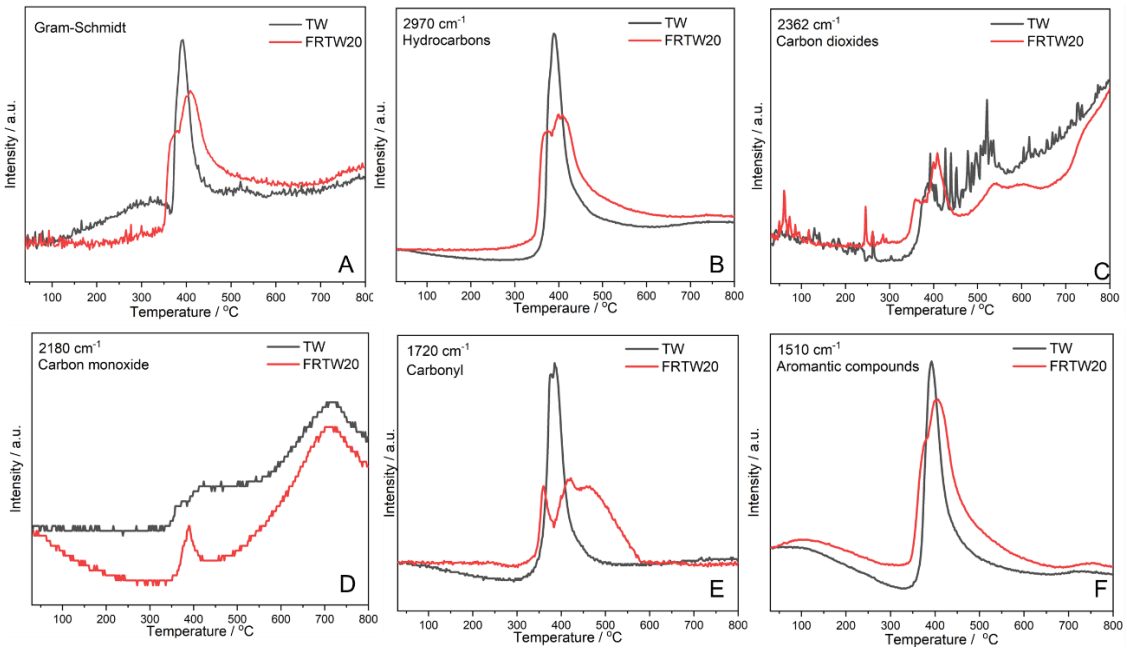

Figure 7. 9 The Gram-Schmidt (GS) curves (A) and FTIR absorbance of five typical (B-F) pyrolysis peaks vs temperature for TW and FRTW20. These five typical compounds are hydrocarbons (B), carbon dioxides (C), carbon monoxide (D), carbonyl compounds (E), and aromantic compounds (F).

The Gram-Schmidt (GS) curves provide a semi-quantitative analysis of pyrolysis volatiles release intensity during combustion. As shown in Figure 7. 9A, the GS intensity for FRTW20 is significantly lower than that of TW, indicating that FRTW20 produces fewer pyrolysis volatiles compared to TW. This reduction in pyrolysis volatiles is primarily attributed to the incorporation of DOPO-ITA. Figure 7. 9B–F display the characteristic absorbance peaks for hydrocarbons (2970 cm^{-1}), carbon dioxide (2362 cm^{-1}), carbon monoxide (2180 cm^{-1}), carbonyl compounds (1720 cm^{-1}), and aromatic compounds (1510 cm^{-1}). The integration of DOPO-ITA results in a notable decrease in the maximum absorbance intensity of these compounds. This reduction is likely due to the formation of compact and continuous char layers, which inhibit the interaction between pyrolysis products and oxygen, thereby decreasing the maximum absorbance intensity of the decomposed products. The decrease in the release of hydrocarbons, aromatic compounds, and carbonyl compounds may contribute to

smoke suppression, while the reduction in CO levels indicates a decrease in smoke toxicity. Overall, the fire safety of TW is enhanced through the chemical bonding of DOPO-ITA.

7.4 Conclusion

We report on a strategy to prepare transparent wood (TW) with excellent transparency, flame retardancy (FR), and improved mechanical properties using a bio-based flame retardant co-curing agent (DOPO-ITA). The epoxy used to fill the wood substrates upon lignin-modification was pre-modified by DOPO-ITA, which was chemically bonded to the epoxy chains via a solvent free polymerization process. Then the DOPO-ITA modified epoxy precursor was used to fabricate TW through pre-polymerization-vacuum infiltration strategy using lignin modified wood. The integration of DOPO-ITA shows little impact on the transparency but a huge improvement on the fire protective and mechanical performance. The prepared flame-retardant transparent wood (FRTW) composites show excellent transparency (up to 84.7% at 550 nm), considerable UV blocking capacity (near zero UV-A and B transmittance), improved tensile strengthen (up to 94.98 MPa), and satisfactory fire protective performance (a LOI of 31.7%, UL-94 V0 rating, and an inhibited combustion process). The peak-HRR of FRTW20 (539.3kW/m^2) experienced a huge reduction of 50.3% compared to TW (1097.3kW/m^2), indicating improved fire safety. Further results from the SEM images of the char residues after cone and TG-IR testing show that the improved FR was mainly caused by the strong FR activity in both the condensed and vapor phases. The release of various pyrolysis volatiles was also reduced after the introduction of DOPO-ITA, indicating a lowered toxicity when FRTW20 encounters fire. The excellent fire performance of FRTW reported here may help to address the otherwise legitimate fire safety concerns associated with the adoption of transparent wood-based substrates for real-word commercial applications. Overall, the combination of excellent visual transparency, mechanical properties, and fire safety presented in this work make FRTW a more promising candidate for future glazing materials.

Chapter 8 Conclusions and suggestions for future research

This chapter summarizes the key findings, main conclusions, and recommendations for future research.

8.1 Thesis Summary

The thesis has presented a collection of novel thermal management materials for both building, personal, and fire safety applications. The research is organized into four main chapters, each addressing a specific aspect of this overarching theme:

Chapter 4 explores the enhancement of the radiative cooling potential of TW through the fabrication of ZnO coatings using a sonochemical deposition method. The resulting coated transparent wood (CTW) demonstrated promising properties for use as window material, including reasonable luminous transmission, low thermal conductivity, and high infrared emissivity. Energy-saving simulations indicated significant potential for cooling energy savings in various climates when compared to commercial low-E glass.

Chapter 5 presents a method for achieving temperature-responsive emissivity in TW by constructing a Fabry-Perot resonator on the wood's surface. The approach, which involved the assembly of AgNWs, PMMA, and W-VO_2 layers, yielded an emissivity contrast that could be tuned based on fabrication parameters. This chapter highlights the feasibility of using this material in energy-saving applications and underscores the method's versatility, as it can be applied to a wide range of substrates.

Chapter 6 applies the concept of radiative cooling regulation to fabrics, resulting in the creation of self-adaptive fabrics with significant solar reflectance and temperature-responsive emissivity. The self-adaptive radiative cooling fabric (SARCF) demonstrated superior thermal management performance in both hot and cold environments when compared to low-e fabrics and white cotton. This chapter showcases the potential for intelligent personal thermal management solutions using these novel materials.

Chapter 7 extends the thermal management concept downwards to the burning process, focusing on manipulating the heat transfer process of TW's combustion to enhance the fire safety. The integration of a bio-based flame retardant co-curing agent (DOPO-ITA) resulted in flame-retardant transparent wood (FRTW) composites that maintained high transparency, improved tensile strength, and exhibited excellent fire protection. This chapter lays the groundwork for the broader adoption of transparent wood in real-world applications by addressing fire safety concerns.

8.2 Conclusions

i. ZnO coatings were successfully applied to transparent wood via a sonochemical method, enhancing its radiative cooling potential. The coated transparent wood exhibited favorable properties for use as energy-efficient window material, with simulations indicating substantial cooling energy savings.

ii. Temperature-responsive emissivity was achieved in transparent wood through a facile and widely applicable solution-processing method. The material demonstrated significant energy-saving potential and versatility, as the approach could be applied to various substrates, including PET, glass, and cement.

iii. The radiative cooling regulation concept was successfully applied to fabrics, resulting in self-adaptive radiative cooling fabrics (SARCF) with significant emissivity contrast and solar reflectance. The SARCF outperformed conventional fabrics in both hot and cold environments, demonstrating the feasibility of intelligent personal thermal management solutions.

iv. A bio-based flame retardant (DOPO-ITA) was synthesized and integrated into transparent wood, significantly improving fire safety and mechanical properties without compromising transparency. The flame-retardant transparent wood

(FRTW) demonstrated superior fire protection and mechanical strength, making it a viable candidate for building applications.

8.3 Suggestions for Future Research

The present work has made significant progress on addressing the fire safety of transparent wood, improving the energy saving potential of transparent wood via ZnO coating and emissivity modulation, and confirming the feasibility and benefits of radiative cooling regulation for textile applications. However, further studies are necessary to improve the high fire safety of transparent wood at lower content, establishing the correlations between the emissivity contrast and fabricating parameters, improving the solar reflectance of SARCF while maintaining its emissivity modulation capacity, and coloration of SARCF for practical applications.

Enhancing Fire Safety with Lower Additive Content:

The integration of flame retardants like DOPO-ITA has significantly improved the fire safety of transparent wood, but this often necessitates a relatively high content of flame retardants. Future research should focus on optimizing the formulation and distribution of these additives to maintain or even enhance fire safety with lower additive content. Achieving this balance would preserve the material's mechanical properties and transparency, reduce costs, and minimize potential environmental impacts associated with higher additive levels. Advanced techniques such as nano dispersion of flame retardants or synergistic combinations of additives could be explored to achieve these goals.

Establishing Correlations Between Emissivity Contrast and Fabrication Parameters:

This research has demonstrated the effectiveness of emissivity modulation in transparent wood and textiles for thermal regulation. However, the precise relationship between emissivity contrast and specific fabrication parameters—such as spinning speed, coating thickness, and material concentration—remains unclear. Detailed studies

are needed to systematically investigate these correlations, which will allow for precise control over the emissivity properties of the materials. By understanding these relationships, future work can optimize performance for specific applications and climates, ensuring that these materials meet the varied demands of real-world conditions.

Improving Solar Reflectance of SARCF While Maintaining Emissivity Modulation:

The Self-Adaptive Radiative Cooling Fabric (SARCF) has shown promise with its emissivity modulation and solar reflectance of 85.19%, making it effective for personal thermal management. However, further improvement of its solar reflectance is necessary to enhance its overall cooling effectiveness, particularly in high-sunlight environments. This enhancement must be achieved without compromising the fabric's ability to modulate emissivity. Research should focus on innovative material designs or coatings that increase solar reflectance while maintaining, or even enhancing, the fabric's emissivity modulation capabilities. Balancing these properties will be crucial for maximizing the cooling benefits of SARCF.

Coloration, washing durability, and biosafety of SARCF for Practical Applications:

For SARCF to gain widespread adoption, particularly in consumer markets, it must meet both functional and aesthetic standards. Developing effective coloration methods that do not interfere with the fabric's thermal properties is essential. Achieving vibrant, durable colors that align with consumer preferences while maintaining the fabric's radiative cooling capabilities is a significant challenge. The washing durability of SARCF needs further investigation. Besides, the biosafety of vanadium is still a concern for wide adoption. Research should explore various dyeing techniques and washing test, and bio-safety test to ensure that SARCF is both aesthetically appealing functionally effective and durable, and biologically safe in regulating thermal properties. Success in these areas will be key to making SARCF a viable option for everyday use in clothing and other consumer products.

By addressing these areas, future research can build on the foundations laid by the present work, pushing the boundaries of thermal management materials and bringing them closer to widespread, practical application.

References

[1] Qin Z, Li M, Flohn J, Hu Y. Thermal management materials for energy-efficient and sustainable future buildings. Chemical Communications. 2021;57(92):12236-53.

[2] Li T, Zhu M, Yang Z, Song J, Dai J, Yao Y, et al. Wood Composite as an Energy Efficient Building Material: Guided Sunlight Transmittance and Effective Thermal Insulation. Advanced Energy Materials. 2016;6(22):1601122.

[3] Li Y, Fu Q, Yu S, Yan M, Berglund L. Optically Transparent Wood from a Nanoporous Cellulosic Template: Combining Functional and Structural Performance. Biomacromolecules. 2016;17(4):1358-64.

[4] Zhu M, Song J, Li T, Gong A, Wang Y, Dai J, et al. Highly Anisotropic, Highly Transparent Wood Composites. Advanced Materials. 2016;28(26):5181-7.

[5] Hu X, Yu R, Wang F, Liu Z, Yang H, Chen C, et al. Fabrication, Functionalities and Applications of Transparent Wood: A Review. Advanced Functional Materials. 2023;33(37):2303278.

[6] Hu X, Zhang Y, Cai W, Ming Y, Yu R, Yang H, et al. Transparent wood with heat shielding and high fire safety properties for energy saving applications. Renewable Energy. 2023;219:119426.

[7] Hu X, Zhang Y, Zhang J, Yang H, Wang F, Bin F, et al. Sonochemically-coated transparent wood with ZnO: Passive radiative cooling materials for energy saving applications. Renewable Energy. 2022;193:398-406.

[8] Hu X, Cai W, Zhang Y, Shi S, Ming Y, Yu R, et al. Facile and Widely Applicable Route to Self-Adaptive Emissivity Modulation: Energy-Saving Demonstration with Transparent Wood. Nano Letters. 2024;24(2):657-66.

[9] Ma Z, Zhao D, She C, Yang Y, Yang R. Personal thermal management techniques for thermal comfort and building energy saving. Materials Today Physics. 2021;20:100465.

[10] Sajjad U, Hamid K, Tauseef ur R, Sultan M, Abbas N, Ali HM, et al. Personal thermal management - A review on strategies, progress, and prospects. International Communications in Heat and Mass Transfer. 2022;130:105739.

[11] Hoyt T, Arens E, Zhang H. Extending air temperature setpoints: Simulated energy savings and design considerations for new and retrofit buildings. Building and Environment. 2015;88:89-96.

[12] Ghahramani A, Zhang K, Dutta K, Yang Z, Becerik-Gerber B. Energy savings from temperature setpoints and deadband: Quantifying the influence of building and system properties on savings. Applied Energy. 2016;165:930-42.

[13] Asefi G, Habibollahzade A, Ma T, Houshfar E, Wang R. Thermal management of building-integrated photovoltaic/thermal systems: A comprehensive review. Solar Energy. 2021;216:188-210.

[14] Smalyukh II. Thermal Management by Engineering the Alignment of Nanocellulose. Advanced Materials. 2021;33(28):2001228.

[15] Abu-Jdayil B, Mourad A-H, Hittini W, Hassan M, Hameedi S. Traditional, state-of-the-art and renewable thermal building insulation materials: An overview. Construction and Building Materials. 2019;214:709-35.

[16] Abedi M, Jazizadeh F, Huang B, Battaglia F. Smart HVAC Systems — Adjustable Airflow Direction. In: Smith IFC, Domer B, editors. Advanced Computing Strategies for Engineering. Cham: Springer International Publishing; 2018. p. 193-209.

[17] Mardiana-Idayu A, Riffat SB. Review on heat recovery technologies for building applications. Renewable and Sustainable Energy Reviews. 2012;16(2):1241-55.

[18] Zhang H, Yang D, Tam VWY, Tao Y, Zhang G, Setunge S, et al. A critical review of combined natural ventilation techniques in sustainable buildings. Renewable and Sustainable Energy Reviews. 2021;141:110795.

[19] Chai J, Fan J. Solar and Thermal Radiation-Modulation Materials for Building Applications. Advanced Energy Materials. 2023;13(1):2202932.

[20] Zhao B, Hu M, Xuan Q, Kwan TH, Dabwan YN, Pei G. Tunable thermal management based on solar heating and radiative cooling. Solar Energy Materials and Solar Cells. 2022;235:111457.

[21] Zhao B, Wang C, Hu M, Ao X, Liu J, Xuan Q, et al. Light and thermal management of the semi-transparent radiative cooling glass for buildings. Energy. 2022;238:121761.

[22] Liang J, Wu J, Guo J, Li H, Zhou X, Liang S, et al. Radiative cooling for passive thermal management towards sustainable carbon neutrality. National Science Review. 2023;10(1):nwac208.

[23] Hu R, Liu Y, Shin S, Huang S, Ren X, Shu W, et al. Emerging Materials and Strategies for Personal Thermal Management. Advanced Energy Materials. 2020;10(17):1903921.

[24] Cai L, Song AY, Li W, Hsu P-C, Lin D, Catrysse PB, et al. Spectrally Selective Nanocomposite Textile for Outdoor Personal Cooling. Advanced Materials. 2018;30(35):1802152.

[25] Guo T, Shang B, Duan B, Luo X. Design and testing of a liquid cooled garment for hot environments. Journal of Thermal Biology. 2015;49-50:47-54.

[26] Li L, Liu W-D, Liu Q, Chen Z-G. Multifunctional Wearable Thermoelectrics for Personal Thermal Management. Advanced Functional Materials. 2022;32(22):2200548.

[27] Xue S, Huang G, Chen Q, Wang X, Fan J, Shou D. Personal Thermal Management by Radiative Cooling and Heating. Nano-Micro Letters. 2024;16(1):153.

[28] Peng Y, Cui Y. Advanced Textiles for Personal Thermal Management and Energy. Joule. 2020;4(4):724-42.

[29] Hu X, Yang H, Jiang Y, He H, Liu H, Huang H, et al. Facile synthesis of a novel transparent hyperbranched phosphorous/nitrogen-containing flame retardant and its application in reducing the fire hazard of epoxy resin. Journal of Hazardous Materials. 2019;379:120793.

[30] Liu B-W, Zhao H-B, Wang Y-Z. Advanced Flame-Retardant Methods for Polymeric Materials. Advanced Materials. 2022;34(46):2107905.

[31] Morgan AB, Gilman JW. An overview of flame retardancy of polymeric materials: application, technology, and future directions. Fire and Materials. 2013;37(4):259-79.

[32] Howell JR, Mengüç MP, Daun K, Siegel R. Thermal radiation heat transfer: CRC press; 2020.

[33] Sparrow EM. Radiation heat transfer: Routledge; 2018.

[34] Modest MF, Mazumder S. Radiative heat transfer: Academic press; 2021.

[35] Janna WS. Engineering heat transfer: CRC press; 2018.

[36] Çengel YA. Heat and mass transfer: fundamentals and applications fifth edition, 2015.

[37] Nellis G, Klein S. Heat transfer: Cambridge university press; 2008.

[38] Rohsenow WM, Hartnett JP, Cho YI. Handbook of heat transfer: Mcgraw-hill New York; 1998.

[39] Mills AF. Heat transfer: CRC Press; 1992.

[40] Kreith F, Black WZ. Basic heat transfer. 1980.

[41] Brewster MQ. Thermal radiative transfer and properties: John Wiley & Sons; 1992.

[42] Marr JM, Wilkin FPJAJoP. A better presentation of Planck's radiation law. 2012;80(5):399-405.

[43] Tao Wq. Heat Transfer Northwestern Polytechnical University Press; 2006.

[44] Zhao B, Hu M, Ao X, Chen N, Pei G. Radiative cooling: A review of fundamentals, materials, applications, and prospects. Applied Energy. 2019;236:489-513.

[45] Hossain MM, Gu M. Radiative Cooling: Principles, Progress, and Potentials. Advanced Science. 2016;3(7):1500360.

[46] Fan S, Li W. Photonics and thermodynamics concepts in radiative cooling. Nature Photonics. 2022;16(3):182-90.

[47] Raman AP, Anoma MA, Zhu L, Rephaeli E, Fan S. Passive radiative cooling below ambient air temperature under direct sunlight. Nature. 2014;515(7528):540-4.

[48] Vall S, Castell A. Radiative cooling as low-grade energy source: A literature review. Renewable and Sustainable Energy Reviews. 2017;77:803-20.

[49] Yu X, Chan J, Chen C. Review of radiative cooling materials: Performance evaluation and design approaches. Nano Energy. 2021;88:106259.

[50] Family R, Mengüç MP. Materials for Radiative Cooling: A Review. Procedia Environmental Sciences. 2017;38:752-9.

[51] Li Z, Chen Q, Song Y, Zhu B, Zhu J. Fundamentals, Materials, and Applications for Daytime Radiative Cooling. Advanced Materials Technologies. 2020;5(5):1901007.

[52] Yin X, Yang R, Tan G, Fan S. Terrestrial radiative cooling: Using the cold universe as a renewable and sustainable energy source. Science. 2020;370(6518):786-91.

[53] Peoples J, Hung Y-W, Fang Z, Braun J, Horton WT, Ruan X. Energy savings of radiative cooling paints applied to residential buildings. International Journal of Heat and Mass Transfer. 2022;194:123001.

[54] Zhao D, Aili A, Yin X, Tan G, Yang R. Roof-integrated radiative air-cooling system to achieve cooler attic for building energy saving. Energy and Buildings. 2019;203:109453.

[55] Li T, Zhai Y, He S, Gan W, Wei Z, Heidarinejad M, et al. A radiative cooling structural material. Science. 2019;364(6442):760-3.

[56] Ma J-W, Zeng F-R, Lin X-C, Wang Y-Q, Ma Y-H, Jia X-X, et al. A photoluminescent hydrogen-bonded biomass aerogel for sustainable radiative cooling. Science. 2024;385(6704):68-74.

[57] Ziming C, Fuqiang W, Dayang G, Huaxu L, Yong S. Low-cost radiative cooling blade coating with ultrahigh visible light transmittance and emission within an “atmospheric window”. Solar Energy Materials and Solar Cells. 2020;213:110563.

[58] Lee KW, Lim W, Jeon MS, Jang H, Hwang J, Lee CH, et al. Visibly Clear Radiative Cooling Metamaterials for Enhanced Thermal Management in Solar Cells and Windows. Advanced Functional Materials. 2022;32(1):2105882.

[59] Huang G, Yengannagari AR, Matsumori K, Patel P, Datla A, Trindade K, et al. Radiative cooling and indoor light management enabled by a transparent and self-cleaning polymer-based metamaterial. Nature Communications. 2024;15(1):3798.

[60] Zhao X, Li T, Xie H, Liu H, Wang L, Qu Y, et al. A solution-processed radiative cooling glass. Science. 2023;382(6671):684-91.

[61] Lin K, Chen S, Zeng Y, Ho TC, Zhu Y, Wang X, et al. Hierarchically structured passive radiative cooling ceramic with high solar reflectivity. Science. 2023;382(6671):691-7.

[62] Baniassadi A, Sailor DJ, Ban-Weiss GA. Potential energy and climate benefits of super-cool materials as a rooftop strategy. Urban Climate. 2019;29:100495.

[63] Wang S, Jiang T, Meng Y, Yang R, Tan G, Long Y. Scalable thermochromic smart windows with passive radiative cooling regulation. 2021;374(6574):1501-4.

[64] Jia Y, Liu D, Chen D, Jin Y, Chen C, Tao J, et al. Transparent dynamic infrared emissivity regulators. Nature Communications. 2023;14(1):5087.

[65] Zhu B, Li W, Zhang Q, Li D, Liu X, Wang Y, et al. Subambient daytime radiative cooling textile based on nanoprocessed silk. Nature Nanotechnology. 2021;16(12):1342-8.

[66] Zeng S, Pian S, Su M, Wang Z, Wu M, Liu X, et al. Hierarchical-morphology metafabric for scalable passive daytime radiative cooling. Science. 2021;373(6555):692-6.

[67] Tong JK, Huang X, Boriskina SV, Loomis J, Xu Y, Chen G. Infrared-Transparent Visible-Opaque Fabrics for Wearable Personal Thermal Management. ACS Photonics. 2015;2(6):769-78.

[68] Hsu P-C, Song AY, Catrysse PB, Liu C, Peng Y, Xie J, et al. Radiative human body cooling by nanoporous polyethylene textile. Science. 2016;353(6303):1019-23.

[69] Cai L, Peng Y, Xu J, Zhou C, Zhou C, Wu P, et al. Temperature Regulation in Colored Infrared-Transparent Polyethylene Textiles. Joule. 2019;3(6):1478-86.

[70] Peng Y, Chen J, Song AY, Catrysse PB, Hsu P-C, Cai L, et al. Nanoporous polyethylene microfibres for large-scale radiative cooling fabric. Nature Sustainability. 2018;1(2):105-12.

[71] Hsu P-C, Liu C, Song AY, Zhang Z, Peng Y, Xie J, et al. A dual-mode textile for human body radiative heating and cooling. Science Advances.3(11):e1700895.

[72] Zhang XA, Yu S, Xu B, Li M, Peng Z, Wang Y, et al. Dynamic gating of infrared radiation in a textile. Science. 2019;363(6427):619-23.

[73] Li X, Liu M, Chen K, Li L, Pei G, Zhao B. Adaptive fabric with emissivity regulation for thermal management of humans. 2024;13(17):3067-75.

[74] Ambat I, Srivastava V, Sillanpää M. Recent advancement in biodiesel production methodologies using various feedstock: A review. Renewable and Sustainable Energy Reviews. 2018;90:356-69.

[75] Coxhead I. A New Resource Curse? Impacts of China's Boom on Comparative Advantage and Resource Dependence in Southeast Asia. World Development. 2007;35(7):1099-119.

[76] D&R International Ltd. 2011 Buildings Energy Data Book 2011 Buildings Energy Data Book, US Department of Energy. 2012.

[77] Pokrajac L, Abbas A, Chrzanowski W, Dias GM, Eggleton BJ, Maguire S, et al. Nanotechnology for a Sustainable Future: Addressing Global Challenges with the International Network4Sustainable Nanotechnology. ACS Nano. 2021;15(12):18608-23.

[78] Anadon LD, Chan G, Harley AG, Matus K, Moon S, Murthy SL, et al. Making technological innovation work for sustainable development. PANS. 2016;113(35):9682-90.

[79] Ali SH. The materials science imperative in meeting the Sustainable Development Goals. Nature Materials. 2018;17(12):1052-3.

[80] THE 17 GOALS. United Nations, Department of Economic and Social Affairs.; 2015.

[81] Puettmann ME, Wilson JB. Life-cycle analysis of wood products: Cradle-to-gate LCI of residential wood building materials. Wood and Fiber Science. 2005:18-29.

[82] Kretschmann D. Mechanical properties of wood. Wood handbook : wood as an engineering material: chapter 5 Centennial ed General technical report FPL ; GTR-190 Madison, WI : US Dept of Agriculture, Forest Service, Forest Products Laboratory. 2010:5.1-5.46.

[83] Toumpanaki E, Shah DU, Eichhorn SJ. Beyond What Meets the Eye: Imaging and Imagining Wood Mechanical–Structural Properties. 2021;33(28):2001613.

[84] Johnsson S, Andersson E, Thollander P, Karlsson MJE. Energy savings and greenhouse gas mitigation potential in the Swedish wood industry. Energy. 2019;187:115919.

[85] Huang J, Zhao B, Liu T, Mou J, Jiang Z, Liu J, et al. Wood-Derived Materials for Advanced Electrochemical Energy Storage Devices. Advanced Functional Materials. 2019;29(31):1902255.

[86] Zhu H, Luo W, Ciesielski PN, Fang Z, Zhu JY, Henriksson G, et al. Wood-Derived Materials for Green Electronics, Biological Devices, and Energy Applications. Chemical Reviews. 2016;116(16):9305-74.

[87] Chen G, Li T, Chen C, Kong W, Jiao M, Jiang B, et al. Scalable Wood Hydrogel Membrane with Nanoscale Channels. ACS Nano. 2021;15(7):11244-52.

[88] Xia Q, Chen C, Yao Y, He S, Wang X, Li J, et al. In Situ Lignin Modification toward Photonic Wood. Advanced Materials. 2021;33(8):2001588.

[89] Wang X, Zhan T, Liu Y, Shi J, Pan B, Zhang Y, et al. Large-Size Transparent Wood for Energy-Saving Building Applications. ChemSusChem. 2018;11(23):4086-93.

[90] Iwamoto S, Nakagaito AN, Yano H, Nogi M. Optically transparent composites reinforced with plant fiber-based nanofibers. Applied Physics A. 2005;81(6):1109-12.

[91] Nogi M, Yano H. Transparent Nanocomposites Based on Cellulose Produced by Bacteria Offer Potential Innovation in the Electronics Device Industry. Adv Mater. 2008;20(10):1849-52.

[92] Berglund LA, Burgert I. Bioinspired Wood Nanotechnology for Functional Materials. Advanced Materials. 2018;30(19):1704285.

[93] Cai H, Wang Z, Xie D, Zhao P, Sun J, Qin D, et al. Flexible transparent wood enabled by epoxy resin and ethylene glycol diglycidyl ether. Journal of Forestry Research. 2021;32(4):1779-87.

[94] Yu Z, Yao Y, Yao J, Zhang L, Chen Z, Gao Y, et al. Transparent wood containing CsxWO3 nanoparticles for heat-shielding window applications. Journal of Materials Chemistry A. 2017;5(13):6019-24.

[95] Zhang L, Wang A, Zhu T, Chen Z, Wu Y, Gao Y. Transparent Wood Composites Fabricated by Impregnation of Epoxy Resin and W-Doped VO2 Nanoparticles for Application in Energy-Saving Windows. ACS Applied Materials & Interfaces. 2020;12(31):34777-83.

[96] Qiu Z, Xiao Z, Gao L, Li J, Wang H, Wang Y, et al. Transparent wood bearing a shielding effect to infrared heat and ultraviolet via incorporation of modified antimony-doped tin oxide nanoparticles. Composites Science and Technology. 2019;172:43-8.

[97] Tang Q, Zou M, Chang L, Guo W. A super-flexible and transparent wood film/silver nanowire electrode for optical and capacitive dual-mode sensing wood-based electronic skin. Chemical Engineering Journal. 2022;430:132152.

[98] Li Y, Fu Q, Yang X, Berglund L. Transparent wood for functional and structural applications. Philosophical Transactons of The Royal Society A: Mathematical, Physical and Engineering Sciences. 2018;376(2112):20170182.

[99] Li Y, Vasileva E, Sychugov I, Popov S, Berglund L. Optically Transparent Wood: Recent Progress, Opportunities, and Challenges. Advanced Optical Materials. 2018;6(14):1800059.

[100] Zhang J, Koubaa A, Tao Y, Li P, Xing D. The emerging development of transparent wood: materials, characteristics, and applications. Current Forestry Reports. 2022;8:333-45.

[101] Wang J, Zhu JG. Prospects and Applications of Biomass-Based Transparent Wood: An Architectural Glass Perspective. Frontiers in Chemistry. 2021;9:747385.

[102] Zhu S, Kumar Biswas S, Qiu Z, Yue Y, Fu Q, Jiang F, et al. Transparent wood-based functional materials via a top-down approach. Progress in Materials Science. 2023;132:101025.

[103] Shan X, Wu J, Zhang X, Wang L, Yang J, Chen Z, et al. Wood for Application in Electrochemical Energy Storage Devices. Cell Reports Physical Science. 2021;2(12):100654.

[104] Li J, Chen C, Zhu JY, Ragauskas AJ, Hu L. In Situ Wood Delignification toward Sustainable Applications. Accounts of Materials Research. 2021;2(8):606-20.

[105] Jiang F, Li T, Li Y, Zhang Y, Gong A, Dai J, et al. Wood-Based Nanotechnologies toward Sustainability. Adv Mater. 2018;30(1):1703453.

[106] Fink S. Transparent Wood – A New Approach in the Functional Study of Wood Structure. Holzforschung. 1992;46(5):403-8.

[107] Wegst UGK, Bai H, Saiz E, Tomsia AP, Ritchie RO. Bioinspired structural materials. Nature Materials. 2015;14(1):23-36.

[108] Katers JF, Snippen AJ, Puettmann ME. Life-Cycle Inventory of Wood Pellet Manufacturing and Utilization in Wisconsin*. Forest Products Journal. 2012;62(4):289-95.

[109] Agarwal UP. Raman imaging to investigate ultrastructure and composition of plant cell walls: distribution of lignin and cellulose in black spruce wood (Picea mariana). Planta. 2006;224(5):1141-53.

[110] Pettersen R. The chemical composition of wood. The Chemistry of Solid Wood In Advances in Chemistry Series 1984;(Book 207) 57-126.

[111] Fahlén J, Salmén L. Cross-sectional structure of the secondary wall of wood fibers as affected by processing. Journal of Materials Science. 2003;38(1):119-26.

[112] Yano H, Hirose A, Inaba S. High-strength wood-based materials. Journal of Materials Science Letters. 1997;16(23):1906-9.

[113] Ansell MP. 1 - Wood microstructure – A cellular composite. In: Ansell MP, editor. Wood Composites: Woodhead Publishing; 2015. p. 3-26.

[114] Chen C, Kuang Y, Zhu S, Burgert I, Keplinger T, Gong A, et al. Structure–property–function relationships of natural and engineered wood. Nature Reviews Materials. 2020;5(9):642-66.

[115] Blomberg J, Persson B, Blomberg A. Effects of semi-isostatic densification of wood on the variation in strength properties with density. Wood Science and Technology. 2005;39(5):339-50.

[116] Zobel BJ, Van Buijtenen JP. Wood variation: its causes and control: Springer Science & Business Media; 2012.

[117] Bertaud F, Holmbom B. Chemical composition of earlywood and latewood in Norway spruce heartwood, sapwood and transition zone wood. Wood Science and Technology. 2004;38(4):245-56.

[118] Konstantinov A, Lomunov A, Iuzhina TN, Gray G. Investigation of wood anisotropy under dynamic loading. Problems of Strength and Plasticity. 2018;80:555-65.

[119] Wu Y, Wang Y, Yang F. Comparison of Multilayer Transparent Wood and Single Layer Transparent Wood With the Same Thickness. Frontiers in Materials. 2021;8:633345.

[120] Fu Q, Yan M, Jungstedt E, Yang X, Li Y, Berglund LA. Transparent plywood as a load-bearing and luminescent biocomposite. Composites Science and Technology. 2018;164:296-303.

[121] Ramage MH, Burridge H, Busse-Wicher M, Fereday G, Reynolds T, Shah DU, et al. The wood from the trees: The use of timber in construction. Renewable and Sustainable Energy Reviews. 2017;68:333-59.

[122] Parthasarathi R, Bellesia G, Chundawat SPS, Dale BE, Langan P, Gnanakaran S. Insights into Hydrogen Bonding and Stacking Interactions in Cellulose. The Journal of Physical Chemistry A. 2011;115(49):14191-202.

[123] Wu Y, Wu J, Yang F, Tang C, Huang Q. Effect of H2O2 Bleaching Treatment on the Properties of Finished Transparent Wood. Polymers. 2019;11(5):776.

[124] Buschle-Diller G, Yang XD, Yamamoto R. Enzymatic Bleaching of Cotton Fabric with Glucose Oxidase. Textile Research Journal. 2001;71(5):388-94.

[125] Bajpai P, Anand A, Bajpai PK. Bleaching with lignin-oxidizing enzymes. Biotechnology annual review. 2006;12:349-78.

[126] Gupta GK, Kapoor RK, Shukla P. Advanced Techniques for Enzymatic and Chemical Bleaching for Pulp and Paper Industries. In: Shukla P, editor. Microbial Enzymes and Biotechniques: Interdisciplinary Perspectives. Singapore: Springer Singapore; 2020. p. 43-56.

[127] Huang D, Wu J, Chen C, Fu X, Brozena AH, Zhang Y, et al. Precision Imprinted Nanostructural Wood. 2019;31(48):1903270.

[128] Montanari C, Ogawa Y, Olsén P, Berglund LA. High Performance, Fully Bio-Based, and Optically Transparent Wood Biocomposites. Advanced science. 2021;8(12):2100559.

[129] Li Y, Fu Q, Rojas R, Yan M, Lawoko M, Berglund L. Lignin-Retaining Transparent Wood. 2017;10(17):3445-51.

[130] Peng X, Li Z, Wang D, Li Z, Liu C, Wang R, et al. A facile crosslinking strategy endows the traditional additive flame retardant with enormous flame retardancy improvement. Chemical Engineering Journal. 2021;424:130404.

[131] Xia Q, Chen C, Li T, He S, Gao J, Wang X, et al. Solar-assisted fabrication of large-scale, patternable transparent wood. Science Advances. 2021;7(5):eabd7342.

[132] Li Y, Yang X, Fu Q, Rojas R, Yan M, Berglund L. Towards centimeter thick transparent wood through interface manipulation. Journal of Materials Chemistry A. 2018;6(3):1094-101.

[133] Höglund M, Johansson M, Sychugov I, Berglund LA. Transparent Wood Biocomposites by Fast UV-Curing for Reduced Light-Scattering through Wood/Thiol–ene Interface Design. ACS Applied Materials & Interfaces. 2020;12(41):46914-22.

[134] Mi R, Li T, Dalgo D, Chen C, Kuang Y, He S, et al. A Clear, Strong, and Thermally Insulated Transparent Wood for Energy Efficient Windows. Advanced Functional Materials. 2020;30(1):1907511.

[135] Qin J, Li X, Shao Y, Shi K, Zhao X, Feng T, et al. Optimization of delignification process for efficient preparation of transparent wood with high strength and high transmittance. Vacuum. 2018;158:158-65.

[136] Montanari C, Olsén P, Berglund LA. Interface tailoring by a versatile functionalization platform for nanostructured wood biocomposites. Green Chemistry. 2020;22(22):8012-23.

[137] Chu T, Gao Y, Yi L, Fan C, Yan L, Ding C, et al. Highly fire-retardant optical wood enabled by transparent fireproof coatings. Advanced Composites and Hybrid Materials. 2022;5(3):1821-9.

[138] Wu J, Liang Y, Xia C, Ma X, Fei B, Wu Y, et al. Laminated Transparent Woods with Adjustable Optical and Enhanced Mechanical Properties. Advanced Materials Technologies. 2023;8(1):2200704.

[139] Montanari C, Li Y, Chen H, Yan M, Berglund LA. Transparent Wood for Thermal Energy Storage and Reversible Optical Transmittance. ACS Applied Materials & Interfaces. 2019;11(22):20465-72.

[140] Jia C, Chen C, Mi R, Li T, Dai J, Yang Z, et al. Clear Wood toward High-Performance Building Materials. ACS Nano. 2019;13(9):9993-10001.

[141] Samanta P, Samanta A, Montanari C, Li Y, Maddalena L, Carosio F, et al. Fire-retardant and transparent wood biocomposite based on commercial thermoset. Composites Part A: Applied Science and Manufacturing. 2022;156:106863.

[142] Standard Test Method for Haze and Luminous Transmittance of Transparent Plastics, ASTM D1003. American Society for Testing and Materials. West Conshohocken2000.

[143] Yaddanapudi HS, Hickerson N, Saini S, Tiwari A. Fabrication and characterization of transparent wood for next generation smart building applications. Vacuum. 2017;146:649-54.

[144] Chen H, Baitenov A, Li Y, Vasileva E, Popov S, Sychugov I, et al. Thickness Dependence of Optical Transmittance of Transparent Wood: Chemical Modification Effects. ACS Applied Materials & Interfaces. 2019;11(38):35451-7.

[145] Chen H, Montanari C, Shanker R, Marcinkevicius S, Berglund LA, Sychugov I. Photon Walk in Transparent Wood: Scattering and Absorption in Hierarchically Structured Materials. Advanced Optical Materials. 2022;10(8):2102732.

[146] Foster KEO, Jones R, Miyake GM, Srubar WV. Mechanics, optics, and thermodynamics of water transport in chemically modified transparent wood composites. Composites Science and Technology. 2021;208:108737.

[147] Zhou J, Xu W. Toward interface optimization of transparent wood with wood color and texture by silane coupling agent. Journal of Materials Science. 2022;57(10):5825-38.

[148] Reinelt S, Tabatabai M, Moszner N, Fischer UK, Utterodt A, Ritter H. Synthesis and Photopolymerization of Thiol-Modified Triazine-Based Monomers and Oligomers for the Use in Thiol-Ene-Based Dental Composites. Macromolecular Chemistry and Physics. 2014;215(14):1415-25.

[149] Vasileva E, Chen H, Li Y, Sychugov I, Yan M, Berglund L, et al. Light Scattering by Structurally Anisotropic Media: A Benchmark with Transparent Wood. Advanced Optical Materials. 2018;6(23):1800999.

[150] Vasileva E, Baitenov A, Chen H, Li Y, Sychugov I, Yan M, et al. Effect of transparent wood on the polarization degree of light. Opt Lett. 2019;44(12):2962-5.

[151] Wu Y, Zhou J, Yang F, Wang Y, Wang J, Zhang J. A strong multilayered transparent wood with natural wood color and texture. Journal of Materials Science. 2021;56(13):8000-13.

[152] Montanari C, Olsén P, Berglund LA. Sustainable Wood Nanotechnologies for Wood Composites Processed by In-Situ Polymerization. Frontiers in Chemistry. 2021;9.

[153] Pang J, Baitenov A, Montanari C, Samanta A, Berglund L, Popov S, et al. Light Propagation in Transparent Wood: Efficient Ray-Tracing Simulation and Retrieving an Effective Refractive Index of Wood Scaffold. Advanced Photonics Research. 2021;2(11):2100135.

[154] Wang Y, Wu Y, Yang F, Yang L, Wang J, Zhou J, et al. A highly transparent compressed wood prepared by cell wall densification. Wood Science and Technology. 2022;56(2):669-86.

[155] Lang AW, Li Y, De Keersmaecker M, Shen DE, Österholm AM, Berglund L, et al. Transparent Wood Smart Windows: Polymer Electrochromic Devices Based on Poly(3,4-Ethylenedioxythiophene):Poly(Styrene Sulfonate) Electrodes. ChemSusChem. 2018;11(5):854-63.

[156] Jungstedt E, Östlund S, Berglund LA. Transverse fracture toughness of transparent wood biocomposites by FEM updating with cohesive zone fracture modeling. Composites Science and Technology. 2022;225:109492.

[157] Arehart JH. Energy Performance Anlaysis of Transparent Wood Composite-Based Glazing Systems in Commerical Buildings: University of Colorado at Boulder; 2017.

[158] Wang Y, Zhang X, Ding X, Zhang P, Shu M, Zhang Q, et al. Imidization-induced carbon nitride nanosheets orientation towards highly thermally conductive polyimide film with superior flexibility and electrical insulation. Composites Part B: Engineering. 2020;199:108267.

[159] Uetani K, Takahashi K, Watanabe R, Tsuneyasu S, Satoh T. Thermal Diffusion Films with In-Plane Anisotropy by Aligning Carbon Fibers in a Cellulose Nanofiber Matrix. ACS Applied Materials & Interfaces. 2022;14(29):33903-11.

[160] Khoshnava SM, Rostami R, Mohamad Zin R, Štreimikienė D, Mardani A, Ismail M. The Role of Green Building Materials in Reducing Environmental and Human Health Impacts. International journal of environmental research and public health. 2020;17(7).

[161] Li L, Wang P, Wang H, Zhang M. Green Building Materials Evaluation and Empirical Research Based on the Regional Endowment. AASRI Procedia. 2012;3:381-6.

[162] Zhang Y, Shan K, Li X, Li H, Wang S. Research and Technologies for next-generation high-temperature data centers – State-of-the-arts and future perspectives. Renewable and Sustainable Energy Reviews. 2023;171:112991.

[163] Bechthold M, Weaver JC. Materials science and architecture. Nature Reviews Materials. 2017;2:17082.

[164] Kaschuk JJ, Al Haj Y, Rojas OJ, Miettunen K, Abitbol T, Vapaavuori J. Plant-Based Structures as an Opportunity to Engineer Optical Functions in Next-Generation Light Management. Adv Mater. 2022;34(6):2104473.

[165] Furszyfer Del Rio DD, Sovacool BK, Foley AM, Griffiths S, Bazilian M, Kim J, et al. Decarbonizing the glass industry: A critical and systematic review of developments, sociotechnical systems and policy options. Renewable and Sustainable Energy Reviews. 2022;155:111885.

[166] Mi R, Chen C, Keplinger T, Pei Y, He S, Liu D, et al. Scalable aesthetic transparent wood for energy efficient buildings. Nature Communications. 2020;11(1):3836.

[167] Zhou J, Liu Y, Yang Z, Wang X, Li Y, Liu F, et al. Turing Pattern-Inspired Highly Transparent Wood for Multifunctional Smart Glass with Superior Thermal Management and UV-Blocking Ability. Advanced Sustainable Systems. 2022;6(8):2200132.

[168] Subba Rao AN, Nagarajappa GB, Nair S, Chathoth AM, Pandey KK. Flexible transparent wood prepared from poplar veneer and polyvinyl alcohol. Composites Science and Technology. 2019;182:107719.

[169] Montanari C, Chen H, Lidfeldt M, Gunnarsson J, Olsén P, Berglund LA. Sustainable Thermal Energy Batteries from Fully Bio-Based Transparent Wood. Small. 2023;n/a(n/a):2301262.

[170] Wang L, Liu Y, Zhan X, Luo D, Sun X. Photochromic transparent wood for photo-switchable smart window applications. Journal of Materials Chemistry C. 2019;7(28):8649-54.

[171] Liu S, Tso CY, Lee HH, Du YW, Yu KM, Feng S-P, et al. Self-Densified Optically Transparent VO2 Thermochromic Wood Film for Smart Windows. ACS Applied Materials & Interfaces. 2021;13(19):22495-504.

[172] Liu Y, Yang H, Ma C, Luo S, Xu M, Wu Z, et al. Luminescent Transparent Wood Based on Lignin-Derived Carbon Dots as a Building Material for Dual-Channel, Real-Time, and Visual Detection of Formaldehyde Gas. ACS Applied Materials & Interfaces. 2020;12(32):36628-38.

[173] Shahzad F, Alhabeb M, Hatter CB, Anasori B, Man Hong S, Koo CM, et al. Electromagnetic interference shielding with 2D transition metal carbides (MXenes). Science. 2016;353(6304):1137-40.

[174] Yang L, Wu Y, Yang F, Wang W. Study on the preparation process and performance of a conductive, flexible, and transparent wood. Journal of Materials Research and Technology. 2021;15:5396-404.

[175] Aldalbahi A, El-Naggar ME, Khattab TA, Hossain M. Preparation of flame-retardant, hydrophobic, ultraviolet protective, and luminescent transparent wood. Luminescence. 2021;36(8):1922-32.

[176] Li Y, Yu S, Veinot JGC, Linnros J, Berglund L, Sychugov I. Luminescent Transparent Wood. Advanced Optical Materials. 2017;5(1):1600834.

[177] Xia R, Zhang W, Yang Y, Zhao J, Liu Y, Guo H. Transparent wood with phase change heat storage as novel green energy storage composites for building energy conservation. Journal of Cleaner Production. 2021;296:126598.

[178] Samanta A, Höglund M, Samanta P, Popov S, Sychugov I, Maddalena L, et al. Charge Regulated Diffusion of Silica Nanoparticles into Wood for Flame Retardant Transparent Wood. Advanced Sustainable Systems. 2022;6(4):2100354.

[179] Chen L, Xu Z, Wang F, Duan G, Xu W, Zhang G, et al. A flame-retardant and transparent wood/polyimide composite with excellent mechanical strength. Composites Communications. 2020;20:100355.

[180] Zhang L, Jiang Y, Zhou L, Jiang Z, Li L, Che W, et al. Mechanical, thermal stability, and flame retardancy performance of transparent wood composite improved with delaminated Ti3C2Tx (MXene) nanosheets. Journal of Materials Science. 2022;57(5):3348-59.

[181] Fan C, Gao Y, Li Y, Yan L, Zhuang Y, Zhang Y, et al. A flame-retardant and optically transparent wood composite. Journal of Applied Polymer Science. 2022;139(39):e52945.

[182] Müller U, Rätzsch M, Schwanninger M, Steiner M, Zöbl H. Yellowing and IR-changes of spruce wood as result of UV-irradiation. Journal of Photochemistry and Photobiology B: Biology. 2003;69(2):97-105.

[183] Xu H, Zeiger BW, Suslick KS. Sonochemical synthesis of nanomaterials. Chemical Society Reviews. 2013;42(7):2555-67.

[184] Pokhrel N, Vabbina PK, Pala N. Sonochemistry: Science and Engineering. Ultrasonics Sonochemistry. 2016;29:104-28.

[185] Yeo J, Wang Y, An AK, Zhang L. Estimation of energy efficiency for educational buildings in Hong Kong. J Clean Prod. 2019;235:453-60.

[186] Sol C, Schläfer J, Parkin IP, Papakonstantinou IJSr. Mitigation of hysteresis due to a pseudo-photochromic effect in thermochromic smart window coatings. BioResources. 2018;8(1):1-6.

[187] Lushiku E, Hjortsberg A, Granqvist CJJoAP. Radiative cooling with selectively infrared-emitting ammonia gas. Journal of Applied Physics. 1982;53(8):5526-30.

[188] Murathan EK, Manioglu G. Evaluation of phase change materials used in building components for conservation of energy in buildings in hot dry climatic regions. Renew Energ. 2020;162:1919-30.

[189] Urge-Vorsatz D, Cabeza LF, Serrano S, Barreneche C, Petrichenko K. Heating and cooling energy trends and drivers in buildings. Renew Sust Energ Rev. 2015;41:85-98.

[190] Zeyghami M, Goswami DY, Stefanakos E. A review of clear sky radiative cooling developments and applications in renewable power systems and passive building cooling. Sol Energ Mat Sol C. 2018;178:115-28.

[191] Imessad K, Derradji L, Messaoudene NA, Mokhtari F, Chenak A, Kharchi R. Impact of passive cooling techniques on energy demand for residential buildings in a Mediterranean climate. Renew Energ. 2014;71:589-97.

[192] Pu J, Shen C, Yang S, Zhang C, Chwieduk D, Kalogirou SAJE. Feasibility investigation on using silver nanorods in energy saving windows for light/heat decoupling. Energy. 2022:123289.

[193] Jeon S, Shin JJapa. Ideal spectral emissivity design for extreme radiative cooling. arXiv preprint arXiv:191009301. 2019.

[194] Nilsson TMJ, Niklasson GA. Radiative Cooling during the Day - Simulations and Experiments on Pigmented Polyethylene Cover Foils. Sol Energ Mat Sol C. 1995;37(1):93-118.

[195] Zhu LX, Raman AP, Fan SH. Radiative cooling of solar absorbers using a visibly transparent photonic crystal thermal blackbody. P Natl Acad Sci USA. 2015;112(40):12282-7.

[196] Zhu LX, Raman A, Fan SH. Color-preserving daytime radiative cooling. Appl Phys Lett. 2013;103(22).

[197] Rephaeli E, Raman A, Fan SH. Ultrabroadband Photonic Structures To Achieve High-Performance Daytime Radiative Cooling. Nano Lett. 2013;13(4):1457-61.

[198] Zhai Y, Ma YG, David SN, Zhao DL, Lou RN, Tan G, et al. Scalable-manufactured randomized glass-polymer hybrid metamaterial for daytime radiative cooling. Science. 2017;355(6329).

[199] Yin XB, Yang RG, Tan G, Fan SH. Terrestrial radiative cooling: Using the cold universe as a renewable and sustainable energy source. Science. 2020;370(6518):786-+.

[200] Zhu MW, Song JW, Li T, Gong A, Wang YB, Dai JQ, et al. Highly Anisotropic, Highly Transparent Wood Composites. Adv Mater. 2016;28(26):5181-+.

[201] Mi RY, Li T, Dalgo D, Chen CJ, Kuang YD, He SM, et al. A Clear, Strong, and Thermally Insulated Transparent Wood for Energy Efficient Windows. Adv Funct Mater. 2020;30(1).

[202] Mi RY, Chen CJ, Keplinger T, Pei Y, He SM, Liu DP, et al. Scalable aesthetic transparent wood for energy efficient buildings. Nat Commun. 2020;11(1).

[203] Wang X, Zhan TY, Liu Y, Shi JT, Pan B, Zhang YL, et al. Large-Size Transparent Wood for Energy-Saving Building Applications. Chemsuschem. 2018;11(23):4086-93.

[204] Qiu Z, Xiao ZF, Gao LK, Li J, Wang HG, Wang YG, et al. Transparent wood bearing a shielding effect to infrared heat and ultraviolet via incorporation of modified antimony-doped tin oxide nanoparticles. Compos Sci Technol. 2019;172:43-8.

[205] Chen L, Xu ZW, Wang F, Duan GG, Xu WH, Zhang GY, et al. A flame-retardant and transparent wood/polyimide composite with excellent mechanical strength. Compos Commun. 2020;20.

[206] Chu Z, Seeger SJRA. Robust superhydrophobic wood obtained by spraying silicone nanoparticles. Rsc Advances. 2015;5(28):21999-2004.

[207] Wang LH, Liu YJ, Zhan XY, Luo D, Sun XW. Photochromic transparent wood for photo-switchable smart window applications. J Mater Chem C. 2019;7(28):8649-54.

[208] Zhang T, Yang P, Chen MZ, Yang K, Cao YZ, Li XH, et al. Constructing a Novel Electroluminescent Device with High-Temperature and High-Humidity Resistance based on a Flexible Transparent Wood Film. Acs Appl Mater Inter. 2019;11(39):36010-9.

[209] Wood RJ, Lee J, Bussemaker MJ. A parametric review of sonochemistry: Control and augmentation of sonochemical activity in aqueous solutions. Ultrason Sonochem. 2017;38:351-70.

[210] Suslick KSJs. Sonochemistry. Science. 1990;247(4949):1439-45.

[211] Suslick KSJAT. The Dawn of Ultrasonics and the Palace of Science. Acoustics Today. 2019;15:4.

[212] Destaillats H, Lesko TM, Knowlton M, Wallace H, Hoffmann MR. Scale-up of sonochemical reactors for water treatment. Ind Eng Chem Res. 2001;40(18):3855-60.

[213] Mason TJ. Ultrasound in synthetic organic chemistry. Chem Soc Rev. 1997;26(6):443-51.

[214] Shen Y, Wang J, Lu Y, Mo L, Zhao S, Qi F, et al. Efficient removal of extractives from wood using an ultrasound-activated persulfate treatment strategy. Wood Science and Technology. 2022;56(1):171-86.

[215] Dheyab MA, Aziz AA, Jameel MS. Recent Advances in Inorganic Nanomaterials Synthesis Using Sonochemistry: A Comprehensive Review on Iron Oxide, Gold and Iron Oxide Coated Gold Nanoparticles. Molecules. 2021;26(9).

[216] Neelakantan NK, Weisensee PB, Overcash JW, Torrealba EJ, King WP, Suslick KSJRa. Spray-on omniphobic ZnO coatings. RSC advances. 2015;5(85):69243-50.

[217] Salat M, Petkova P, Hoyo J, Perelshtein I, Gedanken A, Tzanov TJCp. Durable antimicrobial cotton textiles coated sonochemically with ZnO nanoparticles embedded in an in-situ enzymatically generated bioadhesive. Carbohyd Polym. 2018;189:198-203.

[218] Radmanovic K, Roginic R, Lucic RB, Jovanovic J, Jug M, Sedlar T, et al. Effect of a High Loading Rate on the Compressive Properties of Beech Wood in the Longitudinal Direction. Bioresources. 2021;16(2):4093-105.

[219] Jungstedt E, Montanari C, Ostlund S, Berglund L. Mechanical properties of transparent high strength biocomposites from delignified wood veneer. Compos Part a-Appl S. 2020;133.

[220] He SM, Chen CJ, Li T, Song JW, Zhao XP, Kuang YD, et al. An Energy-Efficient, Wood-Derived Structural Material Enabled by Pore Structure Engineering towards Building Efficiency. Small Methods. 2020;4(1).

[221] Peng Z, Jiang W, Liu H. Synthesis and Electrical Properties of Tungsten-Doped Vanadium Dioxide Nanopowders by Thermolysis. The Journal of Physical Chemistry C. 2007;111(3):1119-22.

[222] Wang S, Jiang T, Meng Y, Yang R, Tan G, Long YJS. Scalable thermochromic smart windows with passive radiative cooling regulation. Science. 2021;374(6574):1501-4.

[223] Noor N, Chew CK, Bhachu DS, Waugh MR, Carmalt CJ, Parkin IPJJoMCC. Influencing FTO thin film growth with thin seeding layers: a route to microstructural modification. J Mater Chem C. 2015;3(36):9359-68.

[224] Wang R, Xin JH, Yang Y, Liu H, Xu L, Hu JJASS. The characteristics and photocatalytic activities of silver doped ZnO nanocrystallites. Appl Surf Sci. 2004;227(1-4):312-7.

[225] Boukir A, Fellak S, Doumenq P. Structural characterization of Argania spinosa Moroccan wooden artifacts during natural degradation progress using infrared spectroscopy (ATR-FTIR) and X-Ray diffraction (XRD). Heliyon. 2019;5(9).

[226] Hajji L, Boukir A, Assouik J, Pessanha S, Figueirinhas JL, Carvalho ML. Artificial aging paper to assess long-term effects of conservative treatment. Monitoring by infrared spectroscopy (ATR-FTIR), X-ray diffraction (XRD), and energy dispersive X-ray fluorescence (EDXRF). Microchem J. 2016;124:646-56.

[227] Agarwal UPJAilc. An overview of Raman spectroscopy as applied to lignocellulosic materials. Advances in lignocellulosics characterization. 1999:201-25.

[228] Agarwal UP, Ralph SAJAs. FT-Raman spectroscopy of wood: identifying contributions of lignin and carbohydrate polymers in the spectrum of black spruce (Picea mariana). Appl Spectrosc. 1997;51(11):1648-55.

[229] Zhao HB, Kwak JH, Zhang ZC, Brown HM, Arey BW, Holladay JE. Studying cellulose fiber structure by SEM, XRD, NMR and acid hydrolysis. Carbohyd Polym. 2007;68(2):235-41.

[230] Chike KE, Myrick ML, Lyon RE, Angel SM. Raman and near-Infrared Studies of an Epoxy-Resin. Appl Spectrosc. 1993;47(10):1631-5.

[231] Hsieh PT, Chen YC, Kao KS, Wang CM. Luminescence mechanism of ZnO thin film investigated by XPS measurement. Applied Physics A. 2008;90(2):317-21.

[232] Brun M, Berthet A, Bertolini JC. XPS, AES and Auger parameter of Pd and PdO. J Electron Spectrosc. 1999;104(1-3):55-60.

[233] Biesinger MC, Lau LWM, Gerson AR, Smart RSC. Resolving surface chemical states in XPS analysis of first row transition metals, oxides and hydroxides: Sc, Ti, V, Cu and Zn. Appl Surf Sci. 2010;257(3):887-98.

[234] Zhang J, Sun LD, Liao CS, Yan CH. A simple route towards tubular ZnO. Chem Commun. 2002(3):262-3.

[235] Rudak O, Barcik S, Rudak P, Chayeuski V, Koleda PJB. Densification of Wood–Chemical and Structural Changes Due to Ultrasonic and Mechanical Treatment. BioResources. 2021;16(4).

[236] Zhong X, Hu M, Deetman S, Steubing B, Lin HX, Hernandez GA, et al. Global greenhouse gas emissions from residential and commercial building materials and mitigation strategies to 2060. Nature Communications. 2021;12(1):6126.

[237] Wang N, Lv Y, Zhao D, Zhao W, Xu J, Yang R. Performance evaluation of radiative cooling for commercial-scale warehouse. Materials Today Energy. 2022;24:100927.

[238] Magnan AK, Pörtner H-O, Duvat VKE, Garschagen M, Guinder VA, Zommers Z, et al. Estimating the global risk of anthropogenic climate change. Nature Climate Change. 2021;11(10):879-85.

[239] Yang N, Fu Y, Xue X, Lei D, Dai J-G. Geopolymer-based sub-ambient daytime radiative cooling coating. EcoMat. 2023;5(2):e12284.

[240] Wang S, Jiang T, Meng Y, Yang R, Tan G, Long Y. Scalable thermochromic smart windows with passive radiative cooling regulation. Science. 2021;374(6574):1501-4.

[241] Rephaeli E, Raman A, Fan S. Ultrabroadband Photonic Structures To Achieve High-Performance Daytime Radiative Cooling. Nano Letters. 2013;13(4):1457-61.

[242] Lee ACL. A study of the continuum absorption within the 8–13 μm atmospheric window. Quarterly Journal of the Royal Meteorological Society. 1973;99(421):490-505.

[243] Jin Y, Jeong Y, Yu K. Infrared-Reflective Transparent Hyperbolic Metamaterials for Use in Radiative Cooling Windows. Advanced Functional Materials. 2023;33(1):2207940.

[244] Li X, Peoples J, Huang Z, Zhao Z, Qiu J, Ruan X. Full Daytime Sub-ambient Radiative Cooling in Commercial-like Paints with High Figure of Merit. Cell Reports Physical Science. 2020;1(10):100221.

[245] Mandal J, Yang Y, Yu N, Raman AP. Paints as a Scalable and Effective Radiative Cooling Technology for Buildings. Joule. 2020;4(7):1350-6.

[246] Zhang Y, Zhu W, Zhang C, Peoples J, Li X, Felicelli AL, et al. Atmospheric Water Harvesting by Large-Scale Radiative Cooling Cellulose-Based Fabric. Nano Letters. 2022;22(7):2618-26.

[247] Wu X, Li J, Jiang Q, Zhang W, Wang B, Li R, et al. An all-weather radiative human body cooling textile. Nature Sustainability. 2023;6:1446–54.

[248] Yao P, Chen Z, Liu T, Liao X, Yang Z, Li J, et al. Spider-Silk-Inspired Nanocomposite Polymers for Durable Daytime Radiative Cooling. Advanced Materials. 2022;34(51):2208236.

[249] Liu Y, Tian Y, Liu X, Chen F, Caratenuto A, Zheng Y. Intelligent regulation of VO2-PDMS-driven radiative cooling. Applied Physics Letters. 2022;120(17):171704.

[250] Tang K, Dong K, Li J, Gordon MP, Reichertz FG, Kim H, et al. Temperature-adaptive radiative coating for all-season household thermal regulation. Science. 2021;374(6574):1504-9.

[251] Cui Y, Ke Y, Liu C, Chen Z, Wang N, Zhang L, et al. Thermochromic VO2 for Energy-Efficient Smart Windows. Joule. 2018;2(9):1707-46.

[252] Ji H, Liu D, Cheng H. Infrared optical modulation characteristics of W-doped VO2(M) nanoparticles in the MWIR and LWIR regions. Materials Science in Semiconductor Processing. 2020;119:105141.

[253] Tang K, Wang X, Dong K, Li Y, Li J, Sun B, et al. A Thermal Radiation Modulation Platform by Emissivity Engineering with Graded Metal–Insulator Transition. Advanced Materials. 2020;32(36):1907071.

[254] Ono M, Chen K, Li W, Fan S. Self-adaptive radiative cooling based on phase change materials. Opt Express. 2018;26(18):A777-A87.

[255] Taylor S, Yang Y, Wang L. Vanadium dioxide based Fabry-Perot emitter for dynamic radiative cooling applications. Journal of Quantitative Spectroscopy and Radiative Transfer. 2017;197:76-83.

[256] Taylor S, Long L, McBurney R, Sabbaghi P, Chao J, Wang L. Spectrally-selective vanadium dioxide based tunable metafilm emitter for dynamic radiative cooling. Solar Energy Materials and Solar Cells. 2020;217:110739.

[257] Nishikawa K, Yatsugi K, Kishida Y, Ito K. Temperature-selective emitter. Applied Physics Letters. 2019;114(21):211104.

[258] Ito K, Watari T, Nishikawa K, Yoshimoto H, Iizuka H. Inverting the thermal radiative contrast of vanadium dioxide by metasurfaces based on localized gap-plasmons. APL Photonics. 2018;3(8):086101.

[259] Kim H, Cheung K, Auyeung RCY, Wilson DE, Charipar KM, Piqué A, et al. VO2-based switchable radiator for spacecraft thermal control. Scientific Reports. 2019;9(1):11329.

[260] Sun K, Riedel CA, Urbani A, Simeoni M, Mengali S, Zalkovskij M, et al. VO2 Thermochromic Metamaterial-Based Smart Optical Solar Reflector. ACS Photonics. 2018;5(6):2280-6.

[261] Gu J, Wei H, Ren F, Guan H, Liang S, Geng C, et al. VO2-Based Infrared Radiation Regulator with Excellent Dynamic Thermal Management Performance. ACS Applied Materials & Interfaces. 2022;14(2):2683-90.

[262] Hendaoui A, Émond N, Chaker M, Haddad É. Highly tunable-emittance radiator based on semiconductor-metal transition of VO2 thin films. Applied Physics Letters. 2013;102(6):061107.

[263] Kats MA, Sharma D, Lin J, Genevet P, Blanchard R, Yang Z, et al. Ultra-thin perfect absorber employing a tunable phase change material. Applied Physics Letters. 2012;101(22):221101.

[264] Kim H, Lahneman D, Rohde C, Piqué A. VO2-based thin-film radiators with variable thermal emissivity. Thin Solid Films. 2022;759:139455.

[265] Berglund LA, Burgert I. Bioinspired Wood Nanotechnology for Functional Materials. Advanced Materials. 2018;30(19):1704285.

[266] Ji H, Liu D, Zhang C, Cheng H. VO2/ZnS core-shell nanoparticle for the adaptive infrared camouflage application with modified color and enhanced oxidation resistance. Solar Energy Materials and Solar Cells. 2018;176:1-8.

[267] Lin S, Wang H, Zhang X, Wang D, Zu D, Song J, et al. Direct spray-coating of highly robust and transparent Ag nanowires for energy saving windows. Nano Energy. 2019;62:111-6.

[268] Deru M, Field K, Studer D, Benne K, Griffith B, Torcellini P. US Department of Energy Commercial Reference Building Models of the National Building Stock. 2011.

[269] Deru M, Field K, Studer D, Kyle B, Griffith B, Paul T, et al. U.S. Department of Energy Commercial Reference Building Models of the National Building Stock2011.

[270] Wyszecki G, Stiles WS. Color science: concepts and methods, quantitative data and formulae: John wiley & sons; 2000.

[271] How Does Emissivity Affect Thermal Imaging? How Does Emissivity Affect Thermal Imaging?2021.

[272] Jung J, Lee H, Ha I, Cho H, Kim KK, Kwon J, et al. Highly Stretchable and Transparent Electromagnetic Interference Shielding Film Based on Silver Nanowire Percolation Network for Wearable Electronics Applications. ACS Applied Materials & Interfaces. 2017;9(51):44609-16.

[273] Majid SS, Shukla DK, Rahman F, Khan S, Gautam K, Ahad A, et al. Insulator-metal transitions in the T phase Cr-doped and M1 phase undoped VO2 thin films. Physical Review B. 2018;98(7):075152.

[274] Jones AC, Berweger S, Wei J, Cobden D, Raschke MB. Nano-optical Investigations of the Metal−Insulator Phase Behavior of Individual VO2 Microcrystals. Nano Letters. 2010;10(5):1574-81.

[275] Gurunatha KL, Sathasivam S, Li J, Portnoi M, Parkin IP, Papakonstantinou I. Combined Effect of Temperature Induced Strain and Oxygen Vacancy on Metal-Insulator Transition of VO2 Colloidal Particles. Advanced Functional Materials. 2020;30(49):2005311.

[276] Nishikawa K, Yoshimura M, Watanabe Y. Phase transition behavior in nanostructured VO2 with M1, M2, and R phases observed via temperature-dependent XRD measurements. Journal of Vacuum Science & Technology A. 2022;40(3):033401.

[277] Jia C, Chen C, Kuang Y, Fu K, Wang Y, Yao Y, et al. From Wood to Textiles: Top-Down Assembly of Aligned Cellulose Nanofibers. Advanced Materials. 2018;30(30):1801347.

[278] Petri DFS. Characterization of spin-coated polymer films. Journal of the Brazilian Chemical Society. 2002;13:695-9.

[279] Ünlü MS, Kishino K, Liaw HJ, Morkoç H. A theoretical study of resonant cavity-enhanced photodectectors with Ge and Si active regions. Journal of Applied Physics. 1992;71(8):4049-58.

[280] Noh H, Chong Y, Stone AD, Cao H. Perfect coupling of light to surface plasmons by coherent absorption. Physical Review Letters. 2012;108(18):186805.

[281] July weather forecast, Yakutsk, Russia. July Weather Forecast, Yakutsk, Russia; 2023.

[282] Roy S, Ansari KJ, Jampa SSK, Vutukuri P, Mukherjee R. Influence of Substrate Wettability on the Morphology of Thin Polymer Films Spin-Coated on Topographically Patterned Substrates. ACS Applied Materials & Interfaces. 2012;4(4):1887-96.

[283] Zhang S, Zhu N, Lv S. Human response and productivity in hot environments with directed thermal radiation. Building and Environment. 2021;187:107408.

[284] Ma Z, Zhao D, Wang F, Yang R. A novel thermal comfort and energy saving evaluation model for radiative cooling and heating textiles. Energy and Buildings. 2022;258:111842.

[285] Wu X, Li J, Jiang Q, Zhang W, Wang B, Li R, et al. An all-weather radiative human body cooling textile. Nature Sustainability. 2023;6(11):1446-54.

[286] Steketee J. Spectral emissivity of skin and pericardium. Physics in Medicine & Biology. 1973;18(5):686.

[287] He M, Zhao B, Yue X, Chen Y, Qiu F, Zhang T. Infrared radiative modulating textiles for personal thermal management: principle, design and application. Nano Energy. 2023;116:108821.

[288] Hsu P-C, Liu X, Liu C, Xie X, Lee HR, Welch AJ, et al. Personal Thermal Management by Metallic Nanowire-Coated Textile. Nano Letters. 2015;15(1):365-71.

[289] Fei L, Yu W, Tan J, Yin Y, Wang C. High Solar Energy Absorption and Human Body Radiation Reflection Janus Textile for Personal Thermal Management. Advanced Fiber Materials. 2023;5(3):955-67.

[290] Zhu Y, Wang W, Zhou Y, Qin R, Qin B, Zhou T, et al. Colored Woven Cloth-Based Textile for Passive Radiative Heating. Laser & Photonics Reviews. 2023;17(11):2300293.

[291] Sun Y, Yu B, Liu Y, Cheng B, Wang J, Yan J, et al. Novel bio-based nanosheets: Improving the fire safety, electromagnetic shielding and mechanical properties of polylactic acid. Composites Part A: Applied Science and Manufacturing. 2024;179:108044.

[292] Wu X-E, Wang Y, Liang X, Zhang Y, Bi P, Zhang M, et al. Durable Radiative Cooling Multilayer Silk Textile with Excellent Comprehensive Performance. Advanced Functional Materials. 2024;34(11):2313539.

[293] Li X, Yang Y, Quan Z, Wang L, Ji D, Li F, et al. Tailoring body surface infrared radiation behavior through colored nanofibers for efficient passive radiative heating textiles. Chemical Engineering Journal. 2022;430:133093.

[294] Larciprete MC, Gloy YS, Li Voti R, Cesarini G, Leahu G, Bertolotti M, et al. Temperature dependent emissivity of different stainless steel textiles in the infrared range. International Journal of Thermal Sciences. 2017;113:130-5.

[295] Sui C, Pu J, Chen T-H, Liang J, Lai Y-T, Rao Y, et al. Dynamic electrochromism for all-season radiative thermoregulation. Nature Sustainability. 2023;6(4):428-37.

[296] Fan Q, Fan H, Han H, Bai Z, Wu X, Hou C, et al. Dynamic Thermoregulatory Textiles Woven from Scalable-Manufactured Radiative Electrochromic Fibers. Advanced Functional Materials. 2024;34(16):2310858.

[297] Chen T-H, Hong Y, Fu C-T, Nandi A, Xie W, Yin J, et al. A kirigami-enabled electrochromic wearable variable-emittance device for energy-efficient adaptive personal thermoregulation. PNAS Nexus. 2023;2(6):pgad165.

[298] Li K, Li M, Lin C, Liu G, Li Y, Huang B. A Janus Textile Capable of Radiative Subambient Cooling and Warming for Multi-Scenario Personal Thermal Management. Small. 2023;19(19):2206149.

[299] Li X, Liu M, Chen K, Li L, Pei G, Zhao B. Adaptive fabric with emissivity regulation for thermal management of humans. 2024.

[300] Wan C, Zhang Z, Woolf D, Hessel CM, Rensberg J, Hensley JM, et al. On the Optical Properties of Thin-Film Vanadium Dioxide from the Visible to the Far Infrared. Annalen der Physik. 2019;531(10):1900188.

[301] Zhang X, Qiu J, Li X, Zhao J, Liu L. Complex refractive indices measurements of polymers in visible and near-infrared bands. Appl Opt. 2020;59(8):2337-44.

[302] Babar S, Weaver JH. Optical constants of Cu, Ag, and Au revisited. Appl Opt. 2015;54(3):477-81.

[303] Wang N, Duchamp M, Xue C, Dunin-Borkowski RE, Liu G, Long Y. Single-Crystalline W-Doped VO2 Nanobeams with Highly Reversible Electrical and Plasmonic Responses Near Room Temperature. Advanced Materials Interfaces. 2016;3(15):1600164.

[304] Wang N, Goh QS, Lee PL, Magdassi S, Long Y. One-step hydrothermal synthesis of rare earth/W-codoped VO2 nanoparticles: Reduced phase transition temperature and improved thermochromic properties. Journal of Alloys and Compounds. 2017;711:222-8.

[305] Calvi L, Leufkens L, Yeung CPK, Habets R, Mann D, Elen K, et al. A comparative study on the switching kinetics of W/VO2 powders and VO2 coatings and their implications for thermochromic glazing. Solar Energy Materials and Solar Cells. 2021;224:110977.

[306] Warwick MEA, Binions R. Advances in thermochromic vanadium dioxide films. Journal of Materials Chemistry A. 2014;2(10):3275-92.

[307] Liu K, Lee S, Yang S, Delaire O, Wu J. Recent progresses on physics and applications of vanadium dioxide. Materials Today. 2018;21(8):875-96.

[308] Li M, Magdassi S, Gao Y, Long Y. Hydrothermal Synthesis of VO2 Polymorphs: Advantages, Challenges and Prospects for the Application of Energy Efficient Smart Windows. Small. 2017;13(36):1701147.

[309] Liu G. Hydrothermal synthesis of vanadium dioxide nanoparticles and its applications 2021.

[310] Li D, Zhao Z, Wang C, Deng S, Yang J, Wang X, et al. Influence of the charge compensation effect on the metal–insulator transition of Mg-W co-doped VO2. Applied Surface Science. 2022;579:151990.

[311] Ding X, Li Y, Zhang Y. Sol-Gel Derived Tungsten Doped VO2 Thin Films on Si Substrate with Tunable Phase Transition Properties. 2023;28(9):3778.

[312] Liang S, Shi Q, Zhu H, Peng B, Huang W. One-Step Hydrothermal Synthesis of W-Doped VO2 (M) Nanorods with a Tunable Phase-Transition Temperature for Infrared Smart Windows. ACS Omega. 2016;1(6):1139-48.

[313] Hilborn R, Walters CJ, Ludwig D. SUSTAINABLE EXPLOITATION OF RENEWABLE RESOURCES. 1995;26(Volume 26):45-67.

[314] Martinka J, Mitterpach J, Štefko T, Wachter I, Rantuch P. Fire hazard of epoxy-based transparent wood. Journal of Thermal Analysis and Calorimetry. 2023;148(19):9893-907.

[315] Zhi M, Yang X, Fan R, Yue S, Zheng L, Liu Q, et al. A comprehensive review of reactive flame-retardant epoxy resin: fundamentals, recent developments, and perspectives. Polymer Degradation and Stability. 2022;201:109976.

[316] Wang CS, Lin CH. Synthesis and properties of phosphorus-containing epoxy resins by novel method. Journal of Polymer Science Part A: Polymer Chemistry. 1999;37(21):3903-9.

[317] Lin CH, Wu CY, Wang CS. Synthesis and properties of phosphorus-containing advanced epoxy resins. II. Journal of Applied Polymer Science. 2000;78(1):228-35.

[318] Yang Y, Wang D-Y, Jian R-K, Liu Z, Huang G. Chemical structure construction of DOPO-containing compounds for flame retardancy of epoxy resin: A review. Progress in Organic Coatings. 2023;175:107316.

[319] Ye G, Huo S, Wang C, Zhang Q, Wang B, Guo Z, et al. Fabrication of flame-retardant, strong, and tough epoxy resins by solvent-free polymerization with bioderived, reactive flame retardant. Sustainable Materials and Technologies. 2024;39:e00853.

[320] Li Y, Fu Q, Rojas R, Yan M, Lawoko M, Berglund L. Lignin-Retaining Transparent Wood. ChemSusChem. 2017;10(17):3445-51.

[321] Watson R. Studies on Model Epoxy Networks [Ph.D.]. England: The University of Manchester (United Kingdom); 1994.

[322] Chen Y, Duan H, Ji S, Ma H. Novel phosphorus/nitrogen/boron-containing carboxylic acid as co-curing agent for fire safety of epoxy resin with enhanced mechanical properties. Journal of Hazardous Materials. 2021;402:123769.

[323] Ma M, Dai N, Liu X, Li C, Yuan Q, Huang F. Reinforcing the poly(silylene arylacetylene)s via strong π-π stacking interactions. Polymer. 2021;229:123976.

[324] Walsh PJ, Li H, de Parrodi CA. A Green Chemistry Approach to Asymmetric Catalysis: Solvent-Free and Highly Concentrated Reactions. Chemical Reviews. 2007;107(6):2503-45.

[325] Xia Q, Chen C, Yao Y, He S, Wang X, Li J, et al. In Situ Lignin Modification toward Photonic Wood. Advanced Materials. 2021;33(8):2001588.

[326] Shao Z, Yue W, Piao M, Ma J, Lv X, Wang D, et al. An Excellent Intrinsic Transparent Epoxy Resin with High Flame Retardancy: Synthesis, Characterization, and Properties. Macromolecular Materials and Engineering. 2019;304(10):1900254.

[327] Xia Q, Chen C, Li T, He S, Gao J, Wang X, et al. Solar-assisted fabrication of large-scale, patternable transparent wood. Science Advances.7(5):eabd7342.

[328] Wang P, Yang F, Li L, Cai Z. Flame retardancy and mechanical properties of epoxy thermosets modified with a novel DOPO-based oligomer. Polymer Degradation and Stability. 2016;129:156-67.

[329] Huo S, Song P, Yu B, Ran S, Chevali VS, Liu L, et al. Phosphorus-containing flame retardant epoxy thermosets: Recent advances and future perspectives. Progress in Polymer Science. 2021;114:101366.

[330] Wang H, Liu Q, Zhao X, Jin Z. Synthesis of reactive DOPO-based flame retardant and its application in polyurethane elastomers. Polymer Degradation and Stability. 2021;183:109440.

[331] Yang S, Wang J, Huo S, Cheng L, Wang M. Preparation and flame retardancy of an intumescent flame-retardant epoxy resin system constructed by multiple flame-retardant compositions containing phosphorus and nitrogen heterocycle. Polymer Degradation and Stability. 2015;119:251-9.

[332] Feng Y, He C, Wen Y, Ye Y, Zhou X, Xie X, et al. Improving thermal and flame retardant properties of epoxy resin by functionalized graphene containing phosphorous, nitrogen and silicon elements. Composites Part A: Applied Science and Manufacturing. 2017;103:74-83.

[333] Deng Y, Wang Y-Z, Ban D-M, Liu X-H, Zhou Q. Burning behavior and pyrolysis products of flame-retardant PET containing sulfur-containing aryl polyphosphonate. Journal of Analytical and Applied Pyrolysis. 2006;76(1):198-202.

[334] Brehme S, Schartel B, Goebbels J, Fischer O, Pospiech D, Bykov Y, et al. Phosphorus polyester versus aluminium phosphinate in poly(butylene terephthalate) (PBT): Flame retardancy performance and mechanisms. Polymer Degradation and Stability. 2011;96(5):875-84.

[335] Sun Y, Yu B, Liu Y, Yan J, Xu Z, Cheng B, et al. Bio-inspired surface manipulation of halloysite nanotubes for high-performance flame retardant polylactic acid nanocomposites. Nano Research. 2024;17(3):1595-606.

[336] Sun Y, Yuan B, Shang S, Zhang H, Shi Y, Yu B, et al. Surface modification of ammonium polyphosphate by supramolecular assembly for enhancing fire safety properties of polypropylene. Composites Part B: Engineering. 2020;181:107588.

[337] Hu X, Li M, Yang J, Liu F, Huang H, Pan H, et al. In situ fabrication of melamine hydroxy ethylidene diphosphonate wrapped montmorillonite for reducing the fire hazards of epoxy resin. Applied Clay Science. 2021;201:105934.

[338] Wang L, Lin X, Li J, Yang H, Feng X, Wan C. Konjac Glucomannan Aerogels Modified by Hydrophilic Isocyanate and Expandable Graphite with Excellent Hydrolysis Resistance, Mechanical Strength, and Flame Retardancy. Biomacromolecules. 2023;24(6):2816-27.

[339] Cuesta A, Dhamelincourt P, Laureyns J, Martínez-Alonso A, Tascón JMD. Raman microprobe studies on carbon materials. Carbon. 1994;32(8):1523-32.

[340] Cai W, Cai T, He L, Chu F, Mu X, Han L, et al. Natural antioxidant functionalization for fabricating ambient-stable black phosphorus nanosheets toward enhancing flame retardancy and toxic gases suppression of polyurethane. Journal of Hazardous Materials. 2020;387:121971.

[341] Xiang S, Chen C, Liu F, Wang L, Feng J, Lin X, et al. Phosphorus and nitrogen supramolecule for fabricating flame-retardant, transparent and robust polyvinyl alcohol film. Journal of Colloid and Interface Science. 2024;669:775-86.

[342] Liang Z, Yu Z, Liu H, Chen L, Huang X. Combustion and emission characteristics of a compression ignition engine burning a wide range of conventional hydrocarbon and alternative fuels. Energy. 2022;250:123717.

[343] Bi X, Song K, Pan Y-T, Barreneche C, Vahabi H, He J, et al. Hollow Superstructure In Situ Assembled by Single-Layer Janus Nanospheres toward Electromagnetic Shielding Flame-Retardant Polyurea Composites. Small. 2024;20(12):2307492.

[344] Zhu Z-M, Wang L-X, Dong L-P. Influence of a novel P/N-containing oligomer on flame retardancy and thermal degradation of intumescent flame-retardant epoxy resin. Polymer Degradation and Stability. 2019;162:129-37.

[345] Xu M-J, Xu G-R, Leng Y, Li B. Synthesis of a novel flame retardant based on cyclotriphosphazene and DOPO groups and its application in epoxy resins. Polymer Degradation and Stability. 2016;123:105-14.

[346] Wang X, Hu Y, Song L, Xing W, Lu H. Thermal degradation mechanism of flame retarded epoxy resins with a DOPO-substitued organophosphorus oligomer by TG-FTIR and DP-MS. Journal of Analytical and Applied Pyrolysis. 2011;92(1):164-70.

[347] Qian X, Song L, Yu B, Wang B, Yuan B, Shi Y, et al. Novel organic–inorganic flame retardants containing exfoliated graphene: preparation and their performance on the flame retardancy of epoxy resins. Journal of Materials Chemistry A. 2013;1(23):6822-30.

[348] Green J. A Review of Phosphorus-Containing Flame Retardants. Journal of Fire Sciences. 1992;10(6):470-87.